

Unclassified

①

108297

Defense Documentation Center

Defense Supply Agency

Cameron Station • Alexandria, Virginia

Logged 7-23-65

Item 1



Unclassified

NOTICE: When government or other drawings, specifications or other data are used for any purpose other than in connection with a definitely related government procurement operation, the U. S. Government thereby incurs no responsibility, nor any obligation whatsoever; and the fact that the Government may have formulated, furnished, or in any way supplied the said drawings, specifications, or other data is not to be regarded by implication or otherwise as in any manner licensing the holder or any other person or corporation, or conveying any rights or permission to manufacture, use or sell any patented invention that may in any way be related thereto.

UNCLASSIFIED

AD 467201

DEFENSE DOCUMENTATION CENTER

FOR

SCIENTIFIC AND TECHNICAL INFORMATION

CAMERON STATION ALEXANDRIA, VIRGINIA



UNCLASSIFIED

14 Rept. no.

SWR-TM-57-2

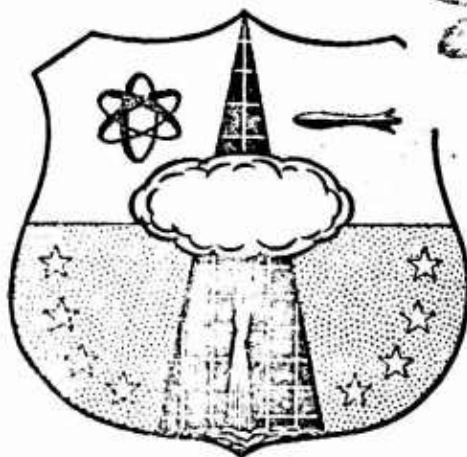
SWC
SWC
TM
57-2
c. 5

~~HEADQUARTERS~~

5) **AIR FORCE SPECIAL WEAPONS CENTER,**

~~AIR RESEARCH AND DEVELOPMENT COMMAND~~

~~KIRTLAND AIR FORCE BASE, NEW MEXICO~~



Ldc

LIBRARY COPY
DO NOT REMOVE FROM LIBRARY

PROCEEDINGS

of

FIRST SHOCK TUBE SYMPOSIUM

26-27 February 1957,

Upper Case

107201
CO
4

SWR-TM-57-2

PROCEEDINGS

of

FIRST SHOCK TUBE SYMPOSIUM

26-27 February 1957

sponsored by
Air Force Special Weapons Center

PROGRAM OF FIRST SHOCK TUBE SYMPOSIUM

Tuesday, 26 February 1957
Massachusetts Institute of Technology

Welcoming Address: Roman R. Birukoff, AFSWC *
Introduction: Jack R. Kelso, AFSWP

Air Force Special Weapons Project's Interest in Shock Tube Research:
Jack R. Kelso, AFSWP

The Air Force Shock Tube as a Research Tool:

Theodore H. Schiffman, Armour Research Foundation

Design and Performance of the General Electric Six-Inch Shock Tunnel Facility:

Walter R. Warren, Missile and Ordnance Systems Dept., General Electric Co.

The Development of a Shock Tube to Generate Variable Stepped Shock Fronts:

Richard I. Condit, Broadview Research and Development

Lunch

Inspection trip to MIT Shock Tube Laboratory

Studies of Transient Air Forces on Two-Dimensional Airfoils:

Emmet A. Witmer, Massachusetts Institute of Technology

Study of Grids in Shock Tubes:

Theodore H. Schiffman, Armour Research Foundation

The Development of the Shock Tube Facility for Airfoils Studies:

J. R. Ruetenick, Massachusetts Institute of Technology

The Surface Film Thermometer: A Versatile Shock Tube Technique:

Daniel Bershader, Lockheed Aircraft Corporation

Wednesday, 27 February 1957
Massachusetts Institute of Technology

Some Observations of Bifurcated Reflected Shock Waves:

Roger A. Strehlow and Arthur Cohen, BRL

Numerical Solution for the Reflection of a Compression Wave from a Rigid Wall:

Theodore H. Schiffman, Armour Research Foundation

The Use of the Shock Tube in Hypersonic Research:

F. R. Riddell and Mac C. Adams, AVCO Research Laboratory

Study of Re-entrant Corners:

Theodore H. Schiffman, Armour Research Foundation

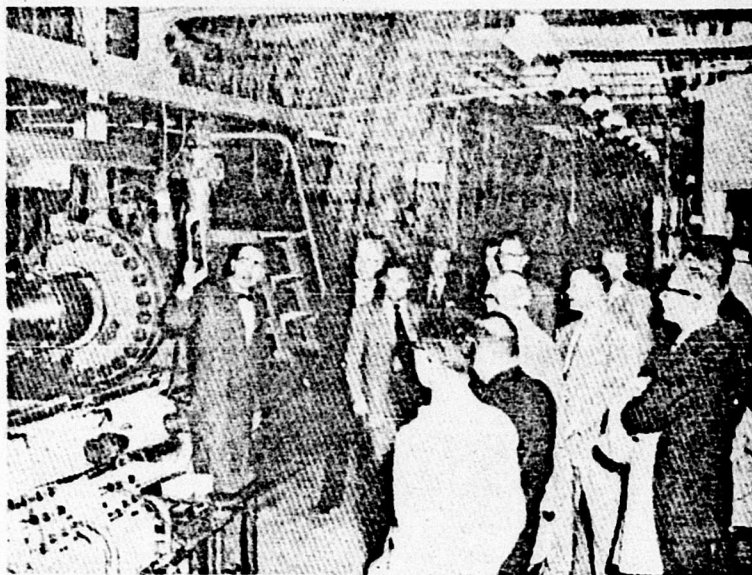
Lunch

Inspection trip to AVCO Laboratories

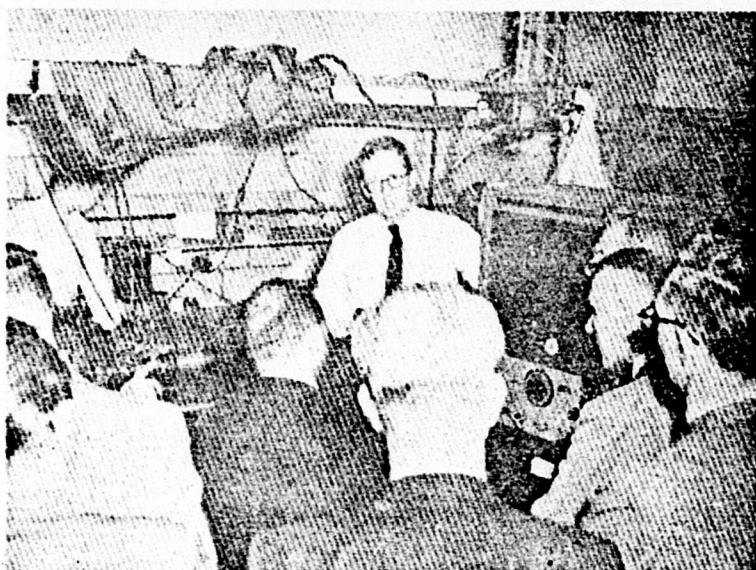
* Eric H. Wang, AFSWC, was originally scheduled to give the welcoming address. However, because of illness, he could not do so. Roman R. Birukoff, AFSWC, kindly consented to give the address instead.

TABLE OF CONTENTS

	<u>Page</u>
Welcoming Address	vii
Air Force Special Weapons Project's Interest in Shock Tube Research	1
The Air Force Shock Tube as a Research Tool	4
Design and Performance of the General Electric Six-Inch Shock Tunnel Facility	28
The Development of a Shock Tube to Generate Variable Stepped Shock Fronts	52
Studies of Transient Air Forces on Two-Dimensional Airfoils	68
Studies of Grids in Shock Tubes	111
The Development of the Shock Tube Facility for Airfoil Studies	125
The Surface Film Thermometer: A Versatile Shock Tube Technique	133
Some Observations of Bifurcated Reflected Shock Waves	143
Numerical Solution for the Reflection of a Compression Wave from a Rigid Wall	157
The Use of the Shock Tube in Hypersonic Research	171
Study of Re-entrant Corners	179



Mr. Bill Stark showing Symposium participants through the AVCO Laboratories.



Mr. John Camm conducting tour of AVCO facilities for Symposium guests.

On the first day of the conference, February 26, 1957, visitors enjoyed a trip through the MIT Shock Tube Laboratory conducted by Dr. Witmer and Dr. Ruetenick.

WELCOMING ADDRESS

Roman R. Birukoff
Air Force Special Weapons Center
Directorate of Research
Structures Division, SWRS

In reviewing the chronological events leading to this First Shock Tube Symposium, I must mention that about two years ago when Wesley Curtiss of BRL and I were discussing progress in shock tube research, I proposed then the idea of a Shock Tube Symposium. He agreed that the idea was sound and that there was a need by all to integrate experiences and exchange information among the numerous shock tube laboratories that had germinated after the war. Years went by. Wesley Curtiss left BRL and took up ceramics. I remained in Air Force shock tube laboratory work, presently under AFSWC.

Last December with the approval and cooperation of Col. E. Giller, Chief of Directorate of Research of the Air Force Special Weapons Center, and Mr. Eric H. Wang, Chief of Structures Division of the same center, questionnaires were mailed for an AFSWC-sponsored first Shock Tube Symposium. The prompt enthusiastic response permitted us to plan this symposium at such an early date. Unfortunately, neither Col. E. Giller nor Eric H. Wang are able to attend - Col. Giller because of other duties, Mr. Wang because he became ill just two weeks ago. Therefore, in behalf of the Air Force Special Weapons Center, I welcome you here. I can assure you that the Center deeply appreciates your enthusiastic response and participation in this venture.

I shall now turn the meeting over to Mr. Jack Kelso of AFSWP who will be the Moderator.

ARMED FORCES SPECIAL WEAPONS PROJECT'S INTEREST
IN SHOCK TUBE RESEARCH

Jack R. Kelso
Armed Forces Special Weapons Project

I would like to discuss the use of the shock tube from the point of view of research in the weapons effects field. Other speakers will discuss the design, development, and operation of shock tubes, and their associated equipment, however, I would like to consider their use in terms of the information thus developed. The use of the shock tube in weapons effects research began with studies of basic phenomena by Mr. L. G. Smith at Princeton during World War II. Information on shock reflections and interactions was obtained at that time which supported certain other theoretical studies being conducted by the National Defense Research Council.

Of course most of this work was applied to the use of high explosive bombs and demolition charges. However, some of the basic theory was carried over into the field of weapon effects for atomic bombs. An example of such incorporation is given in the unclassified, "Effects of Atomic Weapons" published by the Atomic Energy Commission and the Department of Defense in 1950. About this same time work on the diffraction loading of rectangular blocks was initiated at Princeton by Dr. Bleakney under an existing Office of Naval Research contract. Shortly afterward, similar work commenced at the University of Michigan under the direction of Dr. Otto LaPorte, which was subsequently followed by programs of a similar nature at the Ballistic Research Laboratories and the Armour Research Foundation. This information was then applied to the analysis of structures exposed to full scale tests in the Pacific during Operation GREENHOUSE. Since that time a number of shock tubes have been used extensively in the weapons effects field to develop information on the blast loading of various types of structures and other objects as well as certain aspects of basic phenomena. With this background, I should like to discuss the general philosophy governing the use of shock tubes in research and development projects that are supported by the Armed Forces Special Weapons Project. This headquarters is a tri-service organization which conducts research in the weapons effects field. Usually these contracts are administered through various groups within the three Services.

Generally speaking, three types of investigations are carried on in the shock tube. The studies usually concern the following:

- (1) Basic phenomena
- (2) Loading of objects
- (3) Response of objects.

Most of the effort in the weapons effects field is concerned with basic

phenomena and loading of objects, since only limited response tests can be conducted in the shock tube because of size and other considerations. Testing of scaled models representing buildings and similar civil engineering structures to obtain response data is usually unsatisfactory since modelling cannot always account for mass and gravity effects. For this reason response tests are usually confined to proof tests of small components. In the latter case, such objects are exposed in a shock tube to determine their response characteristics insofar as damage and translation are concerned.

The shocks themselves may be either flat-topped waves or peaked waves, depending on their method of generation (either with compressed air or high explosives), as well as the point of observation. Basic phenomena are usually studied by interferometer techniques and Schlieren photography. These methods may also be used to obtain information on the loading of models; but a great deal of analysis is required to accurately define the loading pattern in this way. Consequently, in recent years, miniature pressure-time gages have been positioned within solid models to obtain loading information at various points on the surface. In this way data can be quickly obtained on the same model for various shock strengths and durations. This information is then reduced and used to develop generalized loading schemes which are then employed to predict the blast loading of a full sized structure under various conditions. With a predicted loading, the response of an actual or assumed structure can then be determined analytically.

The Armed Forces Special Weapons Project shock tube research program is primarily designed to obtain information on basic phenomena and the loading of structures. The specific requirements for information are concerned with problems common to the three Services. In many areas detailed information can be obtained by a shock tube program at a very reasonable cost while it could not in the field because of economic or practical reasons. For example, entranceways and ventilation systems can be studied in the shock tube under a variety of conditions. In this way almost an infinite variation of parameters can be obtained.

In discussing the areas of interest to the Armed Forces Special Weapons Project in shock tube research I would like to refer back to the three main categories of such work previously mentioned. Those investigations that are primarily concerned with the effect of the environment on the shock, such as surface roughness or the reflection process, are considered to be studies of basic phenomena. Those investigations which involve the diffraction of shocks around objects are considered to be loading studies. An example of the latter is a test program presently underway which involves variously shaped structures such as arches, cylinders and domes. These are designed to improve our knowledge of weapons effects by determining the relation between free field blast phenomena and the loading of representative targets which can then be extended to full scale conditions through the proper scaling. In many cases the requirement for full scale tests can be reduced or eliminated through shock tube research. In other cases, information can be obtained which will assist in planning or analyzing the results of a full scale test. An example of response testing would be the exposure of dynamic pressure gages and other full scale instrumentation in the shock tube.

These examples of shock tube research that I have just described are

some of those which are in the current Armed Forces Special Weapons Project program. I should like to mention briefly those areas in which further work seems necessary. These concern primarily the development of shock tube capability to provide higher shock strengths and longer durations than those currently in use. With regard to instrumentation, it appears desirable to find a more direct method of measuring particle velocity and dynamic pressure in the shock tube, in view of the departure of shock tube flows from the ideal. For this reason we would like to know what the flow conditions actually are so that the drag coefficients developed from shock tube data for various models may be verified and correlated with wind tunnel data. Of course more information would be obtained on transient drag coefficients when longer durations are obtained in the shock tube.

In conclusion, I should like to say that a great deal of useful information has been obtained in the weapons effects field by means of shock tube research. It appears that present operational procedures are adequate to obtain data on current problems and that this is being done in a very efficient manner. However, future work seems necessary in those areas of interest I have just mentioned in order to meet future requirements.

THE AIR FORCE SHOCK TUBE AS A RESEARCH TOOL

T. H. Schiffman
Armour Research Foundation

The main purpose of the Air Force shock tube as a research tool is to simulate large explosions under laboratory conditions in order to study basic flows, loading, and response of model structures. Auxiliary applications include its use as a short duration wind tunnel for the study of muzzle blast effects on flying aircraft, and as an explosive decompression chamber simulating a pressurized aircraft cabin suddenly vented as a result of enemy fire.

In view of the complexity of such problems, the solutions do not lend themselves readily to an analytical, theoretical approach. Experimental investigations have been utilized in order to obtain the required information.

Initially, loading information on relatively simple geometric obstacles was obtained from tests in small shock tubes. These were limited to two-dimensional configurations because of the available instrumentation techniques.

Later, loading information resulted from two- and three-dimensional shock tube studies, and full scale field evaluations. Shock tube tests under controlled laboratory conditions augment and help design full scale studies which must be limited in number and are fairly expensive.

Two-dimensional shock tube studies were extremely valuable in determining the phenomenology of flow and loading, but the models usually are not representative of the majority of actual structures. Three-dimensional shock tube studies, can be of immense value. They are sufficiently flexible so that the most representative of actual loading conditions - in terms of both blast and structural parameters - can be obtained.

Three-dimensional shock tube studies can be used to maximum advantage where models are larger, more detailed, and complex. Hence, the shock tube itself must be relatively large so that wave reflection from the tube walls will not interfere with the flow field being observed. This concept led to the Air Force sponsorship of a 6-foot diameter shock tube at Gary, Indiana. Feasibility studies for methods of shock generation led first to the erection of an Air Force 2-foot shock tube at Ft. Sheridan, Illinois. Today both shock tubes are operated with the same equipment at Gary, Indiana.

Loading measurements on simple shapes have been augmented by theoretical analysis and engineering judgment whenever possible in order to provide ready extrapolations from simpler to more complex objects.

In the last decade the shock tube has become an important tool for gas dynamics research with application to blast effects research, to transonic aerodynamics, aerodynamics, high temperature gas dynamics, and hypersonic aerodynamics. The literature concerning shock tube theory, design, and application is so extensive it would require an extremely lengthy discussion to cover the subject adequately. However, since most of this material is familiar, we shall just briefly define the flow regions of interest of the Air Force shock tube and some of its operational characteristics.

Figure 1 defines the shock tube as a piece of pipe of uniform cross section, closed at both ends, with a thin diaphragm separating the tube into low pressure and high pressure regions. In the Air Force shock tube, shock wave generation is accomplished by one of three methods: compressed air, explosive gases, or Primacord. Figure 1 illustrates the basic, compressed air shock tube theory. The expansion and combustion chambers are identified respectively, as (1) and (4). At time (t) zero, regions (4) and (1) are filled with gas at a predetermined pressure ratio (P_{41}), but are at rest and in thermal equilibrium.

On rupture of the diaphragm, a wave of compression and another of rarefaction are formed, moving in opposite directions. A contact surface is formed between these two waves which acts, theoretically, like a piston in a cylinder. Ahead of the piston is the shock wave, while behind it is the rarefaction wave. The shock wave compresses the gas in the expansion chamber to an intermediate pressure and accelerates its flow in the same direction as the shock wave. The rarefaction wave reduces the pressure in the combustion chamber to the same intermediate pressure, and accelerates the fluid particles in the direction opposite to the advance of the rarefaction wave, so that the latter follows and eventually overtakes the contact surface and the shock wave. The contact surface divides two regions of constant pressure and particle velocity, but unequal temperatures and hence, Mach numbers, (2) formed between the shock wave and the contact surface (hot flow region), and (3) formed between contact surface and incident rarefaction wave (cold flow region). Some time later, conditions exist in which the reflected rarefaction wave overtakes the incident rarefaction wave. At a slightly later time, the former wave overtakes the contact surface. Still later, it overtakes the shock wave, leading to the customary peaked shock profile, and the shock front is followed by a decaying wave, as generated in atomic blasts.

For example, compressed air up to an initial pressure of 150 psi is presently used in the 2-foot tube, giving 30 psi overpressure at the shock front. Compressed air also seems to offer the best solution for shocks of long durations. In the 6-foot tube, the method demands the provision of considerable compressor capacity. Such a compressor has been installed and is in operation. Vacua to 1/2 psi absolute are obtained in the 6-foot tube and to 5 mm Hg in the 2-foot tube. The timewise variation of flow in the tube is well known, and the flow variables can be computed for a given pressure ratio across the diaphragm.

In Figure 2 we see the shock pressure ratio plotted as a function of diaphragm pressure ratio for various combinations of gases on the high and low pressure sides of the diaphragm. Such a chart is used for calibrating

the pressure sensors dynamically in a 4-inch shock tube. Typical pressure-time variations are illustrated in Figure 3 wherein the pressure distribution in the shock tube is shown at three different times, $t = 0$, 1.7 milliseconds later, and finally 5.2 milliseconds after diaphragm rupture. Let us now consider the shock tube flow regions and indicate some of its applications.

For weapons effects work, we utilize the compressed air shock wave in the expansion section at a distance of 16 compression chamber lengths which results in a peaked profile. If Primacord is used, the profile is peaked earlier. The shock wave is made to diffract around models to be loaded. These might be simple shapes (blocks, cylinders, domes, etc.) or complex shapes such as multistory buildings. "Incidence" refers to the Mach stem or regular reflection region created by the tilting plate on which the model rests. In structures tests, the end of the shock tube can be left open and models can be observed outside of the shock tube, etc.

For muzzle blast tests, we utilize the flat top flow region as a short duration wind tunnel. (The duration is long however compared to the duration of the muzzle blast wave.) The hot flow region furnishes Mach numbers up to 1.89, and the cold flow region up to much higher Mach numbers. The shock tube can be evacuated to simulate any desired altitude. Thus by firing a 50-caliber gun upstream into the compression chamber, one simulates on an instrumented plate the muzzle blast effect of an aircraft firing while flying both subsonic and supersonic. It was found by empirical means that muzzle blast could be correlated to the detonation of a spherical charge of TNT. In this way the various scaling laws of peak pressures, impulse, ambient temperatures, and ambient pressure changes for spherical explosives could be applied to muzzle blast.

For explosive decompression, one utilizes the compression chamber. Tests in the 6-foot shock tube were conducted on equipment furnished by Sperry Gyroscope Company to evaluate the structural response of the Sperry Unit and its mounting when subjected to explosive decompression. Such explosive decompression would be experienced during high altitude flight if a pressurized cabin is suddenly vented as a result of enemy fire.

Another use is for the check out of equipment, both for shock loading or explosive decompression loading.

One of the earliest uses of the shock tube was to study the propagation and interaction of shock waves. At Princeton University considerable effort was expended on fundamental studies of shock propagation and reflection, as well as blast loading on structures. Figure 4 shows the Princeton double block. For this application, the shock wave in the tube simulates the wave resulting from an explosion, and one can determine how the pressure on a model varies with time as the shock wave passes over and downstream of it. For these studies a tube of rectangular cross section is desirable, and use is made of a Mach-Zehnder interferometer in order to obtain a quantitative measurement of the density field. (The shock tube used in the Princeton experiments was 38 feet long and had a 4 inch by 18 inch cross section.)

An instantaneous picture of the flow field in the test section can be

obtained with a short duration light source. In order to get a time history of the flow, a variable time delay is incorporated in the spark source so that on repeated runs, a sequence of pictures taken at the various time intervals will yield the desired result. This is made possible by the excellent reproducibility of shock tube runs. The interferometer measures the density, and the pressure can be computed under the assumption of isentropic flow in regions devoid of shock waves. Hence, it is possible to obtain the pressures on an object as a function of time for the case of a shock wave striking, passing over, and going downstream of the object. Inherent in this method is the limitation of two-dimensionality. It is possible, under suitable conditions, to make quantitative three-dimensional interferograms; however, for arbitrary shapes this is not possible. In order to establish three-dimensional effects a tube of large cross section is essential.

The Foundation also owns an 8-inch by 8-inch square sectional shock tube, 30 feet in length, located at Technology Center. This shock tube is equipped with interferometer and Schlieren systems which permit the exploration of scaled pressure-time boundary conditions for the Air Force shock tubes. Whereas in interferometric work continuous pressure-distance plots are observed at discrete times, with the Air Force shock tube we observe continuous pressure-time plots at discrete points.

Under the sponsorship of the U. S. Air Force, the Armour Research Foundation has placed into operation shock tubes which will permit studies of flows past three-dimensional models. Figure 5 is an artist's sketch of the Air Force Shock Tube Laboratory located in Gary, Indiana. Figure 6 shows the outside and Figure 7 is an inside view. This shock tube laboratory contains the following:

- A 4-inch diameter tube, 15 feet long which is used for calibrating gages.
- A 2-foot diameter tube, 200 feet long composed of 10 lengths, each 20 feet long, with a combustion chamber than can be varied in length from 4 inches to 20 feet by means of wood blocks.
- A 6-foot diameter tube, 150 feet long. This length comprises a minimum combustion chamber 3 feet long, a 5-foot test section, and ordinarily a 40-foot exhaust section, leaving 100 feet maximum or expansion section. The tube thickness is $\frac{5}{8}$ of an inch in the expansion section, and 1 inch in the compression chamber. As a result of using interchangeable tube sections, with the majority 10 feet long, it is possible to set up a wide range of shock wave pressures (over ambient pressures) and durations, the former from 1 psi to 50 psi and the latter variable between 1 and 50 milliseconds.

Normal test duration is 15 to 20 milliseconds. Loading of the combustion chamber and access to the test section is effected by mounting these tube sections on dollies which run on rails extending the full length of the tube. The tube is primarily located in the open, with a building to protect the test section and adjoining lengths, as well as the instrumentation. Having both ends free enables the tube to be fired with the expansion chamber open or closed. The test section and the two 10-foot sections, respectively, leading and trailing it, are provided with 10-foot horizontal stainless steel floor plates to accommodate the test model and to smooth out irregu-

larities in the shock wave before and after striking the model. The model can be mounted on a 20-inch turntable and rotated about a vertical axis to present any face to the shock front. Figure 8 shows the turntable with a three-dimensional double block.

The work is facilitated by such improvements as overhead cranes and a puncturing device and clamps as shown in Figure 9. The clamp has ten hydraulic jacks, each with a 80,000 psi capacity. Shock generation is compressed air, an explosive gas mixture, or Primacord. Compressed air is used with Mylar up to 15 psi and aluminum up to 65 psi compression chamber pressure.

Explosive gas is used in the form of a hydrogen-air mixture of 1 to 4 at atmospheric pressure. A short length of Primacord has been found to be the most effective means of detonating the mixture with a minimum of burning. As such, it satisfactorily fills the range of peak shock duration up to 70 milliseconds with pressures up to 10 psi. The material most commonly used in the compression chamber is Primacord, coiled in a flat spiral at right angles to the axis of the tube. This method offers more versatility over the range of practical weapons effects pressures and durations.

The 6-foot Air Force shock tube was placed in operation on September 1954, and since has functioned continuously with up to 20 shots a day as routine.

Figure 10 shows the instrument room. The instrumentation records pressures in the shock wave and on the model, and the velocity of the shock front over a period of time represented by steadyflow conditions. Therefore, all electronic and photographic equipment available at the shock tube laboratories is controlled by a time delay generator furnishing delays from 1 microsecond to 1 second, initiated from the combustion chamber. This enables any selected portion of the shock phenomena to be recorded on the appropriate instrument. For calibrating the gages dynamically in the 4-inch shock tube, the shock wave velocities are measured electronically by means of light screens viewing through windows set at predetermined intervals in the tube and upstream of the model position. From the velocity one calculates the overpressures by means of one-dimensional shock tube theory.

An 8-megacycle recorder registers time intervals. The light screen photocell output is fed to an amplifier and then to the chronograph where immediate visual indication is given by a bank of lights.

The measurement of response pressures on the model itself, and of the shock pressure generated, is based on the use of special barium titanate gages. The material possesses piezoelectric sensitivity and produces an output signal proportional to the stress applied. This type of gage satisfies all the requirements for gages usable on small models, being diminutive in terms of the model dimensions and effecting no change in model geometry when installed. In addition, the gages respond in less than 20 microseconds, have a sensitivity suited to conventional amplifiers, and are relatively insensitive to acceleration. The gage is a ceramic cylinder 1/8-inch long by 1/8-inch outside diameter, with a wall thickness of 19 mils.

Several such gages are installed in the faces of the model and are

connected to cathode ray oscilloscopes. The 6-foot tube is equipped for eight channels, but this number of channels can be increased as required.

Each oscilloscope may be triggered to give single sweep records at faster sweep speeds than the drum camera could record. An S. I. M. No. 731 camera, with a writing speed of 1 millisecond per inch, makes eight simultaneous records, the oscilloscopes being staggered in the vertical phase and arranged on the circumference of a circle. An L. F. E. oscilloscope with signal input from a gage records the overpressure for each test.

The gages which have been used are the barium titanate gage, the Kissler gage, Rutico gage, and SR4 strain gages. In the future other more powerful piezo electric materials, like zirconate will be investigated.

Before loading models one must be reasonably sure to obtain the desired incidence freestream overpressures and durations.

Figure 11 gives the shock strength as a function of scaled distance for any atmospheric pressure using Primacord as the shock generator. The solid line has also been obtained from an analytic solution independent of the test calibration. By using reduced atmospheres one obtains high shock strengths for relatively low overpressures, low forces, and low acceleration signals, etc. For example, one can obtain shocks of $\xi = 7$ corresponding to over 100 psi in the test section with adequate durations for overpressures of 15 psi corresponding to shocks of $\xi = 2$ at atmospheric pressure.

Figure 12 gives the scaled duration as a function of the scaled distance.

Figure 13 to 15 shows typical weapons effects models. Figure 13 exhibits a scaled beam; Figure 14 a multistory building. Figure 15, the same building mounted on the tilting plate for study in the regular reflection region. Figure 16 and 17 exhibit Sperry equipment installed in the compression chamber for explosive decompression testing. Figure 16 shows the front of the unit; Figure 17 looking towards the panels exhibits this unit inside the tube and incidentally shows the bars of the puncturing device which hold the diaphragm in place insuring a more uniform rupture.

Some of the weapons effects loading programs include a study of long versus short durations, shielding, surface roughness, regular reflection, hollow models with and without interior obstacles, multistory buildings, drag-type buildings, tanks, domes, a study of shock tube temperatures, etc.

A few limited response studies were successfully conducted in which the effect of gravitational forces could be neglected, as in case of wall panel failure.

As an example of equipment checkout, one might cite a few instrumentation checkout of side-on gages like the Rutico gage, "q" gages, and more complex telemetering and oscillographic equipment to be used on large scale field tests.

A test to be conducted soon will be the study of grids to eliminate the reflections from the back end of the tube or from the tilting plate thus permitting longer observations.

In conclusion, the Air Force shock tube, which is the largest shock tube in this country and probably in the world, provides an excellent research tool for (a) weapon effects work which includes basic flow, loading on simple and complex targets, limited response tests, and checkout and calibration of equipment for full scale tests, (b) a short duration wind tunnel to conduct muzzle blast tests simulating firing from planes in flight, and (c) explosive decompression studies which include structural tests and equipment checkout in the compression chambers. These are some of the present applications. Undoubtedly in the future many other applications will be found.

Recently the 6-foot shock tube facility has been modified by strengthening the compression section and nearly doubling the tube length. This will permit overpressures up to 80 psi in the test section with associated durations up to 120 milliseconds.

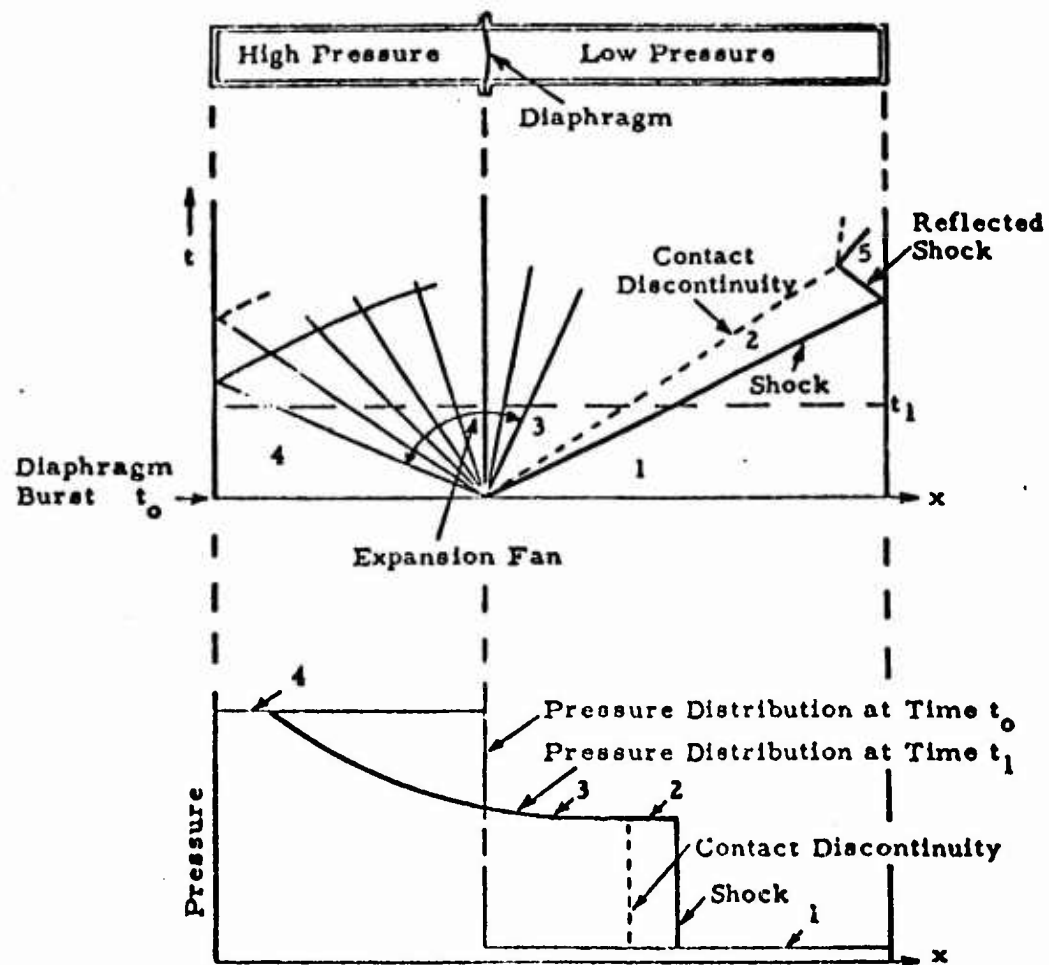


Figure 1. Schematic of Shock Tube Flow
(x - t and p - t diagrams)

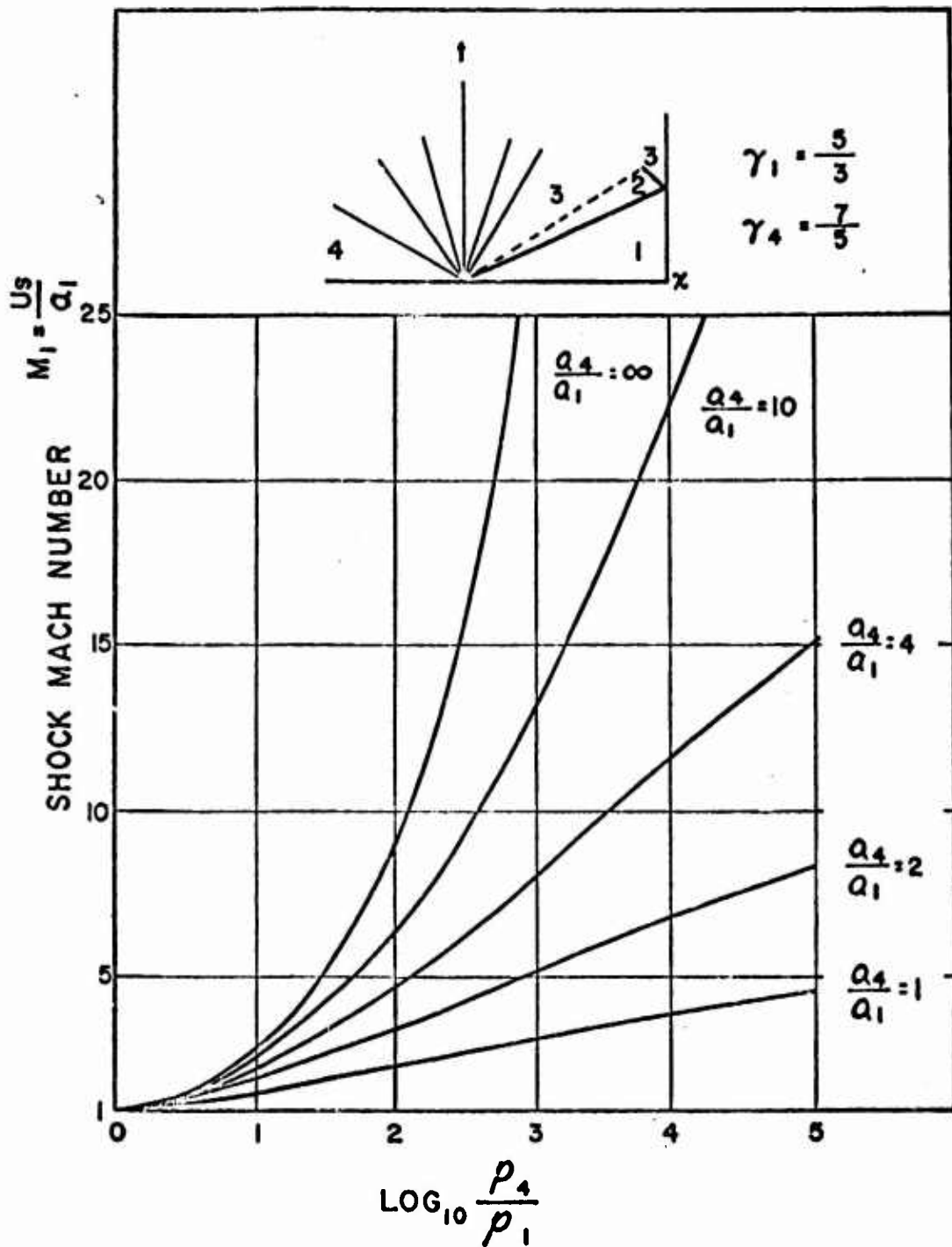


Figure 2. Variation of Shock Mach Number with Diaphragm Pressure Ratio for Various Ratios of Sound Velocity in High and Low Pressure Gases (Diatomic Driver Gas; Monatomic Driven Gas)

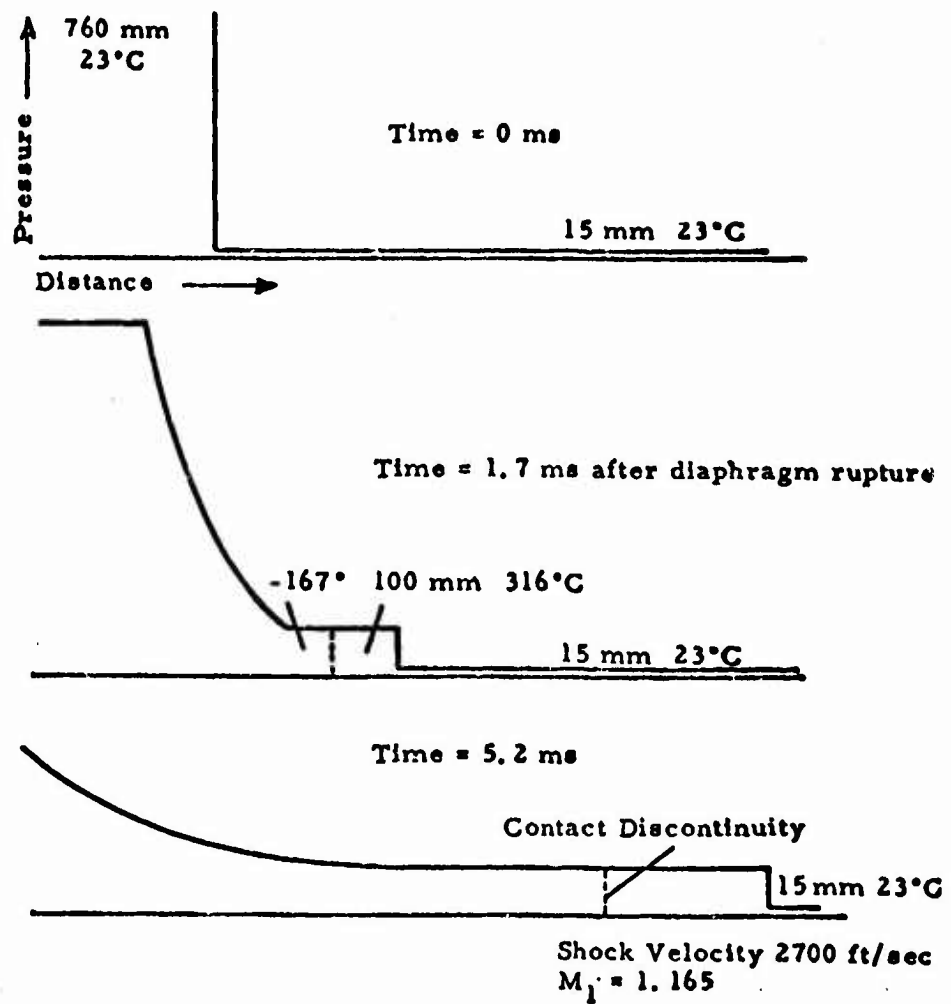


Figure 3. Typical Shock Tube Flow Pressure-Time Variation

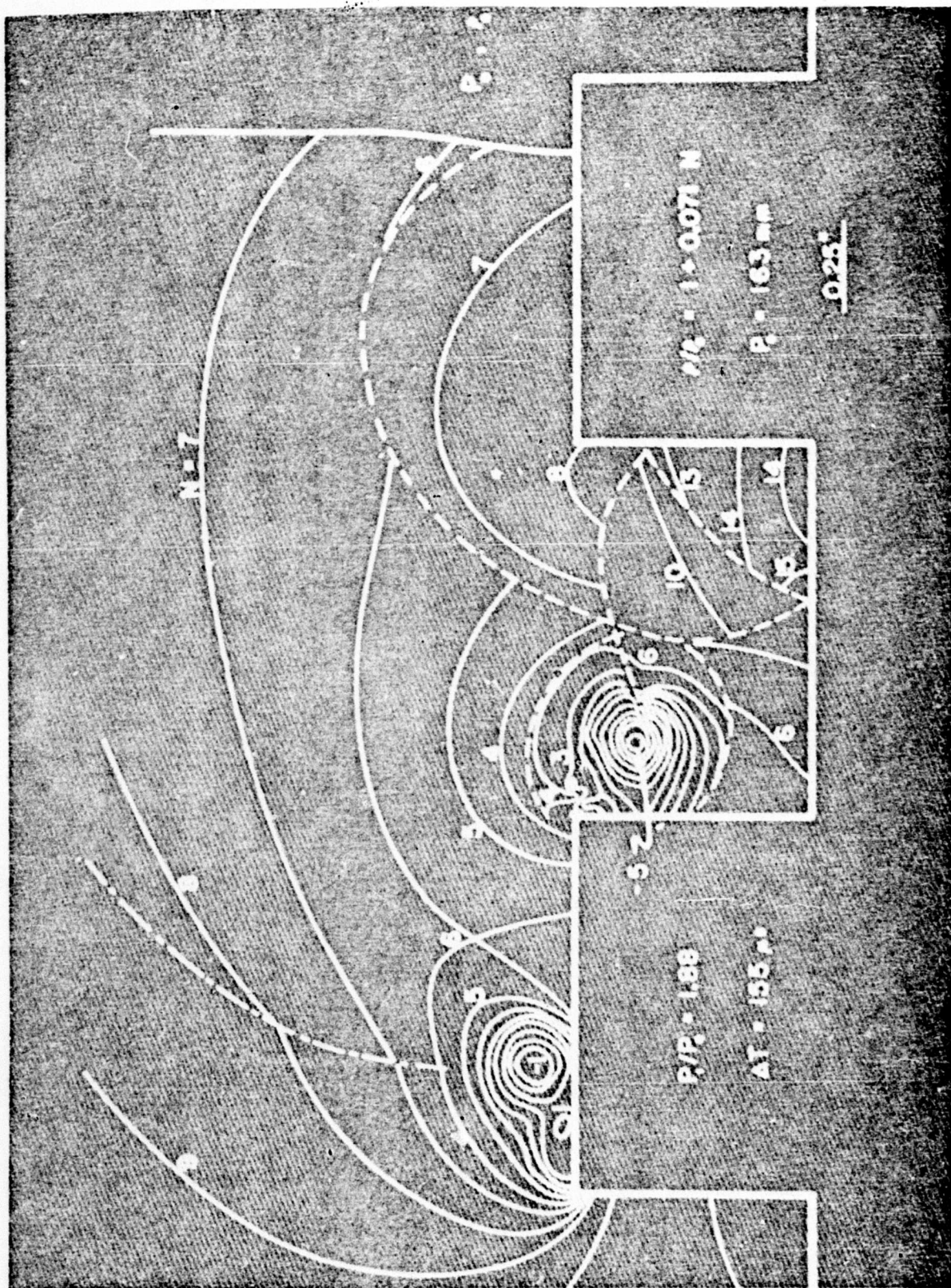
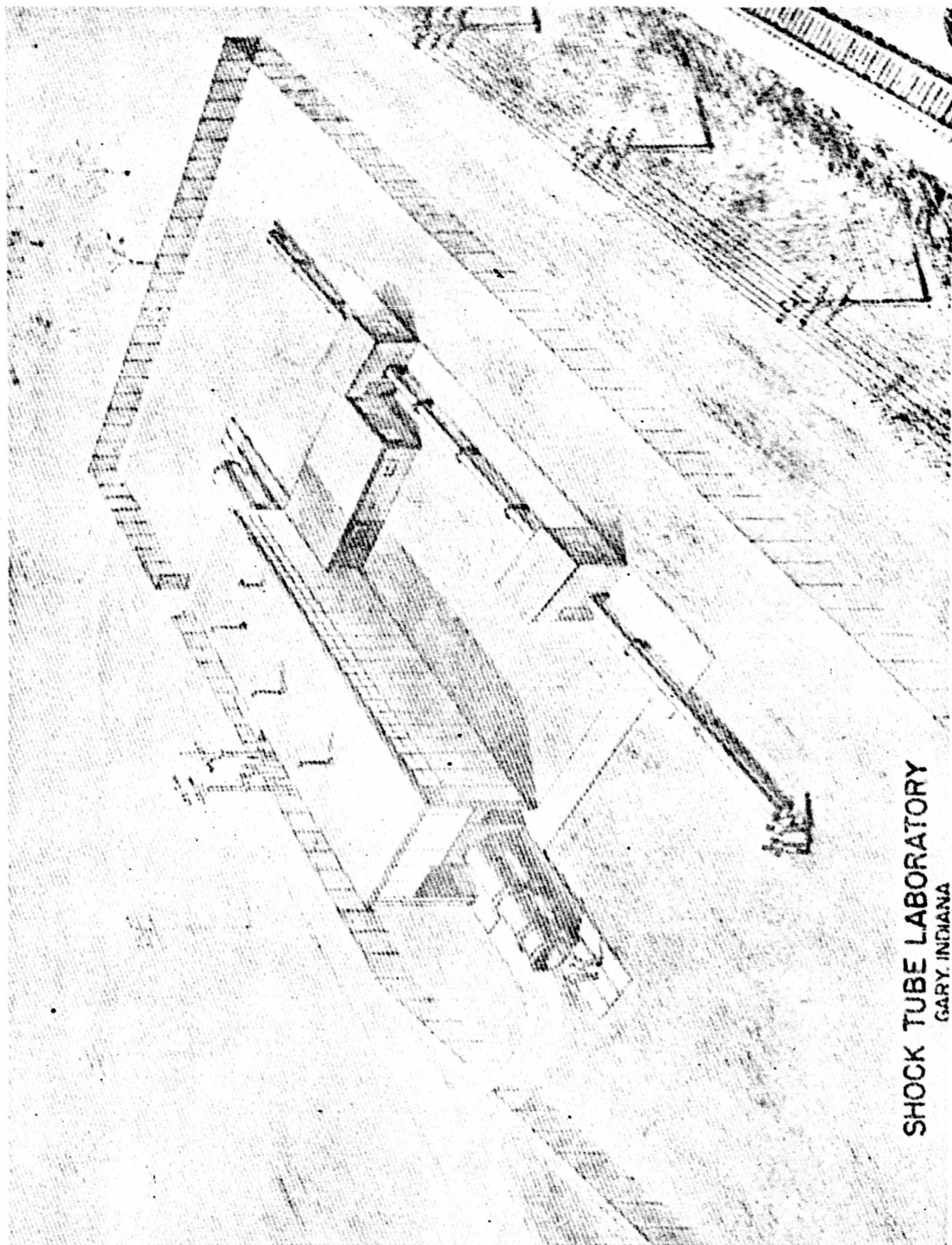


Figure 4. Princeton Double Block



SHOCK TUBE LABORATORY
GARY, INDIANA

Figure 5.

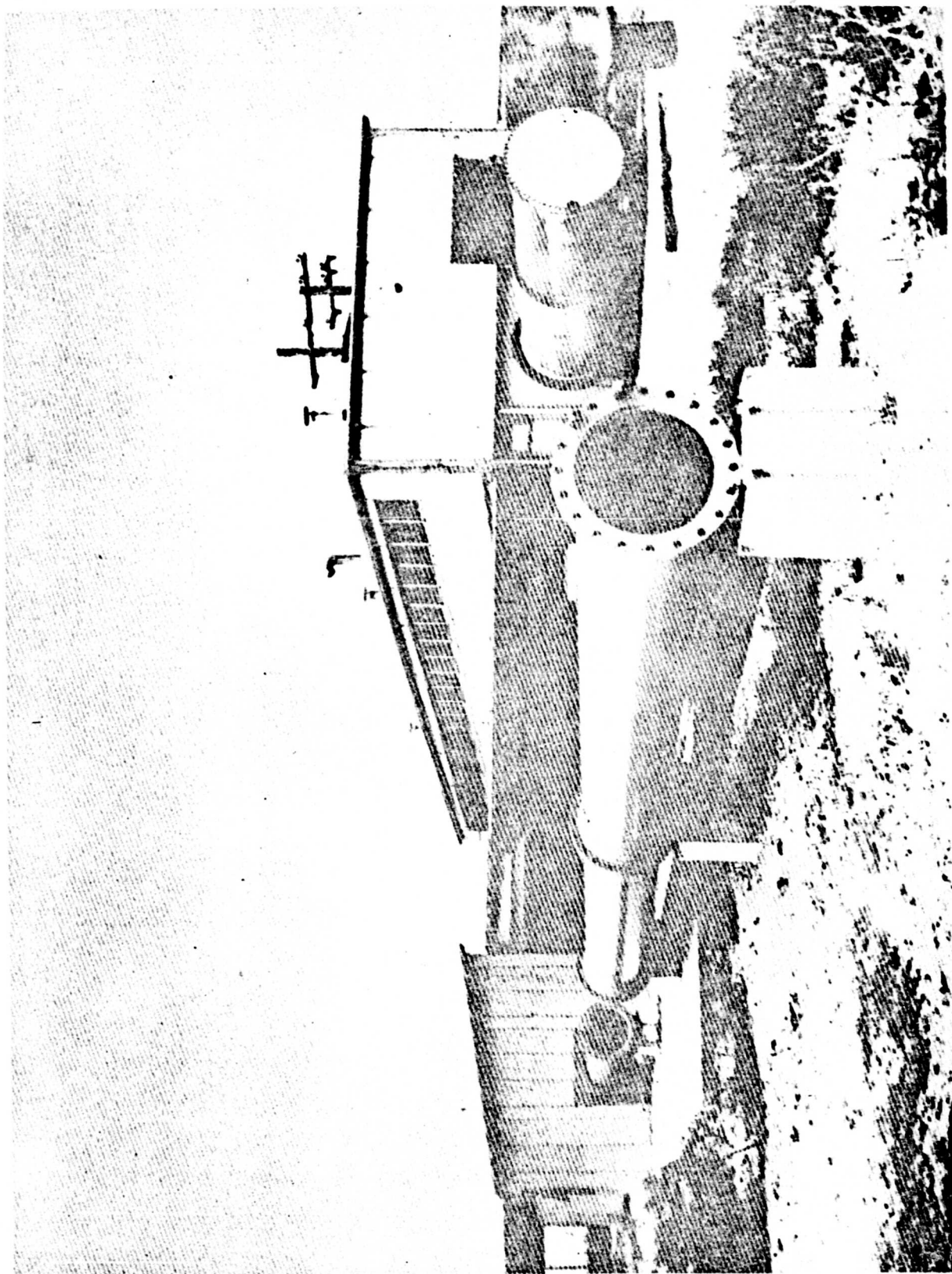


Figure 6. View of 2 ft. Diameter (foreground) and 6 ft Diameter Shock Tube

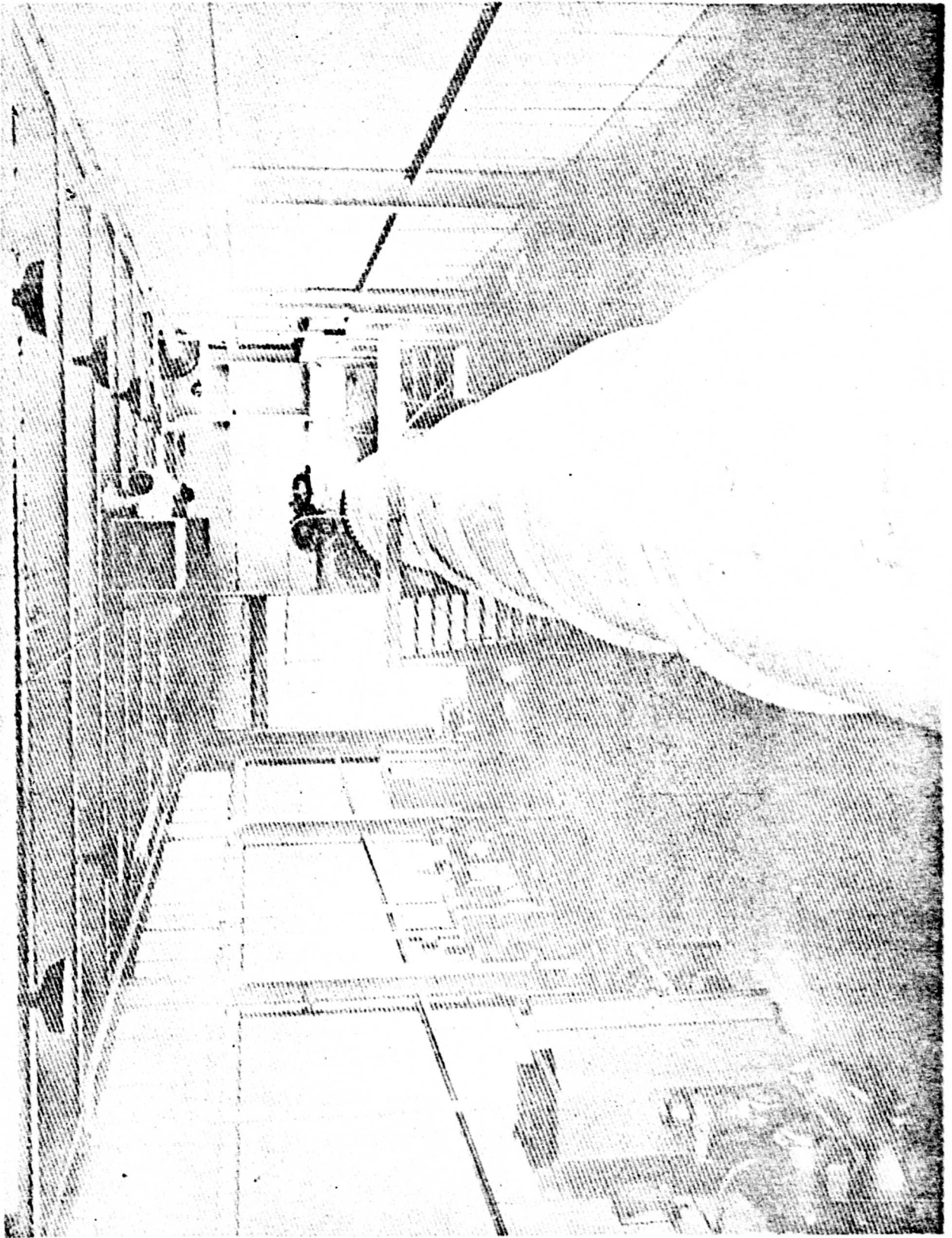


Figure 7. 6 Foot Diameter Shock Tube

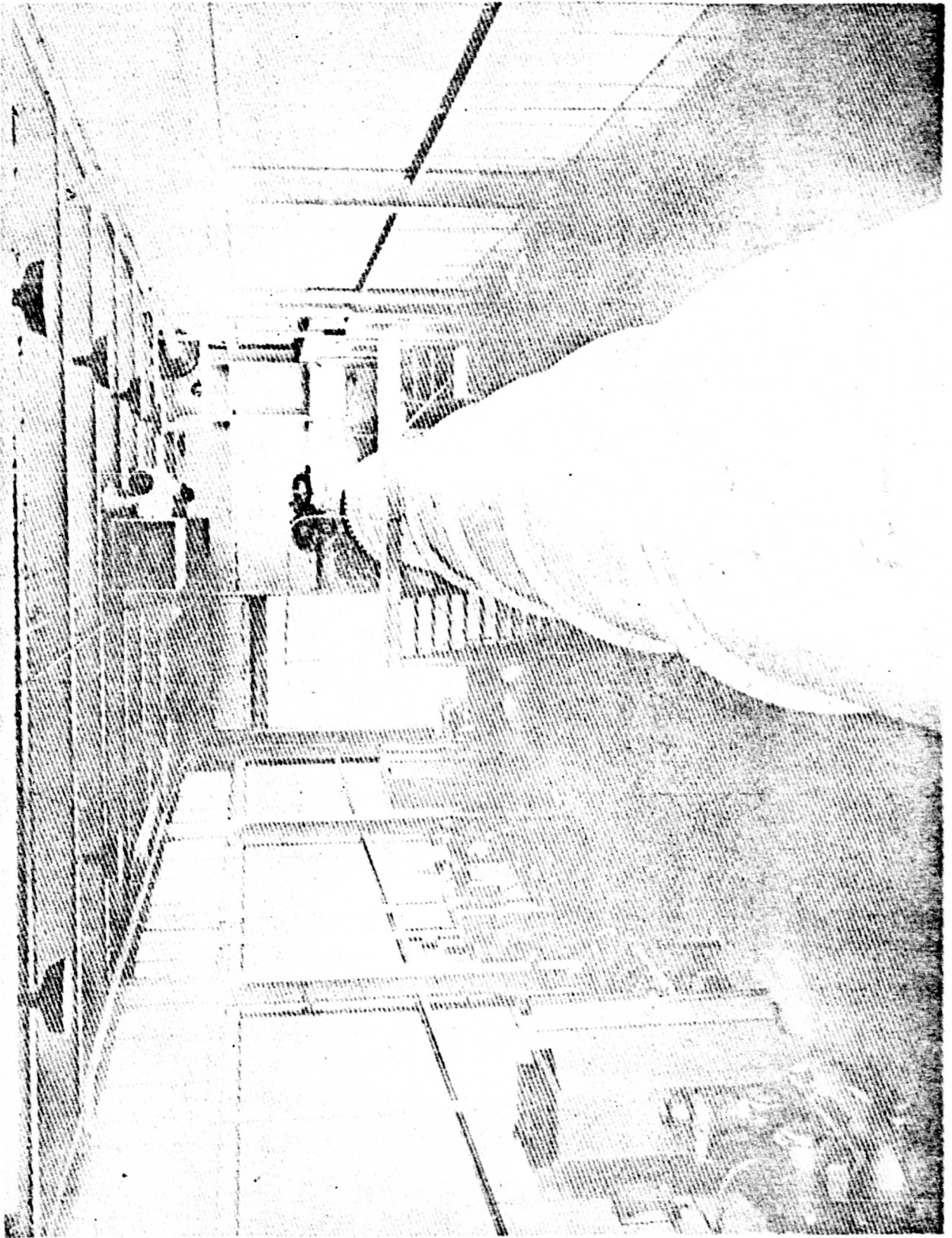


Figure 7. 6 Foot Diameter Shock Tube

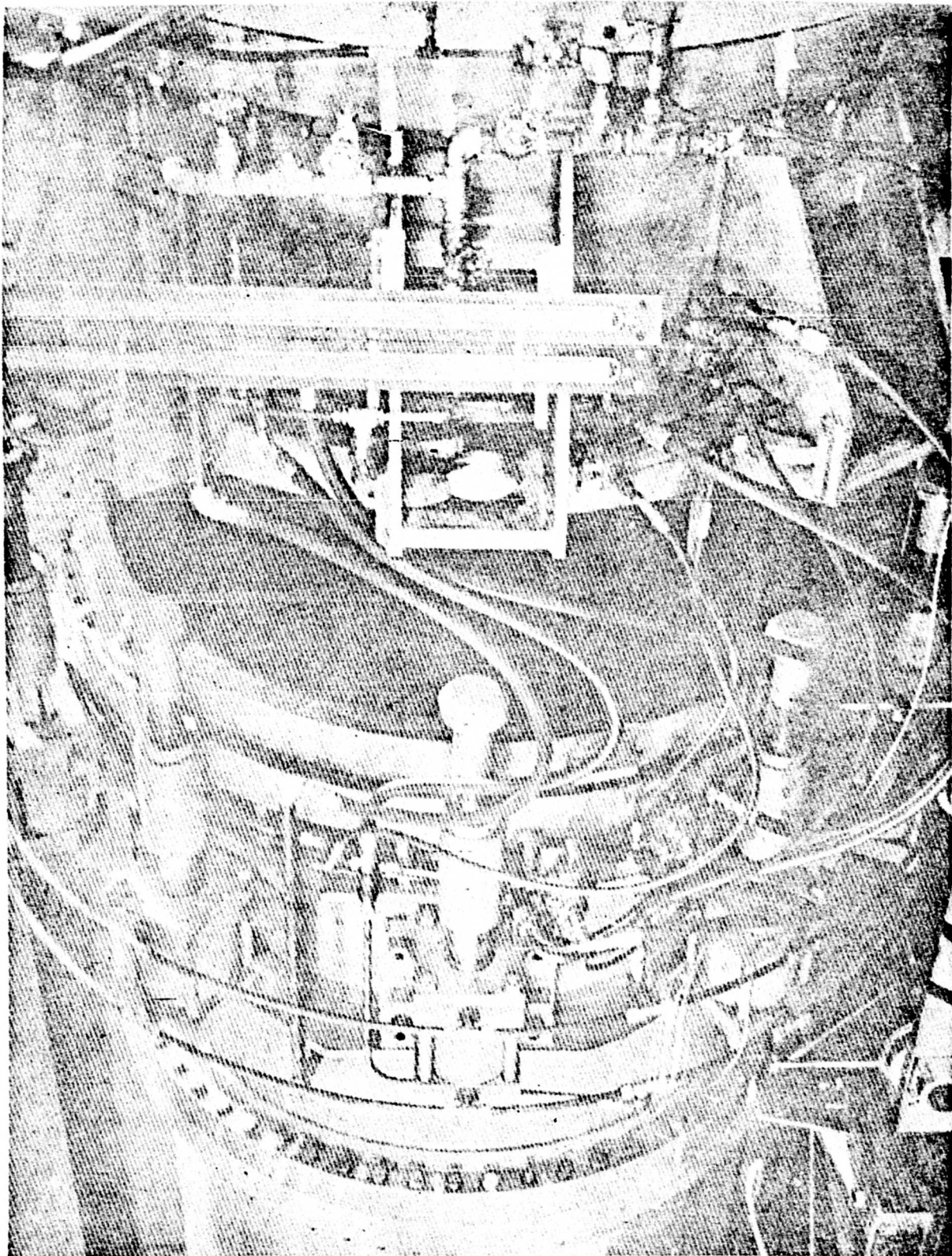


Figure 9. Hydraulic Clamp

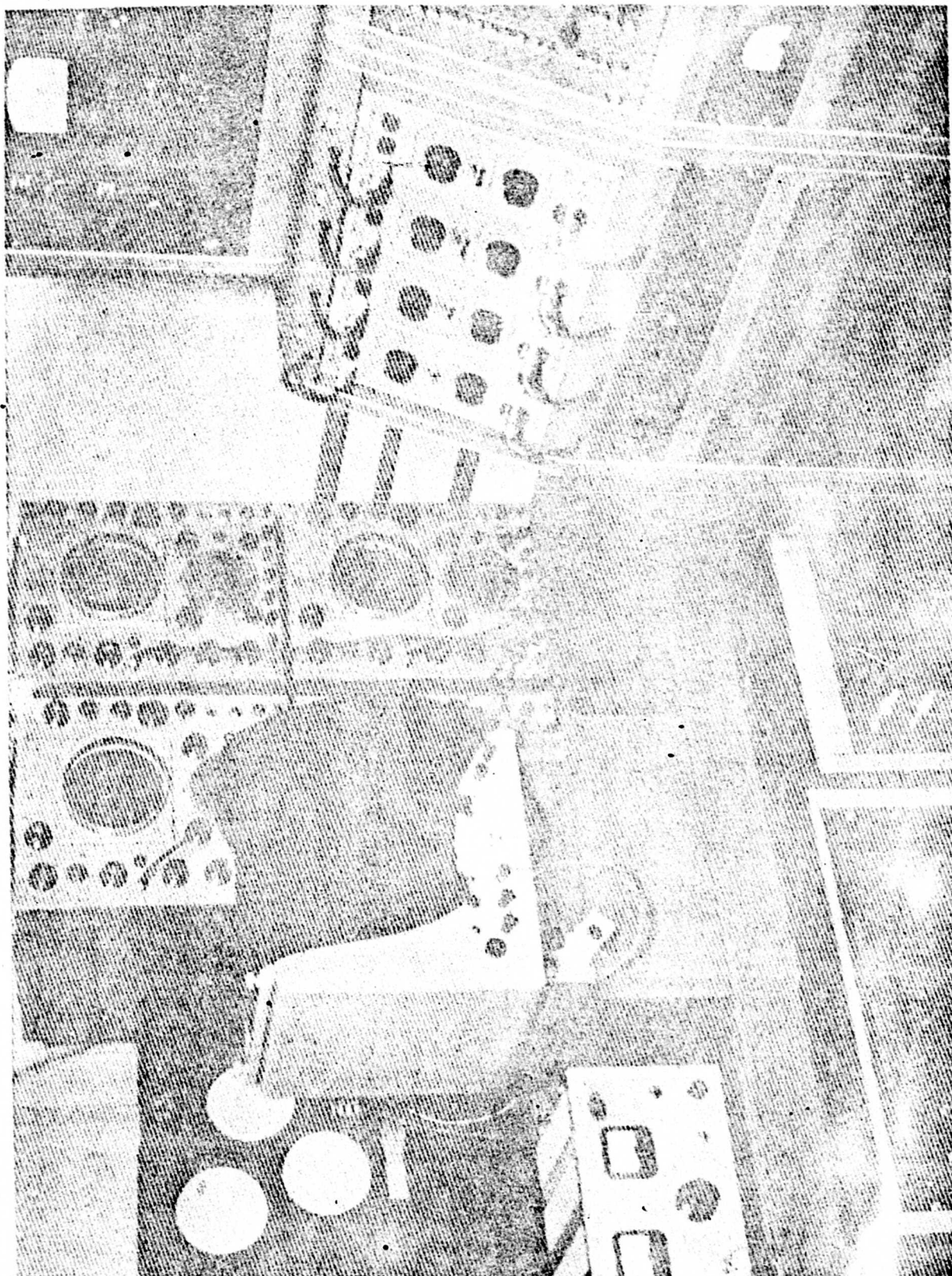


Figure 10. Instrument Room

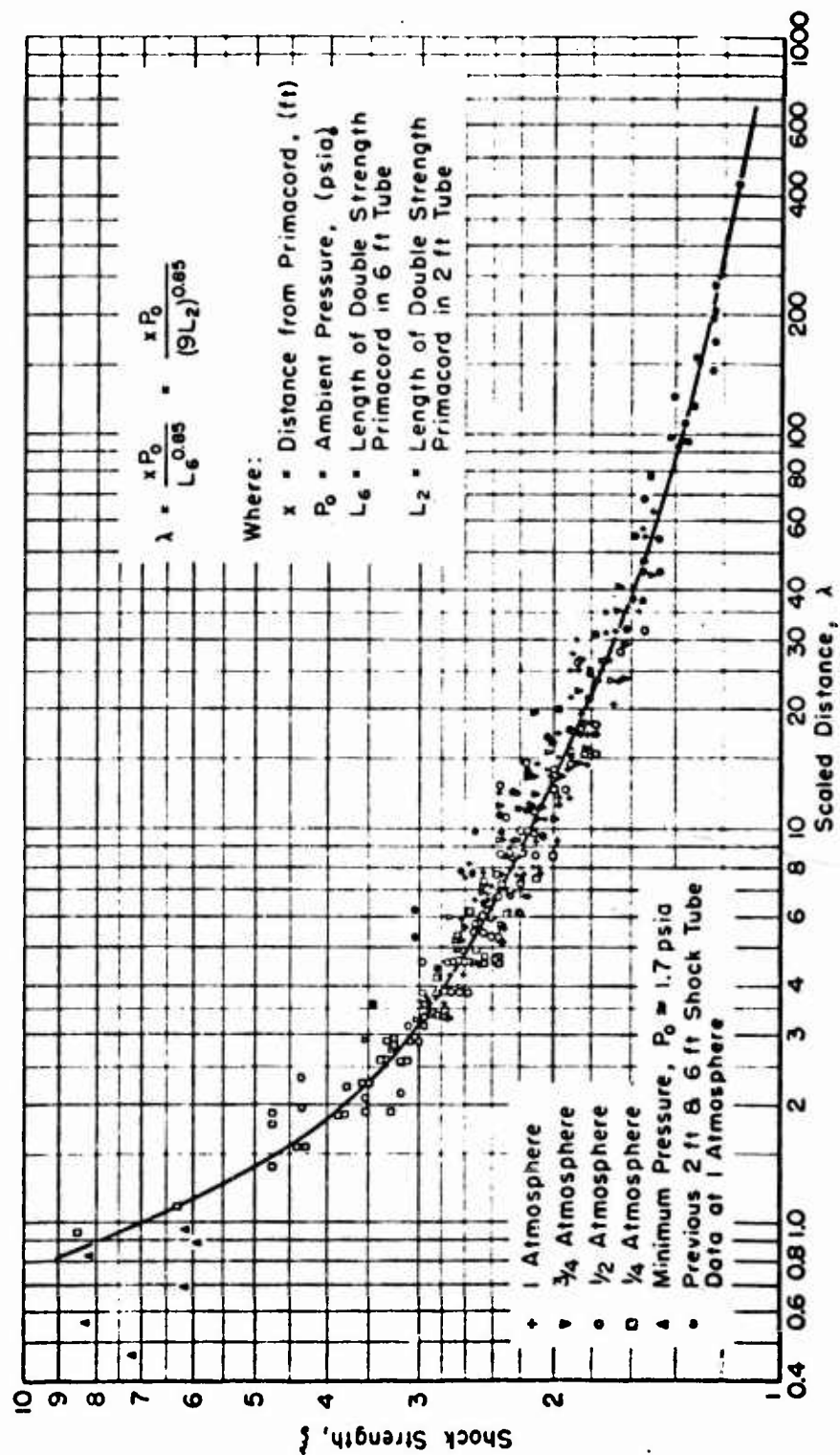


Figure 11. Shock Strength vs Scaled Distance Primacord Calibration

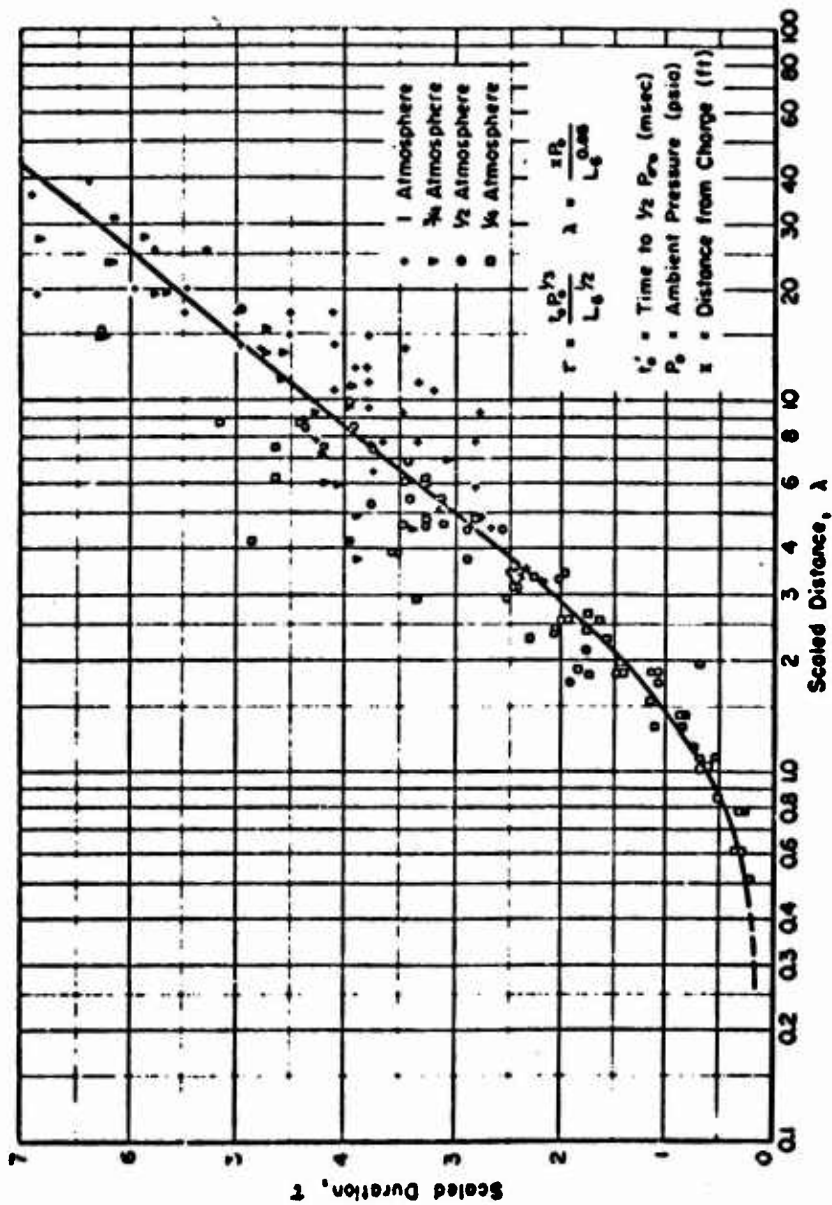


Figure 12. Scaled Duration vs Scaled Distance

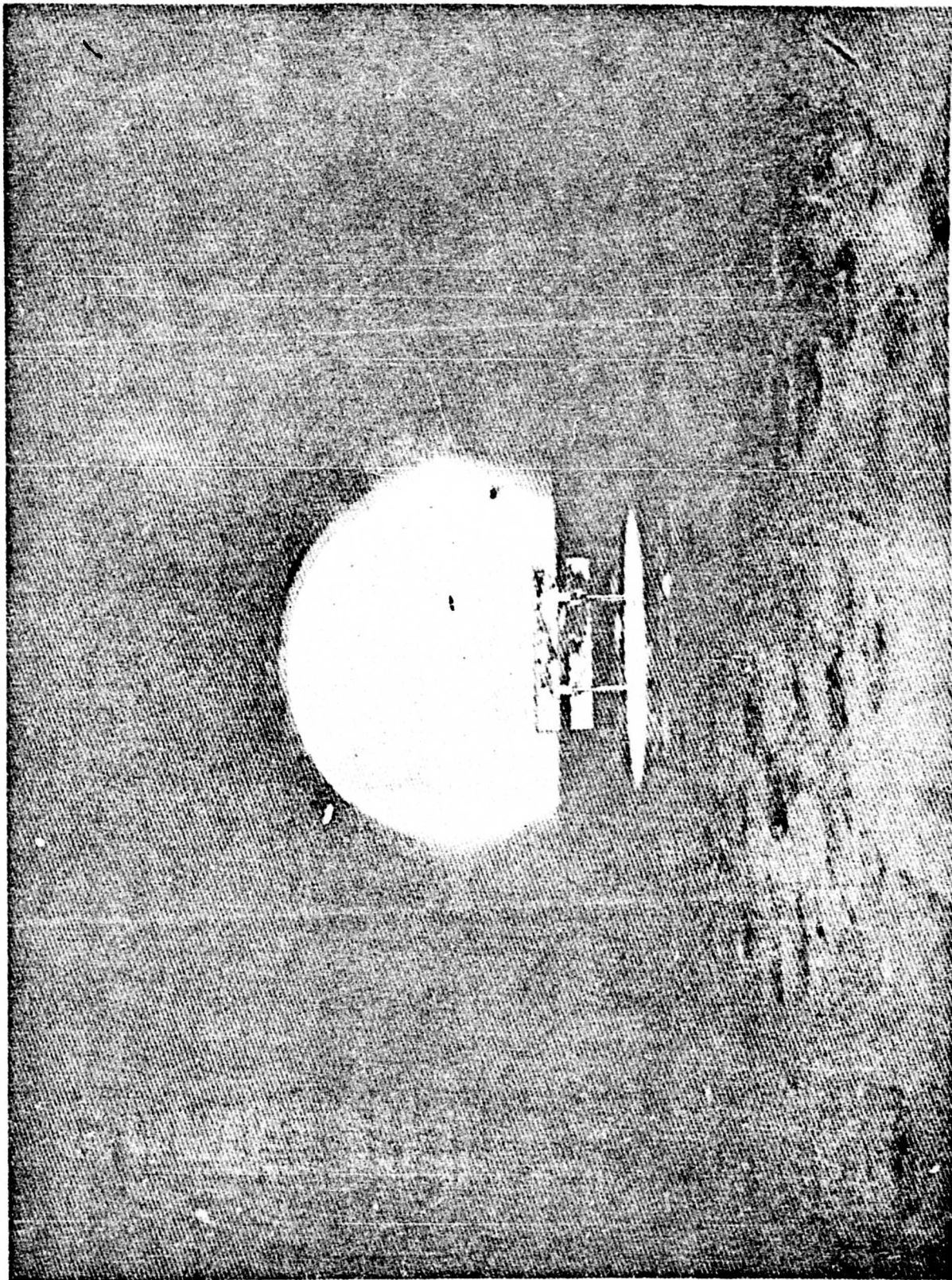


Figure 13. Scaled Beam

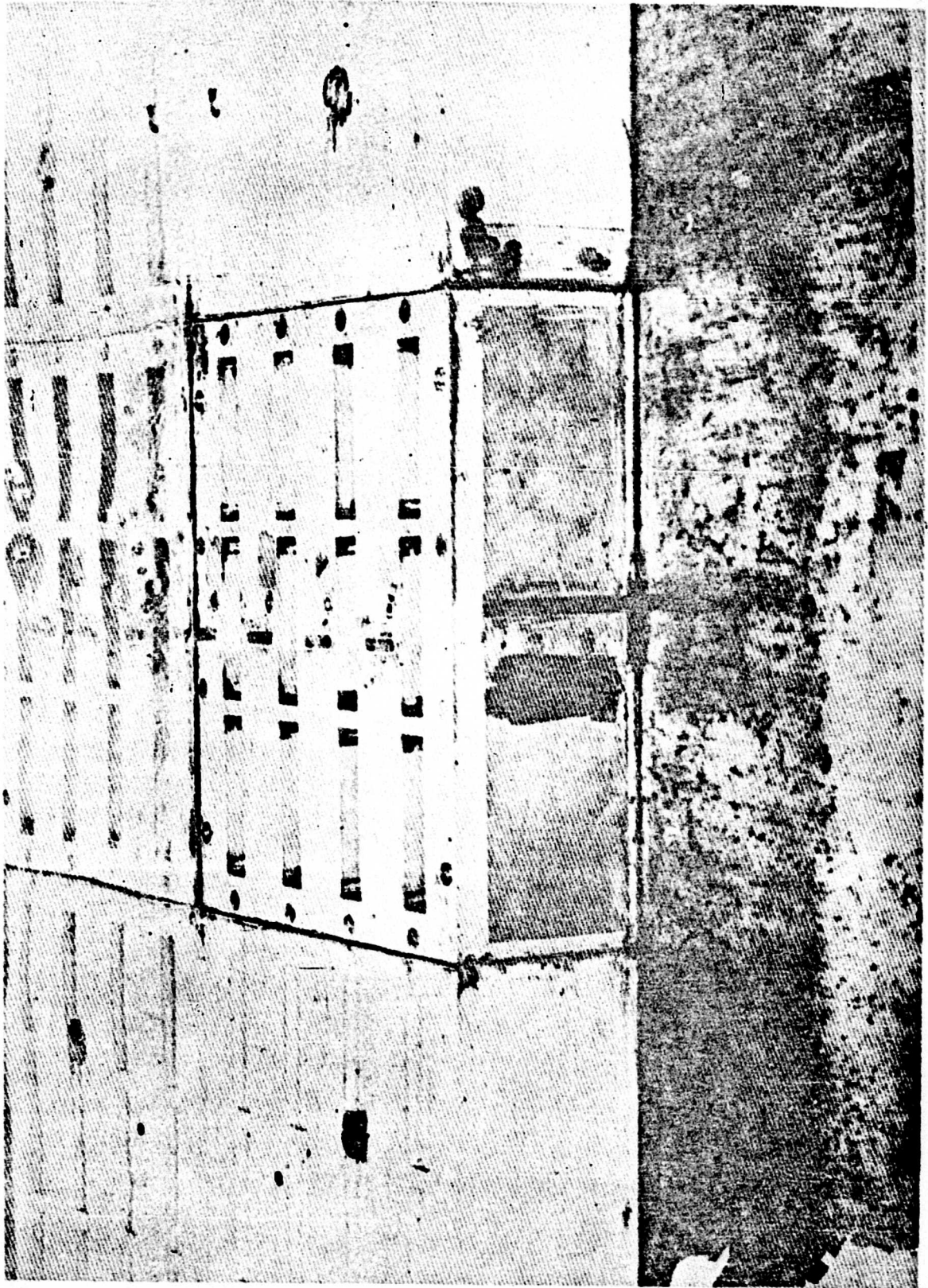


Figure 14. Multistory Building

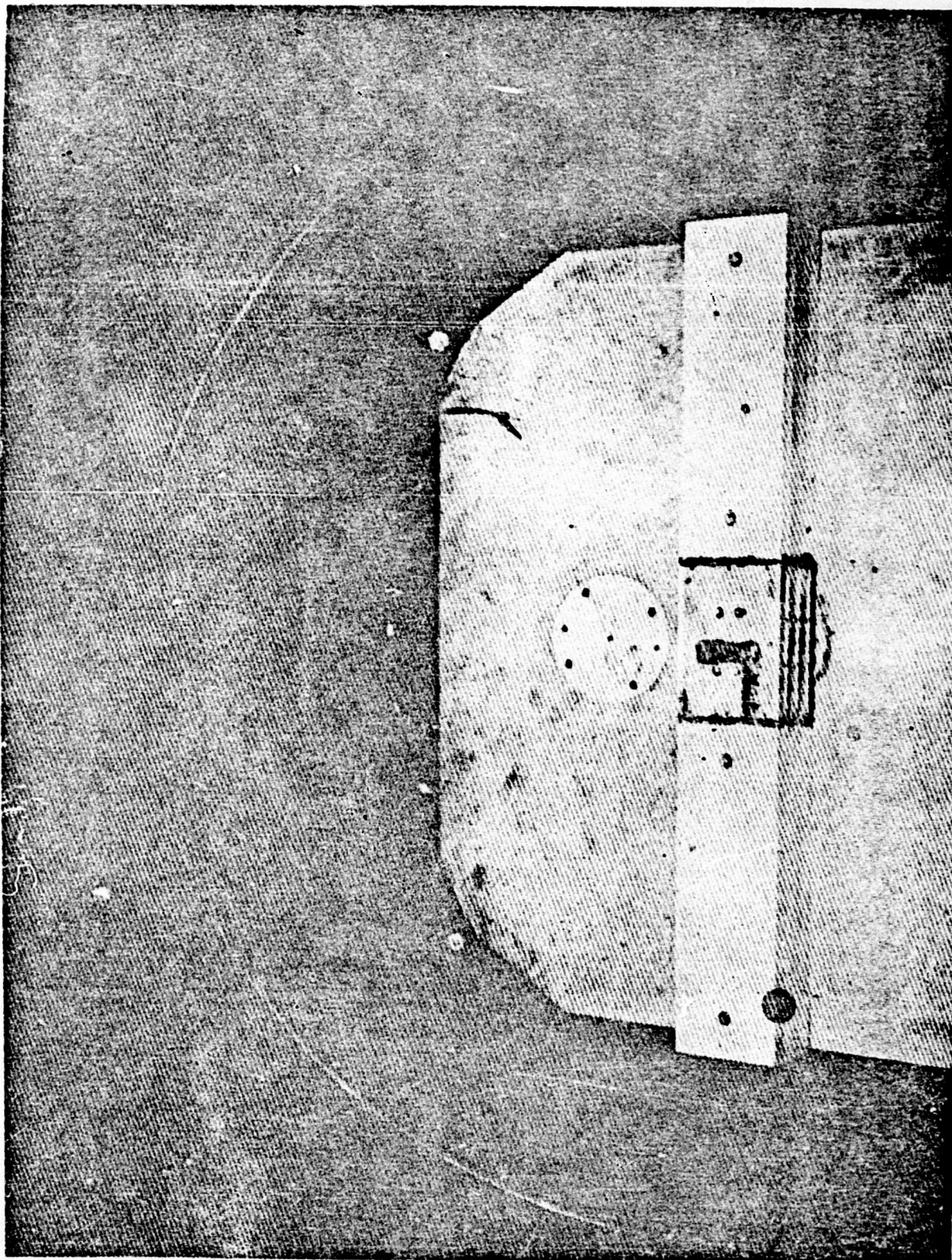


Figure 15. Multistory Building in Regular Reflection Region

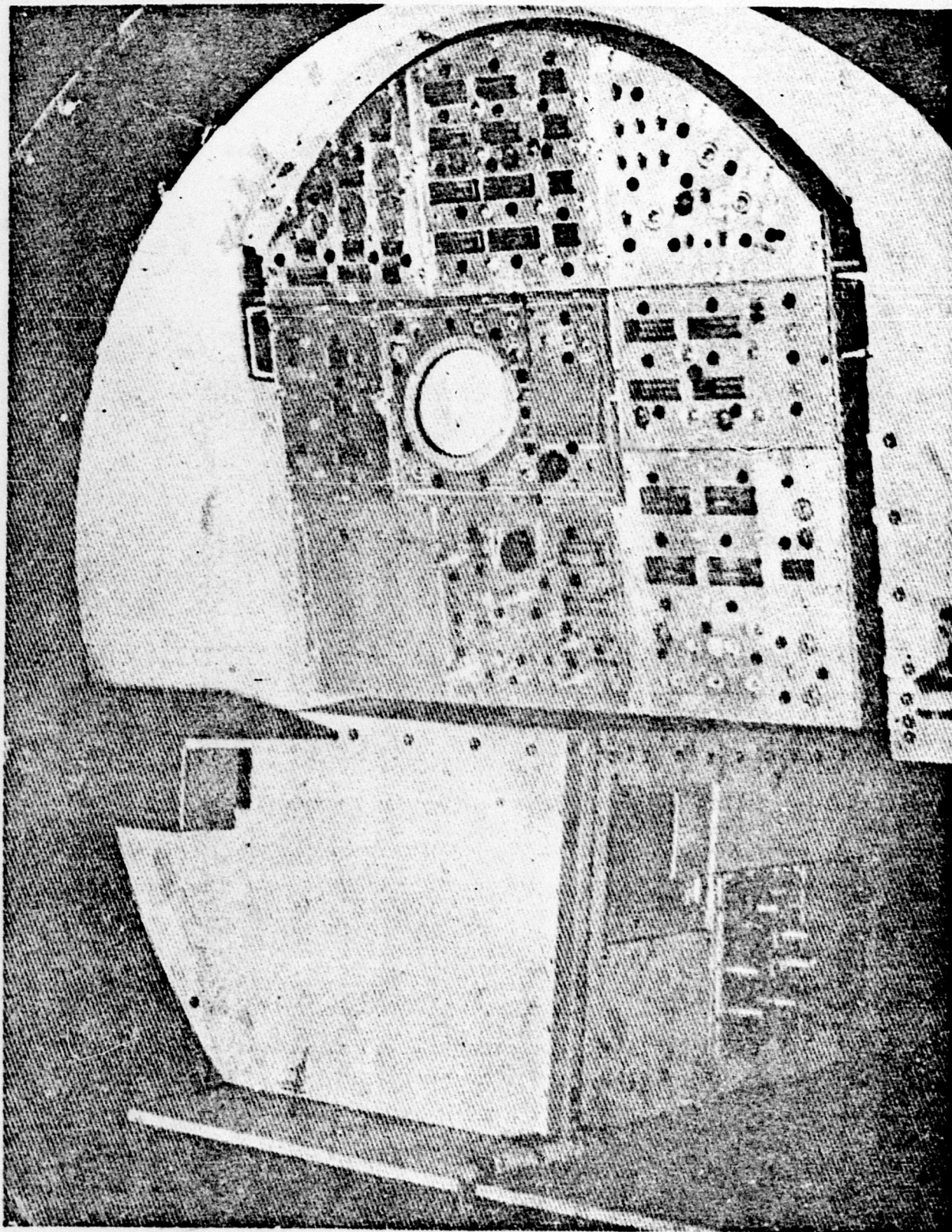


Figure 16. Sperry Navigation Unit in Compression Chamber

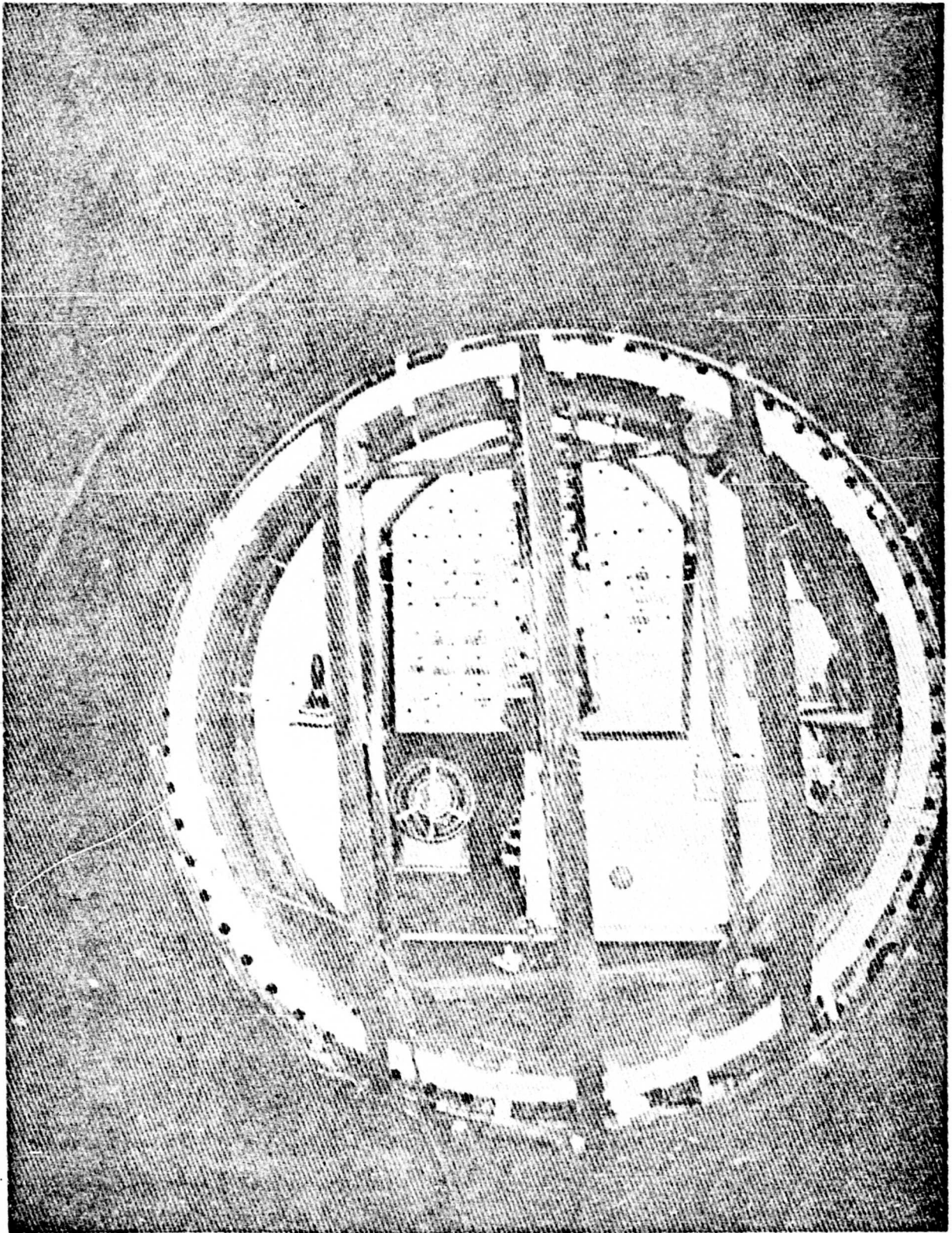


Figure 17. Sperry Navigation Unit behind Puncturing Device

THE DESIGN AND PERFORMANCE
OF THE GENERAL ELECTRIC SIX-INCH SHOCK TUNNEL FACILITY

Walter R. Warren
General Electric

The design of the General Electric Missile and Ordnance Systems Department six-inch hypersonic shock tunnel is discussed and the advantages of several unique design features - various test regions, multiple nozzles, diaphragm clamping section, nozzle opening section, sting - are indicated. The operation of the tunnel is described in terms of its maximum performance. Instrumentation techniques used for measuring model heat transfer rates and pressure distributions and for observing flow fields are described. The performance of the facility is presented in terms of model simulation of free flight conditions and the problem of non-equilibrium flow in the different nozzles is analyzed. Important experimental programs that can be run in the shock tunnel are outlined.

The aerodynamic phenomena associated with high velocity flight at various altitudes are highly complicated because of the many processes that occur. For example, the air moving near the surface of a body travelling through the atmosphere at a hypersonic Mach number (over 10) will be highly dissociated and partially ionized, it will radiate appreciable amounts of energy to cooler surroundings, and it may be in a chemical and thermodynamic state appreciable far from the equilibrium state associated with its translational temperature. This flow situation is difficult to analyze and the need for experimental facilities that establish a suitable environment for model testing is apparent. One facility that is well suited for adaptation to the study of high velocity-high temperature problems is the shock tube or its modification, the shock tunnel.

The General Electric 6-inch shock tunnel has been built specifically for the study of realistic hypersonic flight problems. It is essentially a high performance shock tube in which relatively large size models may be tested over wide ranges of Mach number, Reynolds number, and stagnation enthalpy. The facility is subjected to the usual shock tube limitations and difficulties (short testing times, incident shock wave attenuation, non-equilibrium flows, etc.); however, it is believed that its design and operation characteristics tend to minimize these problems.

The purpose of this paper is to describe the shock tunnel and its performance, to discuss the programs that have been conducted during its development, and to outline its applicability to several important hypersonic studies.

Figure 1 shows the original conception of the shock tunnel. Many of the details have been changed during the development of the facility but the overall size and general layout of equipment are approximately the same.

Three flow regions of high stagnation enthalpy are used for model experimentation (see Figure 2): the flow behind the incident shock wave - region 2 - where the pressure and Reynolds number are high but the flow Mach number is low (below 3); the flow in a non-reflected or straight-through nozzle, where the pressure on a model is lower than it is in the region 2 flow but the flow Mach number is higher (between 4 and 6); and the flow in a reflected nozzle where the pressures are quiet low but the Mach numbers are high (to 16). The size of the models located in the nozzle flows can be five to six times that of the models in the region 2 flow.

An interesting facility modification for reflected nozzle testing is the addition of several nozzles to the downstream end of the driven tube. This is shown in Figure 1 and in more detail in Figure 3. Such a scheme would increase the productivity of an experimental program and would reduce the repeatability problem existing in high performance shock tubes, since it allows the taking of many data during one test. The installation now has only one nozzle but it may be easily adapted to several.

The dimensions of the shock tunnel and its supporting shock tube are given in Figure 4. The short shock tube has the same diametric dimensions as the tunnel. It was first used in the high pressure combustion study that is described in a later section. The primary purpose of the tube is to act as a development facility for the tunnel, although it will also be used for a few basic studies. Programs being run with it now are intended to develop and evaluate heat transfer and pressure instrumentation and to determine the durability and response of various gauge-model combinations.

The driver tube has an 8-inch inner diameter and the walls are 6 inches thick. It is made of SAE 4340 steel and is designed to contain a working pressure 10,000 psi. It has been hydrostatically tested to 25,000 psi; the actual rupture strength should be well over 100,000 psi. The inner surface is chrome-plated to a depth of 0.005 inches. The access ports are located spirally every 45 degrees at an axial spacing of 6 inches. With this system of spark plugs, gas inlets, vacuum lines, and gauges may be placed in almost any desired array. Two diametrically opposed access ports are located every 10 feet in the upstream sections of the driven tube and every foot for the final 26 feet of the tube. The ports allow a 1-inch diameter entrance to the tube and are equipped with blanks that were bored and honed in place. The inner surface of the tubes have a 12 to 16 micro-inch honed finish. Region 2 models are supported in a special 6-inch section that fits between any two large sections of the driven tube.

The reflected nozzle is shown in Figure 4. The throat section is removable and may be replaced by sections with various sized throats. The nozzle is a 3 degree cone which causes some flow divergence at the test section. However, it was thought better to accept a slight flow divergence than to attempt the design of a parallel flow nozzle for the complicated flow conditions of interest. A maximum model diameter of 1 foot is believed

possible in the 30-inch test section. The model is supported on a sting extending through the dump tank. Two 10-inch diameter Schlieren systems (horizontal and vertical) are available for flow observation in the test section.

Figure 5 is a photograph of the installation showing the driven sections of the tube and of the tunnel. The control room is seen in the center of the picture beside the nozzle end of the tunnel. A view of the tunnel looking from the driver house towards the dump tank is shown in Figure 6. The piping to the left of the driver is the gas inlet system. The location of the driver tube in a specially designed room external to the main building is part of the overall safety system which also provides for the complete remote control operation of an experiment from an interlocked panel in the control room.

The high driver pressure needed to operate the tube is obtained by one of three methods: helium pressurized to 2000 psi, constant volume combustion of helium and stoichiometric hydrogen and oxygen mixtures to 10,000 psi, and constant volume combustion of nitrogen and stoichiometric hydrogen and oxygen mixtures to 3000 psi. These three driver techniques were chosen because of their ability to cover the complete range of desirable test conditions and because of their practicality, reliability, and safety compared to other techniques. Maximum performance is obtained with a rich helium, hydrogen, and oxygen mixture although very little advantage is gained by going to mixtures of less than 70% helium (mole fraction).

Various design performance characteristics are illustrated in the following discussions. A 10,000-psi driver produced by an initial 1100-psi, 70% helium combustion mixture will drive a Mach 20 shock into air originally at a pressure of 1 mm of Hg. Considering the reflected nozzle flow with a 3/4-inch throat, a shock Mach number of 6, and air at atmospheric pressure initially in the driven tube, equilibrium temperature and pressure in region 5, which is the stagnation chamber for the nozzle, are 5000 psi and 3600°K, respectively. The equilibrium flow Mach number at the model is 10.6. This condition is produced with an initial combustion charge in the driver of approximately 450 psi. At higher shock Mach numbers the stagnation temperature goes up, of course, but the flow Mach number at the model drops because the expanded gas is still hot.

Several aspects of the design of the tunnel are interesting. One is the large inner diameter of the driven tube. This allows a relatively long tube, and therefore, long testing times with a reasonable length to diameter ratio. The shock wave attenuation losses are thus kept low. Another important feature is the separation of the different tube sections through sleeve-shaft seal designs. This has been done to reduce the transmission of vibrations through the structure. It also allows simple operation of the tunnel. Figure 8 shows the three sections of interest. Consider the diaphragm clamping system. The driver is attached to a sleeve that slides over the driven tube through four hydraulic cylinders. The thrust of each cylinder at full pressure, 7000 psi, is 250,000 pounds. In this arrangement only the sleeve and the hydraulic pistons move when a diaphragm is changed after a run and this is done simply by throwing a switch. The seals are achieved by

shaft mounted "O" rings between the sleeve and the driven tube and by face mounted "O" rings between the diaphragm and both the sleeve and the driver tube. When the diaphragm breaks, it hits only the sleeve and the transmission of vibrations to the driven tube is not large. The sleeve has a removable insert in the flow passage before the area contraction which permits the diaphragms to break out into a round or square support section. A photograph of this system with only two hydraulic cylinders is shown in Figure 8.

The nozzle end of the driven tube is also a sleeve unit activated by hydraulic cylinders. The second diaphragm is located between the end of the driven tube and the sliding block which slips over the removable throat section on another "O" ring shaft seal. Figure 9 is a photograph of the test section end of the shock tunnel.

The bellows mounted seal between the dump tank and the model supporting sting also helps to isolate the model from structural vibrations. A sketch of the complete sting and drive mechanism is given in Figure 10.

The severe shock tube instrumentation problems are well known, as are several methods that are now being employed to make desirable measurements. For model instrumentation in the M.O.S.D. program, three basic types of instrumentation are being employed: thin resistance thermometers to measure surface temperatures from which heating rates may be deduced, piezoelectric pressure transducers to measure body pressure distributions, and high speed photography to study flow establishment and the character of the developed flow. More or less standard instrumentation techniques are used to operate the facility and to determine its performance. A few of these are promoter-type spark plugs with variable ignition energy systems to initiate combustion, pressure gauges and ionization probes used in conjunction with cathod ray oscilloscopes and a multichannel recording oscillograph to determine the shock velocity and the tunnel pressures as a function of time, and thermocouple vacuum gauges and absolute manometers to measure the initial pressures in the driven tube and in the test section.

The thin resistance-type thermal gauges have been developed to a high productivity at Princeton University, the AVCO Advanced Development Research Laboratory, the Cornell Aeronautical Laboratory, and other laboratories. It is planned to use the very thin (the order of 0.1 micron), or surface temperature following gauge as often as possible because of the relative ease of depositing such a gauge on a doubly curved surface without causing flow disturbance. For high Reynolds number testing, when the durability of the thin film becomes critical, the calorimeter, or thick film gauge imbedded in the model surface will be used.

A number of experiments have been made with a miniature Kistler quartz crystal pressure gauge located at the stagnation point of a 2-inch hemisphere in the region 2 flow. From the results of these tests it is believed that this gauge will be quite useful for detailed model studies. For example, the response time of a non-shock mounted gauge in the described flow situation is 4 microseconds and the ringing envelope is about $\pm 5\%$ of the mean value ($p_s = 200$ psi). The mean value remains constant within 3% until the reflected wave appears at the gauge (200 microseconds). Figure 11 is a photograph of

some of the pressure instrumentation being used. To the left is the regular Kistler gauge and in the center is a gauge manufactured by the Atlantic Research Corporation. This instrument has a barium titanate crystal imbedded in an epoxy resin. The miniature Kistler gauge is shown to the right next to the 2-inch hemisphere-cylinder model in which it has been mounted.

The photographic and optical equipment includes a double (horizontal and vertical) 10-inch Schlieren system in conjunction with various photographic techniques. In addition to still sub-microsecond spark and Fastax equipment, there is available a unique rotating mirror, rotating drum, framing camera that allows the taking of sub-microsecond exposures every few microseconds for a continuous period of a few milliseconds. Long duration (1 to 3 milliseconds) exploding wires are used as a light source for this camera. An electronic shutter (Kerr cell) is also available and can be used for still photographs and with a simple drum camera.

It has been mentioned that the aerodynamic properties of the flow in the three test regions are complimentary to each other in terms of the flow Mach and Reynolds numbers. The maximum performance that can be achieved in each region will now be presented in terms of the simulation of state properties in the stagnation region of a blunt body. These calculations are based upon the properties of air in thermodynamic equilibrium and upon a 10,000-psi driver produced by the constant volume combustion of a 70% helium, 30% stoichiometric hydrogen and oxygen mixture.

In the region 2 flow, stagnation region properties at the nose of a blunt model can be produced to match those on a free flight vehicle traveling at a Mach number of 15 at sea level. The maximum simulated flight Mach number increases with altitude until at 130,000 feet an M_f of 30 is simulated. Corresponding calculations for the non-reflected nozzle ($A_m/A_2 = 25$) show simulation at 45,000 feet for an M_f of 16 and at 90,000 feet for an M_f of 30. For the reflected nozzle ($A_m/A_t = 1600$), Mach 17 is simulated at 120,000 feet and Mach 30 at 160,000 feet. It is again pointed out that the test section flow Mach number in each of these cases is, in general, different and usually lower than the simulated Mach number. The usefulness of the nozzle flows is seen, therefore, in providing a considerable Mach number range for an experimental program.

The thermodynamic and chemical state of the gas in the test section is an important characteristic of the nozzle flows. The expanding gas will be somewhere between the frozen (at upstream concentrations) and the equilibrium state depending upon the flow times, or size and design of the facility, and upon the recombination kinetics. Calculations have been made for several different flow models considering air as the expanding gas and for the reflected and non-reflected nozzles. Initial conditions correspond to a shock Mach number of 12 and an initial driven tube pressure of 100 mm of Hg. The flow models are described and the results of the calculations are given in Table I. It is seen that the stagnation pressure at the model nose does not differ largely between the different flow models. Therefore, the Reynolds number of the flow are not greatly affected by departures from equilibrium. The flow Mach numbers do not vary from the equilibrium value by more than 10% except for the last frozen model in the reflected nozzle calculations. At-

tempts will be made to determine the departure from equilibrium in the nozzle flows by measuring the stagnation pressures and upstream pressures during a run.

The test program being followed can be divided into three somewhat distinct phases, the first two of which are preliminary. The initial test series was a study of the combustion driver under conditions in which it was safe to investigate high pressure phenomena. Experiments were run with the short shock tube in a rocket test pit at the General Electric Malta Test Station. The test installation is shown in Figure 12.

There were three general objectives of this program. The first was to determine the test conditions required to produce repeatable combustion over a pressure range of approximately 500 to 10,000 psi, and to match the combustion pressure rise with a cleanly breaking diaphragm near peak pressure. The second was to determine the hazard limits of the facility such as the detonation limits and the ability of the metal diaphragms to stay in one piece after rupturing. The third objective was to become familiar with the operation of the facility.

The first runs were at constant volume conditions and were done to determine the pressure history in the driver throughout the combustion cycle. Promoter-type spark plugs were located along the inner tube surface in a spiral array at distances varied for different tests from 1 to 1-1/2 feet. The pressures were sensed at two stations in the tube by standard Kistler gauges and were recorded on cathode ray oscilloscopes. Some of the results are shown in Figure 13. The maximum pressure rise is generally about 90% of the theoretical value which is calculated on the basis of no dissociation and no heat loss to the surroundings. The heat loss to the cold tube walls is responsible for the drop in pressure after the peak value is reached.

The results shown in Figure 13 are considered to be good. To obtain these pressure rises it was necessary to provide good gas mixing (multiple injection ports through which the gases were swirled into the driver tube), variable ignition energy for certain pressure ranges to retard detonation (not critical below initial pressures of 300 psi, low ignition energy at and above 300 psi), variable ignitor plug locations (1-foot spacing at and below 300 psi, 1-1/2-foot spacing above 300 psi).

Figure 14 presents pressure data obtained when detonation or auto-ignition occurs during constant volume combustion. This is undesirable from the points of view of both safety and tube performance. The 100-psi, 50% helium data is not strictly detonation, but strong waves are produced in the tube. The delayed detonation at 80% helium is interesting and was repeatable. Because of its general occurrence and because of the occurrence of strong detonation at lower helium percentages, the preferred operating percentages are limited to 70% to 75% helium (except at $p_1 = 100$ and 200 psi when it is possible to combust cleanly with 60% to 65% helium mixtures).

Pressure records obtained from the driver when combustion is matched with breaking diaphragms are shown in Figure 15. The first record shows a typical response for a detonable mixture. The trace for $p_1 = 900$ psi is distorted somewhat by extraneous electronic noise. For approximately

75 % of the runs it was possible to obtain good matching (diaphragm breaks within 5% of the peak combustion pressure).

Four different diaphragm materials were tested - annealed copper, 24SO aluminum, SAE 1020 steel, and type 304 stainless steel. Figure 16 is a photograph of copper diaphragms ruptured in the circular support insert. The thicknesses shown are 1/8, 1/4, and 3/8 inch and the diameter is 16 inches. The diaphragms have a milled cross on one face so that a controlled rupture is obtained. The depth of the cut is kept between 10% and 20% of the thickness so that the required diaphragm thicknesses are not excessive. The most desirable diaphragm materials have been found to be copper to 3000 psi and stainless steel from 3000 to 10,000 psi.

The objectives of the second phase of the experimental program, which is being run now, are to calibrate the complete facility and to evaluate the model instrumentation techniques. Certain aspects of this work will, of course, continue for some time.

The third phase, which involves detailed experimental programs, is about to begin. The following list presents some general aerodynamic studies for which the facility is suited.

1. Laminar boundary layer heat transfer
2. Turbulent boundary layer heat transfer
3. Separated flow heat transfer
4. Body pressure distributions
5. Flow field characteristics

ACKNOWLEDGEMENT

The construction and operation of this facility within the Missiles and Ordnance Systems Department was sponsored by the Air Force under Contract AF -04(645)-24. The author gratefully acknowledges this sponsorship.

A major portion of the design of the facility and of the instrumentation was originated by Dr. Y. A. Yoler of the Missiles and Ordnance Systems Department.

Table

COMPARISON OF TEST SECTION AIR PROPERTIES WITH
FROZEN AND EQUILIBRIUM EXPANDING FLOW MODELS

$$M_s = 12$$

$$P_1 = 100 \text{ mm Hg}$$

Flow Model	M_m	P_m/P_1	P_m/P_1	T_m/T_1	P_s/P_1	P_s/P_1	T_s/T_1
Non-Reflected Nozzle, $A_m/A_2 = 25$							
1. Equilibrium Throughout (Region 2, expansion through nozzle, through normal shock, to stag- nation)	4.68	.295	2.80	9.69	2.73	80.7	22.8
2. Equil. in Region 2, Frozen through nozzle Equil. across Normal shock Equil. to stagnation	5.11	.288	2.44	7.55	2.34	68.7	22.6
Reflected Nozzle, $A_m/A_t = 1600$							
1. Equilibrium Throughout (Region 5, expansion through nozzle, through normal shock to stag- nation)	6.73	$\frac{6.77}{10^3}$	$\frac{4.80}{10^2}$	7.10	$\frac{8.43}{10^2}$	2.45	20.6
2. Equil. in Region 5, Frozen through nozzle Equil. across Normal shock Equil. to stagnation	6.36	$\frac{6.40}{10^3}$	$\frac{5.68}{10^2}$	6.77	$\frac{6.82}{10^2}$	1.80	18.6
3. Equil. in Region 5, Frozen to $A/A_t = 400$, Const p to Equil. at $A/A_t = 654$, Equil. to test section Equil. across Normal shock Equil. to Stagnation	4.92	$\frac{8.90}{10^3}$	$\frac{9.85}{10^2}$	9.86	$\frac{9.31}{10^2}$	2.71	20.6

Subscripts: m refers to test section properties before normal shock
s refers to stagnation conditions at nose of model

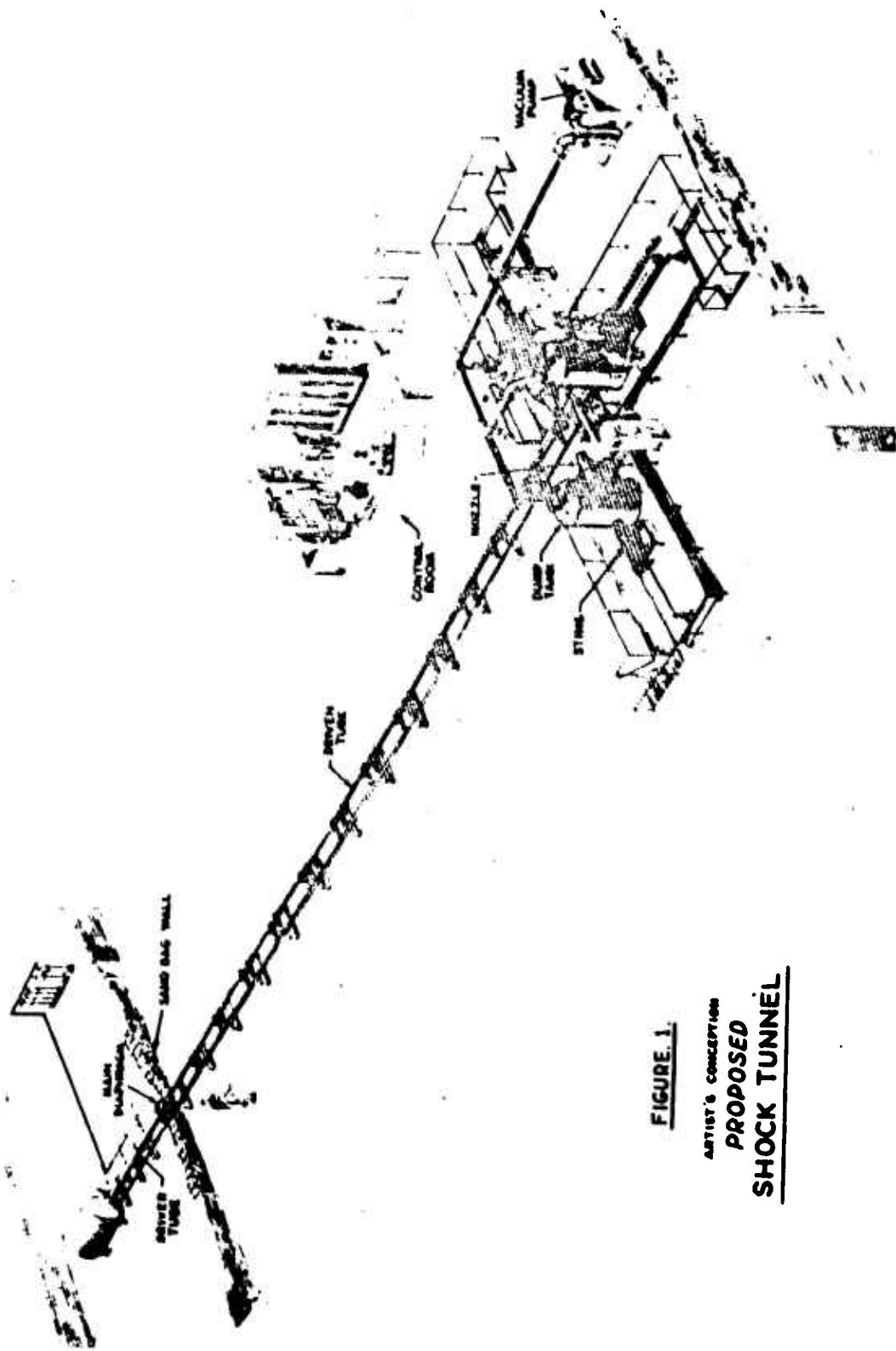


FIGURE 1.
ARTIST'S CONCEPTION
PROPOSED
SHOCK TUNNEL

Figure 1. Artist's Conception - Proposed Shock Tunnel

REGIONS AVAILABLE FOR AERODYNAMIC EXPERIMENTATION

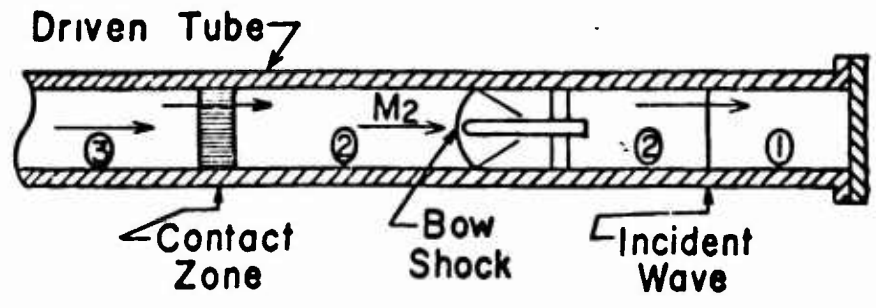
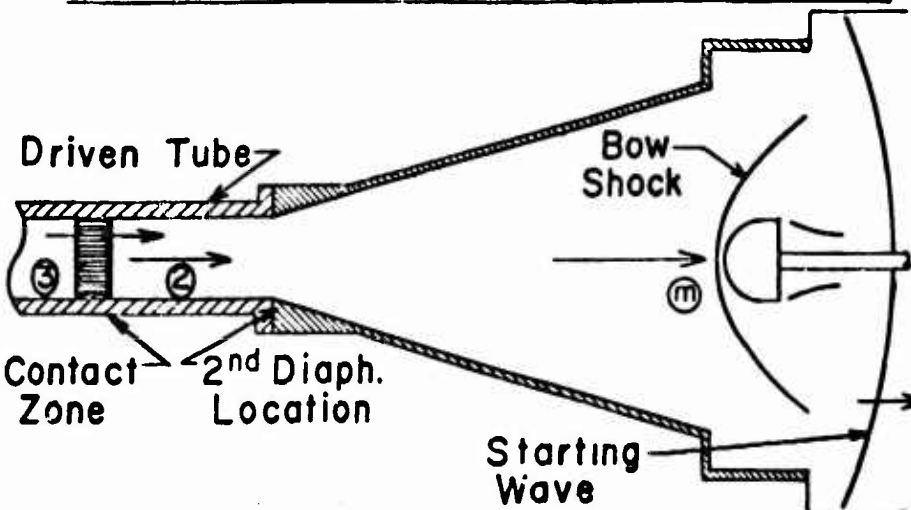
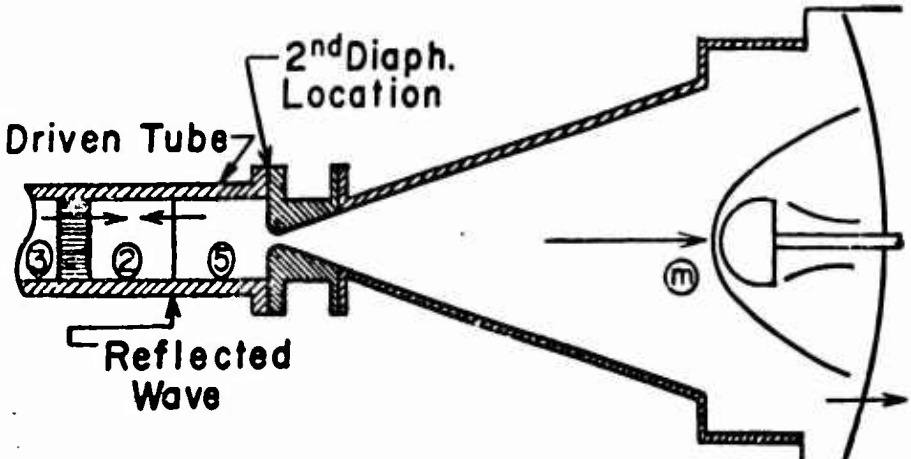
<p><u>Model Located in Straight Driven Tube</u></p> 	<p>Small Model Low M_2 (2-3) High Re Simulation</p>
<p><u>Model Located in Straight-Through Nozzle</u></p> 	<p>Large Model Moderate M_m (4-6) Moderate Re Simulation</p>
<p><u>Model Located in Reflected Nozzle</u></p> 	<p>Large Model High M_m (6-16) Low Re Simulation</p>

Figure 2. Regions Available for Aerodynamic Experimentation

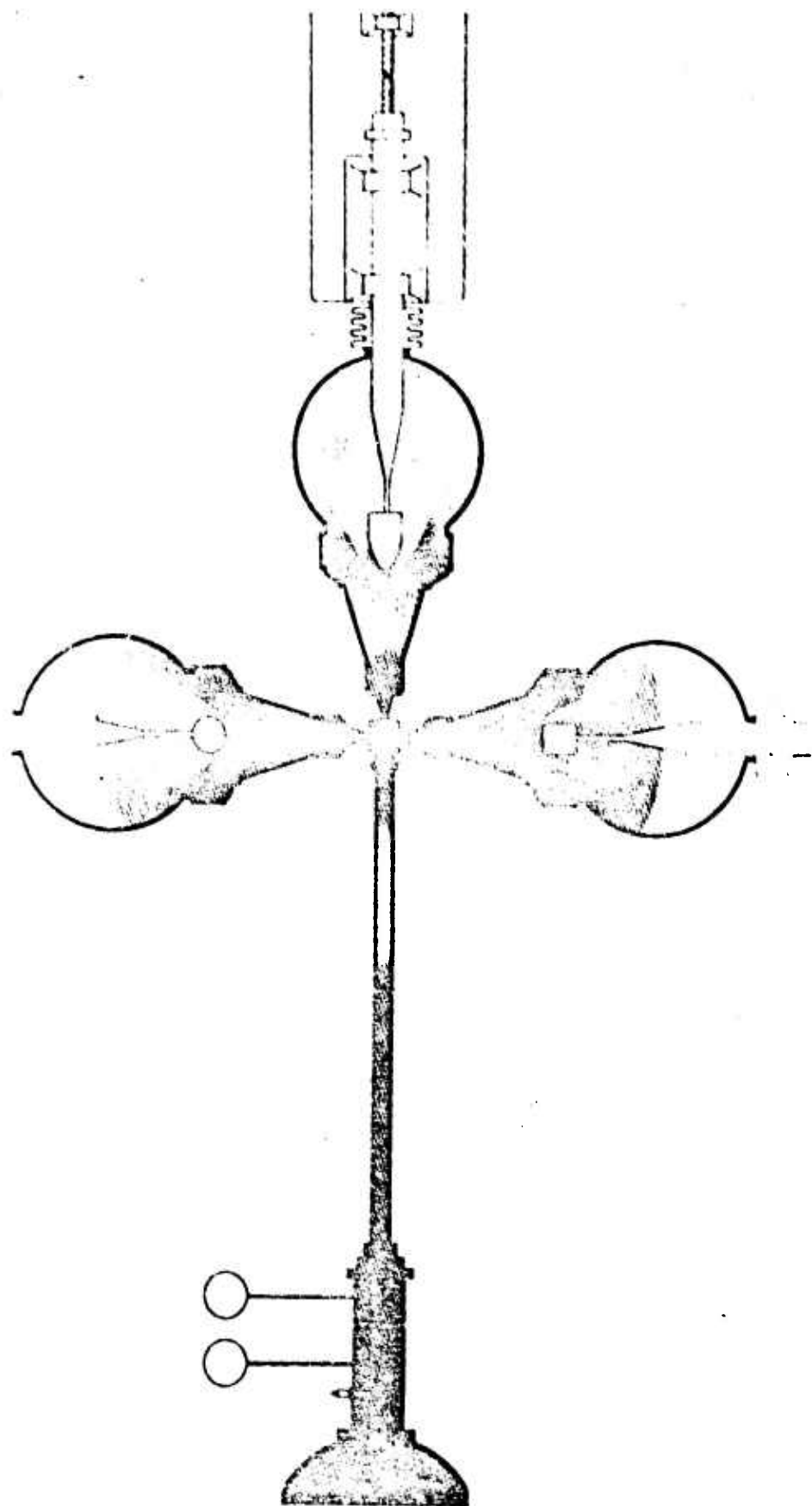
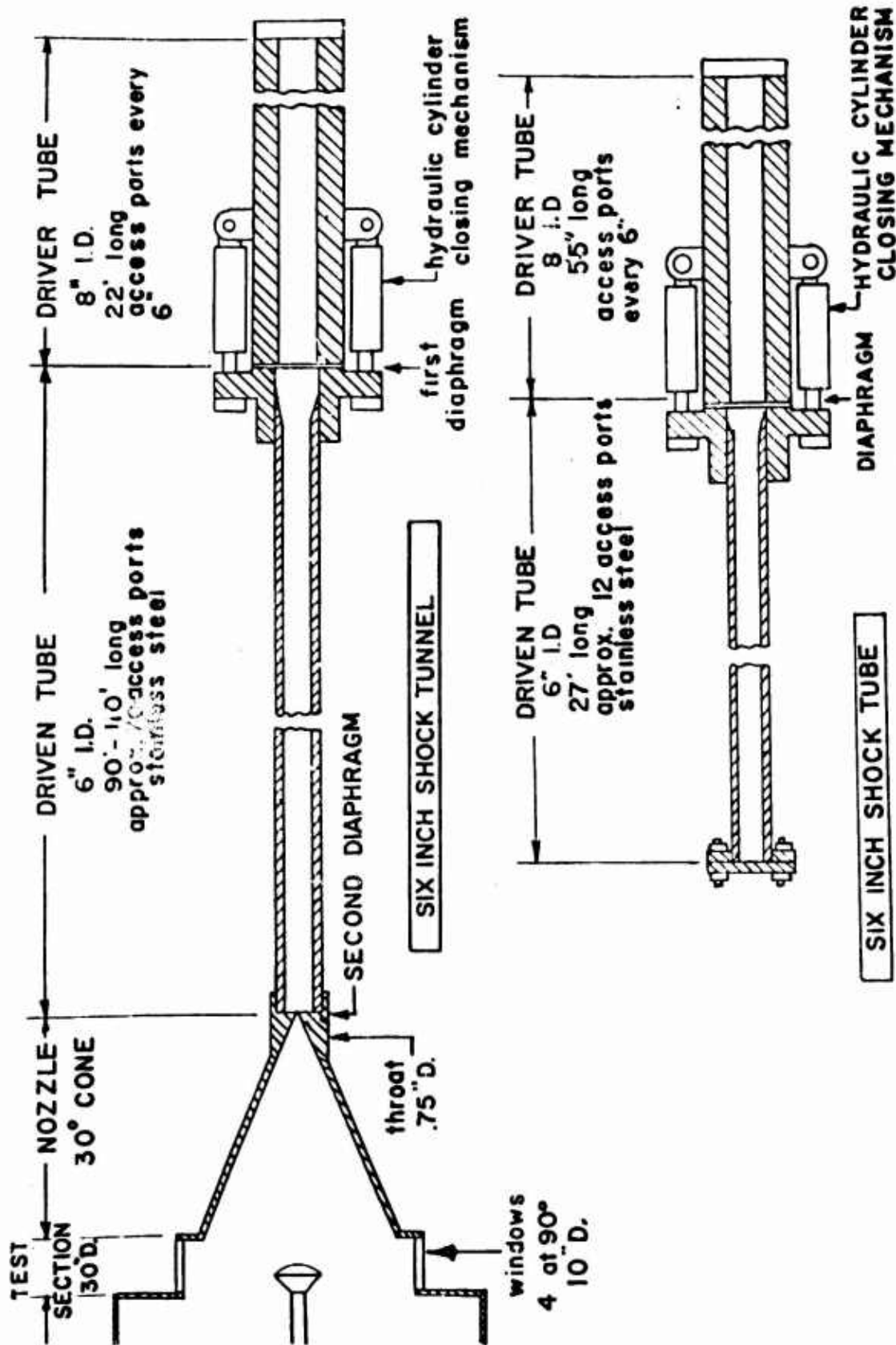


FIGURE 2D

Figure 3. Multiple Nozzle Reflected Shock Tunnel



SCHEMATIC DRAWING OF SIX INCH SHOCK TUNNEL & SHOCK TUBE FACILITIES

M.O.S.D. AERODYNAMIC LABORATORY

Figure 4. Schematic Drawing of Six Inch Shock Tunnel and Shock Tube Facilities - MOSD Aerodynamic Laboratory

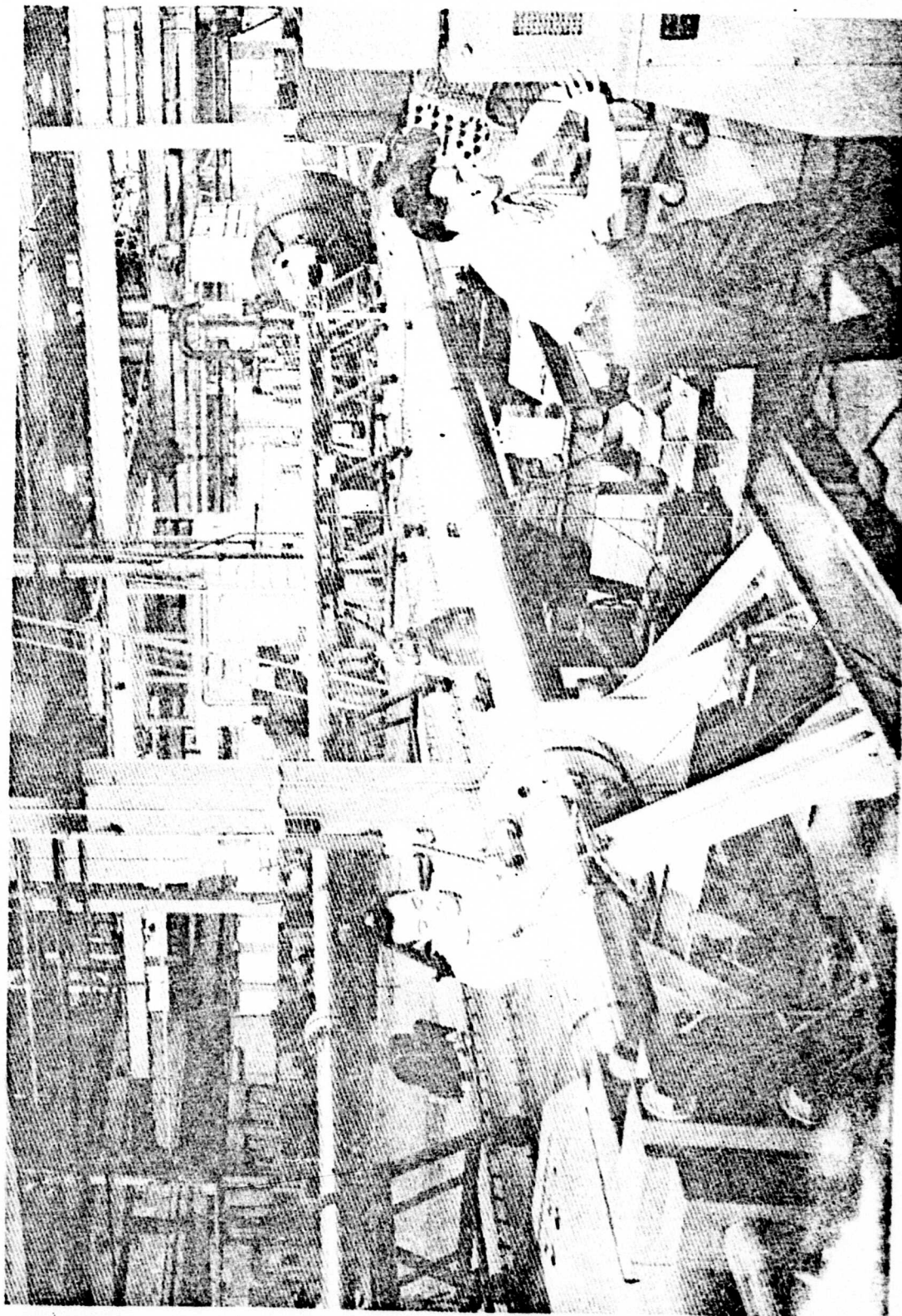


Figure 5. MOSD Shock Tube and Shock Tunnel

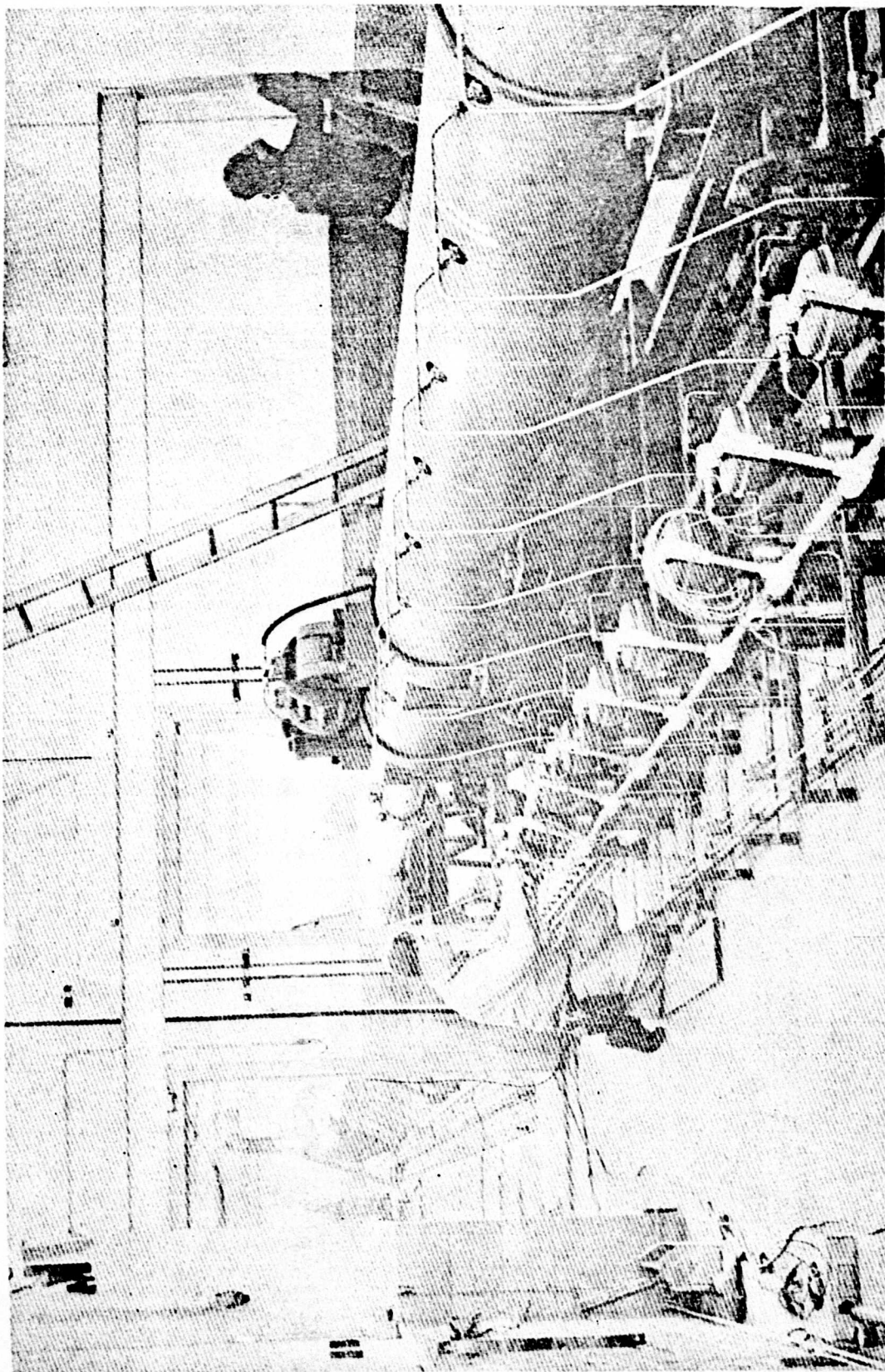


Figure 6. MOSD Shock Tunnel - Driver end

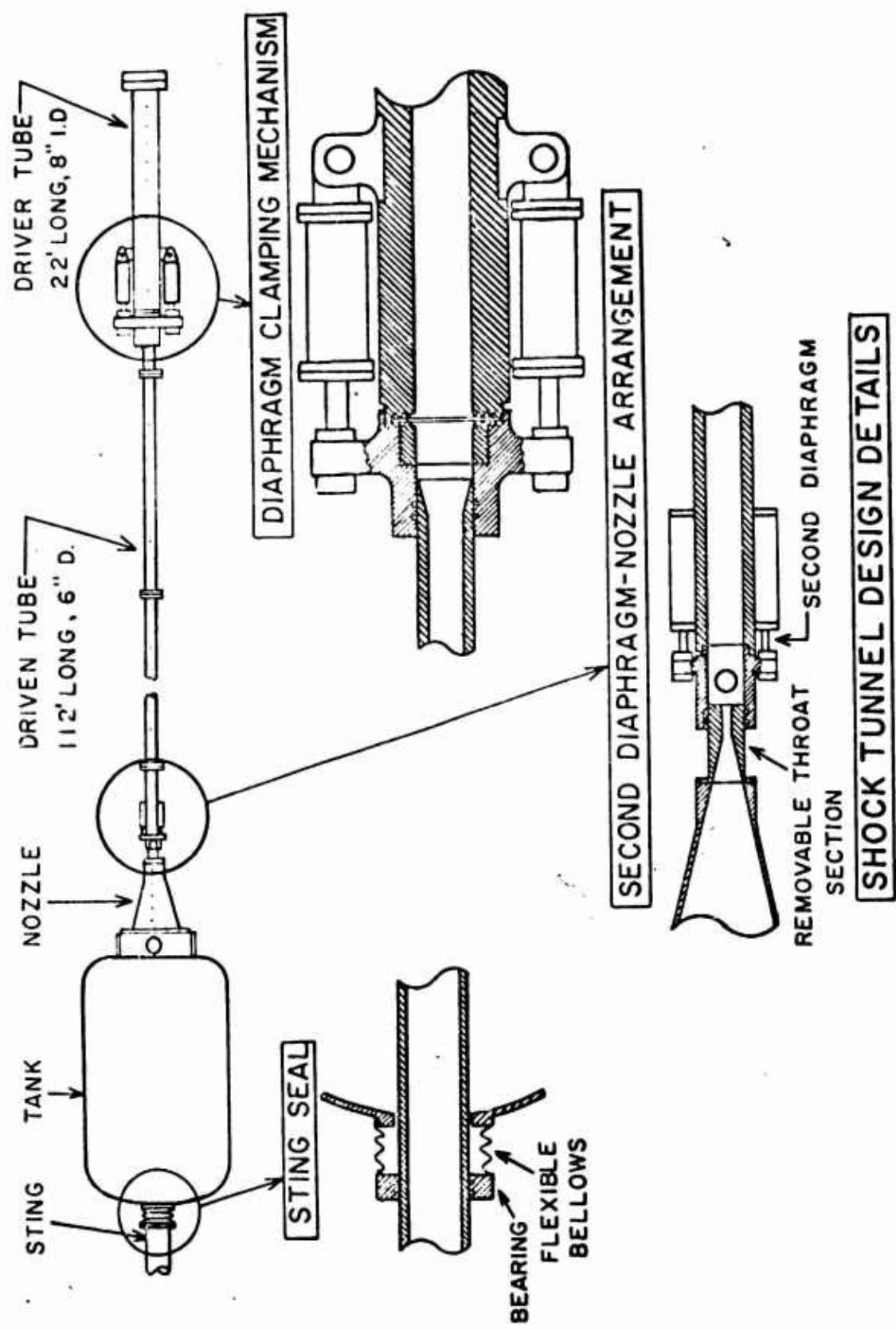


Figure 7. Shock Tunnel Design Details

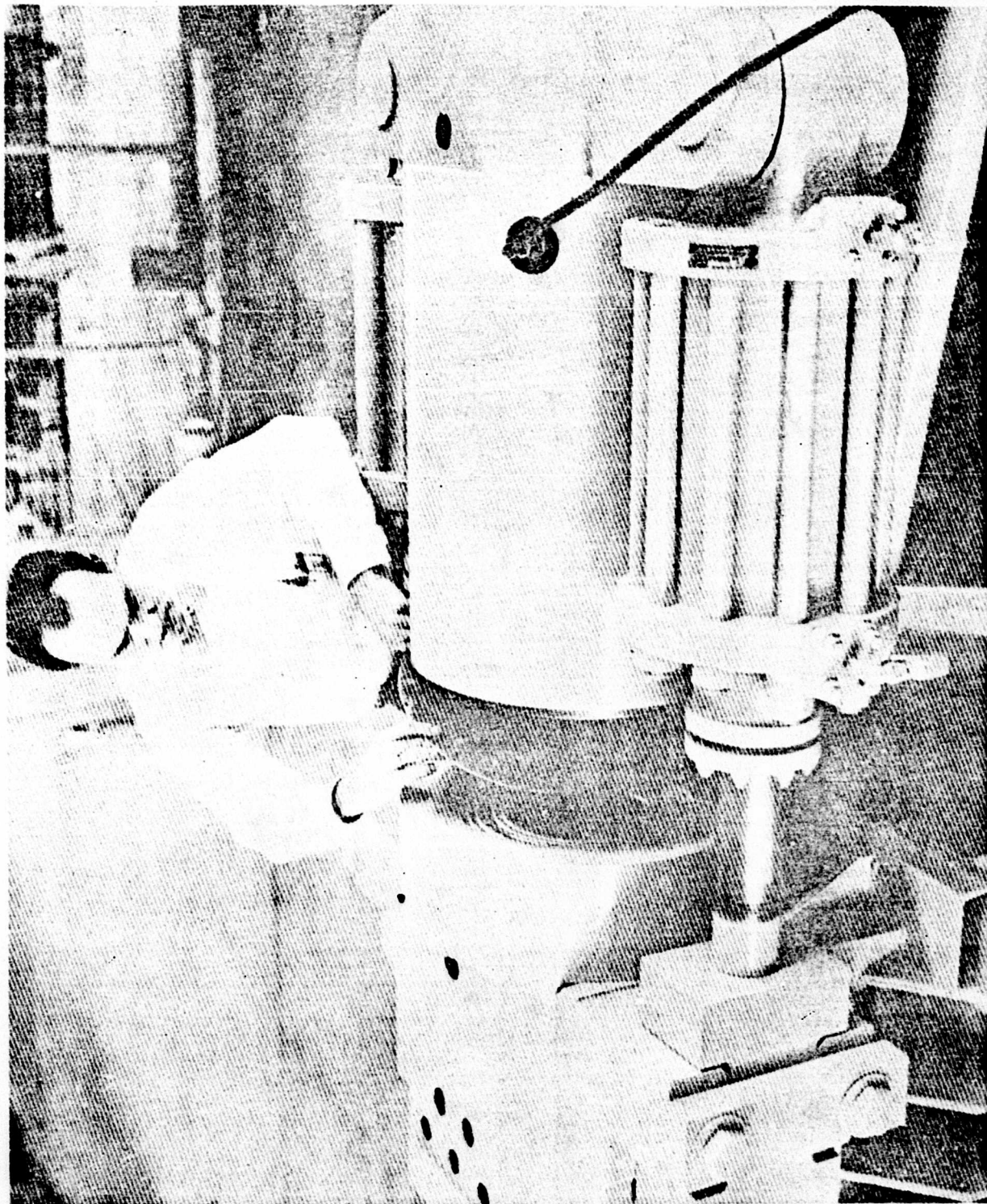


Figure 8. Main Diaphragm Clamping Mechanism

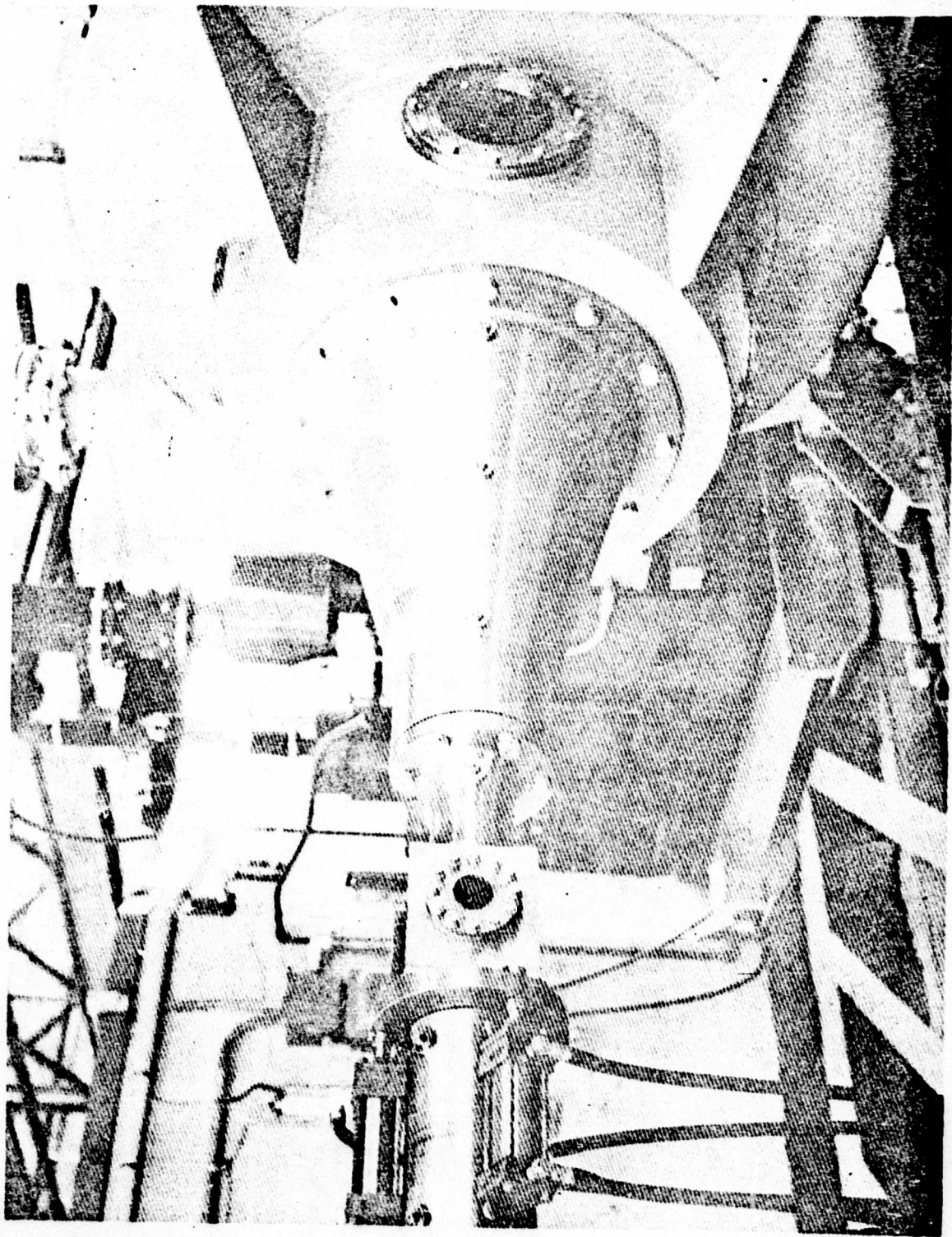


Figure 9. Second Diaphragm Clamping Mechanism, Nozzle, and Test Section

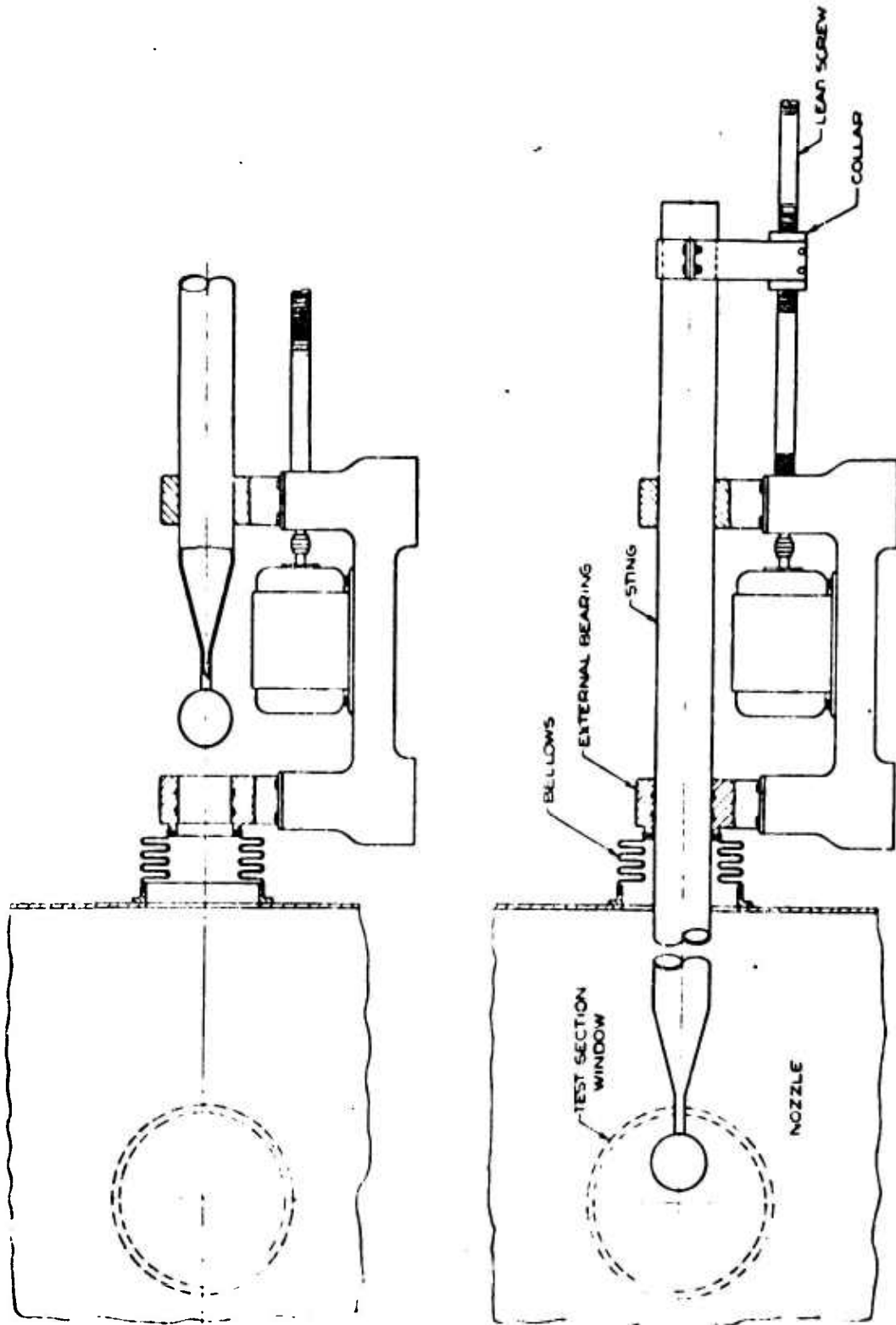


FIGURE 5C
STING SUPPORT AND RETRACTION MECHANISM
 Figure 10. Sting Support and Retraction Mechanism

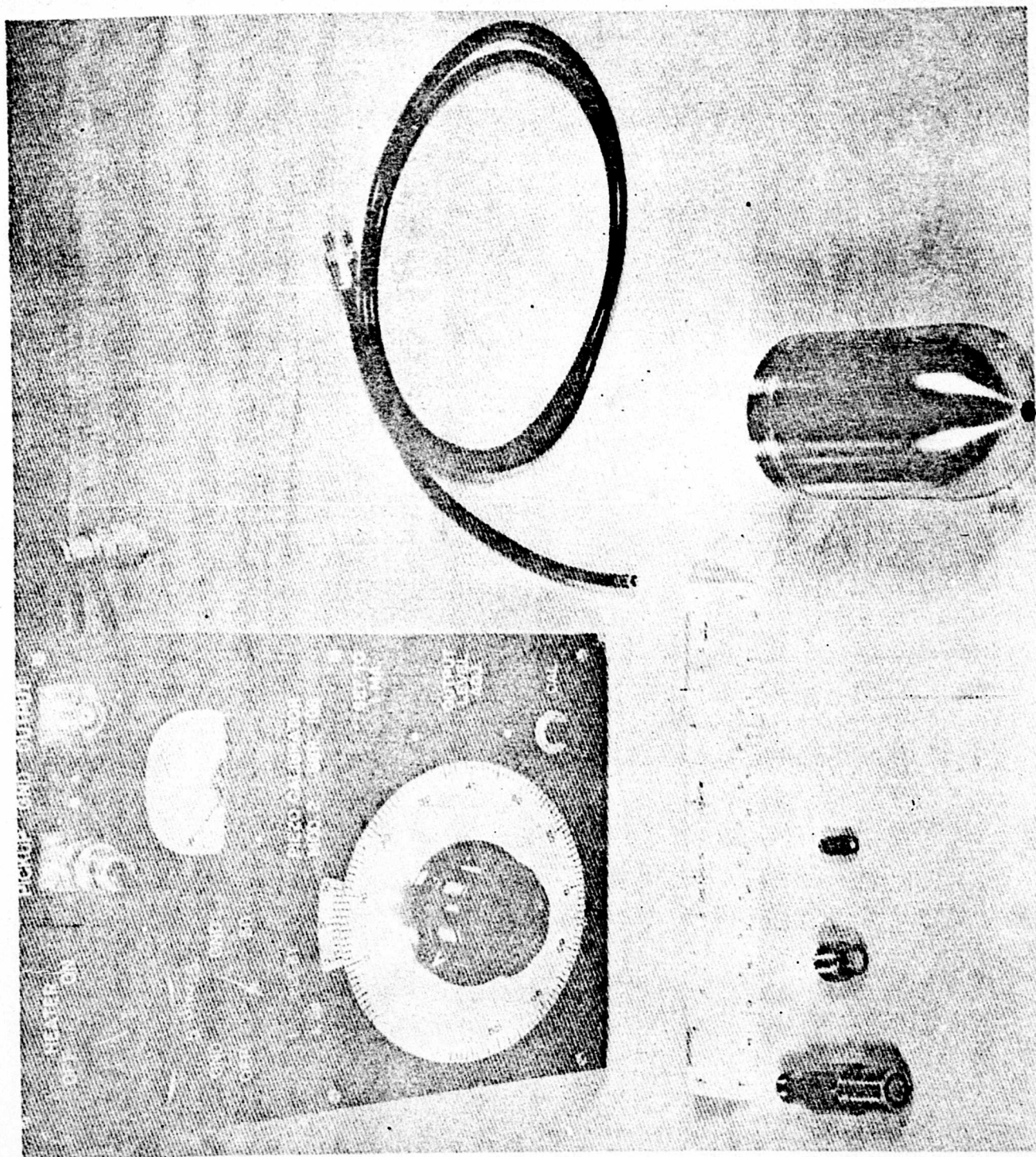


Figure 11. Pressure Instrumentation

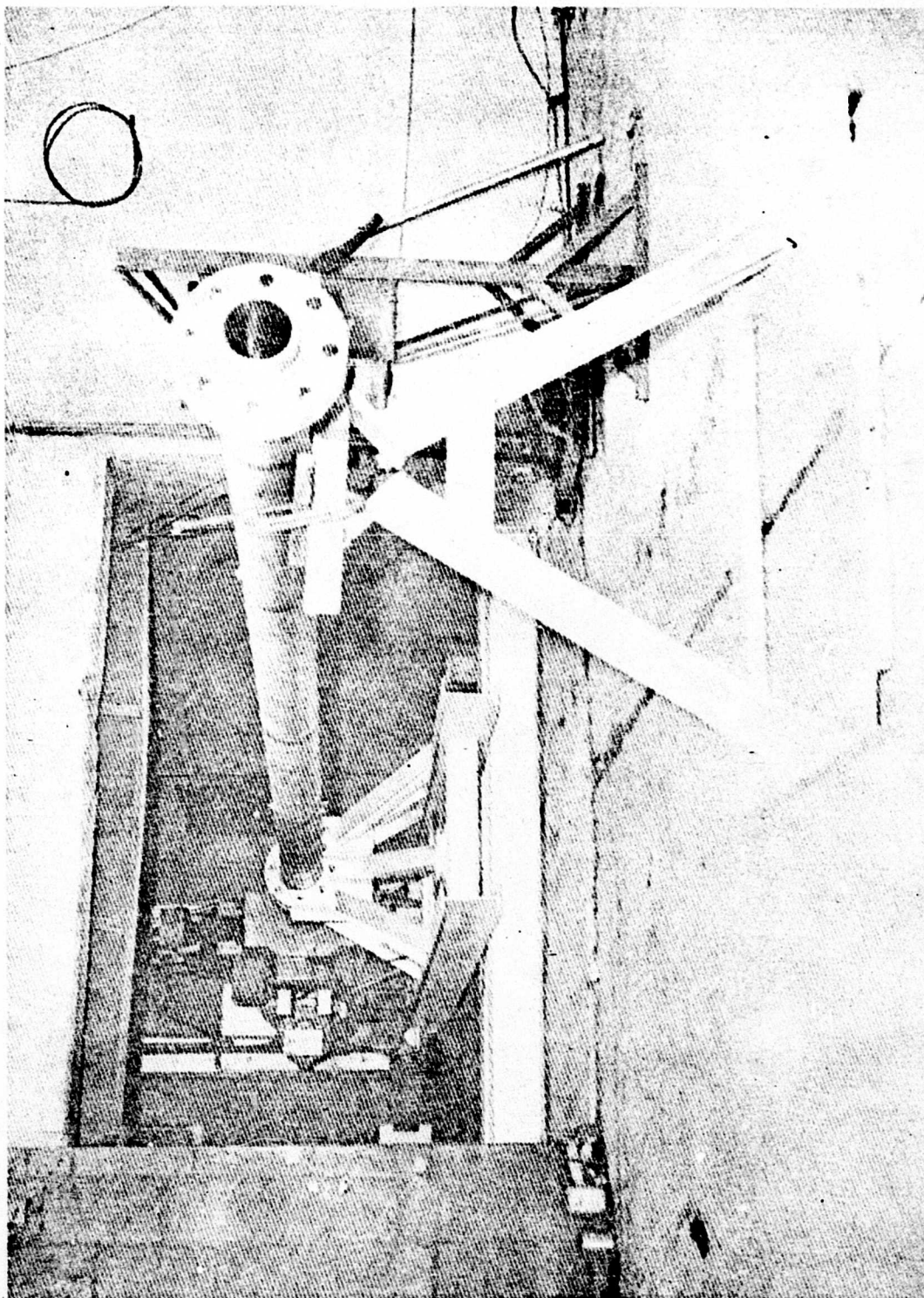
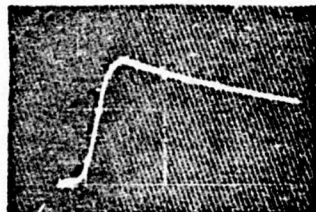
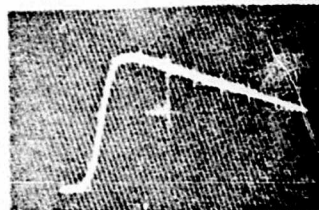


Figure 12. Installation of Six Inch Shock Tube in Rocket Test Pit for Combustion Studies

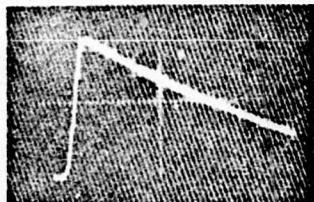
TYPICAL CONSTANT VOLUME COMBUSTION PRESSURE RECORDS OVER OPERATION RANGE OF DRIVER MALTA TEST PROGRAM, OCT 1956



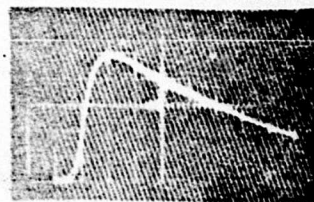
$p_1=100\text{psi}$ %He=70
 $p_f=835\text{psi}$
 10ms/cm sweep



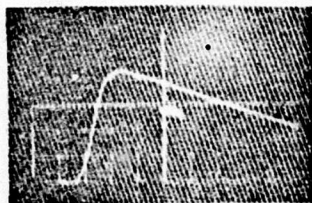
$p_1=200\text{psi}$ %He=70
 $p_f=1930\text{psi}$
 10ms/cm sweep



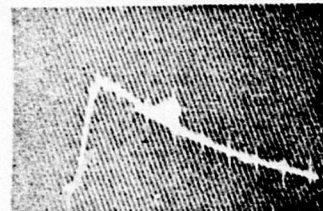
$p_1=200\text{psi}$ %He=60
 $p_f=2180\text{psi}$
 10ms/cm sweep



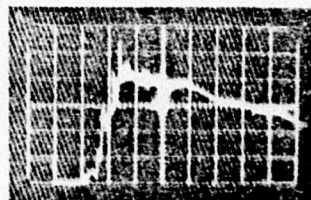
$p_1=300\text{psi}$ %He=70
 $p_f=2615\text{psi}$
 10ms/cm sweep



$p_1=500\text{psi}$ %He=70
 $p_f=4130\text{psi}$
 10ms/cm sweep



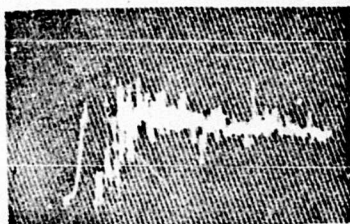
$p_1=600\text{psi}$ %He=70
 $p_f=4800\text{psi}$
 20ms/cm sweep



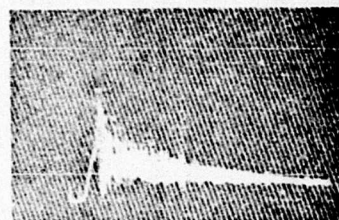
$p_1=1000\text{psi}$ %He=70
 $p_f=9280\text{psi}$
 10ms/cm sweep
 gauge adapter range

Figure 13. Typical Constant Volume Combustion Pressure Records over Operation Range of Driver

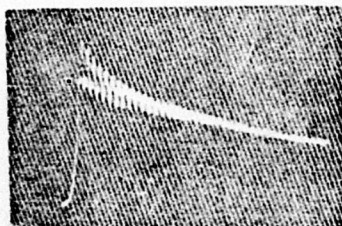
CONSTANT VOLUME COMBUSTION PRESSURE RECORDS
WHEN DETONATION OCCURS
MALTA TEST PROGRAM, OCT. 1956



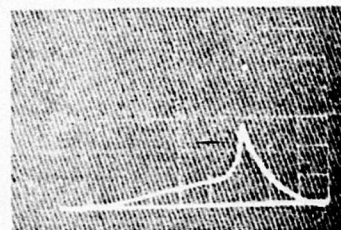
$p_i = 300 \text{ psi}$ %He=60
 10 ms/cm sweep
 4000psi full scale
 gauge with adapter



$p_i = 300 \text{ psi}$ %He=65
 10 ms/cm sweep
 5000psi full scale
 gauge with adapter



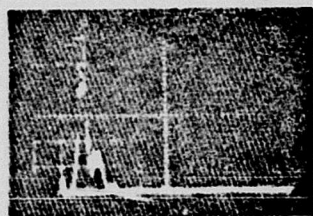
$p_i = 100 \text{ psi}$ %He=50
 10 ms/cm sweep
 1200psi full scale



Delayed Detonation
 $p_i = 300 \text{ psi}$ %He=80
 50 ms/cm sweep
 2700psi full scale

Figure 14. Constant Volume Combustion Pressure Records when Detonation Occurs

COMBUSTION PRESSURE RECORDS IN DRIVER TUBE WITH BREAKING DIAPHRAGMS MALTA TEST PROGRAM, OCT. 1956



$p_1 = 100\text{psi}$ %He = 50
10ms/cm sweep
1000psi full scale

Detonation
Break
←



$p_1 = 120\text{psi}$ %He = 60
 $p_{\text{max}} = 860\text{psi}$
5ms/cm sweep



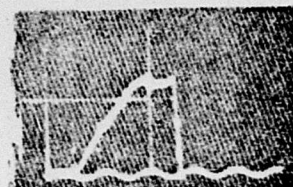
$p_1 = 200\text{psi}$ %He = 70
 $p_{\text{max}} = 1670\text{psi}$
5ms/cm sweep



$p_1 = 300\text{psi}$ %He = 70
 $p_{\text{max}} = 2550\text{psi}$
2ms/cm sweep



$p_1 = 630\text{psi}$ %He = 70
 $p_{\text{max}} = 5150\text{psi}$
10ms/cm sweep

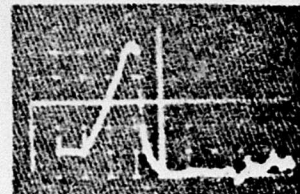


$p_1 = 900\text{psi}$ %He = 70
 $p_{\text{max}} = 6600\text{psi}$
10ms/cm sweep



$p_1 = 1220\text{psi}$ %He = 70
 $p_{\text{max}} = 11,400\text{psi}$

10ms/cm sweep



$p_1 = 10,200\text{psi}$

Figure 15. Combustion Pressure Records in Driver Tube with Breaking Diaphragms

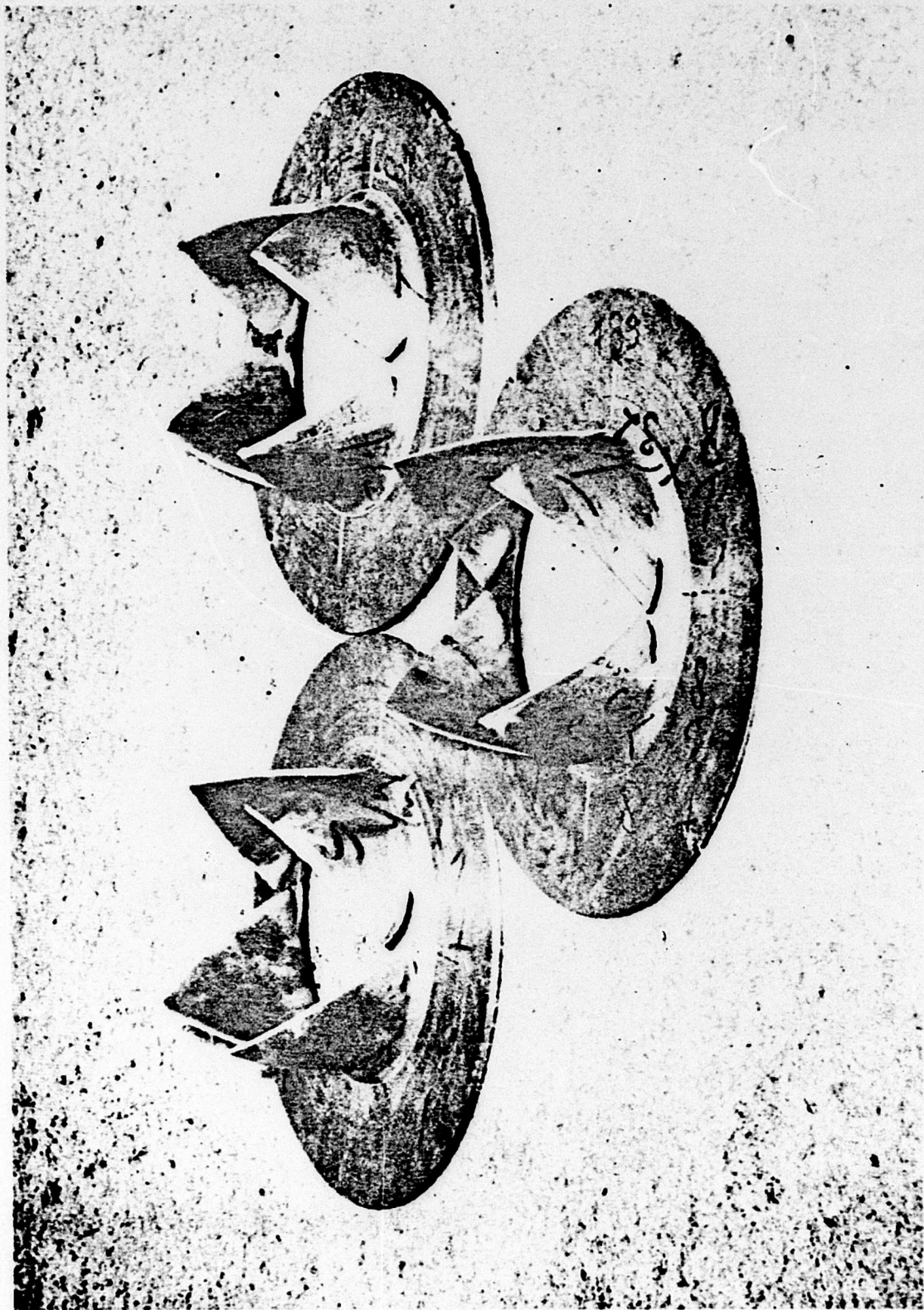


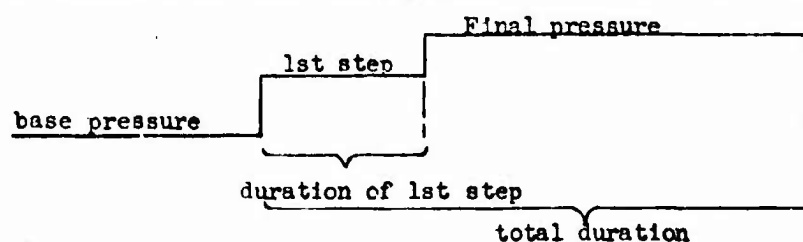
Figure 16. 16 Inch Diameter Copper Diaphragm 1/8, 1/4, 3/8 Inch Thick

DEVELOPMENT OF A SHOCK TUBE TO
GENERATE VARIABLE STEPPED SHOCK FRONTS

Richard I. Condit and Robert V. Steele*
Broadview Research and Development

As reported in preliminary form at the December 1953 meeting of the American Physical Society at Stanford University, California, we have had some success in replacing the bursting diaphragm of conventional shock tubes with electromechanical devices. These so-called "shock wave valves" allow the gas in the compression chamber to be dumped repeatedly with merely the push of a button and with no intervening requirement for disassembly or replacement of parts. A sketch illustrating the operating features of one of these devices is shown in Figure 1. Initially the same pressure is placed in both the compression chamber and the actuating chamber. The resulting pressure differential across the central part of the large diaphragm seals off the compression chamber from the expansion chamber. Operation of the valve occurs when the quick-release solenoid is suddenly tripped, thereby releasing the pressure in the actuating chamber and causing the large flexible diaphragm to be thrown open to release the gas in the compression chamber into the expansion chamber. If the rate of appearance of gas in the expansion chamber is sufficiently fast, the compression wave that results will develop into a shock wave as it moves down the tube. Thus shock waves can be conveniently produced without the inconvenience of disassembly after each shot, or flying fragments from broken diaphragms. (Incidentally large arrays of such shock wave valves would seem to be especially attractive for giant shock tubes, where both disassembly and diaphragm puncture tend to become either difficult or tedious.)

In searching for a useful application for such devices, we were informed that there was a need for a laboratory arrangement which could produce a variable stepped shock front whose pressure characteristics were as follows:

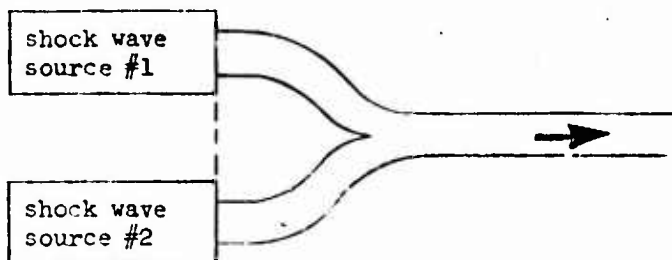


final pressure: 5 - 20 psi: total duration: 20 milliseconds
ht of 1st step: 25 - 75% of final pressure duration of 1st step: 2 - 8 milliseconds

* Now with Pratt and Whitney Co., Inc.; Livermore, California

It is to be noted that the intended use was in calibrating pressure gauges, so that the pressure profile was all important, and the conditions of gas flow of little importance. Consequently in our development efforts we have considered only pressure-time characteristics and have ignored the associated gas flow phenomena.

It seemed to us that here was an interesting opportunity for the use of shock wave valves, and we therefore proposed to develop an arrangement to produce the desired pressure profile using two separate shock wave valves. Their times of actuation were to be so coordinated as to dump first one and then the other into the expansion chamber. The variable duration of the first step was to be provided by the spacing between the times of actuation of the two units. The variable heights of the two steps were to be provided by the different pressures placed in the separate compression chambers. On this basis it was decided to proceed with the development of a generator of variable stepped shock fronts. The size of the installation was to be such as to supply the desired stepped wave to a shock tube having an inside diameter of about 4-1/2 inches. The scheme is illustrated below.



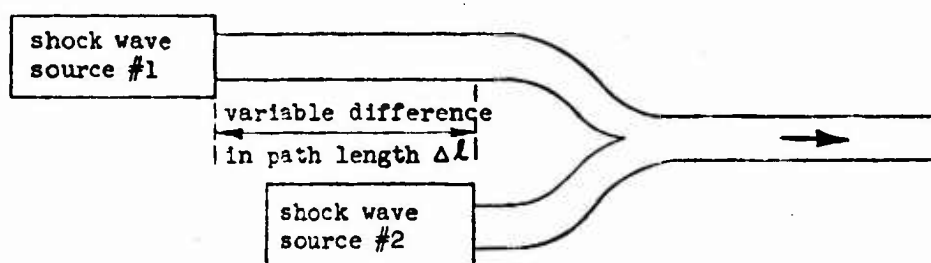
Time of actuation of #1 with respect to #2 is to be variable and such as to produce the desired stepped shock front.

Early efforts soon demonstrated that a single shock wave valve could be readily constructed to produce satisfactory shock waves for a 4-1/2 inch tube in the pressure range of interest. However the possibility of readily synchronizing the time of operation of two such shock wave valves to the desired accuracy turned out to be very remote indeed. Since the shortest separation in time of the two steps was to be 2 milliseconds, this meant that the time of operation of each shock wave valve had to be reproducible to a small fraction of 2 milliseconds. Thus one requires the two electromechanical-pneumatic assemblies to maintain a reproducible relative time of operation of something like 100 microseconds. Such a high degree of accuracy in the time of operation of the simple devices constituting our shock wave valves was soon shown to be several orders of magnitude away from that which was readily attainable. Rather than attempt to carry out the development along these lines with such extreme requirements for improvement, it seemed better to reconsider, and to search for some other principle for generating stepped shock fronts, some principle that would seem to be more naturally compatible with the specified requirements. Thus part way through the development it seemed necessary to abandon this procedure and start over again.

In our ruminations about what to try next we gradually became conscious of the significant apparent difference in the timing requirements if the base could be changed from time to distance. When 1 millisecond or so is viewed as the time interval between the operation of electromechanical

devices it appears as a very severe requirement. However, since in 1 milli-second a shock wave travels roughly 1 foot, the accurate positioning which is readily possible with respect to 1 foot suggests that a fine equivalent breakdown in time should be easy if it could be based on the distance travelled by the shock wave.

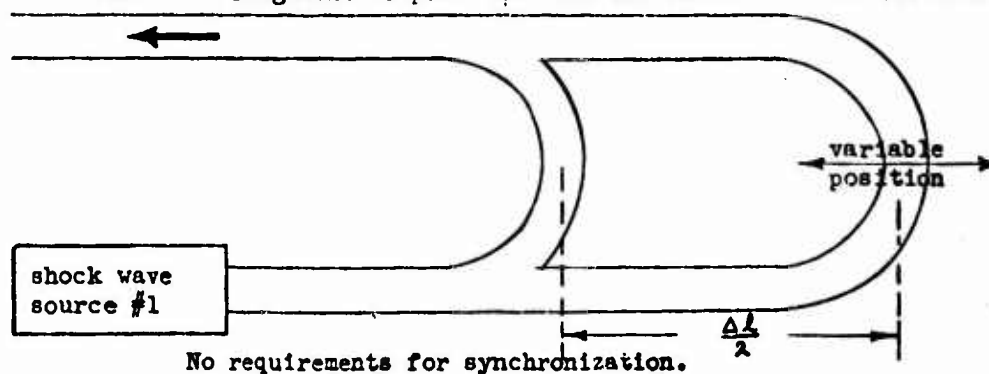
Pushing on this favorable thought, it seemed that if the two compression chambers for the stepped shock front were placed at different distances, then they could be initiated simultaneously and still get the desired output pressure profile. This scheme is illustrated below.



Time of actuation of #1 and #2 to be simultaneous; their variable separation in distance is to provide the desired stepped shock front.

Although this scheme was more attractive than the original one it still has a significant requirement for synchronized timing, since two operations must be done simultaneously. Clearly an improvement would seem to follow if all requirements for synchronized operations were eliminated. This would seem to necessitate the use of but one source of shock waves. Thus the need was for an arrangement employing but one source of shock waves (and therefore no requirements for synchronization) and a variable differential path length (to allow the necessary separation in time of the stepped shock wave).

Such an arrangement is possible with the scheme illustrated below.



No requirements for synchronization.

Thus all requirements would seem to be met in principle by using but one source of shock waves and two branch ducting between the source and the measurement section. The difference in path length could be made variable by extending the longer branch in a manner similar to that of a trombone. (Because of this similarity this shock wave generator has been referred to as a "trombone".) Actually, the variable length of the first step in the pressure profile is provided by an array of flanged pipes of different lengths which can be inserted into the longer branch. This procedure of a series of fixed steps in the longer branch was employed rather than a continuously variable sliding arrangement for simplicity, to provide a smooth interior wall, and to more readily withstand the 20-psi shock forces.

For the single source of shock waves, it was decided to utilize a conventional shock tube compression chamber and frangible diaphragm assembly since there were no longer any requirements for synchronized times of operation and since such a source is probably superior for calibration purposes. The general arrangement of the resulting shock wave generator is shown in Figure 2.

Fig. 2 shows the assembly for a difference of path length of 8 feet (two 4-foot pipes). Path length differences of 4 feet (two 2-foot pipes) and 12 feet (two 2-foot plus 4-foot pipe combinations) were also provided. The compression chamber pipe was made sufficiently long to provide the specified 20 milliseconds total duration. The diaphragm and diaphragm-puncturing mechanism were conventional and located just ahead of the "Y" branching.

To control the distribution of pressure between the two ducts, a hollow tube called a "scoop" was placed within each passageway of the input "Y". Each of these was moveable as required from the outside. To build up the pressure of the first step, the scoop in the leading duct was pushed forward. Similarly to build up the pressure in the second step (and reduce the pressure in the first step) the scoop in the leading duct would be withdrawn and the scoop in the trailing duct advanced. Only one scoop was effective at a time; the scoop in the trailing duct served for first step pressures from 0% to 50% of the total pressure, while that in the leading duct served for first step pressures from 50% to 100% of the total.


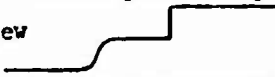
Samples of oscillograms of pressure versus time obtained with this apparatus are shown in Figure 3. The upper series shows how the duration of the first step gets greater as the differential path length is increased. The lower series shows how the relative height of the first step decreases as the scoop in the leading duct is withdrawn and that in the trailing duct is advanced.

From an extended series of such data we can obtain the pressure height of the first step as a function of the total pressure, for various positions of the scoops. These relations are shown in Figure 4. In Figure 4, the path length difference has been held constant at 8 feet. The fact that each line is straight reveals that the distribution of gas between the two ducts is fairly independent of the gas pressure (within the limits of the available data). The spread among the lines shows how the total pressure can be distributed at will among the two ducts by adjustments in scoop positions.

While the main effect of the differential path length is to determine the duration of the first step, and the main effect of scoop position is to determine the relative height of the first to the second step, there is actually some interaction between these two effects. This interaction of scoop position on the duration of the first step stems from the variations in shock wave velocity with pressure level. If all shock waves progressed through the trombone passages at a constant velocity, then the height and duration of the first step would be strictly independent. Actually, as the pressure rises, the shock wave velocity increases somewhat, so that the same differential path length will lead to first steps having slightly different durations.

These interactions between length and height of the first step are documented in Figure 5. Figure 5 gives the duration of the first step as a function of path length difference for various scoop positions and several different total pressures (compression chamber pressures). It can be seen that the general average duration decreases as the pressure is raised (arrow positions drop with increasing pressure). Additionally, the spread in duration for different scoop settings tends to increase as pressures get higher. These interactions complicate somewhat the adjustment of the apparatus but in no way prevent it from satisfying the given specifications.

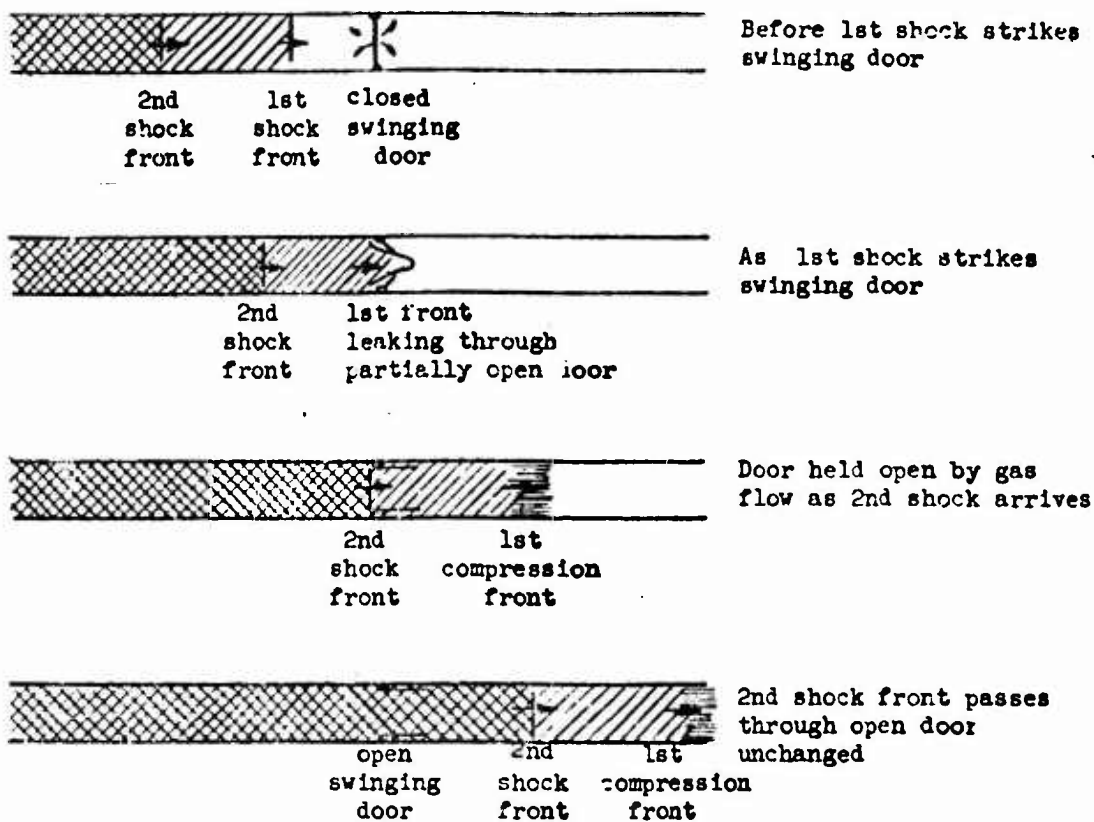
As described, the trombone was found to yield satisfactory stepped shock fronts over the specified range of interest.

However with this goal achieved, it was determined that a "slight" deviation from the original specifications was highly desirable. To wit, the first step should have a slowly-rising compression wave for the leading edge rather than a discontinuous shock wave. However the leading edge of the second step should remain a shock wave. Thus the desired pressure profile was changed from the original  to the new 

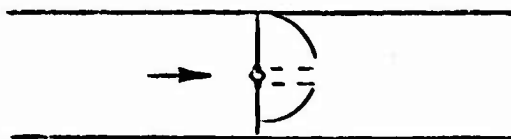
So the development effort was not yet finished.

Since all other specifications seemed to be met by the trombone as described, it seemed desirable to attempt to supply the additional feature of a slowly rising front by adding some new component in such a way that the favorable results already achieved were not sacrificed. Therefore the initial attempt (and the approach actually adopted) was to leave the trombone as it was--arranged to produce two shock waves--and then to add something which would degrade the leading shock wave into a compression wave. It seemed conceivable that the leading shock wave could be degraded into a compression wave by causing it to open some kind of a door which initially blocked the shock tube. With such arrangement, the shock might leak past just a little at a time as the door just opened, and then later it might be nearly unimpeded after the door was wide open. It was hoped that the impedance to gas flow presented by such an opening door would yield a compression wave when acted on by the incident shock wave. However the second shock front would presumably pass through the doorway unmodified, since the door would already be opened when it arrived.

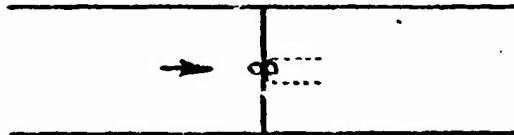
Schematically, the leading shock wave is forced to open up a swinging door somewhat as follows:



Actually, with a tube of circular cross section it is not convenient to hinge the swinging door at the wall, so a central post was added as a support and pivot point. The first swinging doors for the trombone were made of metal door hinges.



Unfortunately these metal assemblies could not be made to withstand more than a few shocks. After that they were generally damaged beyond repair. However, rubber diaphragms clamped between two central posts would survive many shocks and when properly arranged would produce the desired compression wave.



The proper arrangement of these "flappers" consisted of a suitable ratio of mass to restoring force for a given region of operating pressures. If the mass was too small for the given shock pressure, the shock front would pass through the flapper assembly with scarcely any degradation. If the restoring force of the rubber were too great the flapper would partially close against the flowing gas and the resulting constriction would show up as a dip in the pressure profile in place of the desired flat top.

Figure 6 shows two oscillograms of the stepped fronts from the trombone when the first step was degraded to a compression wave. Correct and incorrect operation of the flapper is shown.

With a suitable combination of metal weights added to various rubber diaphragms, it was possible by empirical trials to evolve a family of flappers which would degrade the leading edge of the first shock to a compression wave over the entire pressure range of interest.

The only apparent drawback to this procedure was that the majority of flappers were not self-cocking. After each employment they had to be reset by hand, a process requiring disassembly of that part of the trombone.

In a final development effort some success was achieved with rubber diaphragms cut in the form of a star and mounted between flanges. The arrangement of these rubber "stars" is shown in Figure 7. These devices tended to reset themselves automatically, so they could be used repeatedly without disassembly. Here again it was necessary by trial to determine the proper ratio of mass-to-restoring force for the petals of these star-cut diaphragms. Mass was increased by adding metal weights to the tips of the petals. Restoring force was reduced by undercutting the rubber in the region at the base of the petals where the extreme flexing was to be expected. In the limited time available for these finishing touches it was not possible to achieve re-cocking star assemblies for the entire pressure range of interest. However a significant replacement of flappers by stars was accomplished.

It is to be noted that the compression wave in the leading edge of the first step following the degradation by the star or flapper assembly is only transitory, since it tends to build back up into a steep-fronted shock wave as it travels on down the expansion chamber. Because of these inevitable changes, as long as a compression wave is required, it is only possible to produce the desired pressure profile at one distance from where degradation occurs. In our set-up, the point of observation, i.e. the point for pressure gauge calibration, was to be about 10 feet beyond the position of the star or flapper assembly. At distances closer than 10 feet, the compression wave would have a slower rise time and at greater distances a faster rise time than at the designated point

of observation.

The final array of stars and flappers which were supplied to provide the degraded leading edge for the stepped shock front throughout the pressure range of interest is shown in Figure 8. It can be seen that the range of effectiveness of any one degrader is not extensive and consequently a sizeable number of different units are required.

Thus the specifications created for the variable stepped shock front were finally satisfied by this development. It is interesting to note that the resulting equipment was a far cry from the pair of shock wave valves originally envisioned.

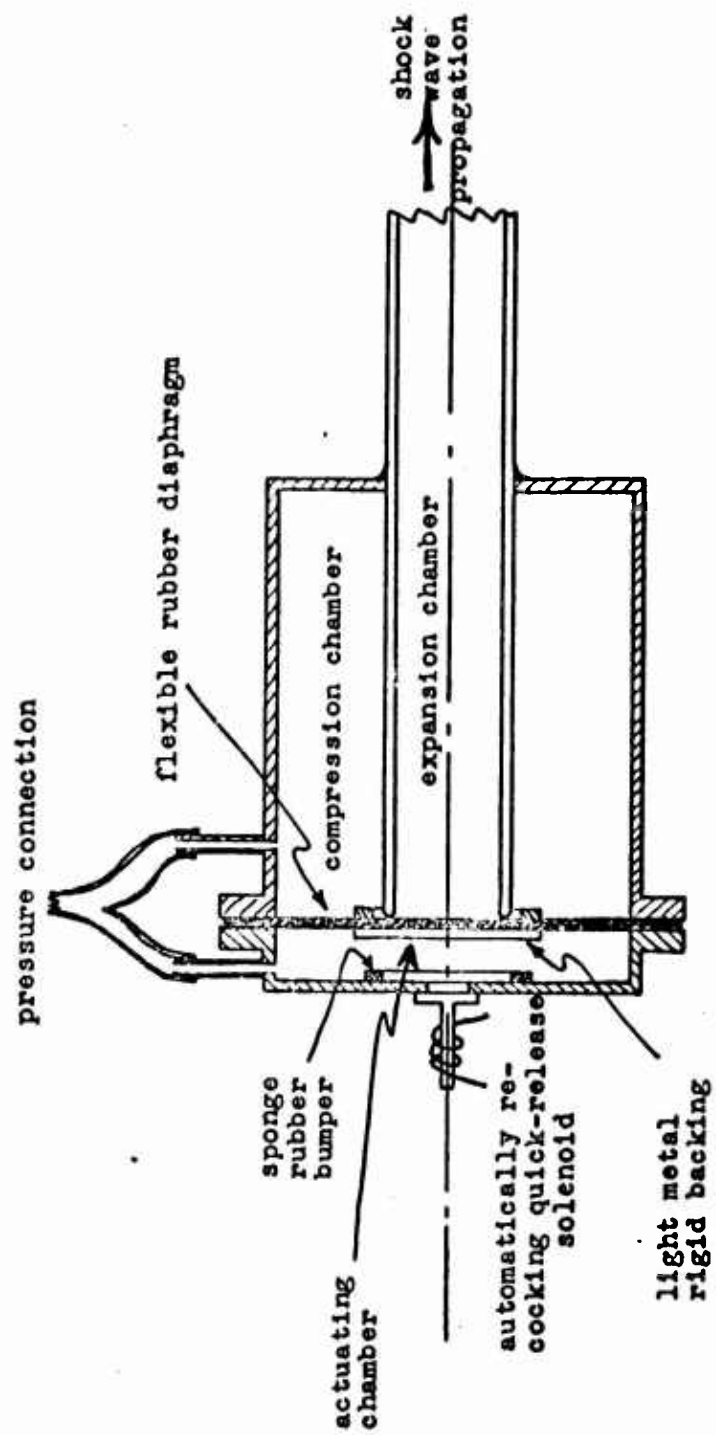


Figure 1. Schematic Representation of "Shock Wave Valve"

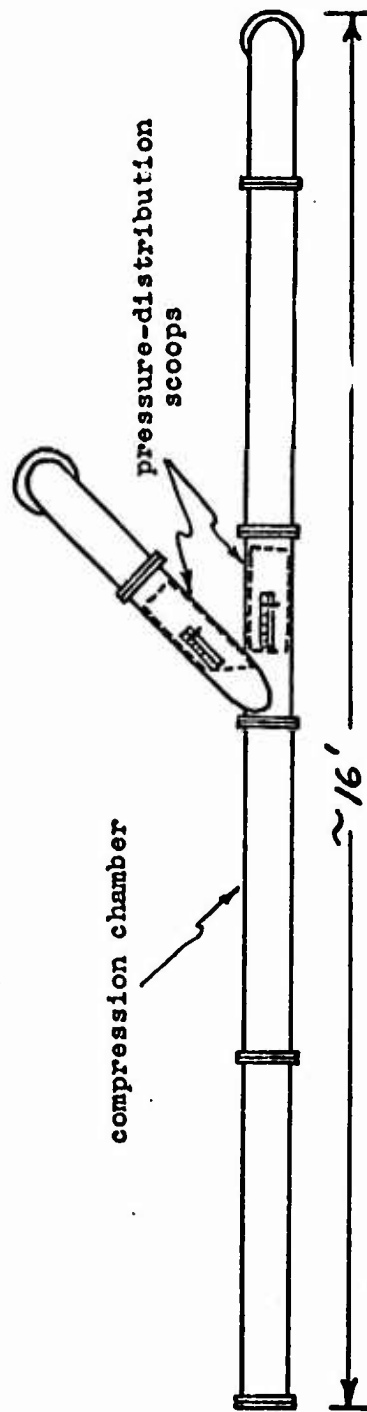
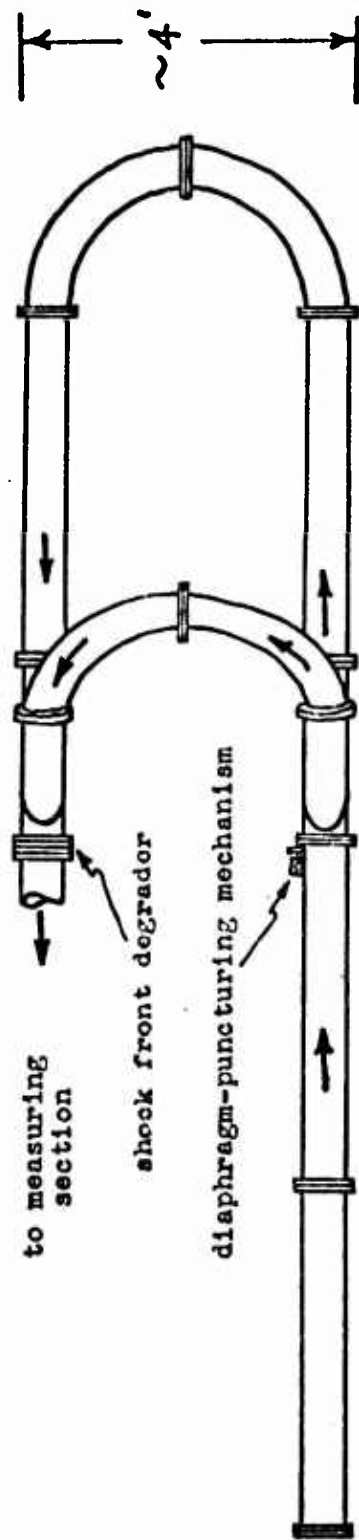
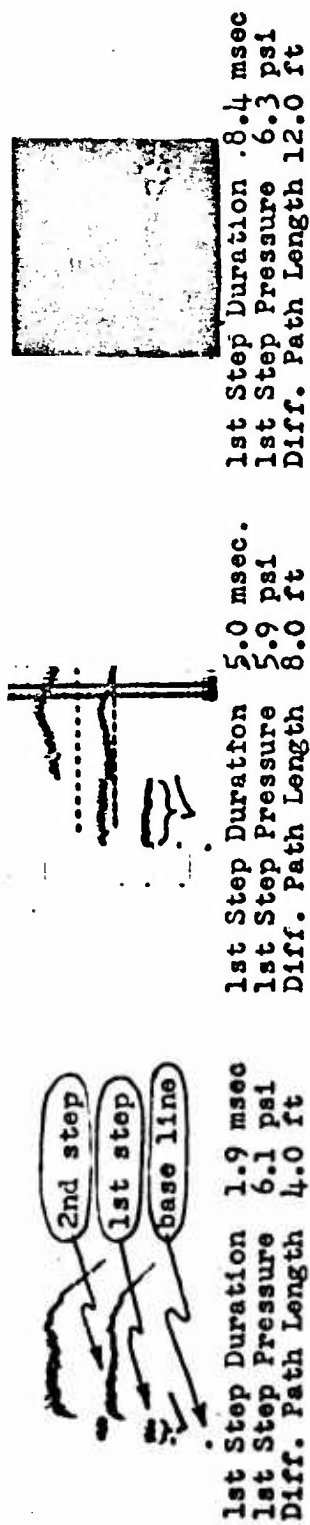
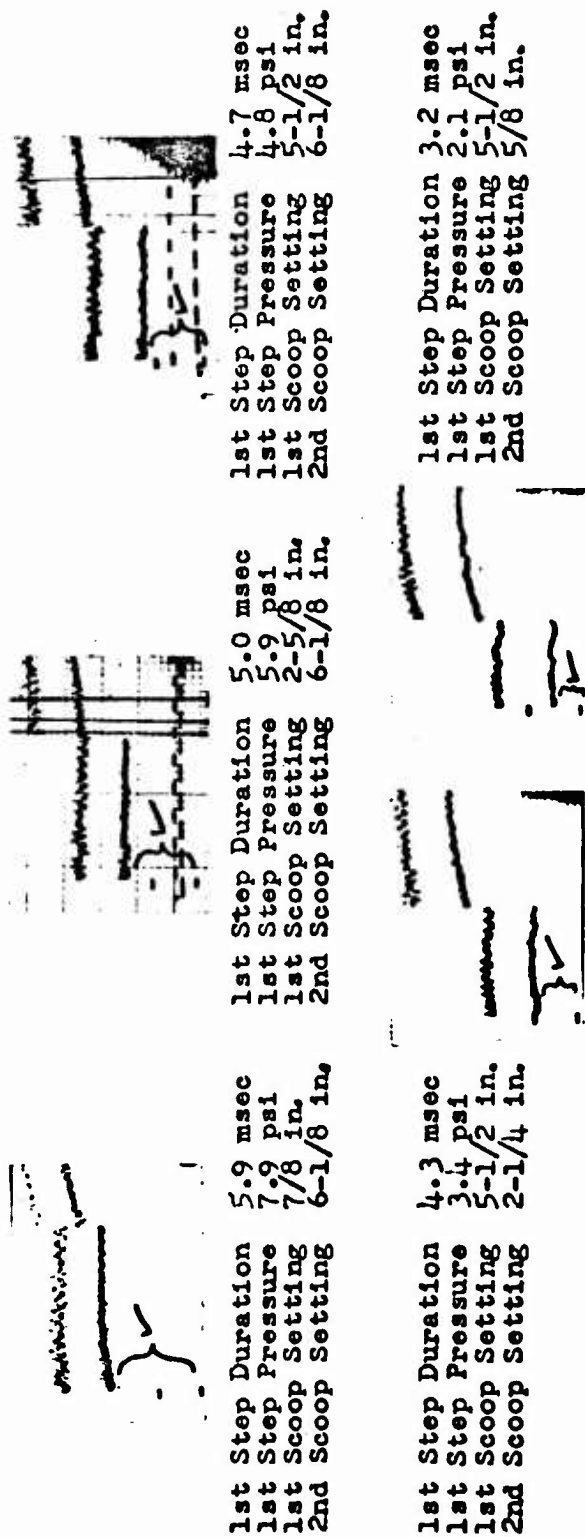


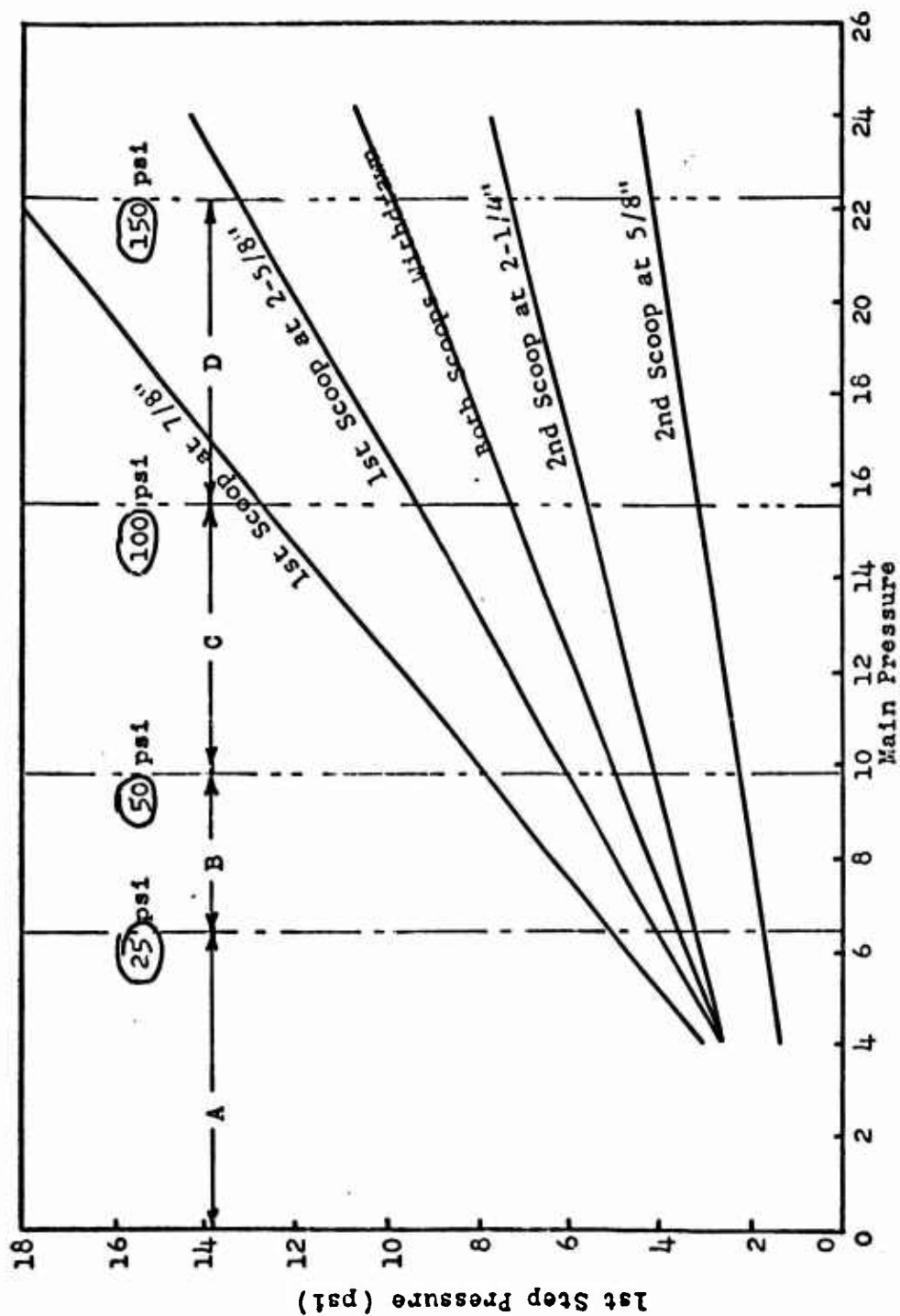
Figure 2. General Arrangement of Special Shock Tube to Generate Variable Stepped Shock Fronts

Figure 3. Variation of 1st Step Duration by Changing Differential Spool Lengths
Main Pressure Constant at 9.8 psi Leading Duct Scoop Fixed at 2-5/8 inches
(Dual beam oscillograms of pressure vs time are shown; two gauges per shot)



Variation of 1st Step Pressure by Changing Scoop Positions
Main Pressure Fixed at 9.8 psi Differential Path Fixed at 8 ft





Letters A, B, C, D indicate compression chamber pressure ranges: A- 0-25; B- 25-50; C- 50-100; D- 100-150.

Figure 4. Variation of 1st Step Pressure as a Function of Scoop Setting at Different Main Pressures

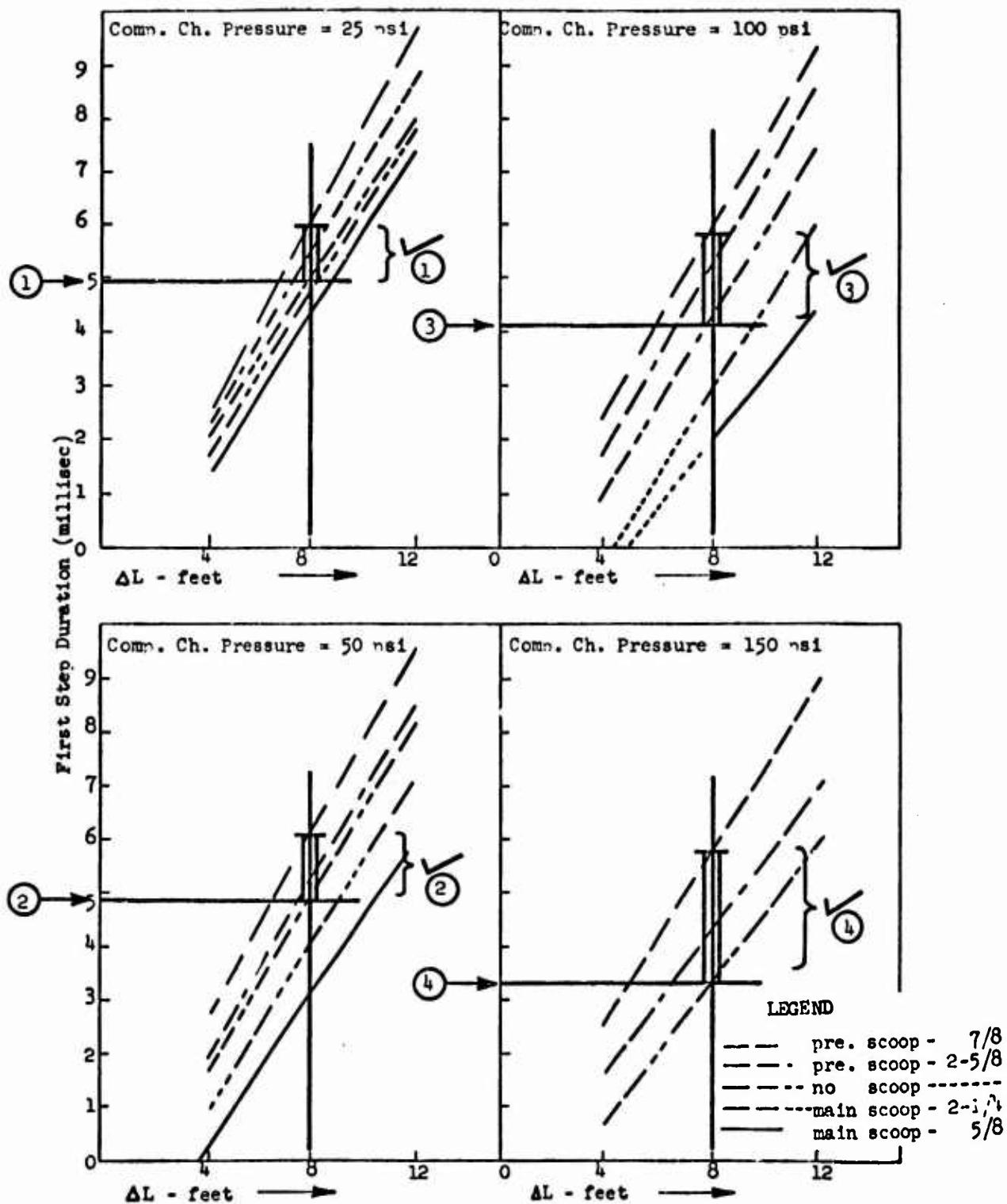
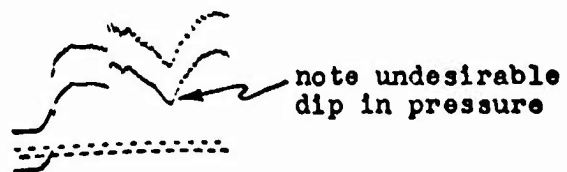
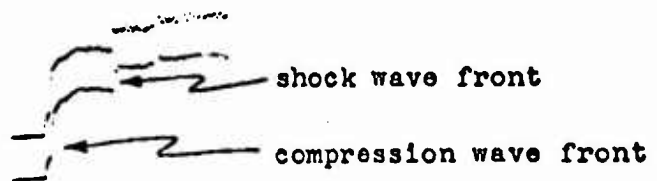


Figure 5. Variation of First Step Duration as a Function of Differential Path Length for Various Compression Chamber Pressures

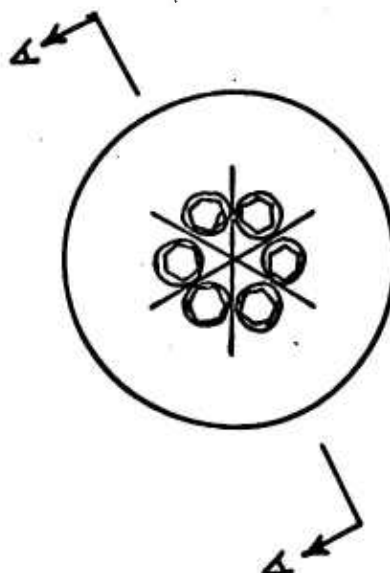


Premature Closing



Correct Opening

Figure 6. Examples of Premature Closing and Correct Opening of Slope Generator



SECTION A-A

Figure 7. 1/4 Inch Thick Star Assembly

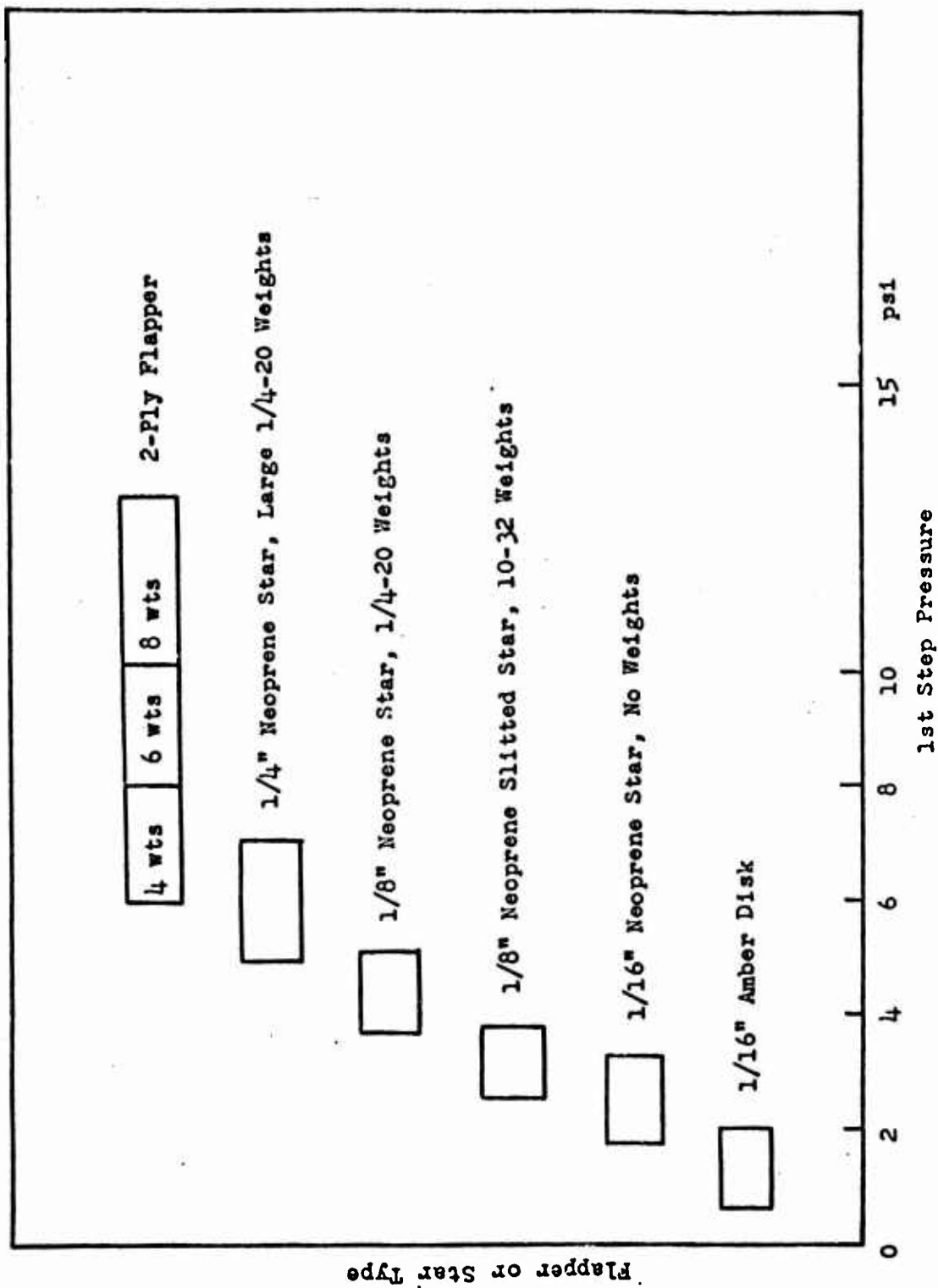


Figure 8. Bar Graph of Slope Generator Assemblies for Different Pressures

STUDIES OF TRANSIENT AIR FORCES
ON TWO-DIMENSIONAL AIRFOILS*

Emmett A. Witmer
Massachusetts Institute of Technology

The shock tube facility at M.I.T. was designed to serve a three-fold purpose: (a) to study blast airloads on aircraft, (b) to investigate structural response to such airloads, and (c) to conduct basic fluid mechanics studies. Accordingly, the design of this facility was preceded by a study of the aerodynamics areas to be investigated and appropriate measurement techniques for each experiment study. For studies of two-dimensional airflow development (about airfoils, simple shapes, the wall boundary layer, and so forth), the interferometer appeared to offer many advantageous features. For boundary-layer work, a narrow tube was indicated. Sting mounting of two-dimensional models was rejected because of the associated optical and flow interference effects. Clamping these models between the test section windows themselves was the selected technique; this technique, in turn, indicated the need for a narrow tube. In addition, a very deep tube was indicated in order to reduce the interference effects from the top and bottom walls. In the final analysis, space limitations for the facility limited the tube depth. Studies of air forces on finite-span wings and of response of structural models to blast-induced air forces requires a tube of relatively large cross-section in order to minimize respectively aerodynamic interference effects and the problems of building suitable structural-response models. The result of these and other similar considerations is the 8 by 24-inch cross section of this tube.

The requirement that transient air forces be measured from the instant of shock impingement until steady state air forces were achieved on the model in the (theoretically) uniform hot gas flow determined the length of the shock tube. Theory² predicts that for low Mach number flows, the sought-for steady state air force condition is essentially achieved in roughly twelve-chordlengths of flow. Taking a 4-inch chord airfoil and, rather arbitrarily, a 90 foot-per-second material velocity condition as a basis, the shock tube length(s) resulting are as given in Figure 1. The selection of a smaller

* Since the group attending the symposium visited the M.I.T.-W.A.D.C. shock tube facility at which time a number of shock tube features and experiments were discussed, a number of items were deleted from this paper as presented. The omitted material is included here, briefly, primarily for those readers who were unable to attend the symposium.

material velocity (to meet this flow-length criterion) would have greatly increased the required length of the shock tube. It should be pointed out that the steady state air force condition is achieved in even fewer flow chord lengths for the higher subsonic and for supersonic flow Mach numbers, excepting the region near Mach 1. Figure 2 shows the theoretically available flow duration in terms of flow chord lengths for a 4-inch chord model. The flow duration at the test section is limited at low Mach numbers by the arrival of the shock reflected from the closed end of the expansion chamber. At higher Mach numbers, the arrival of the contact surface (or region) terminates the hot gas flow at the test section. In practice, it is found that the contact surface arrives earlier than predicted by ideal shock tube theory^{3, 4, 5}. For the present tube configuration, this earlier contact surface arrival is indicated by the experimental data in Figure 2; air is the working medium in all cases shown.

For aerodynamic studies, it is desirable that measurements be made at the largest feasible Reynolds number in order that extrapolation to free flight conditions of interest can be carried out with better reliability. With a model of fixed chord and using (room) air as a working medium, these higher Reynolds numbers can be achieved most conveniently by an increase of the flow density. This, in turn, means pressurizing the expansion chamber of the shock tube. At the 250-psi a maximum design pressure selected for this shock tube, the available flow Reynolds numbers in air per foot of model chord length is given in Figure 3 as a function of flow Mach number. Note that Reynolds numbers in excess of 3×10^6 are available for flow Mach numbers ranging from 0.05 to 1.2. If helium, for example, were used in the compression chamber, even larger Reynolds numbers could be realized with air as the working medium in the hot gas region; these are also shown in Figure 3.

Figures 4, 5, and 6 show respectively an overall view of the shock tube, the diaphragm section, and the test section together with the interferometer and the shock detecting stations. Incidentally, the nominal flow Mach number produced in the shock tube is obtained by a conventional measurement of the shock velocity (just ahead of the test section) and measurement of temperature of the expansion-chamber air.

In the following, a brief outline of some of the problems, in each of the originally mentioned three areas, which have been or are planned to be investigated are given. Results of interferometric measurements of transient airflow development about a double-wedge airfoil in $M = 0.4^*$ hot gas flow will be reviewed in somewhat more detail. This will serve to point up some of the problem areas in the measurement techniques realm as well as problems posed by the basic shock tube flow itself.

In general, the response of aircraft structures to transient air loads can be predicted satisfactorily without the inclusion of gravitational forces. Only elastic and inertial simulation of an aircraft structure is required. Generally speaking, scaling of a prototype aircraft structure cannot be achieved realistically when the scaling reduction factor exceeds roughly 4.

* In this paper, Mach number M refers to the (particle) Mach number of the hot gas flow region. Shock Mach number is never used.

However, a mathematical model describing the dynamic behavior of prototype aircraft structures can generally be devised. The dynamic characteristics of this mathematical model are often simulated by much smaller than one-quarter scale models; at the same time, the internal structure may be quite dissimilar to that of the prototype. If, on the other hand, one wishes to investigate failure modes of a prototype structure under dynamic loading conditions, the model simulation must be carried out to a much more complete degree.

Figure 7 illustrates a simple cantilever-mounted rectangular airfoil model consisting of an aluminum sheet-spar covered with balsa wood which has been contoured to a typical airfoil shape. This model was set at a small angle of attack and was then subjected to a shock wave and its afterflow. The response of this elastic model was measured by means of strain gages mounted on opposite sides of the spar near the root; a typical strain-time record is shown in Figure 8. Upon being struck by the shock, the model begins to vibrate and tends to seek an equilibrium strained position corresponding to the steady state air loads produced on the model in the "uniform" hot gas flow field behind the shock. For this case, the shock reflected from the closed end of the expansion chamber arrives at the test section at about 0.043 second after the arrival of the incident shock and stops the flow. The model then tends to seek its initial "unstrained" position. Subsequently, the model is observed to respond to a whole succession of waves which, for some time, continue to reflect from the closed ends of the shock tube.

Similar studies have been conducted wherein a smaller cantilever model, similarly instrumented, has been placed at a number of positions downstream as well as above and below the streamwise plane of the model shown in Figure 7. Tests were run to study the effect of the "starting vortex" (and the subsequent downwash field) from the upstream airfoil on the response of the downstream airfoil (tail). For each position of the tail model, tests were run at the same initial flow conditions both in the presence and in the absence of the upstream cantilever-wing model. The response of the tail was observed to vary quite markedly, depending upon its location both downstream and normal to the wing stream plane. In Reference 6 the characteristics of such downwash for the two-dimensional incompressible flow case are treated, and the response of simple systems to the associated airloading is discussed.

Another example of aeroelastic and structural response studies conducted in the shock tube follows. The question posed was that of the time required to produce flutter of a wing should the wing find itself abruptly in a field of flow in which the material velocity were in excess of that required to produce flutter in steady state flow. A cantilever flutter model consisting of an aluminum H-spar, covered with balsa wood, and airfoil contoured, was designed and built (see Figure 9). In order to control the torsional stiffness of the model, the balsa wood contouring was slit chordwise at a number of spanwise stations. The contour was preserved and the balsa covering protected (from diaphragm particles and other foreign matter) by a thin rubber sheet applied to the model. For this model, the ratio of the first bending to the first torsion-mode frequency was approximately unity. The model was strain-gage instrumented both (a) to reveal in vibration tests, the bending and torsional frequencies of the model and (b) to permit measuring model response in the actual shock tube experiments. The model was

cantilever mounted and was subjected to shock-initiated flow starting at small material velocities. The material velocity of the shock-initiated flow was increased by small increments in succeeding runs. During each run, the (strain) response of the model was oscillographically recorded. At small material velocities, the vibratory response decayed essentially monotonically until the initial hot gas flow was terminated by the reflected shock. On the other hand, when the shock-initiated material velocity exceeded the steady state flutter speed of the model, the vibratory response was observed to decay for a short period of time and then diverged. The early arrival of the shock reflected from the closed end of the expansion chamber stopped the flow and prevented catastrophic failure of the flutter model. Typical response records are given in Figure 10 for material velocities both well below and well above the flutter speed. The time at which the response began to diverge noticeably in the Figure 10 record corresponds to approximately 22 flow chord lengths; steady state air forces are observed to be developed, for such flow conditions, in roughly 10 flow chord lengths. The aerodynamic time lag observed may be entirely different for other combinations of steady state flutter flow Mach number, bending frequency, torsional frequency, mass ratio, and so forth.

An additional aeroelastic response study conducted consisted of subjecting thin-walled cylindrical shell models to the shock wave and measuring the model's strain-time response at a number of points along the periphery⁸. The shock wave overpressures employed were such that the observed response remained in the (linear) elastic region. For these models the response modes are of the "dilatory" variety, whereas, the modes of most importance in the case of the wing-tail cantilever models and the aforementioned flutter models were those of bending and torsion; the responses again in these latter cases were confined to the elastic region. Sections of typical aircraft lifting-surface structures were suitably mounted between the shock tube walls and placed at various orientations with respect to the incident shock. For the case in which the shock struck the nose of the airfoil and enveloped the structure symmetrically, skin-panel vibrations and vibrations of the rib structure were produced; these modes of vibration may be thought of as "dilatory" modes. Such modes were excited to the extent that permanent damage resulted in some cases and only elastic response in others. Figure 11a shows a (nose-on) symmetrical exposure condition wherein dilatory modes were dominant; rib-crushing was a typical type of damage produced, and skin-dishing was another. Such damage is termed "overpressure damage". In Figure 11b, a typical model arrangement is illustrated for which "beam-bending" modes were dominant. For the latter case, first, elastic-response tests were conducted. These were followed by tests in which the response produced extended far beyond the elastic region. The incipient "failure" of the structure in the beam-bending mode of response occurred through local buckling of the structure. After such a buckle occurs, the linear elastic-restoring force characteristics of the model no longer exist; as the model continues to deflect, the restoring force characteristics continually change in an irreversible non-linear manner. Damage resulting from such beam-bending modes of vibration is termed "gust damage".

An analysis to predict the elastic and the post-elastic responses of such structural models must properly include the pertinent restoring force characteristic of the structure as a function of the controlling deflection

parameter(s); the air loads causing the response must also be properly taken into account. The latter are unquestionably the more difficult to treat.

A primary purpose in developing this shock tube facility was to investigate air loads produced on airfoils and other aerodynamic bodies by a shock wave and the associated flow field. Two-dimensional airfoils (an NACA 65-010 and a 10% thick symmetrical double-wedge) were mounted between the test section windows as illustrated in Figure 12. The airfoil was set at some pre-selected angle of attack relative to the floor of the shock tube, and was then subjected to shock-initiated flow. Shock-initiated flow Mach numbers of 0.40, 1.28, and 1.5 were employed in tests on the double-wedge airfoil which was set at angles of attack of 0, 4, and 8.3 degrees. The NACA 65-010 airfoil has been tested at $M = 0.4$ and angles of attack of 0, 5, 10, 15, and 30 degrees. At least two Reynolds numbers were employed in testing each airfoil. During each firing of the shock tube, in these tests, a single interferogram of the flow about the airfoil was made at a pre-selected time after the flow-initiating shock impinged upon the leading edge of the model, using a spark light source of 1-microsecond duration and filtered to a 30°A band centered at 4481°A . By repeating such runs and varying the time at which the interferogram was recorded, a reasonably complete measure of the flow pattern development from shock incidence to steady state flow conditions was obtained.

To illustrate some of the measurements obtained and some of the interpretation problems involved in such measurements, a set of runs for the double-wedge airfoil at $M = 0.4$ will be discussed. Figure 13 illustrates a series of infinite fringe flow interferograms taken at various chord lengths of particle flow, s/c, after the shock struck the leading edge of the model. For this set of runs, the angle of attack is 4 degrees and the flow Reynolds number based on the model chord is 1,210,000. This and other sets of runs for the double-wedge airfoil are discussed in some detail in Reference 9.

Having information available on the effective wave length of the light used, the test section width, and the pertinent value of the Gladstone-Dale constant, the difference in mean density from one fringe to the next in the infinite fringe flow interferogram is a known value. Thus if the field density at any point in the flow is known, the density at all fringe positions throughout the flow field are readily determined. Having the density distribution, one proceeds to determine the surface pressure distribution on the airfoil. Except where discontinuities are present in the flow field it is reasonable, under these test conditions, to regard the flow as isentropic in translating density to pressure. In assessing the pressure distribution on the airfoil, one observes that the boundary layer in some regions has a respectable thickness. It is assumed that the pressure gradient across the boundary layer is negligible; hence, the surface pressure is the same as that at the outer edge of the boundary layer. Note that on the upper surface behind the sharp leading edge of the airfoil, there is a region of separated flow in the near steady state flow condition. This is a region in which a reliable determination of surface pressure distribution is most difficult. Incidentally, in order to provide independent information on the complete pressure distribution and to guide interferogram interpretation in these separated flow regions, direct pressure distribution measurements are planned using a miniature pressure sensor which is currently being developed in the laboratory. A discussion of interferogram interpretation for those cases involving discontinuities in the flow field may be found in Reference 9.

Once the surface pressure distribution is known, one can evaluate the lift, the moment, and the pressure drag (and other interesting quantities) experienced by the airfoil. This information can be converted to the more convenient coefficient form if the freestream flow properties are known. Ideally, the hot gas flow is a step function. Actually, non-ideal flow behavior is observed; non-ideal diaphragm removal and boundary layer growth are some of the factors responsible. Measuring white light finite (width) fringe displacement time histories in the flow by means of a strip film camera and by means of a series of single-spark white light interferograms, time histories of the freestream flow density were determined. If one postulates that at some (late) time after shock passage, for example, the density increase over that observed immediately behind the shock were due to one shock, two shocks, or a large number of weak compression waves, the resulting predicted material velocity is found to vary but little from one assumed model to any other. Hence, if such a flow model is postulated, one may, throughout the flow, calculate the material velocity and thus the (tentative) time history of the dynamic pressure of the freestream flow. Figure 14 illustrates the resulting time history of the free stream dynamic pressure for the conditions of this experiment; the shock-velocity-indicated material Mach number immediately behind the shock at the measuring station was 0.4. Figure 15 shows the variation of lift coefficient with elapsed flow chord lengths (s/c) when the lift coefficient is based upon the dynamic pressure immediately behind the shock. Figure 16 illustrates the aerodynamic time variation of the lift coefficient based upon local (time) values of the density-indicated dynamic pressure. In both figures, curves of lift response to a step-function incompressible flow⁶ are given; these provide only rough theoretical-experimental comparisons since the theoretical flow model is somewhat different from the conditions applying in the shock tube experiments. Figure 17 shows similar results for the (early) so-called "shock diffraction phase" of the loading.

Figure 18 illustrates a series of infinite fringe interferograms for the double-wedge airfoil at a nominal shock-initiated flow Mach number of 1.28 and an angle of attack of 4 degrees. The shock should be detached at this Mach number. The last picture in this series was taken in the (much higher Mach number) cold gas flow following the contact surface. Note that this cold gas flow, in contrast to the hot gas flow, is quite non-uniform. It is interesting also to observe the oscillatory wake which appears in the latter stages of the hot gas flow pictures.

In addition to the two-dimensional airfoil experiments mentioned, plans have been made for conducting similar experiments on finite-span wings using the aforementioned miniature pressure sensors for pressure distribution measurements. These measurements will be supplemented by high speed photographic studies of the behavior of tufts distributed over the surface of the wing. Incidentally, such tuft studies have been made on the two-dimensional NACA 65-010 airfoil using a Fastax camera operated at 16,000 frames per second. The tuft behavior has been correlated with measurements made at corresponding times from interferograms.

Mention should be made of the fact that in such shock tube studies, the question of (classical, non-viscous) wall interference in addition to wall-boundary-layer interference must be taken into consideration. Such

interference is not serious in the very early stages of the flow; however, multiple wave reflections and wall-boundary-layer interference are clearly evident later on in the flow. Although steady state wall interference effects have been treated extensively in the literature, the transient condition of interest here has not been studied.

Other simple models have been subjected to shock-initiated flow and the resulting flow patterns observed. These have included bodies of square, rectangular, and circular cross section. Figure 19 shows a sequence of infinite fringe interferograms of the flow about a $1/4$ by 2 inch rectangular model for a Mach number of 0.17. In Figure 20, Schlieren picture and an infinite-fringe flow interferogram taken in separate runs but at nearly the same aerodynamic time in the flow are shown; here the flow Mach number is 0.45. A $5/16$ -inch diameter model was subjected to $M = 0.17$ flow and interferograms obtained; a sequence of these pictures is shown in Figure 21. Note that symmetrical vortices are first shed; later in the flow, the Karman-type vortex street develops.

Several tests were also conducted on an axially symmetric body consisting of a simple cone-type nose followed by a cylindrical afterbody¹⁰; a half model was attached to the side wall of the shock tube. Surface pressures were sensed at several streamwise positions along the body by means of barium titanite pressure transducers. The pressure-time histories were recorded by photographing the sweeping trace of a cathode ray oscilloscope. Similar measurements have been made of pressure-distribution time histories on two low-aspect-ratio finite-span rectangular wings cantilever-mounted from the shock tube wall¹¹; however, the pressure leads from the model surface to the barium titanite pressure transducers were of such a length and diameter that the frequency response of the sensing system was reduced to the point where the diffraction loading could not be observed. Only the latter stages of the flow development and the steady state air forces were successfully measured. This measurement limitation will be removed by the miniature pressure sensors now being developed in the laboratory.

In support of theoretical work by Hobbs in Reference 6, experiments were conducted in which a two-dimensional airfoil was placed just upstream of the test section and set at a small angle of attack. A schematic of this arrangement is shown in Figure 22, part a. The path of the "starting vortex" was observed both in space and in time by photographing the vortex at successive time delays in a series of repetitive tests. Excellent repetition was observed. One prime end result was that of measuring the downwash induced by the vortex at various points in its vicinity. Following a suggestion by Dr. Ruetenik, a small diameter wire was strung between the test-section windows. Photographs were taken defining the wake behind this fine wire when the subject vortex was at various positions with respect to the wire; the inclination of this wake served to indicate the "downwash velocity" component produced at the sensing wire, since the freestream flow velocity was reasonably well known. While this technique has yielded useful results, the inherent uncertainties indicate the need for a more precise measurement method. A satisfactory prediction of this "indicial" downwash field permits, in turn, with the aid of available theory, the prediction of air forces on airfoils which come under the influence of such an "indicial vorticity field".

Incidentally, in the earlier-described wingtail elastic response tests, the influence on tail response of the "starting vortex" from the wing was observed while that vortex passed near the tail. Part b of Figure 22 shows the space-time history of the vortex path. The vortex does not immediately upon its initial appearance acquire a downstream velocity equal to the material velocity itself. It starts its journey slowly and soon attains essentially a velocity equal to the material velocity. For the case illustrated in Figure 22, the vortex arrived at the test section center line late by approximately one-eighth of a chord length based upon a constant value of shock-velocity-indicated material velocity.

Both on its own merits and for a meaningful reduction of the previously described transient air force measurements, it is important that the basic free-stream flow in the shock tube be known accurately. Over the complete range of available and/or practical operating conditions, one is interested in a complete time history of:

- | | |
|-----------------------|-----------------------------|
| (a) density | (f) mass flow |
| (b) pressure | (g) turbulence level |
| (c) temperature | (h) flow "cleanliness" |
| (d) material velocity | (i) the wall boundary layer |
| (e) dynamic pressure | |

Measurements have been made of items (a) and (b) in many shock tubes^{5, 12}. Time histories of these quantities have been very strongly linked to the dimensions of the tube cross sections and lengths employed through the associated boundary layer development, non-ideal diaphragm bursting, and other effects. All of the items listed above are interdependent. Numerous papers^{5, 13-16} have been written on non-ideal shock tube flow, shock attenuation, and boundary layer development; review of these papers will not be attempted here.

Some exploratory measurements have been made at M.I.T. by Dr. Ruetenik seeking to measure stream temperature, material velocity, and mass flow with a hot wire anemometer; he will discuss this topic in his paper.

The question of the turbulence level of the shock-initiated hot gas flow is one that appears as of now to be unanswered. The cold gas flow, on the other hand, has been observed to be quite irregular --- irregular to the point where the value of using this flow for air force studies on models is open to question. As to the hot gas flow, this laboratory has proposed to conduct a series of tests designed to examine the turbulence level present. Also to be explored is the degree of repeatability of such turbulence levels and time histories in "repetitive" runs.

Flow "cleanliness", in the sense used here, pertains to the number and strengths of trailing shocks and rarefaction waves appearing in the hot gas flow which is considered to be the flow region of primary interest for transient aerodynamic studies on models. The trailing wave family appears to depend upon the diaphragm support configuration employed, the pre-burst curvature of these diaphragms, diaphragm rupture rate, amount of diaphragm remaining, and distance of the diaphragm from the test station, as well as any wall protuberances or irregularities. Such effects have been noted to a

greater or lesser degree in all shock tube facilities. Everyone agrees that every feasible step should be taken to minimize these effects.

Wall-boundary layer studies have been undertaken here^{18, 18, 19} and at Princeton¹⁴. Both wall temperature and interferometric measurements¹⁴ have been reported at Princeton. Only interferometric measurements have thus far been made at M.I.T. Some of these results will be discussed in Dr. Ruetenik's paper²⁰.

Aside from the ideal step-function flow previously considered, there are certain problems wherein flow time histories other than a step-function are of interest. Blast-type profiles are of particular interest. Such profiles can be produced in the shock tube by explosions²¹ (gaseous mixtures, solids, etc.), by arranging rarefaction overtaking of the primary shock²², by the use of an auxiliary diaphragm placed upstream of the test station²³, and by the shock and flow expansion through a slit²⁴, to mention a few. Such profiles do not exactly duplicate those observed in free-air three-dimensional explosions; the greater part of the positive phase is similar but differences arise in the latter stages of these shock tube blast-like profiles.

In order to better simulate the condition in which a wing in steady (high-speed) flight is struck by a blast wave, work is in progress to devise appropriate flows in the shock tube. A number of techniques have been considered. One technique which shows promise has been explored here. It is shown schematically in Figure 23; the geometry must be tailored to the primary operating conditions selected. This technique consists of producing shock-initiated flow in the usual manner; near the test station, a part of the initial shock is split-off and entrapped. This entrapped shock is then reflected at a time such that when the resulting wave expands into the primary flow, this auxiliary blast-like wave arrives at the model being tested at a time when essentially steady state air forces have already developed on the model.

An attempt has been made herein to review some of the shock tube activities carried out at M.I.T. A number of the measurement problems encountered at M.I.T. are common to all shock tube facilities. By reviewing the deficiencies in (and of) measurement techniques particularly, as well as ideas on unresolved shock tube flow characteristics, with those who face common and allied problems, it is hoped that a mutual interchange of ideas and experience will expedite studies which face each of us.

If we seek ultimately to predict the responses of various structures to transient air forces, we must have an accurate knowledge of the applied air loads. It is clear that such air force information cannot be determined to the precision required or in a form needed for practical use by attempting to infer such airloads information from structural response data. Finally, aside from questions of basic shock tube flow characteristics themselves, the usefulness of the shock tube as a tool for providing air force information and/or for developing appropriate methods for predicting structural response is critically dependent upon the availability of rapidly responding precision instrumentation.

ACKNOWLEDGEMENTS

The detailed design and early construction of this shock tube was carried out by Mr. Thomas Parsons, Mr. E. H. Godfrey, Mr. K. C. Rathburn, and the writer under the supervision of Professors H. G. Stever, R. L. Bisplinghoff, and J. W. Mar. The final assembly has been carried out by the writer with the very able assistance of Mr. Vaughn L. Beals, Mr. G. Reitano, and Mr. E. DiFrancesco. Dr. Walter Herrmann carried out certain modifications of the optical support and control elements in the interferometer and in its external suspension. These modifications were most skillfully designed, and effected a substantial improvement in the stability and operational facility of the interferometer. More recently Dr. J. R. Ruetenik has carried out modifications to the shock tube proper, has very ably developed instrumentation of considerable value in shock-tube experiments, and has carried out detailed studies in the shock tube itself. The assistance of Dr. J. R. Ruetenik in collecting certain information included in this paper is also gratefully acknowledged.

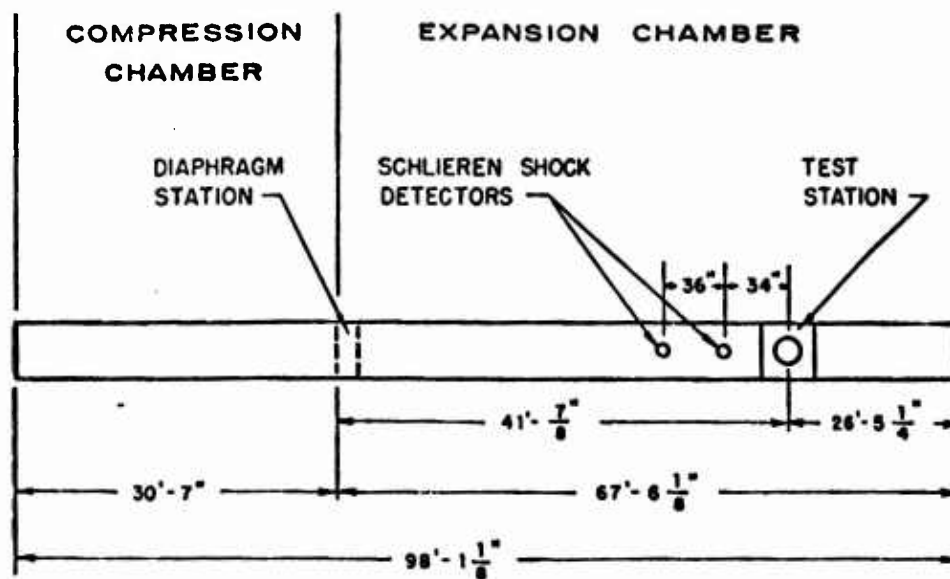
This shock tube facility is the property of the U. S. Air Force, sponsored under contract to the Aircraft Laboratory, W.A.D.C. Their cooperation in all phases of this work has been most helpful. All design and construction work as well as most of the research carried out in this shock tube laboratory has been sponsored by the Air Force.

REFERENCES*

1. Stever, H. G. and Bisplinghoff, R. L., The Shock Tube in Aerodynamic and Structural Research, Proceedings of the National Academy of Sciences, Vol. 40, No. 7, pp. 557-565, July 1954
2. Wagner, H., Über die Entstehung des dynamischen Auftriebes von Tragflügeln, Z. angew. Math. Mech., Bd. 5, Heft 1, February 1925
3. Geiger, F. W. and Martz, C. W., The Shock Tube as an Instrument for the Investigation of Transonic and Supersonic Flow, Engineering Research Institute, University of Michigan, U. S. Navy Contract No. N6-ONR-232, June 1949.
4. Lukasiewicz, J., Shock Tube Theory and Applications, National Aeronautical Establishment Report No. 15, Ottawa, Ontario, Canada, 1952
5. Glass, I., Martin, W. and Patterson, G. N., A Theoretical and Experimental Study of the Shock Tube, Institute of Aerophysics, University of Toronto, UTIA Report No. 2, November 1953
6. Hobbs, N. P., Indicial Downwash and its Structural Effect on the Horizontal Tail, Sc. D. Thesis, Department of Aeronautical Engineering, Massachusetts Institute of Technology, (also WADC TR 56-164) August 1956
7. Beals, V. L., Jr., An Experimental Investigation of Flutter in Supercritical Transient Flow, S. M. Thesis, Department of Aeronautical Engineering, Massachusetts Institute of Technology, August 1954
8. Grimes, C. K., Structural Response of Shell Structure in the Elastic-Plastic Range Due to Rapidly Applied Load, S. M. Thesis, Department of Aeronautical Engineering, Massachusetts Institute of Technology, January 1956
9. Ruetenik, J. R. and Witmer, E. A., Transient Aerodynamics of Two-Dimensional Airfoils. Part I - Interferometric Measurements of Two-Dimensional Airflow Development about a Symmetrical Double-Wedge Airfoil in Shock-Initiated Subsonic Flow, Massachusetts Institute of Technology, WADC TR 54-368, Part I, August 1956
10. O'Brien, T. F. and Witmer, E. A., Shock-Induced Transient Pressures on an Axially Symmetric Body in the Shock Tube, Department of Aeronautical Engineering, Massachusetts Institute of Technology, 1954
11. Lemnios, A., A Preliminary Investigation of the Effect of Reynolds Number on the Indicial Lift in the Transonic Range, S. M. Thesis, Department of Aeronautical Engineering, Massachusetts Institute of Technology, June 1954

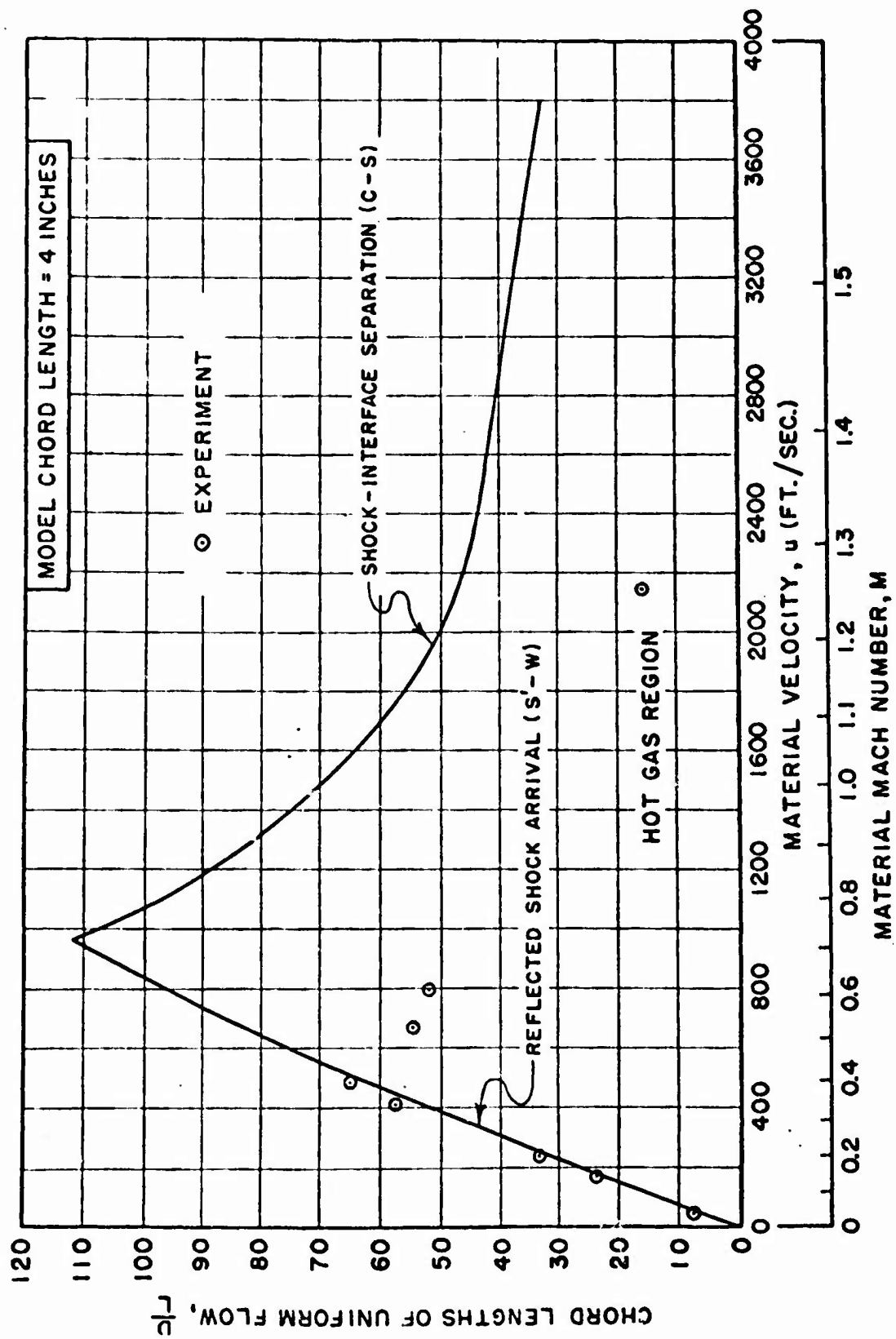
* There are numerous other papers and reports dealing with certain of the topics covered in this paper. The references cited here serve as example sources; no attempt has been made to present a complete bibliography. Hence reference is not made to many excellent papers in this field.

12. Mack, J. E., Density Measurement in Shock Tube Flow with the Chrono-Interferometer, Lehigh University, U. S. Navy Contract No. N7 ONR 39302, 15 April 1954
13. Hollyer, Robert M., Jr., A Study of Attenuation in the Shock Tube, Engineering Research Institute, University of Michigan, U. S. Navy Contract No. N6 ONR -232-TO IV, Project M720-4, 1 July 1953
14. Bershader, B. and Allport, J., On the Laminar Boundary Layer Induced by a Travelling Shock Wave, Department of Physics, Princeton University, U. S. Navy Contract N6 ori-105, Tast II, May 1956
15. Trimpi, R. L. and Cohen, N. B., A Theory for Predicting the Flow of Real Gases in Shock Tubes with Experimental Verification, NACA TN 3375, 1955
16. Mirels, H., Attenuation in a Shock Tube Due to Unsteady Boundary Layer Action, NACA TN 3375, August 1956
17. Stever, H. G., Witmer, E. A. and Herrmann, W., The Growth of the Boundary Layer Behind a Shock Wave. 50 Jahre Grenzschichtforschung. F. Vieweg and Sohn., Braunschweig, 1955
18. Divone, L. G., Investigation of the Density Distribution in the Boundary Layer of a Subsonic Shock-Induced Flow, S. M. Thesis, Department of Aeronautical Engineering, Massachusetts Institute of Technology, May 1956
19. Ruetenik, J. R. and Divone, L. G., Interferometric Measurements of the Laminar Boundary Layer on a Shock Tube Wall, presented at American Physical Society, Annual Meeting 1957.
20. Ruetenik, J. R., Development of the Shock-Tube Facility for Airfoil Studies, AFSWC Shock Tube Symposium, M.I.T., February 1957
21. Dickens, R. G. and Cushing, V. J., (Unclassified Title) Three-Dimensional Shock Tube Facility, Armour Research Foundation, Illinois Institute of Technology, Phase Report 1, Contract AF33(616)-220, Project MO34-O, August 25, 1953 (Confidential, Security Information)
22. Lee, R. C. K., Ruetenik, R. R. and Witmer, E. A., Shock Tube Flow Investigations, Part 1 - An Exploratory Study of the Generation of Blast-Type Profiles in the Shock Tube by the Reflection Method, Massachusetts Institute of Technology, WADC TR 54-383, Part 1, August 1956
23. White, D. R. and Weimer, D. K., A Method for Modification of the Pressure Profile in a Shock Tube, Technical Report 11-12, Department of Physics, Princeton University, U. S. Navy Contract No. NR 061-020, N6 ori-105, Task II, April 1952
24. Peterson, E. H., Investigation of a Method for Generating a Cylindrical Shock Wave, S. M. Thesis, Department of Aeronautical Engineering, Massachusetts Institute of Technology, January 1956



INTERNAL CROSS-SECTION	8" x 24"
INTERNAL LENGTH	98'-1 $\frac{1}{8}$ "
APPROXIMATE TOTAL WEIGHT OF SHOCK-TUBE PROPER	13 Tons
MAXIMUM DESIGN PRESSURE	250 psia
MAXIMUM REYNOLDS NO. WITH A 4-IN. CHORD MODEL WITH AIR-AIR OPERATION	6,750,000
MAXIMUM MACH NO. CURRENTLY OBTAINABLE WITH AIR IN THE EXPANSION CHAMBER	1.5

Figure 1. Summary of Physical Data on the M.I.T.-W.A.D.C. Shock Tube



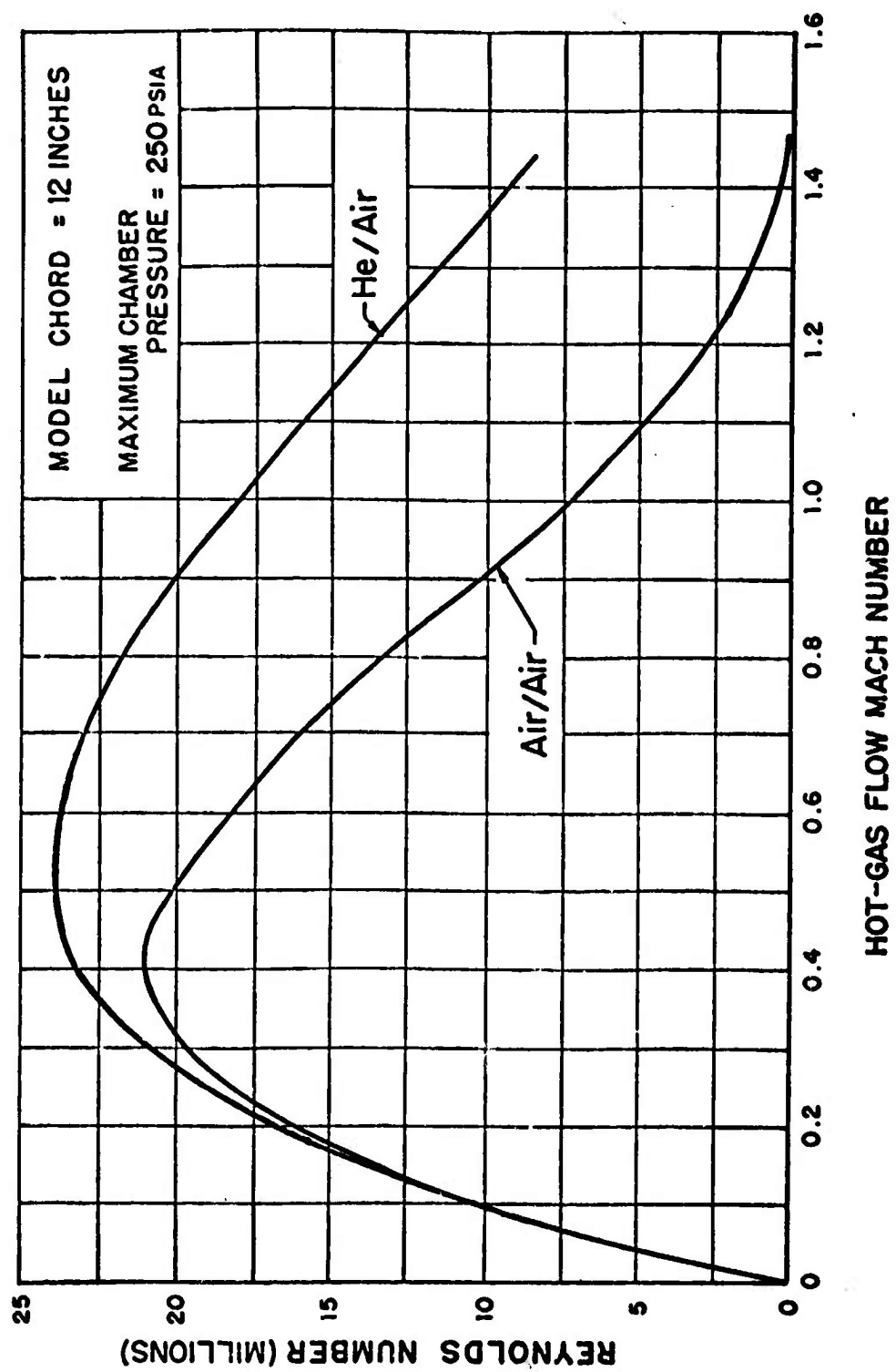


Figure 3. Reynolds Number as a Function of Flow Mach Number

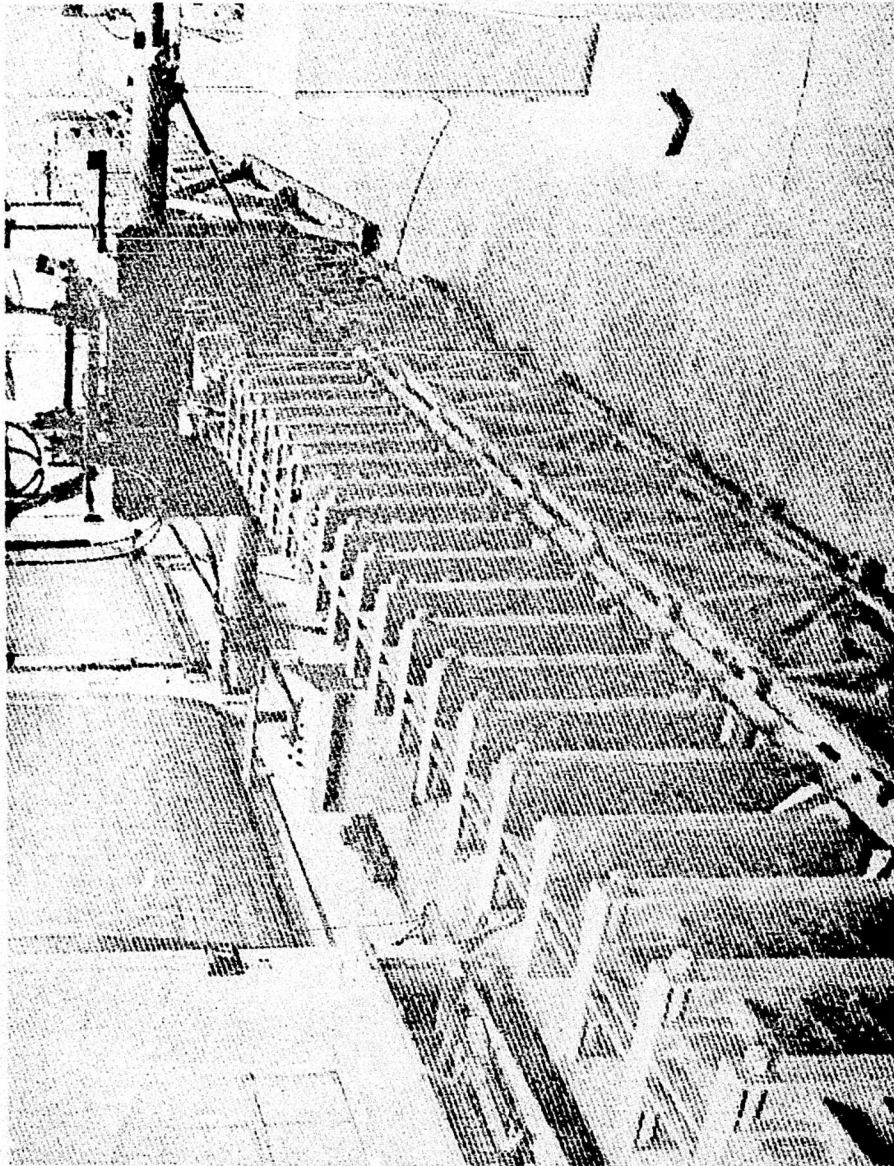


Figure 4. Overall View of the Shock Tube

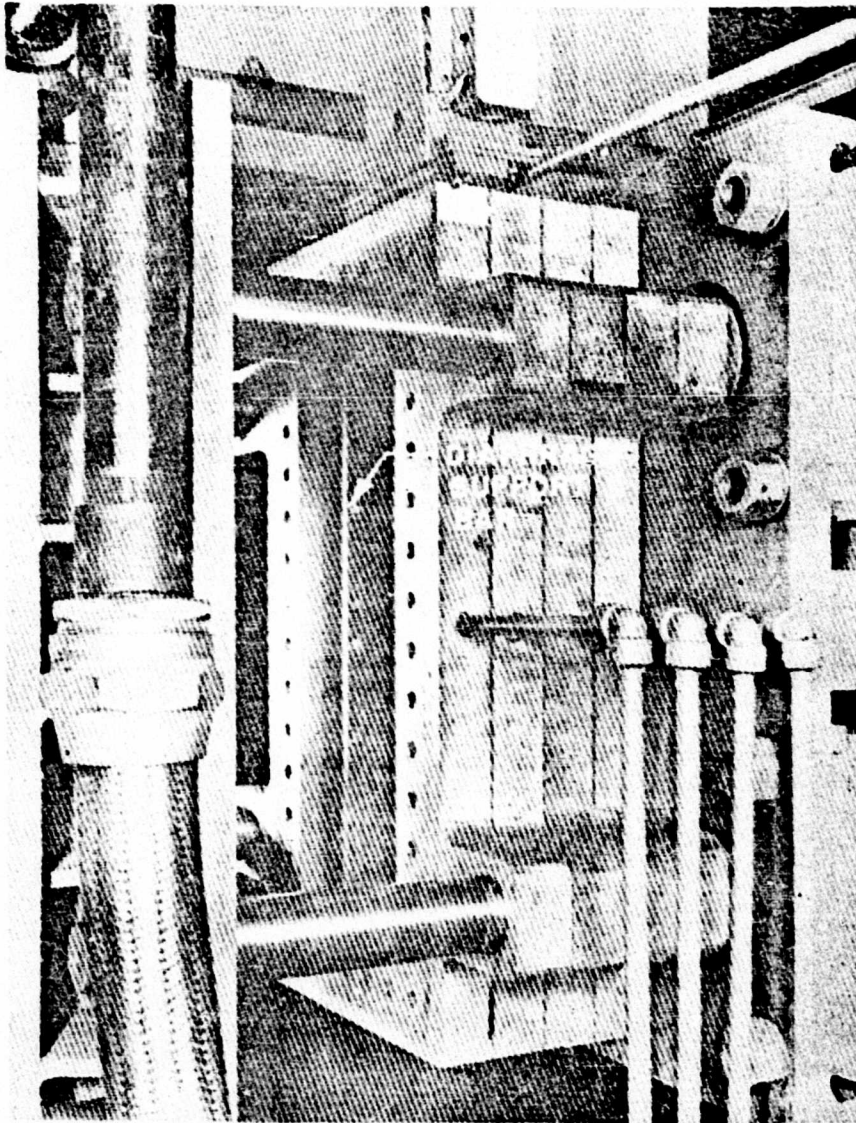
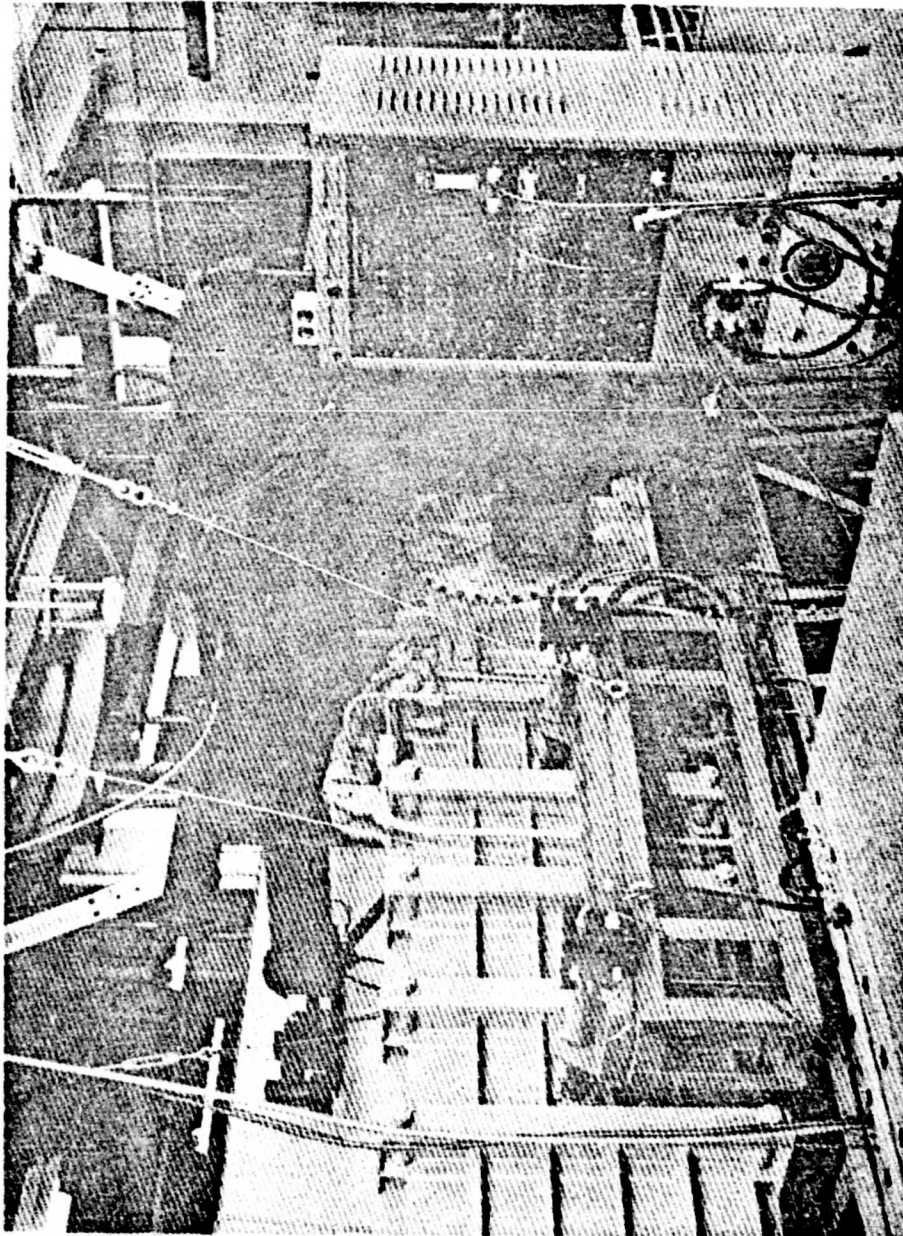
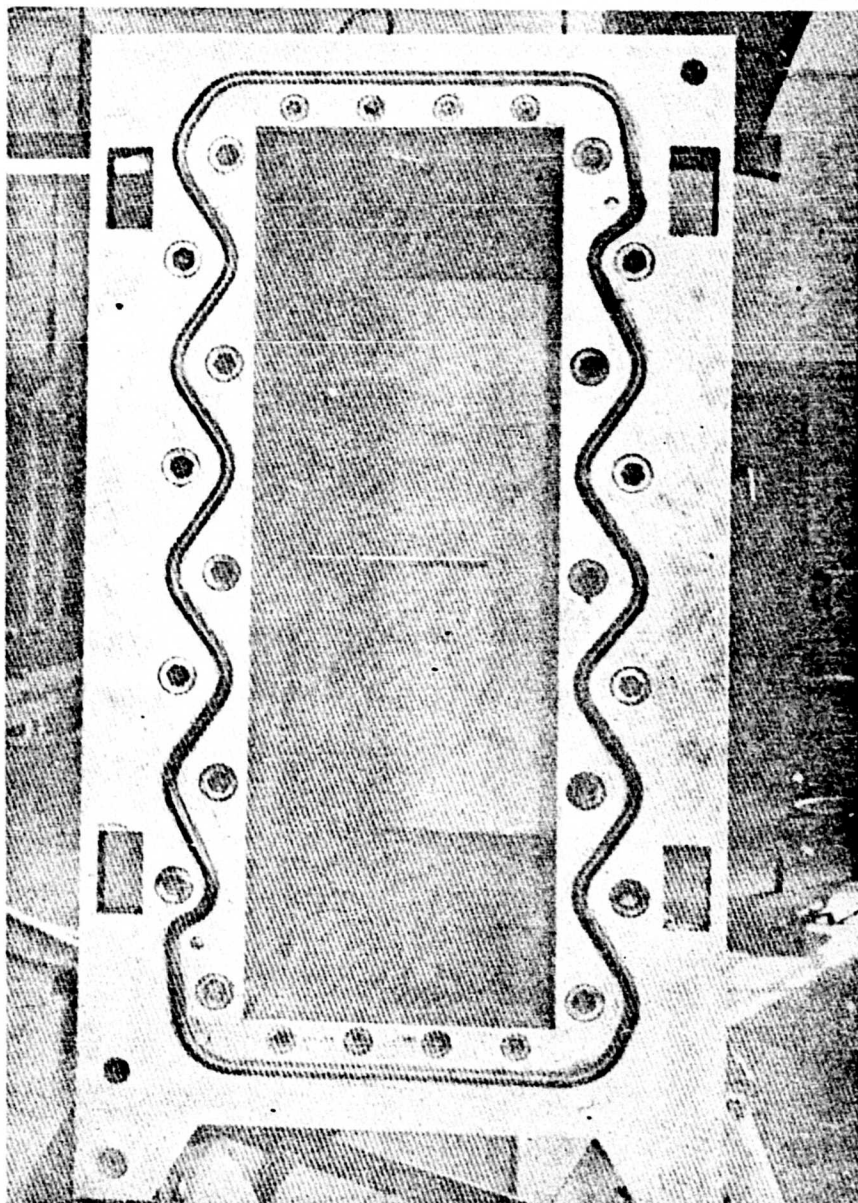


Figure 5. View of the Diaphragm Section



**Figure 6. View of the Test Section, the Interferometer, and the Shock
Detecting Stations**



**Figure 7. Rectangular Elastic Wing Cantilevered
from the Shock Tube Wall**

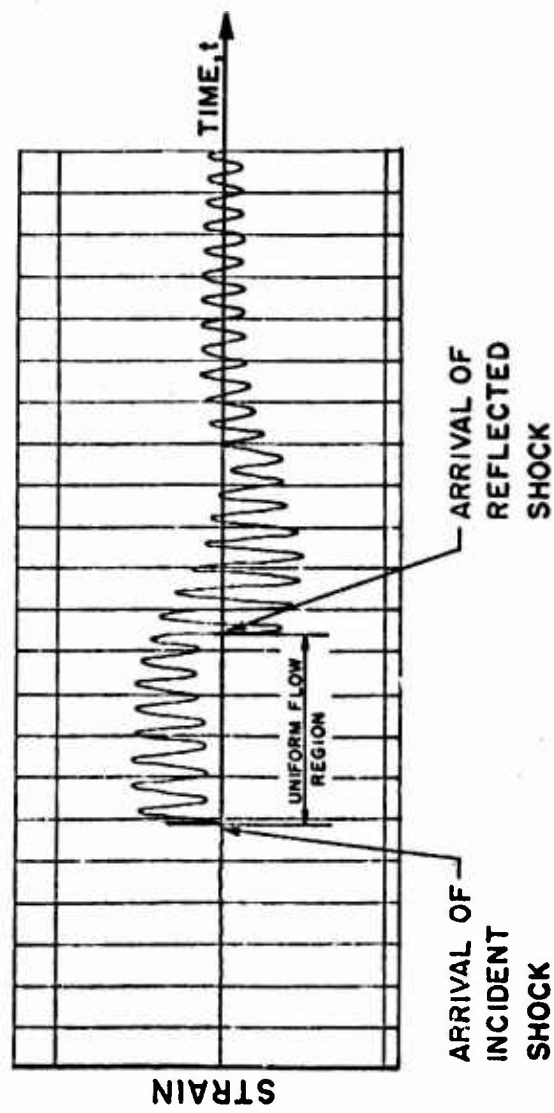
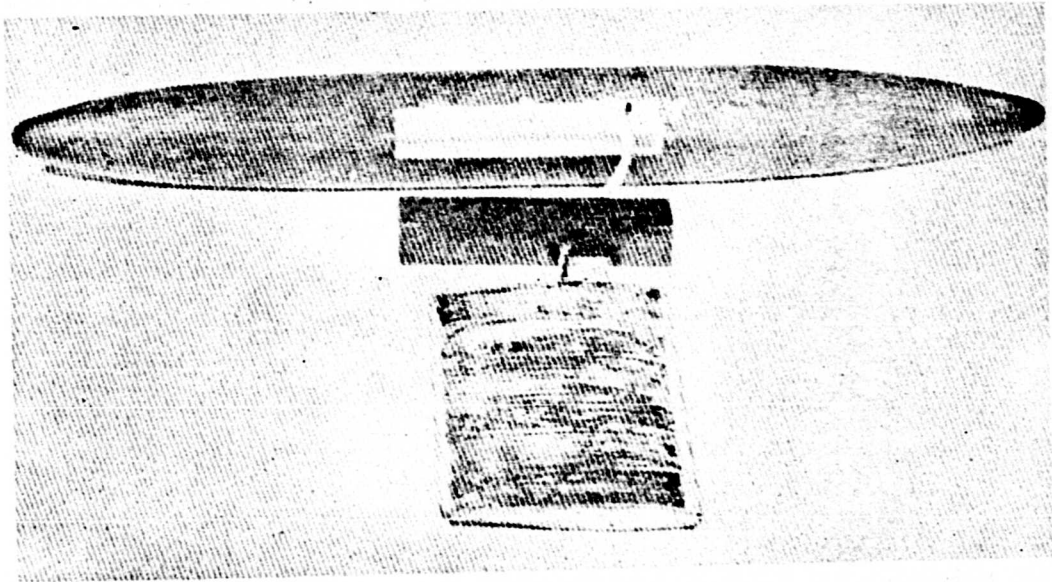
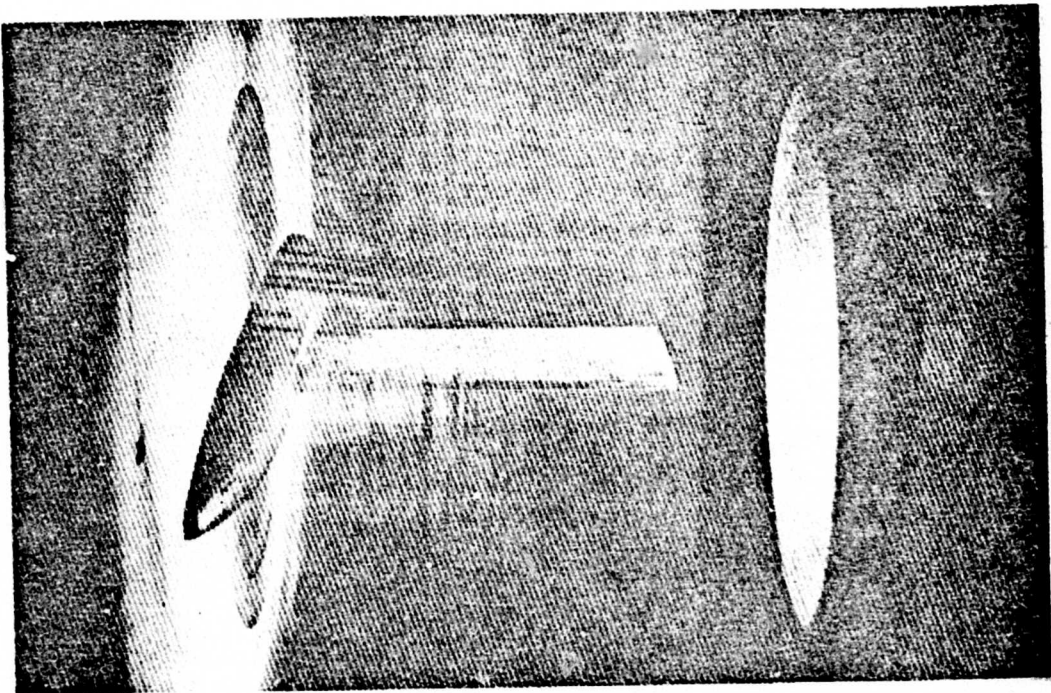


Figure 8. Response of Elastic Cantilevered Wing to Shock-Initiated Flow

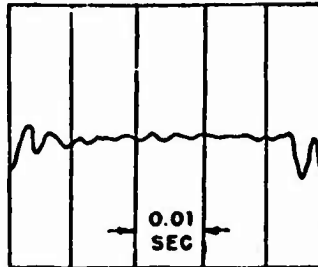


(a) CONSTRUCTION FEATURES



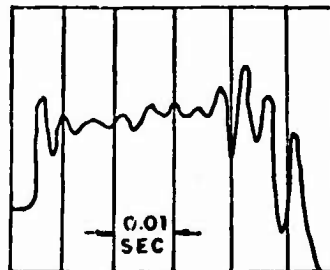
(b) MODEL MOUNTED IN THE TEST SECTION

Figure 9. Flutter Model



$u = 184$ MPH

(a) AT LESS THAN FLUTTER SPEED



$u = 298$ MPH

(b) BEYOND FLUTTER SPEED

Figure 10. Typical Strain-Time Responses of the Flutter Model

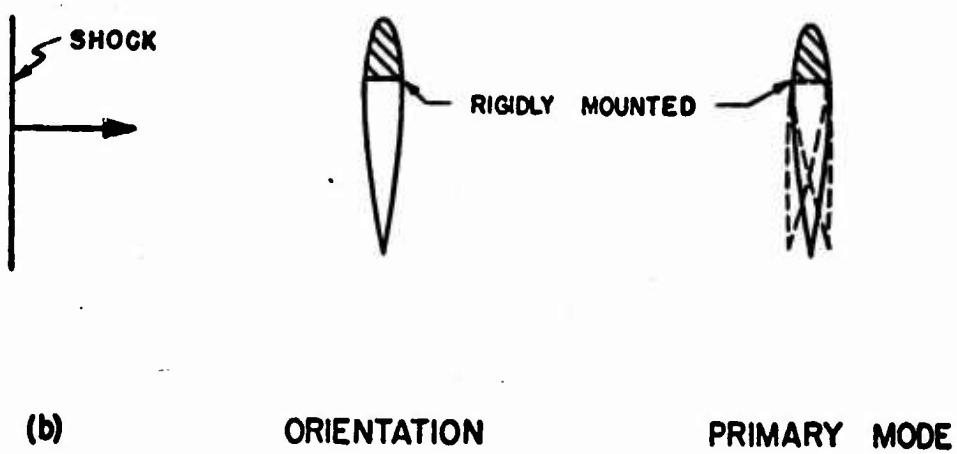
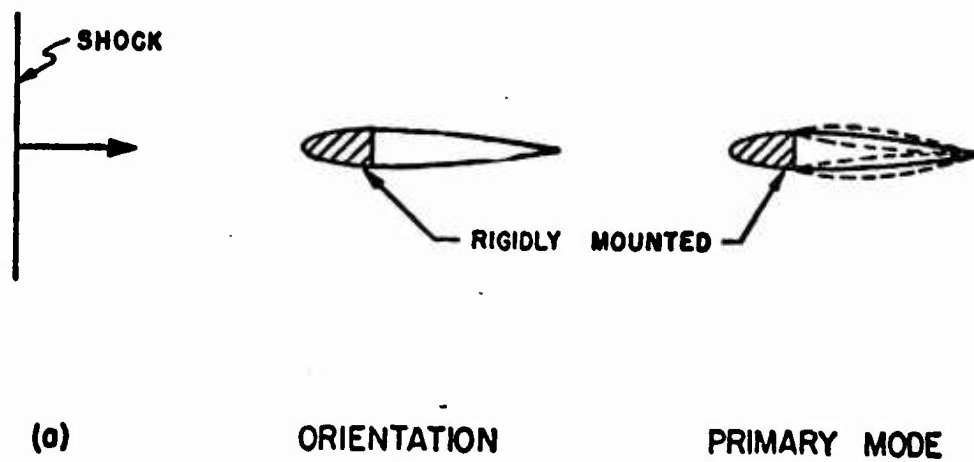


Figure 11. Schematic of Model-Shock Configurations
in Some Structural Response Tests

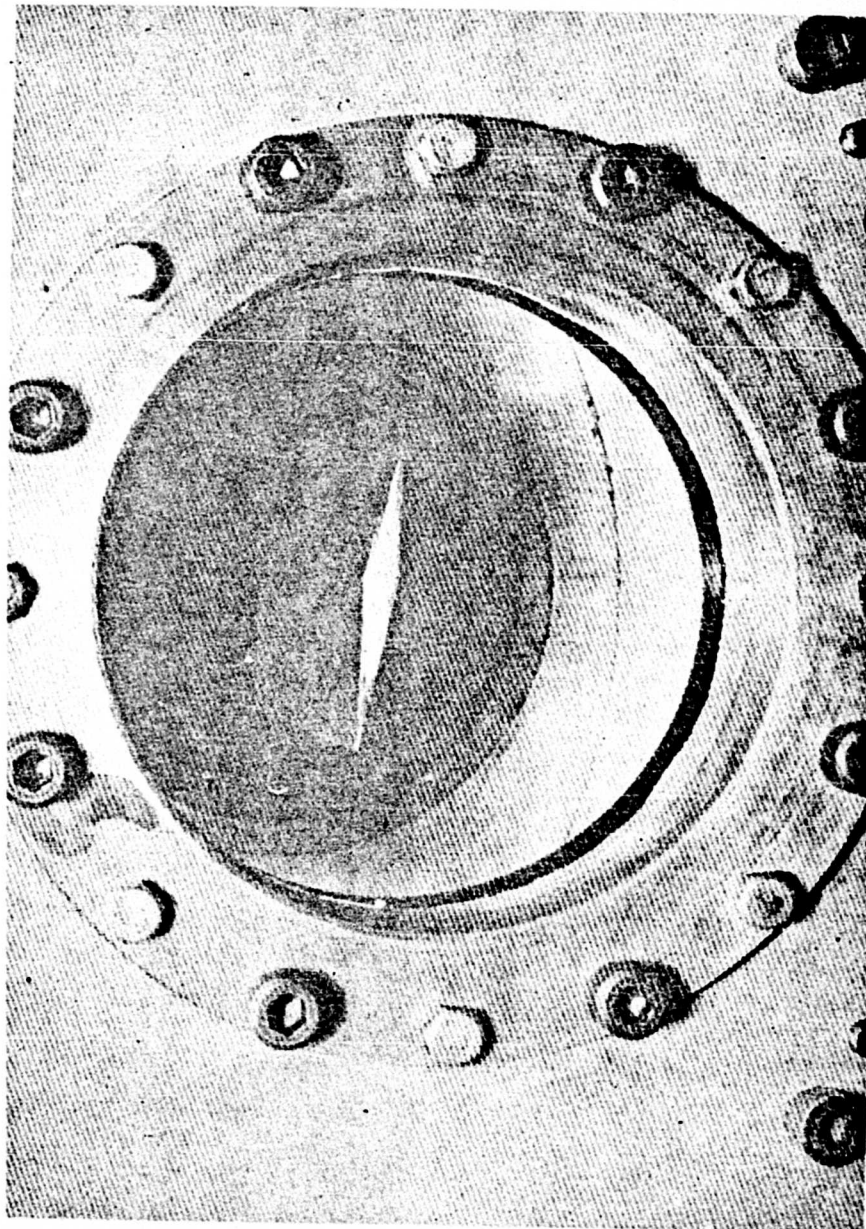
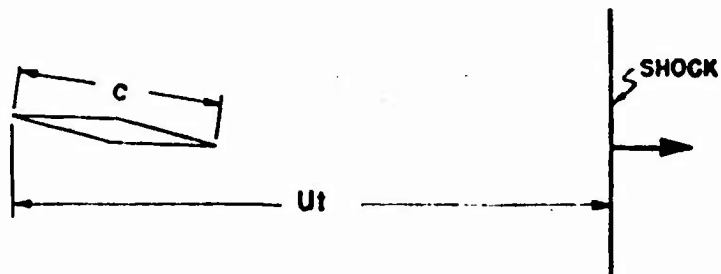


Figure 12. Double-Hedge Airfoil Mounted between Shock Tube Windows



U = SHOCK VELOCITY
 u = MATERIAL VELOCITY
 t = MEASURED FROM SHOCK IMPINGEMENT AT L. E.
 s/c = $(ut)/c$ = FLOW CHORDLENGTHS ELAPSED FOR ANY GIVEN PICTURE

NOMENCLATURE

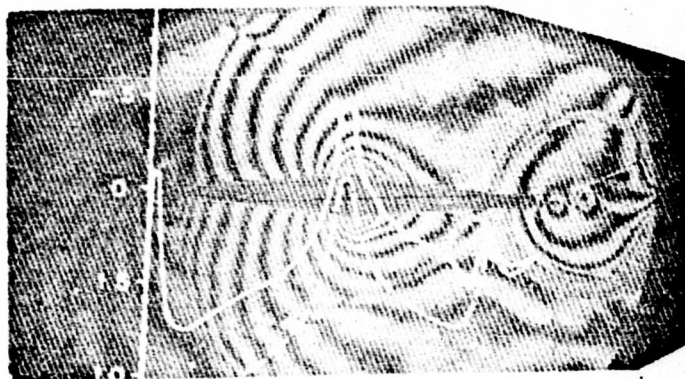


$$s/c = 0.03$$

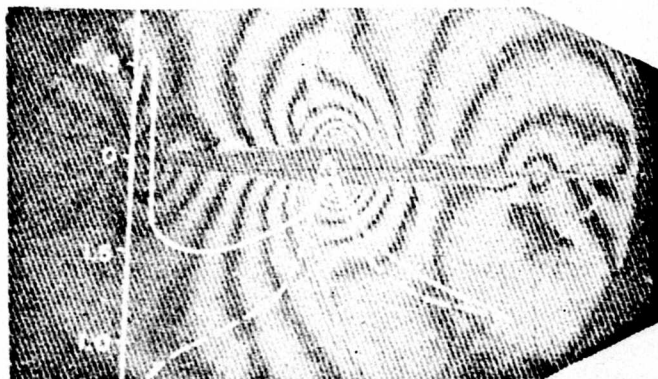
Figure 13. Sequence of Infinite Fringe Flow Interferograms for the Double-Wedge Airfoil; $M = 0.4$, $\alpha = 4^\circ$



$$s/c = 0.32$$

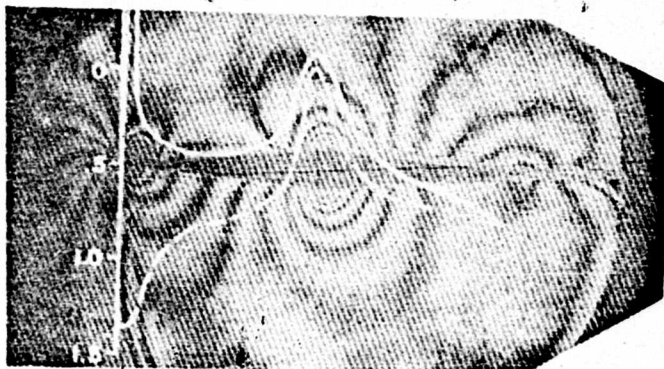


$$s/c = 0.42$$



$$s/c = 0.75$$

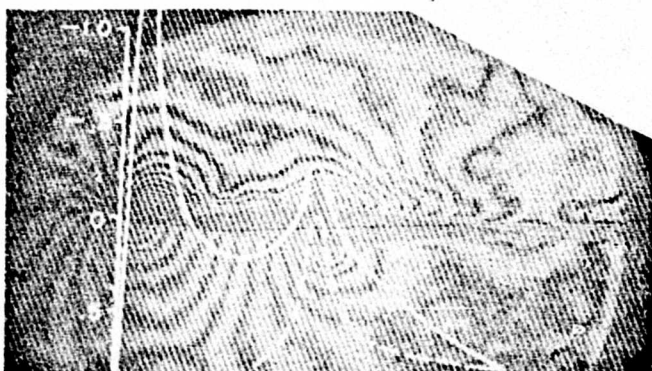
Figure 13. Continued



$$s/c = 1.0$$



$$s/c = 19.6$$



$$s/c = 50$$

Figure 13. Continued

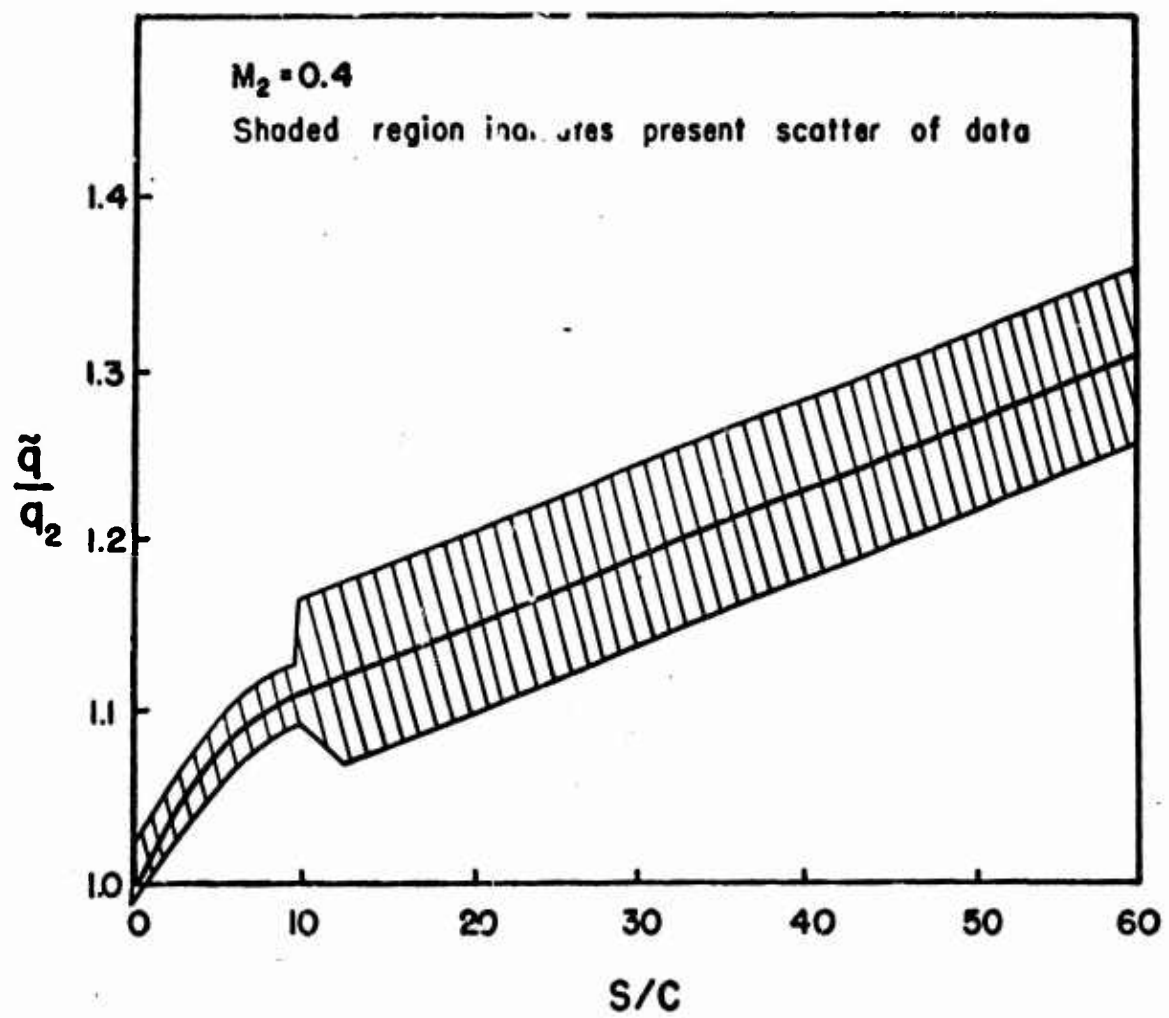


Figure 14. Tentative Estimate of the Freestream Dynamic Pressure in the Flow Following the Flow-Initiating Shock as Indicated by Density-Time Measurements

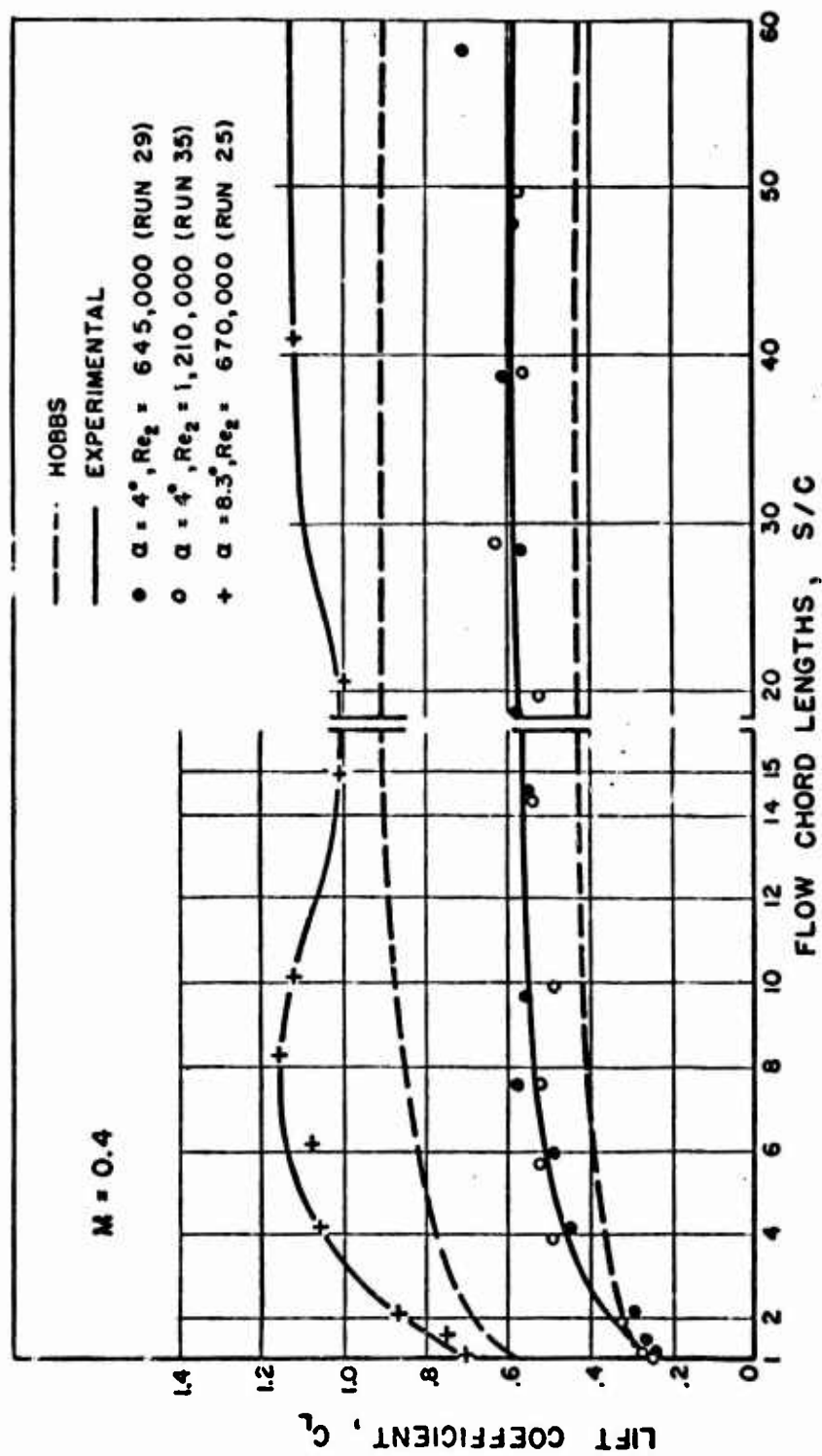


Figure 15. Variation of Uncorrected Lift Coefficient during the Post-Diffractive Flow Period

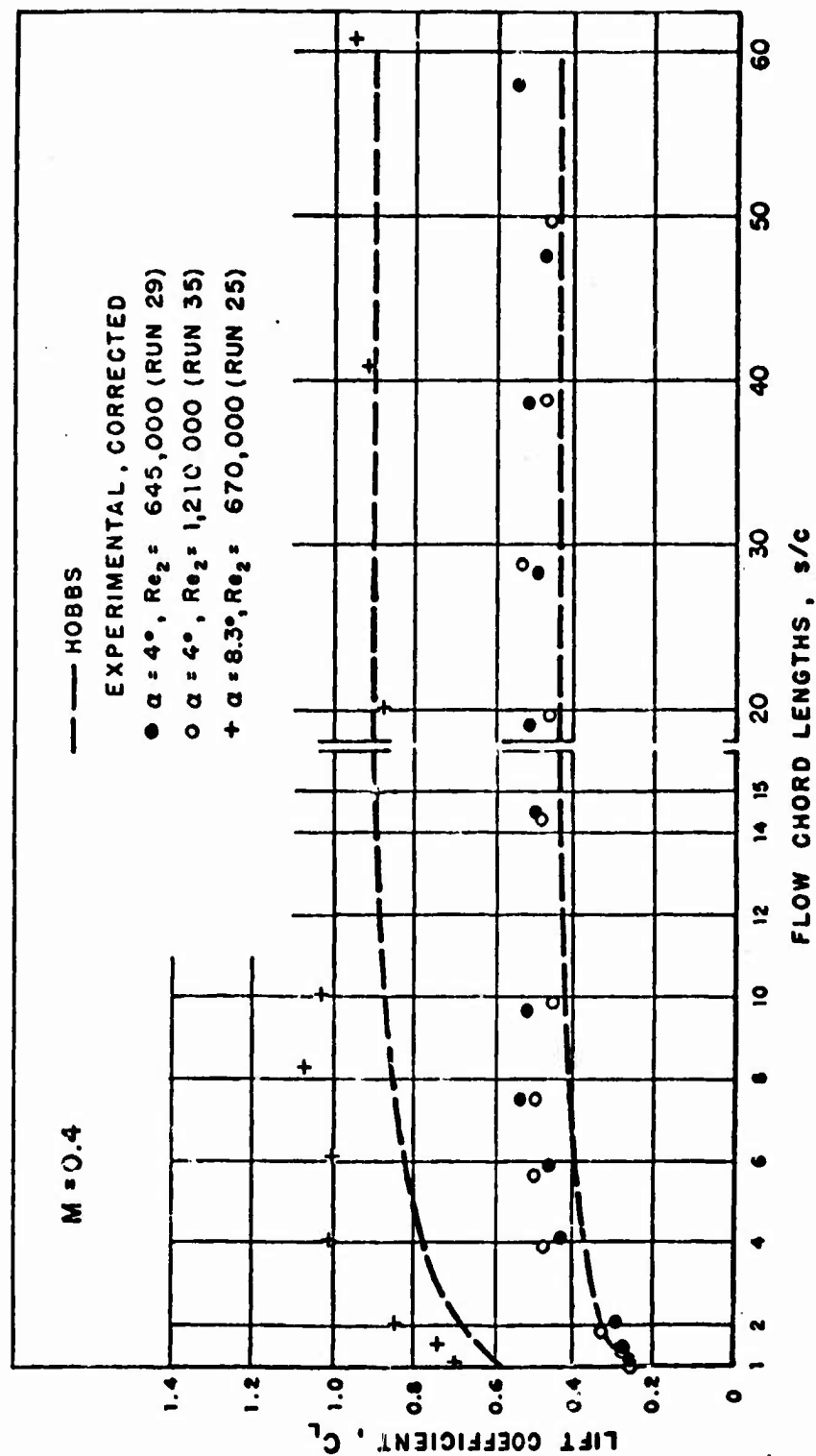


Figure 16. Variation of Lift Coefficient during the Post-Diffractive Flow Period, after Applying the Tentative Correction for Freestream Dynamic Pressure

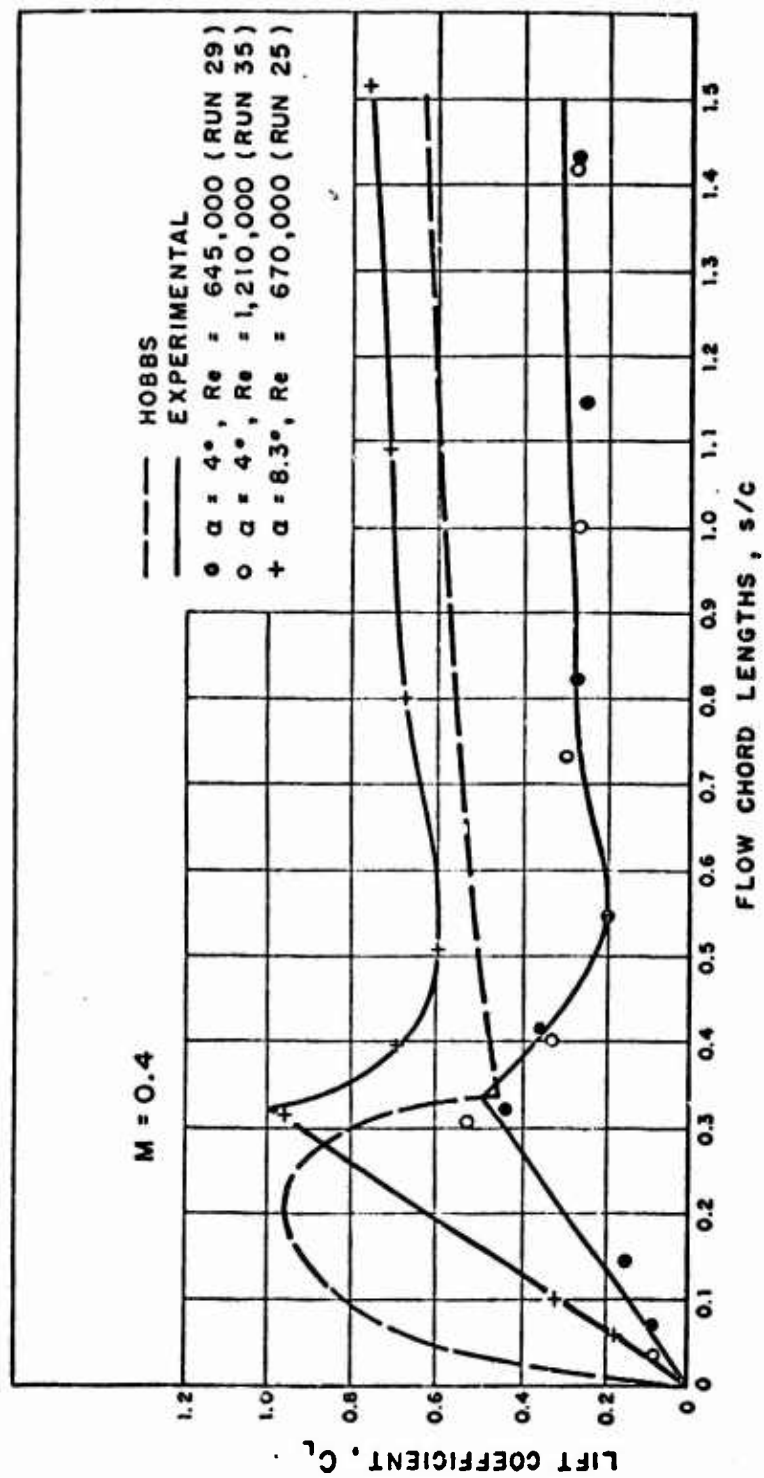
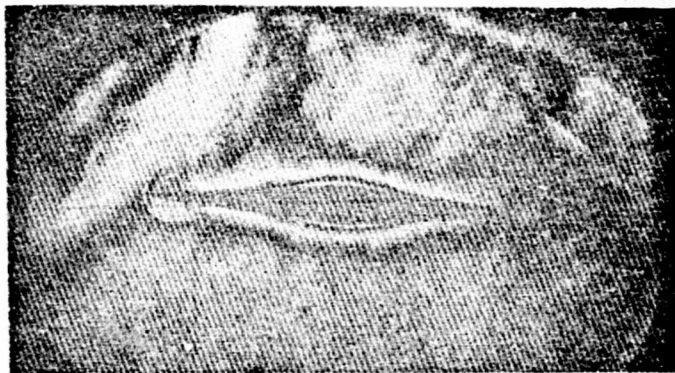


Figure 17. Variation of Uncorrected Lift Coefficient during the
Diffusive Flow Period



$$s/c = 0.08$$



$$s/c = 0.51$$



$$s/c = 0.83$$

Figure 18. Flow Interferogram Sequence; Double-Wedge
Airfoil; $M = 1.28$, $\alpha = 4^\circ$

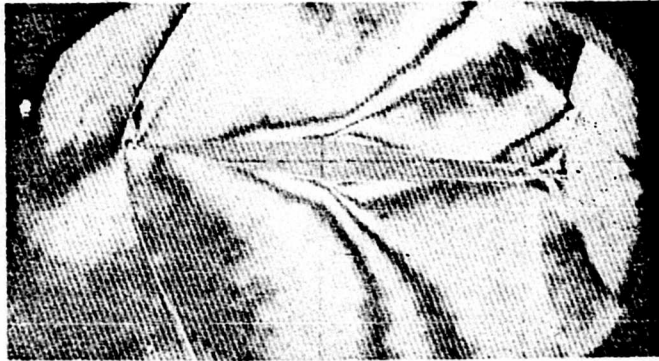


$$s/c = 0.99$$



$$s/c = 1.51$$

Figure 18. Continued

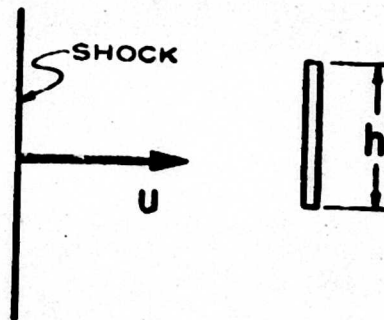


$$s/c = 2.04$$



IN COLD-GAS REGION

Figure 18. Continued



$$\tau = .U_1/h/2$$

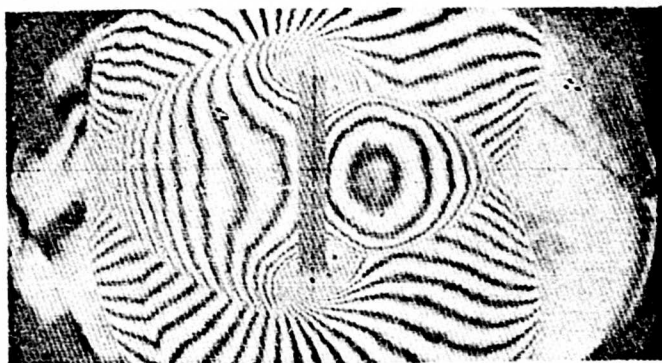


$$\tau = 0.125$$



$$\tau = 1.161$$

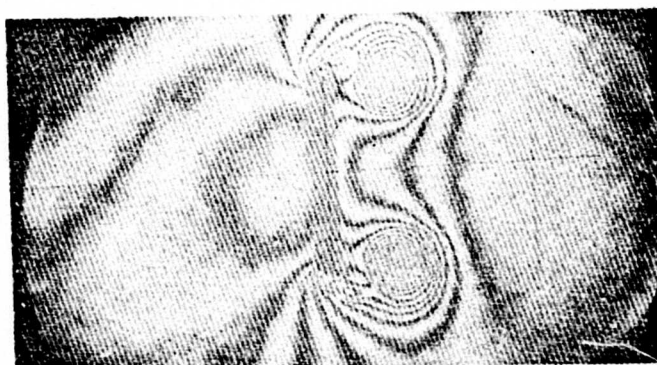
Figure 19. Flow Interferogram Sequence; Flat Plate Model; $M = 0.17$



$\tau = 2.43$

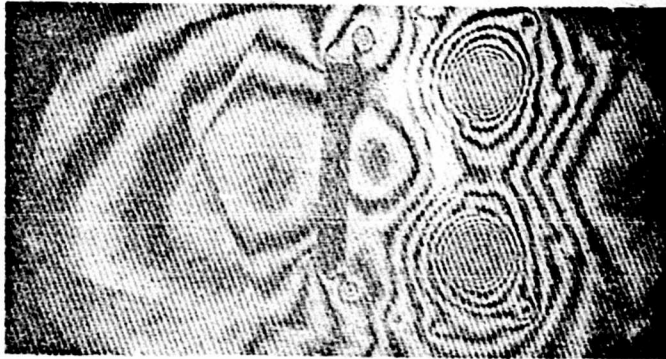


$\tau = 3.48$

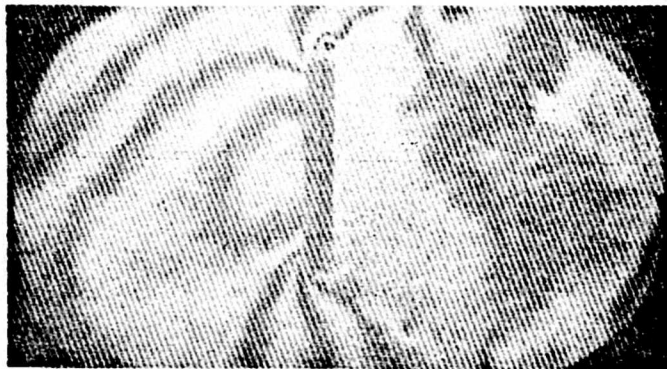


$\tau = 10.49$

Figure 19. Continued

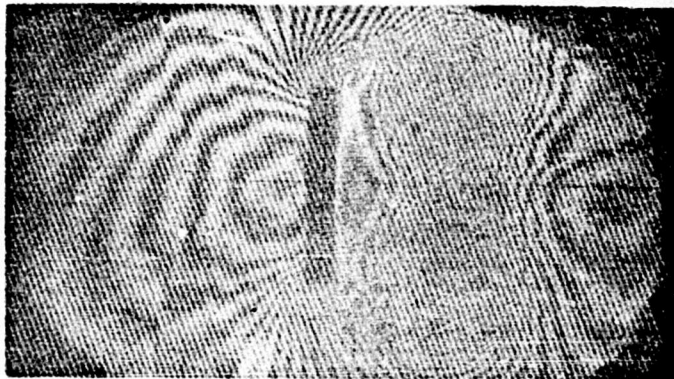


$\tau = 29.93$

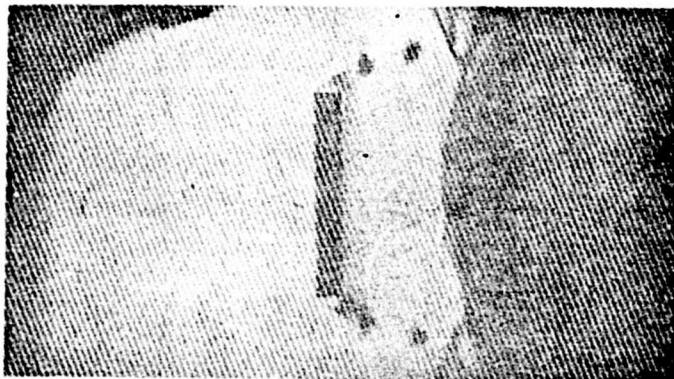


$\tau = 204.23$

Figure 19. Continued

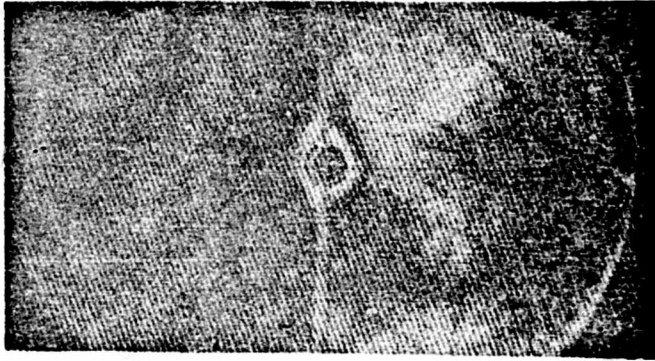


INTERFEROGRAM

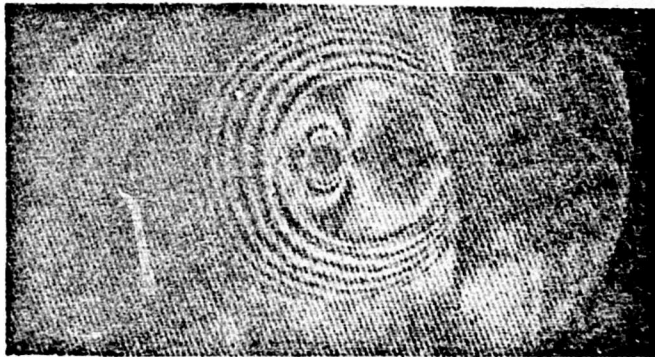


SCHLIEREN PHOTOGRAPH

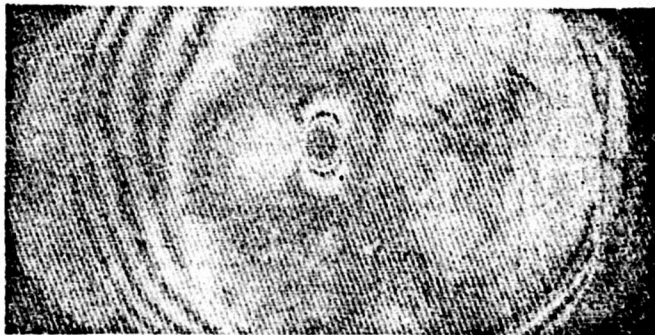
**Figure 20. Interferogram and Schlieren Pictures
Obtained at a Common Elapsed Time;
 $M = 0.45$**



$$\tau = (U_t)/\text{CYL. RADIUS} = 0.40$$



$$\tau = 8.48$$



$$\tau = 17.82$$

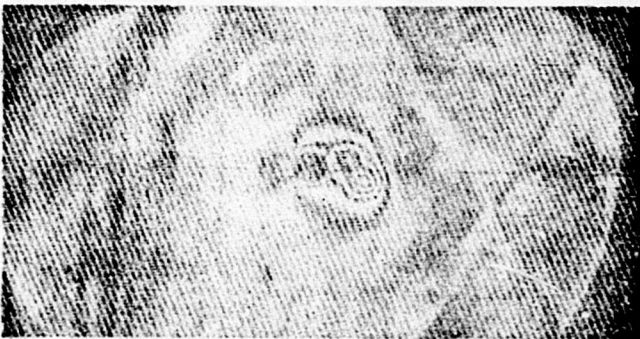
Figure 21. Sequence of Interferograms; Circular Cylinder; $M = 0.17$



$\tau = 30.5$

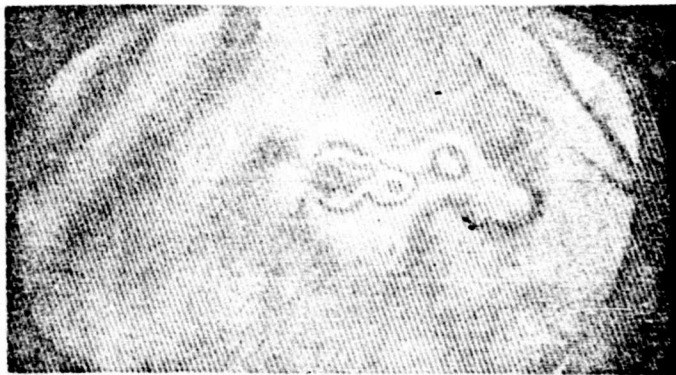


$\tau = 80.9$

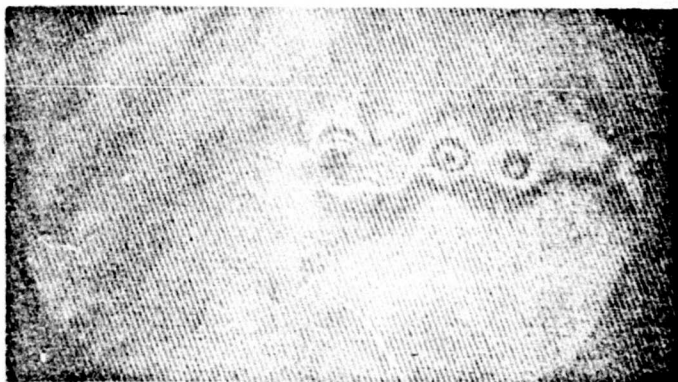


$\tau = 113.4$

Figure 21. Continued



$\tau = 193.1$

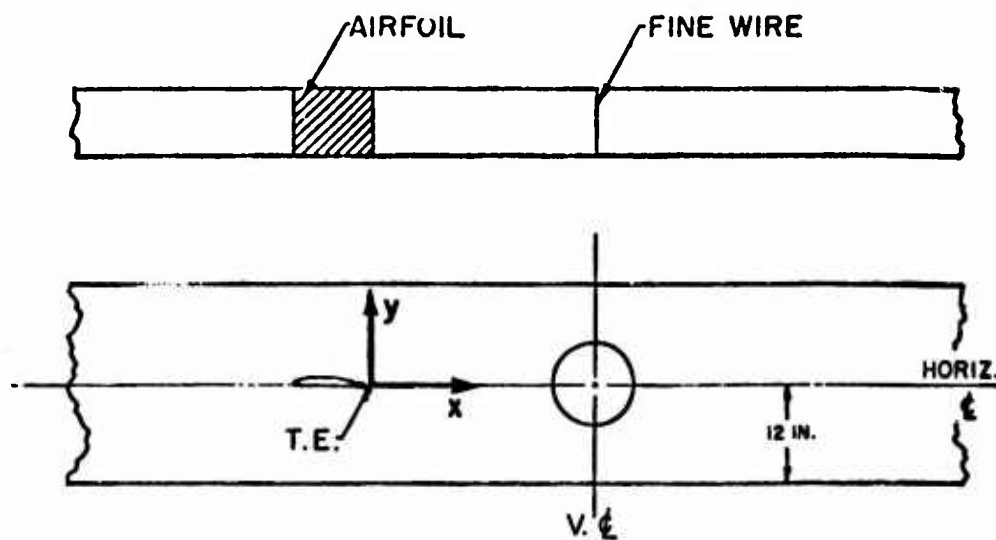


$\tau = 389.1$

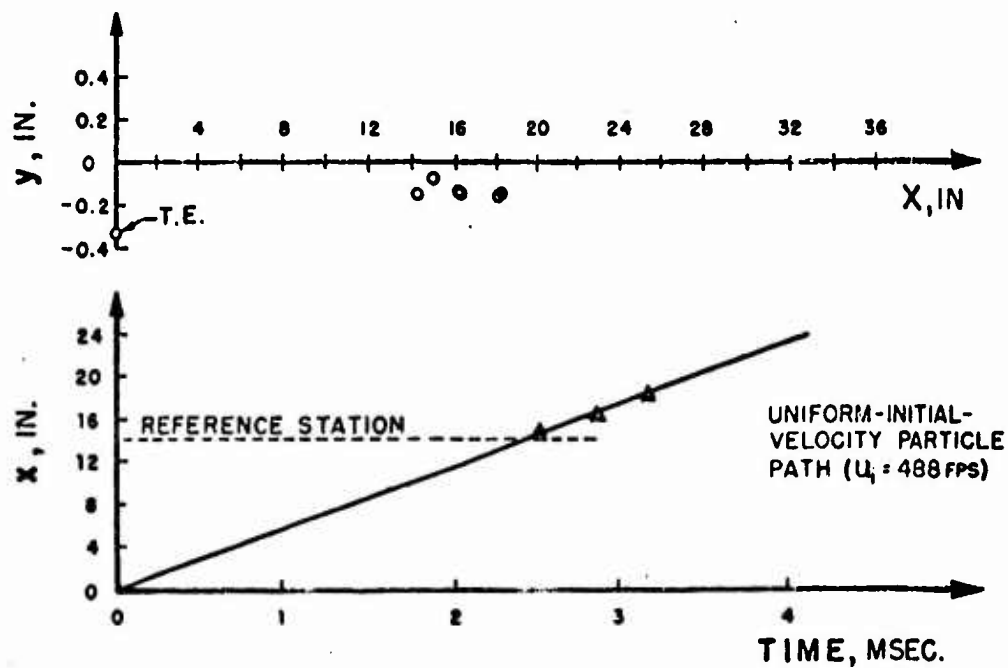


$\tau = 963.5$

Figure 21. Continued

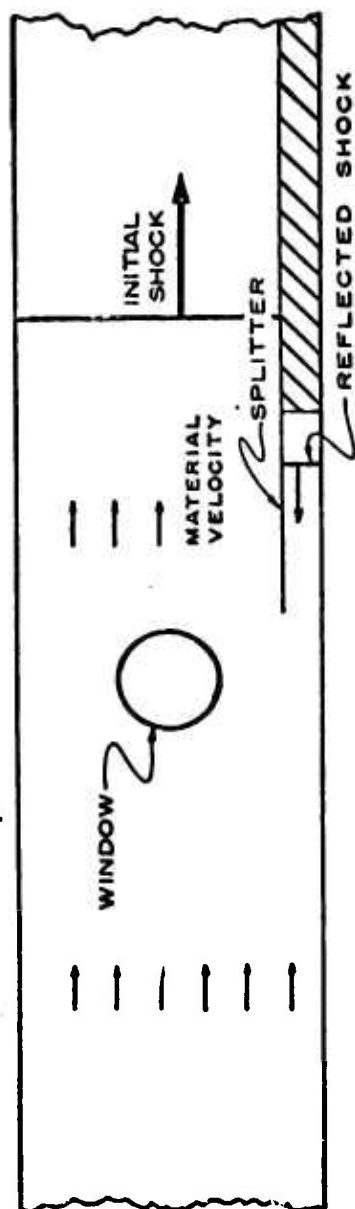


(a) SCHEMATIC LAYOUT

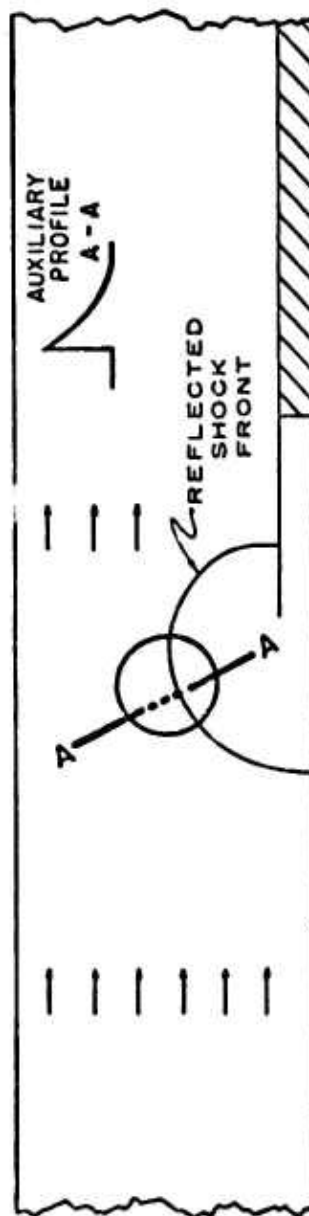


(b) VORTEX MOTION DATA

Figure 22. Schematic for Vortex Motion and Vortex-Induced Downwash Study



EARLY PATTERN



LATER PATTERN, SUBSONIC BASIC FLOW

Figure 23. Scheme for Generating a Basic Flow Field with a Blast-like Profile
Produced Later at the Test Station

STUDY OF GRIDS IN SHOCK TUBES

A. Wiedemann
Armour Research Foundation

The work reported in this talk was sponsored by the Air Force Special Weapons Center in connection with the operation of the Air Force Shock Tube Laboratory. The objective was to determine quantitatively the effectiveness of grids in shock tubes to eliminate, or reduce, the reflected signals from the end of the shock tube. We considered two specific problems: (1) placing the grid at the end of a constant area channel, and (2) placing the grid inside a constant area channel. I will present the results of both, but because of the time limitation I will omit the details of the second case which are quite similar to those of the first.

It is well known that when a flat-topped blast wave (that is, a shock wave followed by a uniform flow field) is incident upon the closed end of a shock tube, the shock wave is reflected and moves back upstream leaving a uniform flow field downstream. Also, if the end of the tube is open, the ensuing interaction results in the propagation of a rarefaction wave back upstream, such that either the exit pressure is equal to the original ambient pressure, or the flow at the exit is choked (that is, the exit Mach number is unity). The pressure variations that would be observed a short distance upstream from the end of the tube are illustrated in Figure 1 for these cases.

For any grid with an area ratio, say, σ , which is defined as the ratio of open area to total area, between the limits zero (the closed case) and unity (the open case), a weaker shock wave or rarefaction wave will be propagated back upstream. It appears reasonable to assume that there exists a critical area ratio, say, $\bar{\sigma}$ for which no signal will be propagated back upstream.

Observations of the interaction of shock waves and grids in constant area channels indicate that the resulting flow can be approximated by steady flow through the grid (or nozzles) and quasi-steady flow throughout the remainder of the flow field. In other words, the diffraction signals coalesce after they have propagated several nozzle lengths (some characteristic dimension of the nozzle). The radial gradients are small compared to the axial gradients (except in the nozzle), hence, a one-dimensional analysis is applicable. Figure 2 illustrates the flow fields which result. Regions 1 through 4 are relatively free of disturbances and are assumed to be uniform in the analysis. For the case where the grid is placed at the end of a constant area channel, the region to the right of the "grid position" does not exist, and either a shock wave is reflected back upstream--as shown here--or a rarefaction is reflected back upstream.

The nozzles placed at the end of the tube can be either converging-diverging or converging with a sudden expansion. The boundary conditions imposed by the grid are: (1) The exit pressure is equal to the original ambient pressure, or (2) the flow in the throat of the nozzle is choked. The exit pressure state is in the throat for the converging nozzle and at the end of the nozzle for the converging-diverging nozzle. The equations used are: (1) the Rankine-Hugoniot equations for the states separated by shock waves, (2) the isentropic non-steady flow equations for states separated by a centered rarefaction wave, and (3) the steady one-dimensional isentropic flow equations between the entrance, throat, and exit states in the nozzle. I will not present these equations here since most of you are quite familiar with them. If we go back to Figure 1, we can define a quantity which will measure the degree of the disturbance. This quantity will be called δ and is defined as

$$\delta = \frac{P_{\sigma'} - P_{\sigma}}{P_{\sigma}}$$

If ξ is the shock strength of the incident shock wave (that is, the ratio of the absolute pressures across the shock wave), ξ' is the strength of the reflected shock wave, and η is the strength of the rarefaction wave, then

$$\delta = \frac{\xi(\xi' - 1)}{\xi - 1} \quad \text{for the reflected shock wave}$$

and

$$\delta = \frac{\xi(\eta - 1)}{\xi - 1} \quad \text{for the reflected rarefaction wave.}$$

A numerical solution of the governing system of equations results in the plots of Figure 3, which was made for a gas with a ratio of specific heats of 1.4. All the numerical results presented here are based upon this value.

The results for both types of nozzles are presented. The dashed line is the locus of solutions where the flow just becomes choked. Once the throat becomes choked, the solutions for both nozzles are identical. The region to the left of the dotted line is the region where the flow is not choked. The numerical results indicate that there is a σ for which δ vanishes, and an explicit relation is obtainable. The solution is presented in Figure 4. The solution for σ is broken down into three ranges of ξ : for $1 \leq \xi \leq \xi_1$, which is the region where the flow is not choked; for $\xi_1 \leq \xi \leq \xi_2$, which is the region where the flow in the throat is choked but the flow behind the incident shock wave is still subsonic; and for $\xi_2 \leq \xi$, which is for the case where the flow behind the incident shock wave is supersonic. These equations are presented in Figure 5, and you will note the small difference between the two types of nozzles. The solution for the latter range ($\xi_2 \leq \xi$) is the trivial one, namely $\sigma = 1$.

The strength of the reflected wave (for $\xi > 4.86$ open end as no signal comes back, either shock wave or rarefaction wave) were also obtained and are

presented in Figures 6 and 7. The difference between the two types of nozzles is small, and therefore only these two plots are presented here.

Since we were primarily interested in the interaction of a peaked blast wave, (which, incidentally, is generated by detonating a "plane" charge of high explosive) a solution was obtained for a typical blast wave as encountered in the Shock Tube Laboratory. For these calculations a shock strength of two was selected so that the entire flow field could be considered isentropic. The solutions were obtained by the method of characteristics; a graphical treatment was employed in this particular case. As a basis for comparison, solutions were obtained for the given blast wave incident upon (1) a closed end, (2) an open end, and (3) a partially open end. The area ratio used in the latter case was one which completely eliminates the reflected signal from the incident shock wave ($\sigma = 0.6$). The flow in the throat of the nozzle was initially choked. The wave diagrams for these three cases are presented in Figure 8. Time is measured in units of the positive phase duration (t_0) of the blast wave (at the initial position), and distance is measured in units of $a_0 t_0$ where a_0 is the ambient sound velocity. The wave attenuates as it propagates downstream toward the end of the shock tube. In Figure 8 you see the reflected shock wave from the closed end, the reflected rarefaction wave followed by a compression wave for the open end, and finally the much less disturbed flow field for the critical area ratio grid. The flow is initially choked in the nozzle--the dashed line represents rarefaction waves. Then the boundary condition changes as the pressure drops so that the pressure in the throat is equal to ambient pressure (the pressure just outside the tube); the solid lines represent compression waves.

The effectiveness of the grid can be seen in Figure 9, where the pressure variation is presented for the three cases at three positions upstream from the grid. First we have the position $x/a_0 t_0 = 0$, which is the position where we imposed the given blast wave, then at $x/a_0 t_0 = 0.5$, and finally at $x/a_0 t_0 = 0.75$. The solid line represents the pressure variation if the tube were infinitely long (no end effect). The dot-dash line is for the case of a closed end. The dotted line is for the case of an open end, and the last line is for the case where the grid area ratio was approximately 0.6. The grid has the effect of decreasing the magnitude of the disturbance and in delaying its arrival at a given station back upstream.

I will now discuss briefly the results of the case where a grid is placed in a constant area channel and is struck by a flat-topped blast wave. We will refer back to Figure 2. The nozzle used in treating this case was the converging-diverging nozzle. If we neglect friction, as was done previously, we would expect no effect of the grid until the strength of the incident shock wave was great enough to choke the flow in the throat of the nozzle. Then both a reflected and transmitted shock wave exist. As the strength of the incident shock wave is increased a third shock wave, a standing shock wave, exists in the nozzle. As the shock strength of the incident wave is further increased, this auxiliary shock wave is swept downstream behind the transmitted shock wave. The same simple one-dimensional equations are used as before, however, due to the shock pattern there must exist an entropy discontinuity. It is shown in Figure 2 as the "interface". The conditions at the interface require that the pressure and particle velocity of states 3 and 4 be identical.

Again a numerical procedure must be used to obtain the results. The strength of the reflected shock wave (ξ') is the same as shown before in Figure 6. The strength of the transmitted shock wave (ξ'') is presented in Figure 10. The region to the left of the dotted line is the region where a standing shock wave exists in the nozzle. The strength of the auxiliary shock wave was determined but is not presented here. The strength of this shock wave was quite strong and had its maximum value at the breakaway point, that is, along the dotted line.

Some crude estimates were made as to the effect of friction and these estimates indicated that friction could be neglected. The area ratio is the principal variable governing the interaction of the blast wave with the grid.

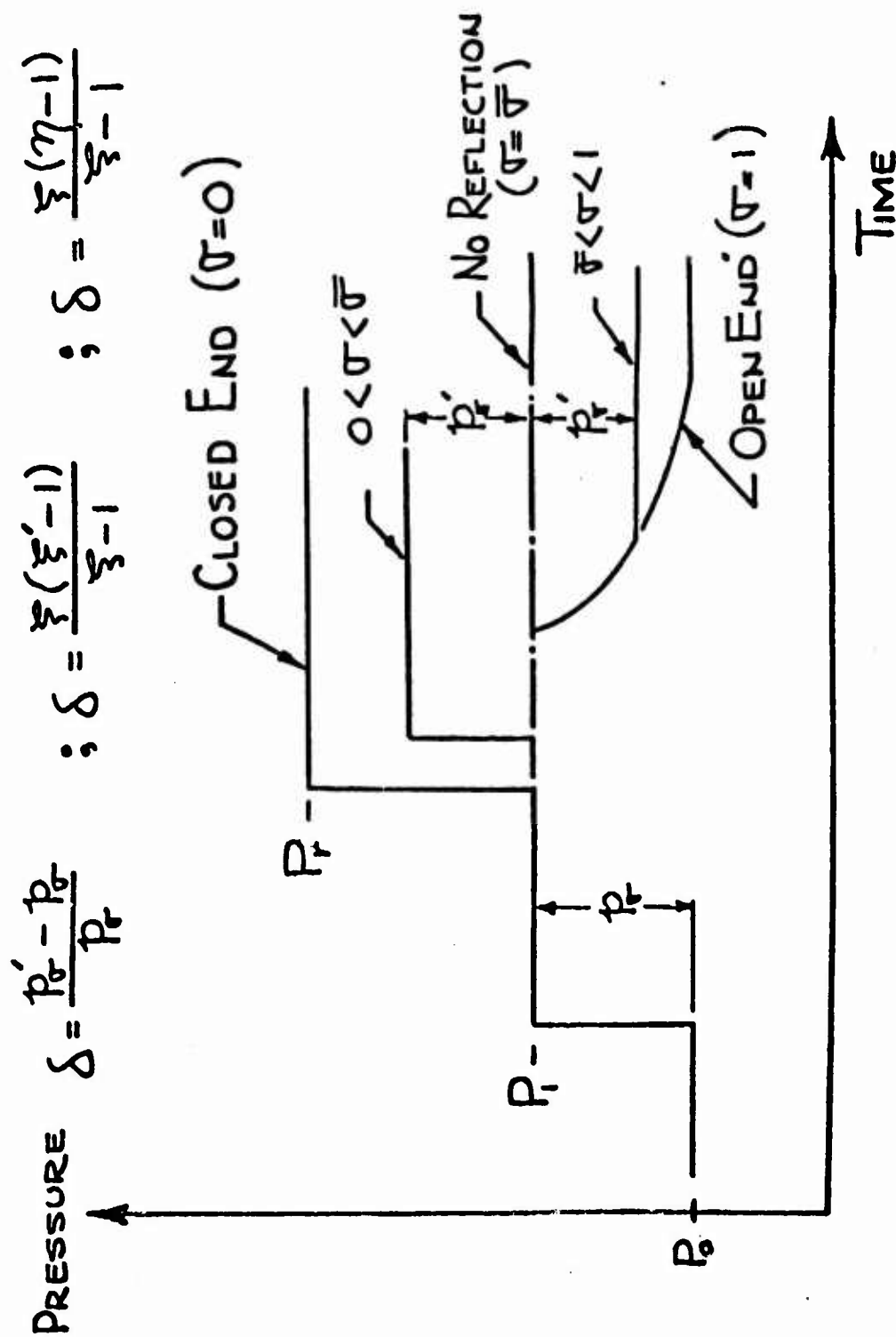


Figure 1. Pressure Variation near the End of the Shock Tube for Flat-Topped Blast Wave

WAVE DIAGRAM

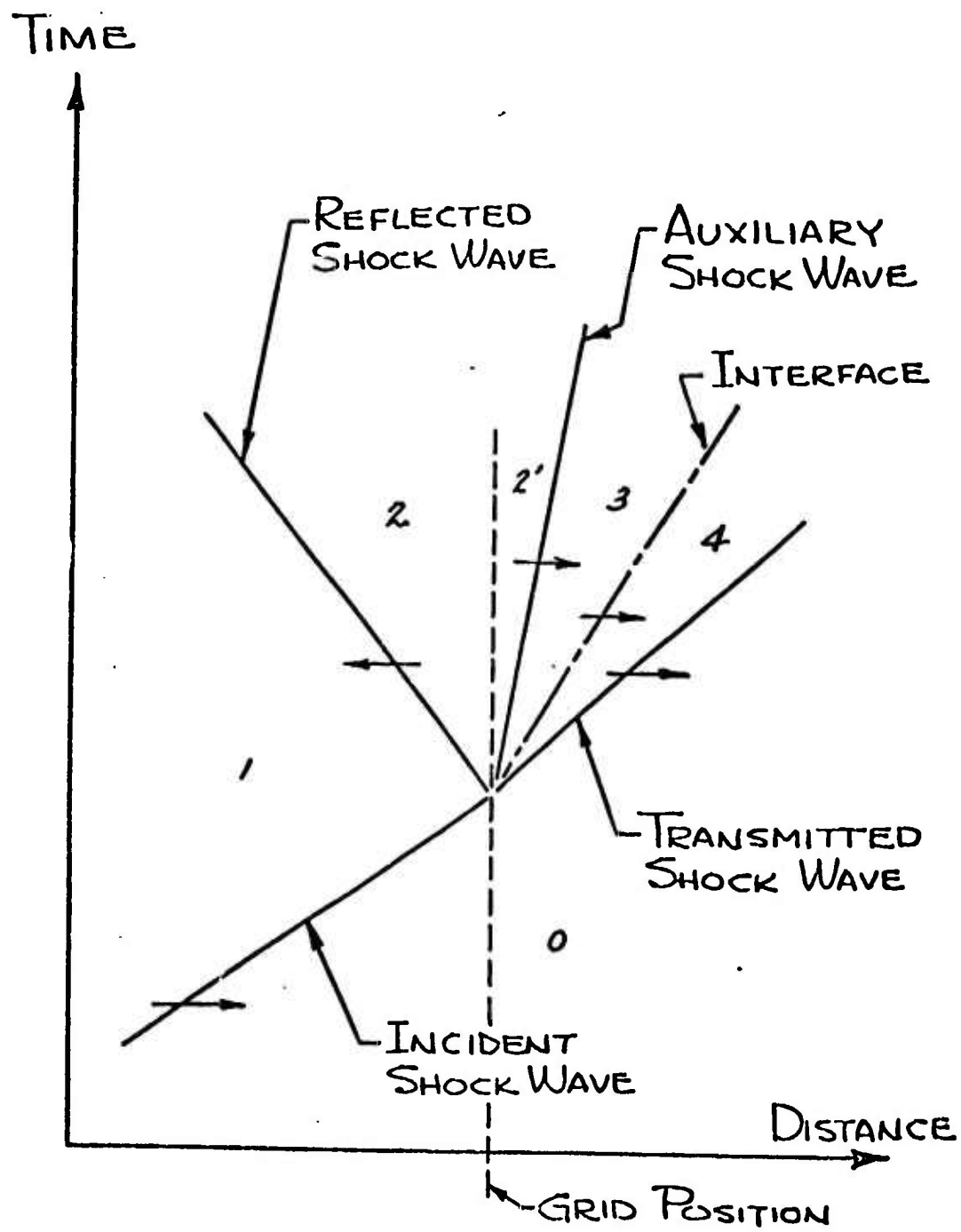


Figure 2. Wave Diagram of Flow Field in Constant Area Channel

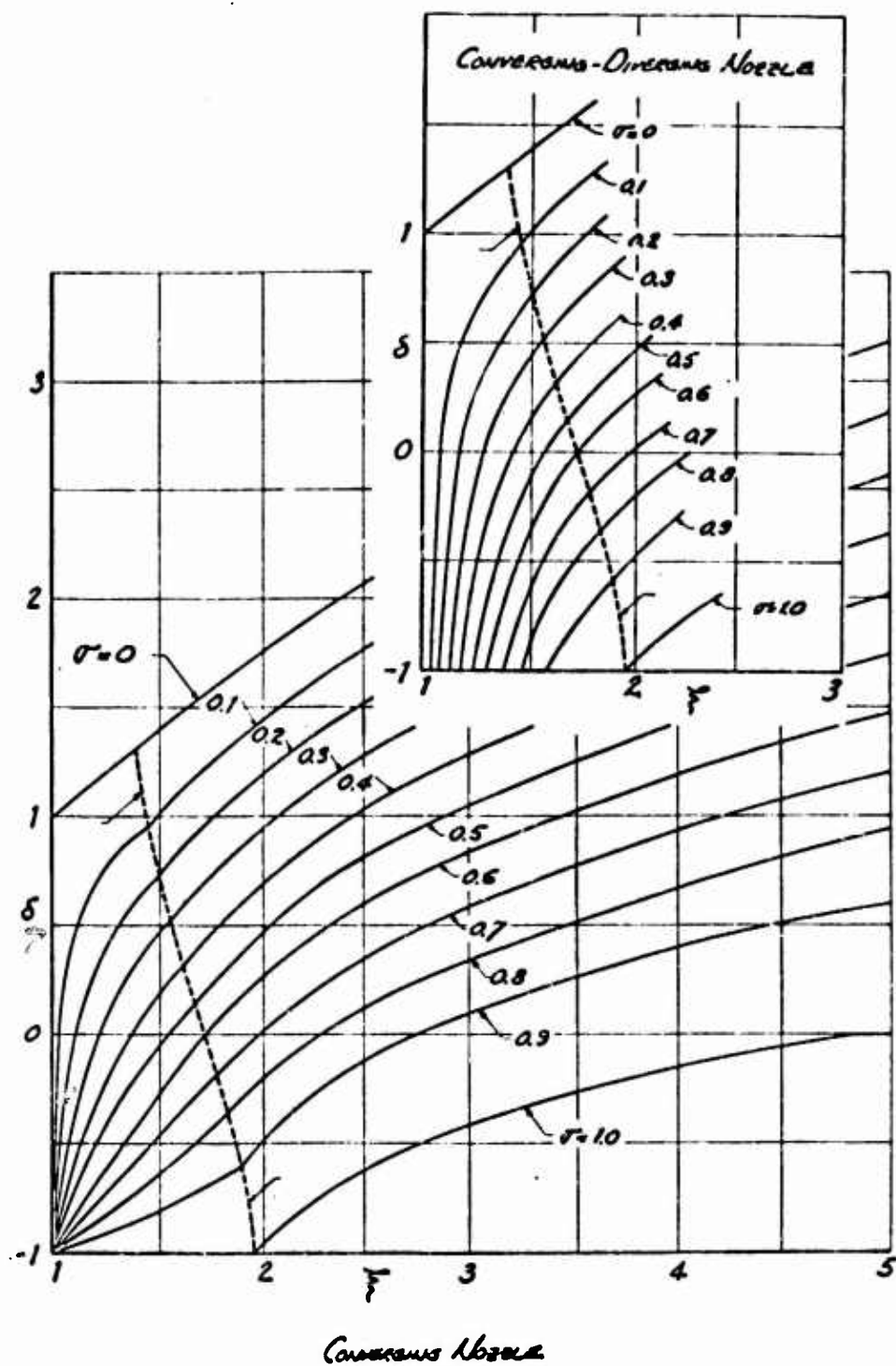


Figure 3. Disturbance δ as a function of ξ and σ

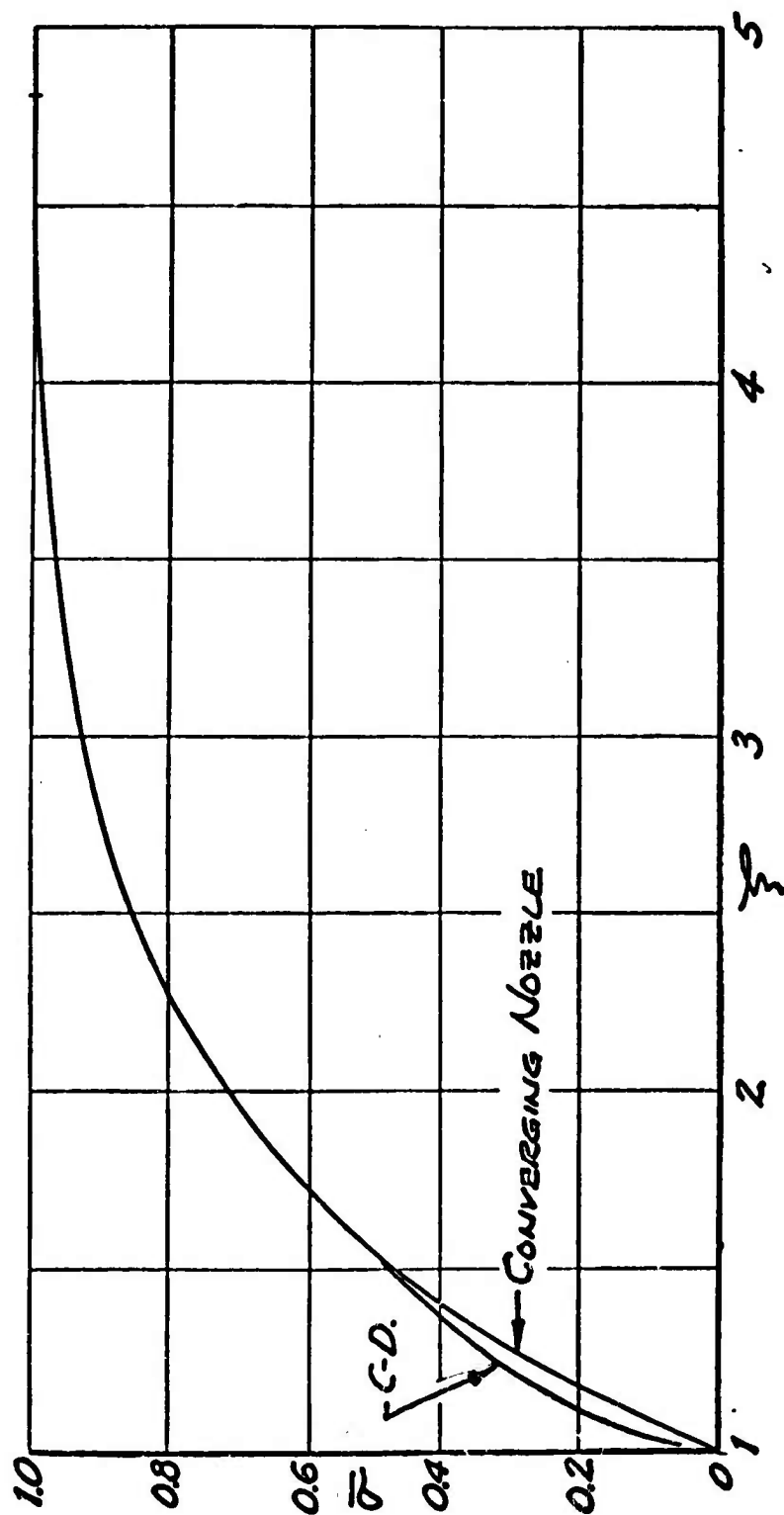


Figure 4. Solution for Complete Elimination of Reflected Signal

CONVERGING NOZZLE $(1 \leq \xi \leq \bar{\xi})$

$$\bar{\sigma} = \frac{(\xi)^{\frac{1}{k}}}{\sqrt{1 + \frac{k\xi(\mu+\xi)}{(\xi-1)^2} \left[1 - (\xi)^{-\frac{2}{\mu-1}}\right]}} \quad (1)$$

CONVERGING NOZZLE $(\bar{\xi} \leq \xi \leq \bar{\bar{\xi}})$
 CONVERGING-DIVERGING NOZZLE $(1 \leq \xi \leq \bar{\bar{\xi}})$

$$\bar{\sigma} = \left[\frac{2}{k+1} \left\{ 1 + \frac{(\xi-1)^2}{k\xi(\mu+\xi)} \right\} \right]^{-\frac{\mu}{2}} \cdot \frac{(\mu-1)(\xi-1)}{\sqrt{\xi(\mu+1)(\mu+\xi)}} \quad (2)$$

$$\mu = \frac{k+1}{k-1}$$

Figure 5. Equation of Solution for Complete Elimination of Reflected Signal

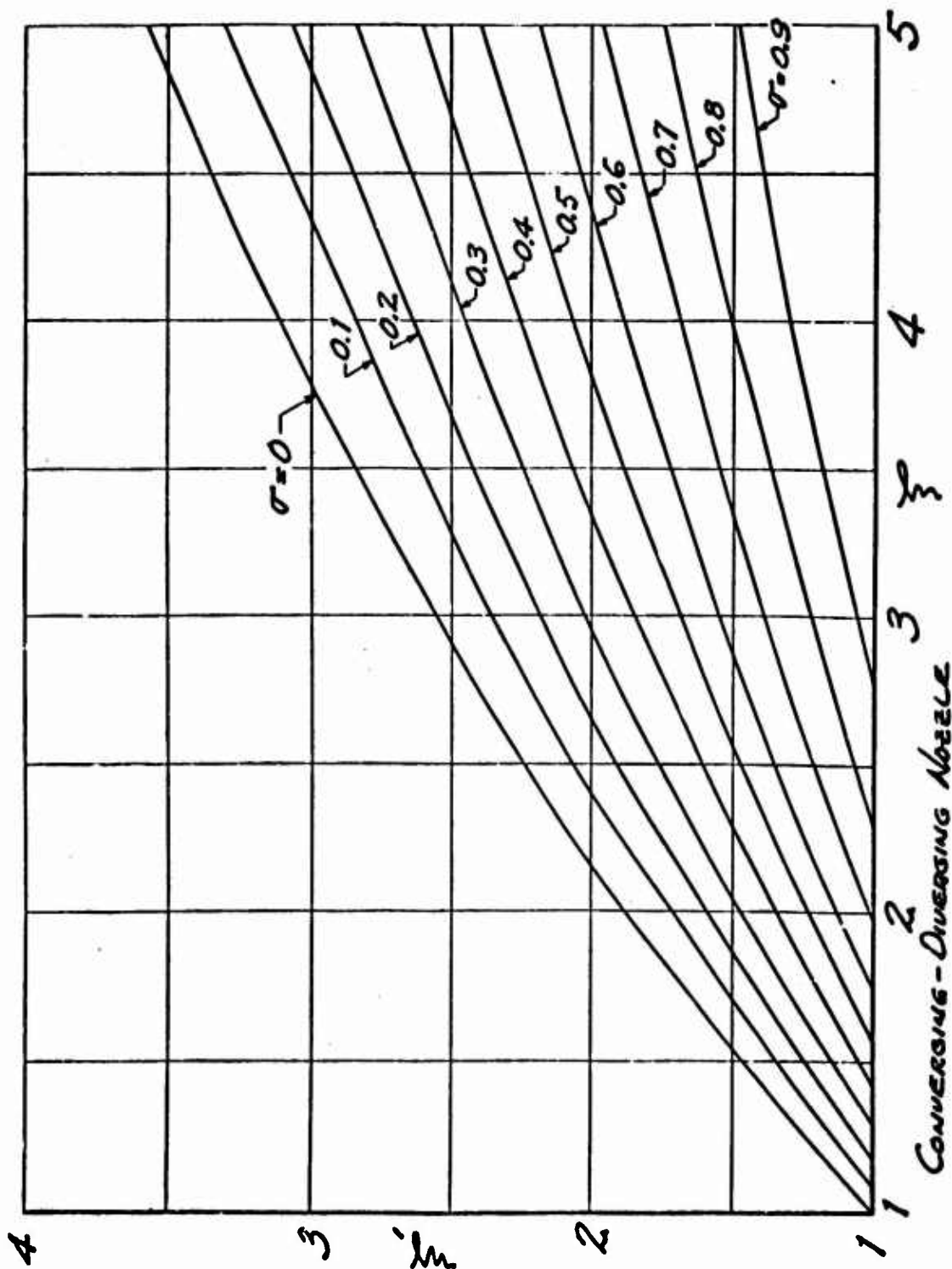


Figure 6. Reflected Shock Strength

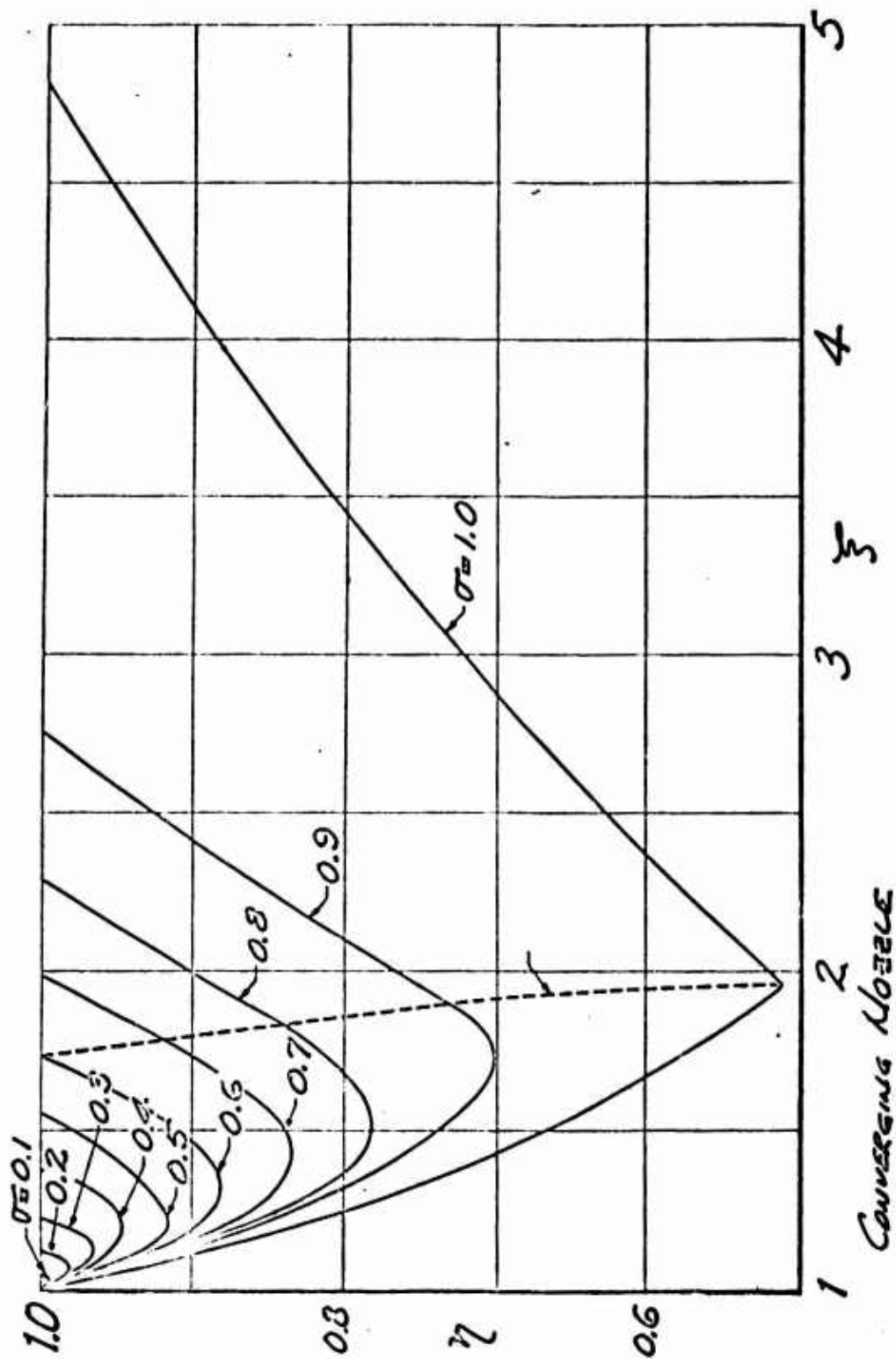


Figure 7. Strength of Reflected Rarefaction Wave

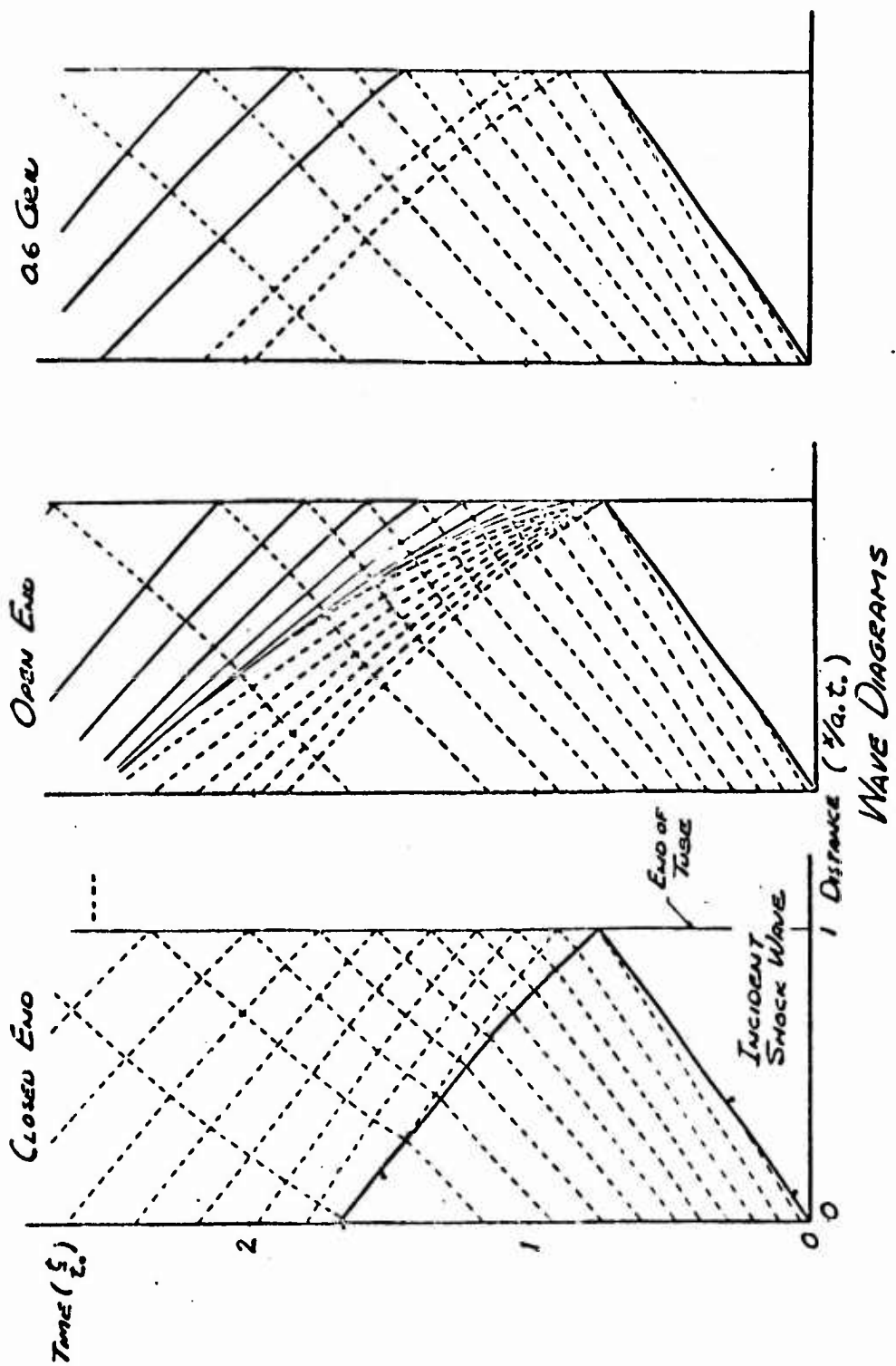


Figure 8. Wave Diagrams for Peaked Wave Incident upon End of Shock Tube

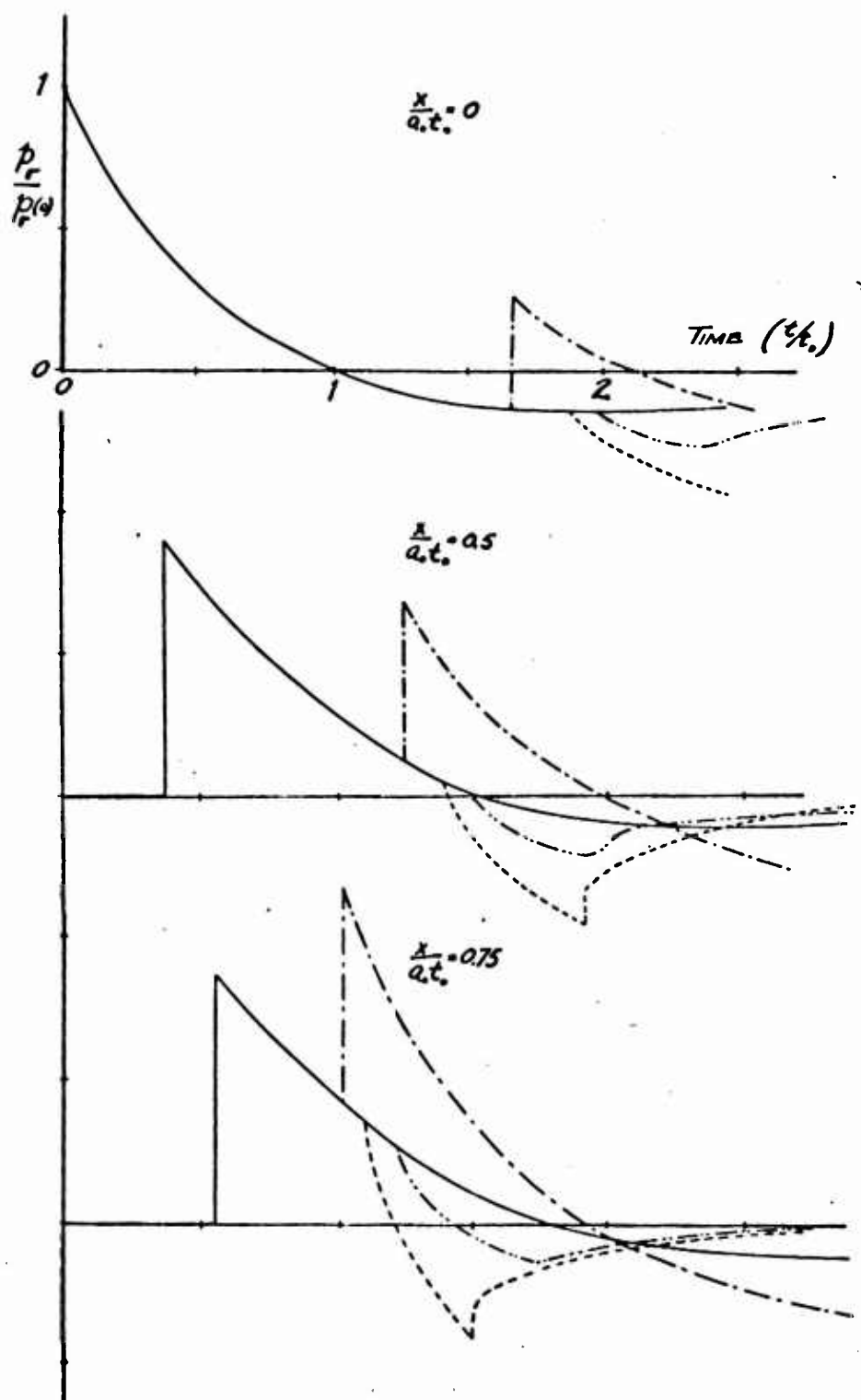
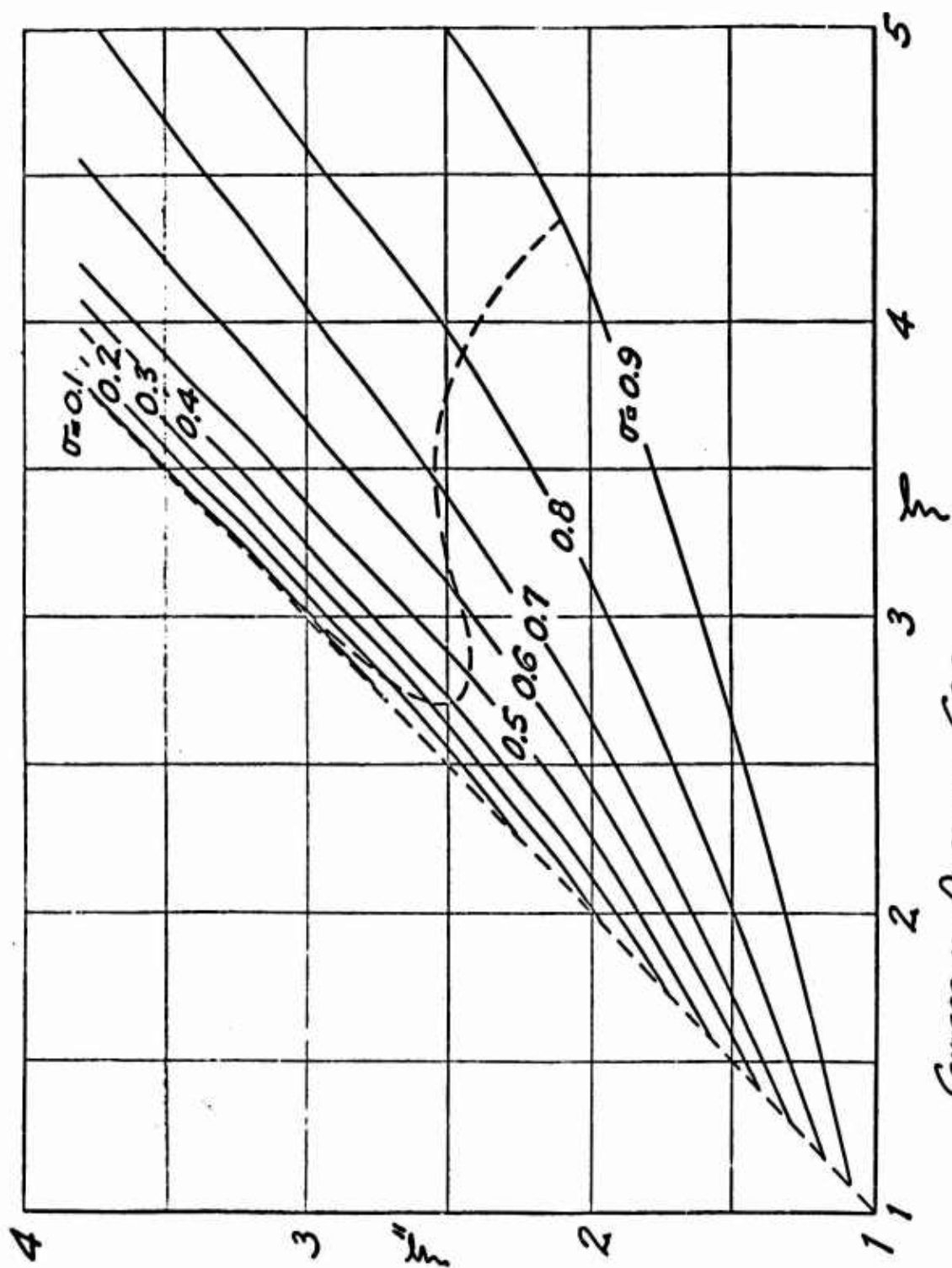


Figure 9. Pressure Variations near the End of the Shock Tube for Peaked Wave Blast



CONVERGING-DIVERGING GRID.

Figure 10. Transmitted Shock Strength

DEVELOPMENT OF THE SHOCK TUBE FACILITY FOR AIRFOIL STUDIES

J. R. Ruetenik
Massachusetts Institute of Technology

The M.I.T.-W.A.D.C. 8 by 24-inch shock tube was built principally to study the transient forces on airfoils and other aerodynamic objects upon immersion in a blast wave, although structural response experiments also occupied a prominent role in the planning of this facility.

A delay until complete measurements of the flow field were made was felt inadvisable, so shortly after completion of the shock tube, a 4-inch chord double-wedge airfoil was installed in the tube and the measurements previously described by Dr. Witmer¹ were made. In order to test the reliability of the measurements, the data after the flow field had achieved a "steady state", which was conservatively chosen as 20 chord lengths, were compared to wind tunnel measurements made at Cornell Aero. Lab.² and Langley Field³, Figure 1. At an angle of attack of 4 and 8.3 degrees, the lift coefficient in the shock tube, which is represented by circles in Figure 1, was respectively 58 and 48% greater than in the wind tunnels.

A number of explanations came to mind: the possibility of reduced separation at the corners of the airfoil by the heat transfer from the hot gas to the cool model, or by a larger turbulence level due to, among other causes, diaphragm particles and the rupturing process. But these explanations were considered insufficient since the values of the lift data were greater than the flat-plate theory. The uncertainty in the interferogram fringe measurement and the Gladstone-Dale constant were estimated to be only 5 to 10%. This was 2-1/2 years ago, before much was known about the flow following the shock in a shock tube, so a series of measurements were made of the density history without an airfoil following shock passage, similar to Mack's⁴ measurements at Lehigh.

The interferometer was located at the test section and adjusted for white light fringes oriented perpendicular to the shock tube axis. The camera view was blocked, except for a narrow slit perpendicular to the fringes. Numerous strip films were made over a range of initial pressure ratios, as well as single-spark exposures at various delay times. Figure 2, which was from a run with $M_2 = 0.5$, shows the first 2-1/2 milliseconds following shock passage, and is typical of the runs. In Figure 2, the slit image is vertical and sweeps from left to right. The shock passes from top to bottom so that the upper fringes which are behind the shock appear before the lower fringes ahead of the shock terminate.

To test for vibrations transmitted through the interferometer struc-

ture, the interferometer was raised above the shock tube, the tube fired, and a strip-film was taken. The fringes were as straight during the 45 milliseconds following shock passage, which is the longest test period, as they are in this figure preceding shock arrival.

Consider first the details of the fringes in Figure 2 following shock passage. Note the steps in the fringes which correspond to weak shocks which have not yet overtaken the initial shock. These weak shocks are often seen in the single-exposure interferograms. In addition, there is a considerable waviness in the fringes, which indicates that the flow is not as smooth as shock tube flow was once believed to be. Of course the interferometer measures fluctuations in wall-boundary layer as well as the so-called "freestream", but calculations indicate that the fringe shift due to the window-boundary layer is quite small: so it is concluded, for the present, that the fringes indicate the density variation in the freestream.

These fluctuations originate in two principal sources. First is the diaphragm rupture with its non-planar release of the high pressure gas, and curved initial shock with Mach stems and reflected waves, etc. But correlation of attenuation data with the attenuation theories of both Hollyer⁵ and Mirels⁶ indicate that the wall-boundary layer induces pressure waves which are more important to attenuation, and could quite reasonably be causing the density fluctuations in the freestream. And, of course, these waves do overtake the shock since the shock is subsonic with reference to the gas behind. Further evidence of the character of the freestream flow is the much lower values of the transition Reynolds number of the wall-boundary layer, as observed at this laboratory and at others, than would be expected by the increased stability of the laminar-boundary layer by the wall cooling. M.I.T. measurements⁷ at $M_2 = 0.7$ indicate that the transition Reynolds number, based on the particle velocity and distance traveled and properties behind the shock, is about 2 million. And yet Lee's calculations⁸ for a flat-plate boundary layer at this Mach number and wall to freestream temperature ratio appropriate for the test condition cited give a minimum critical Reynolds number, based on distance from the leading edge, of 60 million. Of course, the velocity and temperature profile are somewhat different, but this effect is not believed to be significant. Incidentally, in other shock tubes, the transition Reynolds number was somewhat lower, which may be due to the smaller tube diameter and the consequent increase in boundary effects. The M.I.T. wall-boundary layer measurements were reported at the annual meeting of the American Physical Society⁷, and are to be submitted as a W.A.D.C. report. The present conclusion would be that the freestream needs further investigation in order to compare shock tube flow to wind-tunnel flow. For blast wave studies, however, the flow may be quite similar.

Return now to the strip-film tests. It was desired to obtain the time development of the dynamic pressure during the 45-millisecond test period from the strip-films in order to explain the large steady state lift values. The dynamic pressure was computed at the end of the time period from the density using three models. It was postulated that the density increase was due to (1) a stronger shock, (2) a second shock following the initial shock, and (3) an infinity of shocks, an isentropic compression, following the initial shock. The values of the dynamic pressure agree within one percent for all three flow models.

The density history compiled from many runs is shown in Figure 3. Here s/c is the chord lengths of flow at the test station, and $c = 4$ inches corresponding to the two airfoils tested. An s/c of 60 corresponds to 40 milliseconds of flow for this case. The quantity \bar{q} is the dynamic pressure following shock passage, and q_2 is the value immediately behind the shock at the test section station. The solid curve is an average of the data; the shaded region indicates the data scatter. It is interesting to note that the subsequent boundary layer measurements showed that the boundary layer was laminar until about $s/c = 6$. The greater scatter of data thereafter apparently represents the effect of the irregular growth of the turbulent boundary layer during each run, and from run to run.

Braun and Mirels have computed the change in properties at a fixed station following shock passage, an extension of Mirels NACA TN 3278 attenuation work*. They worked out two cases: one a completely laminar-boundary layer from the shock to the rarefaction wave, and the other completely turbulent. We computed the dynamic pressure rise from their equations for $M_2 = 0.4$ at the test station and with their kind permission have compared the result in Figure 3. The agreement with the theory based upon a turbulent boundary layer is very encouraging, and indicates the importance of the wall-boundary layer on the flow. The value with a laminar boundary layer (at $M_2 = 0.35$) is much nearer unity.

The solid curve has been employed to correct the airfoil measurements in the shock tube, as represented by the squares in Figure 1. The steady state C_L values at 4 and 8.3 degrees were brought to within 30 and 24% respectively of the wind tunnel data. It is consoling however to note that the agreement with flat-plate theory is excellent. More recently similar measurements have been conducted in the M.I.T. facility on a more conventional subsonic airfoil, the NACA 65.010 profile. At an angle of attack of 5 degrees, the corrected steady state data are only 5% above wind tunnel data, which is quite good.

But near stall, the interferometer that has been employed for these measurements is at a disadvantage for several reasons. First, it measures all along the span giving a spanwise average. The boundary layer on the airfoil tends to separate first at the wing ends where it interacts with the wall-boundary layer. The wind tunnel measurements, on the other hand, are generally made near the center of the airfoil. Secondly, near stall a vortex forms on the top surface, and there is some uncertainty as to how to determine the surface pressure from the vortex fringes in this region of strong viscous effects and large density gradients. Therefore a program to develop a pressure sensor to measure the mid-span pressure directly is proceeding currently in this laboratory. Incidentally, the difference between the double-wedge pressure profiles and the wind tunnel profiles was almost entirely limited to the front upper surface. The direct pressure measurement is expected to re-

* Described in a private communication, and to be forthcoming in an NACA technical note entitled "Nonuniformities in Shock Tube Flow Due to Unsteady Boundary-Layer Action", by W. H. Braun and H. Mirels.

move this uncertainty. The possibility of temporarily obtaining very high lift values before the onset of stall, which has been indicated by interferograms, has intensified the interest in this measurement.

The pressure sensor being developed here consists of two barium titanate crystals, one on the upper surface of the airfoil and one on the lower. The signals are fed into a high impedance differential amplifier so that only a difference signal is recorded. It is important to obtain the difference as early as possible in the network since at $M_2 = 0.4$ the dynamic pressure is only 25% of the shock overpressure, so to measure the lift to 10% accuracy, and taking $C_L = 0(1)$, would require measuring the difference to 2% of the pressure rise. At higher Mach numbers this requirement is less severe. Crystals were selected primarily to miniaturize the pickups. The electronic portion of the pressure measuring is now satisfactory. The input impedance of the pickup, lead, and amplifier input is about 2 by 10 inch ohms, and the capacitance is about 300 micro-micro farads, with a time constant of one minute--a 5-second time constant gives only a one percent fall off in a 50-millisecond test period. These values may be juggled later to reduce the noise from the large grid resistance to less than one percent. Efforts are now being made to remove the heat transfer effects on the gage from the hot gas, and the program will then be aimed at determining the accuracy of the sensor.

Another program will be conducted to measure the mass flow and temperature behind the shock with the hot wire anemometer. The equipment is ready for testing in the shock tube, and will follow the program of the pressure sensor development.

A total-pressure probe with a fairly short inlet passage to a strain gage pickup has also been constructed. It is planned to measure the desired dynamic pressure more directly.

Finally, plans have been made to test a "moving" airfoil subjected to a blast loading. The plan is to use the initial shock to establish a steady state flow, and entrap a portion of the shock in an auxiliary channel. The channel would be constructed in such a manner that the reflecting waves would then form into a "blast" wave and pass over the airfoil. Tests involving varying "blast" wave strengths and orientations with respect to the airfoil chord line will be included.

ACKNOWLEDGEMENTS

This work was carried out under the sponsorship of the Aircraft Laboratory, W.A.D.C. Appreciation is expressed to Dr. E. A. Witmer of this laboratory under whose supervision this work was carried out for his encouragement and suggestions throughout these studies, as well as the many others who have made these results possible.

REFERENCES

1. Witmer, E. A., Application of the Shock Tube to Transient-Airforce and to Structural-Response Studies, AFSWC Shock Tube Symposium, M.I.T., February 1957
2. Bartlett, G. E., and Peterson, J. H., Wind-Tunnel Investigation of Double-Wedge Airfoil at Subsonic Speeds, Bumblebee Rep. No. 53 (Contract NOrd-8993), Cornell Aero. Lab., August 1946
3. Humphreys, M. D., An Investigation of a Lifting 10-Percent-Thick Symmetrical Double-Wedge Airfoil at Mach Numbers up to 1, NACA TN 3306, November 1954
4. Mack, J. E., Density Measurement in Shock Tube Flow with the Corono-Interferometer, Lehigh University, Inst. of Res. TR 4, April 1954
5. Hollyer, R. N., Jr., Attenuation in the Shock Tube: Laminar Flow, Jour. of Appl. Physics, V. 27, N. 3, pp. 254-61, March 1956
6. Mirels, H., Attenuation in a Shock Tube Due to Unsteady-Boundary-Layer Action, NACA TN 3278, August 1956
7. Ruetenik, J. R., and Divone, L. V., Interferometric Measurements of the Laminar Boundary Layer on a Shock Tube Wall, Paper delivered at the 1957 Annual Meeting of the American Physical Society
8. Lees, L., The Stability of the Laminar Boundary Layer in a Compressible Fluid, NACA Rep. 876, 1947

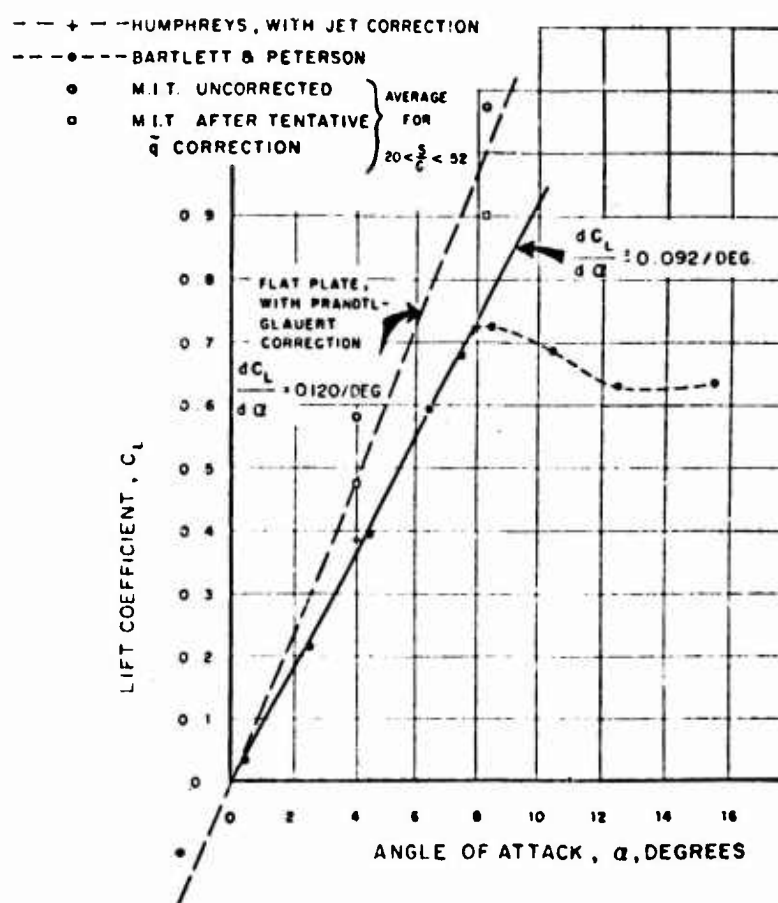


Figure 1. Comparison of Steady-State Lift Coefficient Versus Angle of Attack, $M_2 = 0.4$

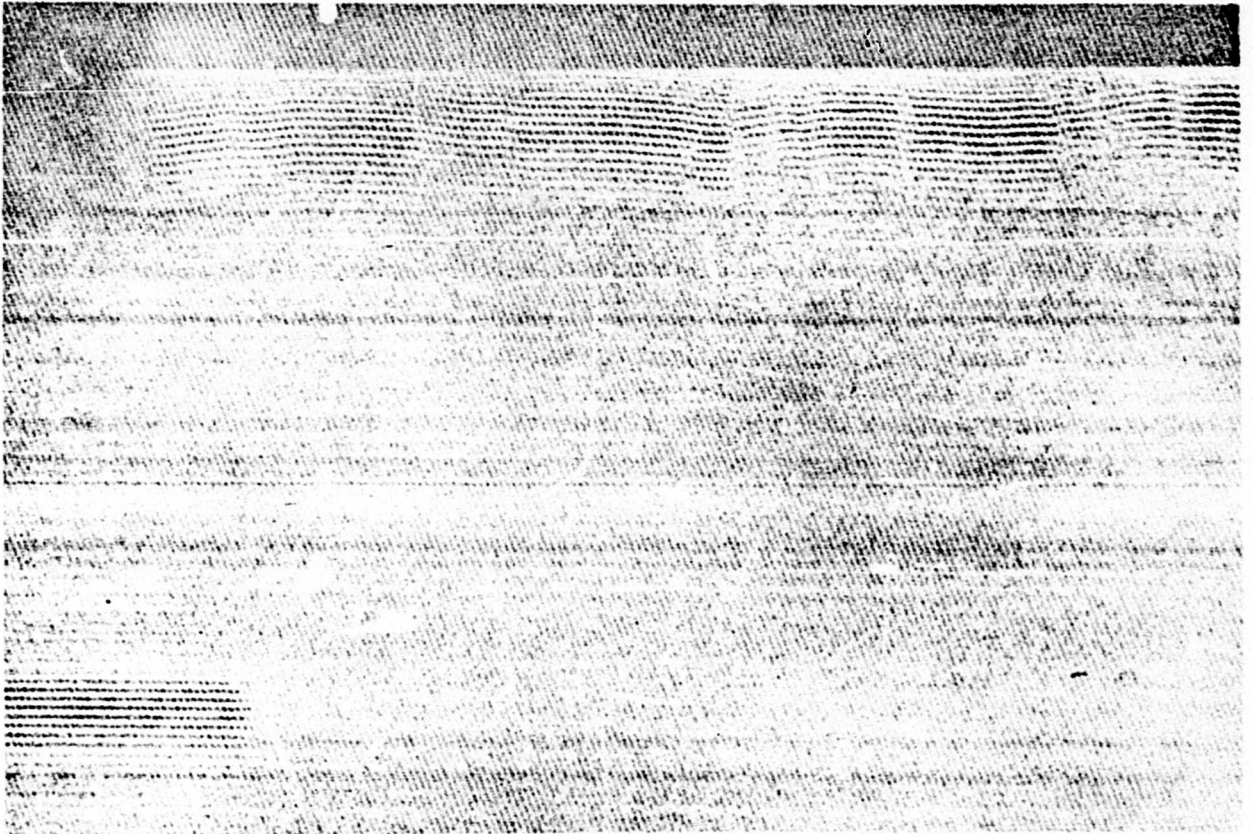


Figure 2. White Light Strip Interferogram of Flow Field at Shock Arrival with $M = 0.5$. Interval between Marks at Top is One Millisecond

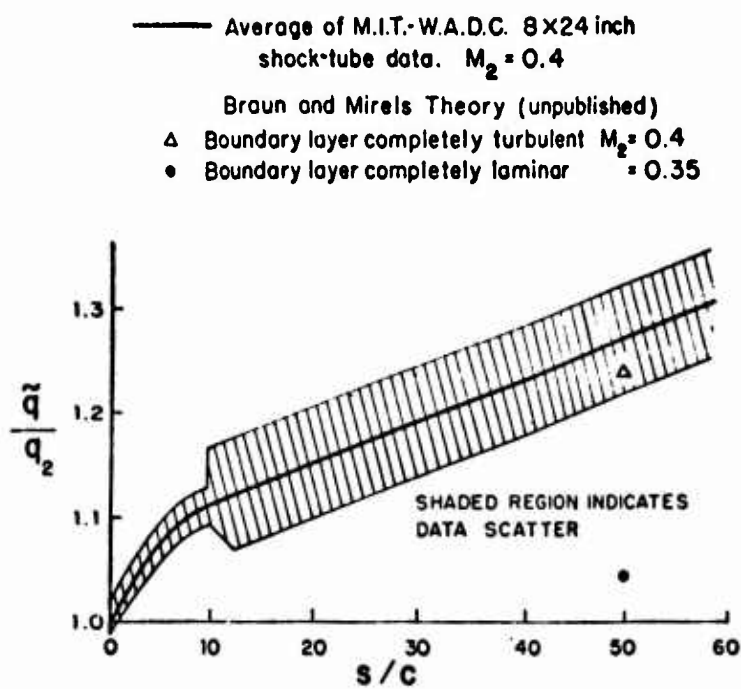


Figure 3. Freestream Dynamic Pressure Following Shock Passage. Computed from Interferometric Measurements

THE SURFACE FILM THERMOMETER: A VERSATILE SHOCK TUBE TECHNIQUE

Daniel Bershader
Lockheed Aircraft Corporation

Thermal measurements in the shock tube must, of necessity, be performed with rapid response instrumentation, preferably in the microsecond range. In recent years groups at Princeton and Lehigh, as well as several other laboratories, have employed the thin film resistance thermometer in order to measure surface temperature and heat transfer. Such films are typically several hundred atoms thick and display a resistance of the order of 100 ohms. The technology of their preparation is now well developed.

When current is supplied from a source whose impedance is high compared to that of the film, a change in film temperature produces a proportional change in potential difference across its terminals. Further, if Joule heating of the film can be neglected by comparison with the heat transfer taking place, then the latter may be determined in a straightforward manner from the time variation of film temperature.

The present discussion centers on some physical aspects of the transient thermal behavior of film thermometers and includes an application to the study of shock-induced laminar-boundary layer heat transfer.

Application of a temperature step to a system is a standard way to study its transient response. We begin with a semi-infinite slab whose surface lies in the plane $y = \text{const}$. If the temperature is abruptly changed from T_0 to T_a at time $t = 0$, then the surface heat transfer varies with

$t^{-1/2}$ according to the relation¹

$$\left. \frac{\partial T}{\partial y} \right)_{\text{surf}} = - \frac{(T_a - T_0)}{\sqrt{\pi \beta_s t}} \quad (1)$$

One can as well formulate the reverse problem² which consists of specifying a $t^{-1/2}$ type heat transfer as the forcing function. It then turns out that the surface temperature adjusts stepwise.

Consider next a finite slab of thickness δ lying on a perfect insulator. The exact solution to a temperature step applied at the free surface of the slab is given on page 84 of Reference 1, but a good approximation is obtained by equating the average rate of heat transfer into the film with its thermal energy increase rate. To do this we denote by $\bar{T}(t)$ the average

temperature of the slab at time, t . Then

$$k \frac{T_a - \bar{T}(t)}{\delta/2} = c \frac{d\bar{T}(t)}{dt} \quad (2)$$

For the initial condition $\bar{T}(0) = T_0$, the solution is

$$T_a - \bar{T}(t) = (T_a - T_0)e^{-t/\tau} \quad (3)$$

where τ is a time constant given by

$$\tau = \frac{\delta C}{2k} = \frac{RC}{2}$$

if the thermal resistance, R , be so defined. For a gold film 2 micro-inches thick, τ is about 10^{-11} seconds. In other words, in 10^{-11} seconds, the slab's (film would be a more appropriate word here) average temperature has $1/e$ of the total applied step yet to accomplish. Through an obvious rearrangement of the exponent in Eq. 3, the state of affairs just described can be said to apply when the diffusion depth $\sqrt{\beta_f t}$ equals the film thickness δ .

The time constant discussed above does not correctly represent the step-response for the more general case of a film (or finite slab) on a semi-infinite backing material of arbitrary thermal properties. One finds then¹ that the surface heat transfer is obtainable from

$$\left. \frac{\partial T}{\partial y} \right|_{\text{surf}} = \frac{-(T_a - T_0)}{\sqrt{\pi \beta_f t}} \left\{ 1 + 2 \sum_{n=1}^{\infty} \left(\frac{\Omega - 1}{\Omega + 1} \right)^n \cdot e^{-\frac{n^2 \delta^2}{\beta_f t}} \right\} \quad (4)$$

A few special cases of Eq. 4 are pertinent. Firstly, if $\Omega = 0$, the resultant expression applies to a film on a perfect insulator as discussed above. Secondly, we note that the above equation corresponds to Eq. 1 for times $t \ll \tau$. This is reasonable since the film would appear as a semi-infinite slab until the thermal diffusion penetrated to the interface.

Thirdly, it is evident that for very long times the exponentials in Eq. 4 approach unity. The series may then be summed to give

$$\left. \frac{\partial T}{\partial y} \right|_{f, \text{surf}} = - \frac{\Omega (T_a - T_0)}{\sqrt{\pi \beta_f t}} \quad (4a)$$

For sufficiently long times it is evident (see next paragraph) that the heat transfer to the film is being transmitted to the backing with very little further increase in film temperature. Thus,

$$k \frac{\partial T}{\partial y} \Big|_{f, \text{surf}} = k \frac{\partial T}{\partial y} \Big|_{f, \text{int}} = k \frac{\partial T}{\partial y} \Big|_{b, \text{int}}$$

and Eq. 4a may be rewritten as follows

$$\frac{\partial T}{\partial y} \Big|_{b, \text{int}} = \frac{k_f}{k_b} \frac{\partial T}{\partial y} \Big|_{f, \text{surf}} = - \frac{(T_a - T_o)}{\sqrt{\pi \beta_b t}} \quad (4b)$$

Equation 4b is an exact duplicate of Eq. 1 for the step-response of a semi-infinite slab made of the backing material. This is the desired situation in which the film plays a negligible role in the heat transfer, but behaves as a surface thermometer by recording the true surface temperature of its backing material. It is important to note, however, that the backing material is normally some insulator such as glass, Lucite or quartz, with thermal properties considerably different than, say, the metal wall of a shock tube. For this reason the surface heat transfer for a given applied temperature, or conversely and more important, the observed temperature change for a given applied heat transfer must be corrected accordingly. If the latter is of the $t^{-1/2}$ type mentioned earlier, the observed modified temperature "step" of the surface (see subsequent discussion in this section) is inversely proportional to the quantity $\sqrt{k \rho c_p}$. A film deposited on a cellulose tape backing will, for example, show a temperature rise approximately 50 times that taking place at an adjacent steel surface. Indeed, such "amplification" proves to be a welcome factor for the experimentalist.

Residual ambiguity in the above discussion centers in the terms "very long times" and "sufficiently long times". To resolve these matters, we inquire first for the film-backing interface temperature as a function of time following application of a temperature step to the film's exposed surface. From page 263, we have

$$T_{\text{int}} - T_o = \frac{2(T_a - T_o)}{n+1} \sum_{n=0}^{\infty} \left(\frac{n-1}{n+1} \right)^n \operatorname{erfc} \frac{(2n+1)\delta}{2\sqrt{\beta_f t}} \quad (5)$$

It turns out that a gold film with $\delta = 500\text{\AA}$ ($\tau = 1.2 \times 10^{-11}$ sec) placed on a cellulose tape backing displays an interface temperature rise equal to 89% of the applied step $T_a - T_o$ in a time $2\tau (=RC)$. Thus, the average temperature of the film rises to considerably over 90% of the applied temperature step in this negligible period of time. This is generally consistent with the result of the more simplified calculation resulting in Eq. 3. Further

calculations, however, would show a longer asymptotic tail on the temperature rise curve for the case of the arbitrary backing material, reflecting the heat transfer across the interface.

Again, for purposes of the application discussed in the next section, there is more immediate interest in the surface heat transfer as a forcing function rather than the temperature. Neglecting thermal resistance of the film, Bromberg² has obtained a solution for a $t^{-1/2}$ type heat transfer into a small thermal capacitance which, in turn, rests on a backing material of arbitrary thermal properties. The energy transfer is expressed by

$$\dot{q}_{f,surf} = C_f \frac{dT}{dt} + \dot{q}_{b,int} \quad (6)$$

His result reveals a characteristic time parameter for the asymptotic rise in question given by

$$\tau^* = \frac{C_f^2}{(k\rho c_p)_b} \quad (7)$$

The time response, $T(t)$, of the film is of the "inertial" type with a steep rise in the beginning, followed by a highly tapered curve. It is found that 57% of the asymptotic rise takes place in a time $t = \tau^*$, 82% for $t = 9\tau^*$, and 94% for $t = 100\tau^*$. For the gold - "Scotch" tape combination of our previous example, $\tau^* = 0.27\mu\text{seconds}$. The total rise, incidentally, is identical with that represented by Eq. 1 in which the backing material plays the role of the slab.

By comparing the above result with the earlier discussion of the semi-infinite slab, we see the effect of the film on the transient response. The reversibility of forcing functions and effects that obtains between a surface temperature step and a $t^{-1/2}$ surface heat transfer for the semi-infinite slab no longer strictly holds for the film and backing combination, as both Eq. 4 and the Bromberg calculation show. However, outside the time resolution represented by, say, $100\tau^*$, one does have an effective step-temperature reaction to a $t^{-1/2}$ surface heat input.

Recent experiments^{3,4} have shown that the temperature rise observed when a travelling wave passes over a film thermometer located on the side wall of a shock tube is essentially stepwise in nature*. This response, as we have seen, implies a surface heat input varying with $t^{-1/2}$. Examination of the laminar-boundary layer formed by the flow following the wave confirms this implication. The layer in question is a quasi-steady type since its structure is time-independent when viewed from a frame moving with the

* Figure 1 is an oscillogram demonstrating the rise.

shock wave. There are several similarities between this layer and the steady state boundary layer formed, say, on a flat plate in a wind tunnel flow. In particular, the shock-generated layer displays a heat transfer rate varying with the inverse square root of distance from the shock wave. Since the shock itself is assumed to move at uniform velocity, distance from shock is proportional to time to an observer in the laboratory reference frame. Thus

$$d_{\text{surf}} \sim \frac{1}{\sqrt{x}} \sim \frac{1}{\sqrt{t}}$$

The thin film thermometer provides two bits of information when applied to the present problem. Firstly, it gives a direct check on the wall temperature rise, providing the wall temperature boundary condition required for solution of the energy equation and subsequent comparison between theory and experiment. Secondly, one can deduce from the measured temperature step the magnitude of the heat transfer, leading to a numerical determination of the parametric constant for the process.

In the experiments described in Reference 3, the shock Mach number was about 2.5 and the observed temperature rise was 2°C for the gold-cellulose tape film assembly, corresponding to around 0.04°C for the rise at the steel wall. Clearly, then, one could use a constant temperature wall approximation for solution of the boundary layer equations. Combination of the boundary layer heat transfer expression with Eq. 1 yields the following expression³ for the desired parametric heat transfer-skin friction constant L_w (please refer to list of symbols).

$$L_w = \frac{2\sigma \Delta T}{i_{*,1}^{(st)} - i_{*,\text{surf}}} \sqrt{\frac{(\rho k c_p)_b}{\pi \rho_2 \mu_2 (1 - \rho_1/\rho_2)}} \quad (8)$$

Satisfactory agreement was found among values of L_w determined in this fashion, by interferometric evaluation of the boundary layer, and by theory.

By neglecting heat conduction in the solid in the direction of travel of the shock wave, we have been able to treat the present problem as one-dimensional. Justification for this approach has been given by Rott and Hartunian:⁵ with respect to the shock wave the two-dimensional heat equation reads

$$u_2 \frac{\partial T}{\partial x} = \beta \left(\frac{\partial^2 T}{\partial x^2} + \frac{\partial^2 T}{\partial y^2} \right) \quad (9)$$

In analogy with Prandtl's classical treatment of the incompressible, isothermal-boundary layer, one non-dimensionalizes the above equation such that derivatives are of equivalent order. This is done by introducing reference values x_0 and δ respectively and set

$$x^* = \frac{x}{x_0} \quad ; \quad y^* = \frac{y}{\delta}$$

Equation 9 then becomes

$$\frac{\partial T}{\partial x^*} = \beta^* \left(\frac{\partial^2 T}{\partial y^{*2}} + \left(\frac{\delta}{x_0} \right)^2 \frac{\partial^2 T}{\partial x^{*2}} \right) \quad (10)$$

where

$$\beta^* = \frac{\beta x_0}{u_2 \delta^2}$$

In line with the assumption that $\delta \ll x_0$, certainly justified for values of x larger than, say, 10 shock wave thicknesses, the second term on the right may be discarded. To show this more explicitly, we note that by adjusting the derivatives to have the same orders of magnitude, one implies from Eq. 10 that the non-dimensional diffusivity, β^* , is of unity order. This leads directly to the following estimate for δ/x_0

$$\delta/x_0 \approx \left(\frac{u_2 x_0}{\beta} \right)^{-1/2} \quad (11)$$

For a wave travelling at Mach 2.5 over a steel wall, one computes a value of $\delta/x_0 = 0.0016$ for $x_0 = 1$ inch. The only difference from the Prandtl treatment is that here we deal with the thermal diffusivity instead of the kinematic viscosity so that the quantity $\frac{u_2 x_0}{\beta}$ may be interpreted as a type of thermal Reynolds number. Because thermal diffusivities of typical solids are smaller than kinematic viscosities of typical fluids, the thermal-boundary layer approximation in the solid is, as Rott points out, better than the equivalent viscous boundary layer approximation in the fluid for this type of problem.

LIST OF SYMBOLS

Subscripts

a	applied
o	refers to reference or initial value
s	slab
surf	surface
int	interface
f	film
*	means that quantity is non-dimensionalized with respect to its value in the external stream. Thus $i_* = i/i_2$
1	upstream of shock
b	backing material
2	external stream adjacent to boundary layer

Superscripts

*	indicates non-dimensionalization, according to discussion in text
---	---

Other Symbols

x	distance parallel to wall of shock tube, measured backward from shock
y	coordinate perpendicular to wall, measured from surface
t	time
u	velocity (with <u>respect</u> to shock wave unless otherwise noted)
T	temperature
ΔT	temperature rise observed on film
k	thermal conductivity
-	average
δ	(a) thickness of film resistance thermometer (b) thickness of thermal layer in solid
C	thermal capacitance of film = $C_p \rho \delta$
τ	time constant of film = $\frac{\delta C}{2k}$
R	thermal resistance of film = δ/k
β	thermal diffusivity = $k/\rho C_p$
ρ	density
Ω	ratio of thermal constants = $\sqrt{\frac{(k\rho C_p)_b}{(k\rho C_p)_f}}$

C_p specific heat at constant pressure
 $\text{erfc } x = \frac{2}{\sqrt{\pi}} \int_x^{\infty} e^{-\xi^2} d\xi$
 \AA Angstrom unit = 4×10^{-9} inches
 \dot{q} heat flux
 τ^* time parameter for $t^{-1/2}$ type heat transfer to a film on the surface of an arbitrary backing material = $C_p^2 / (k \rho C_p)_b$
 L_w parametric constant for boundary layer viscous shear and heat transfer

$$= \left\{ \frac{4x}{\rho_2 \mu_2 (u_{\text{surf}} - u_2)^3} \right\}^{1/2} \eta$$

 μ viscosity coefficient
 η wall shearing stress
 σ Prandtl number = $\frac{\mu C_p}{k}$
 i enthalpy = $C_p T$ if C_p be assumed constant
 $i_{*,1}^{(st)}$ non-dimensional stagnation value of enthalpy with respect to laboratory frame

REFERENCES

1. Carslaw and Jaeger, Conduction of Heat in Solids, Oxford, 1947
2. Bromberg, Robert, Use of the Shock Tube Wall Boundary Layer in Heat Transfer Studies, Jet. Prop., 26, 737, 1956
3. Bershader, Daniel and Allport, John, On the Laminar Boundary Layer Induced by a Travelling Shock Wave, Princeton University Tech. Report II-22, May 1956
4. Emrich, R. and Chabai, A., Measured Wall Temperature Jump upon Shock Passage, Bull. Am. Phys. Soc., January 1956
5. Rott, N. and Hartunian, R., On the Heat Transfer to the Walls of a Shock Tube, Dept. of Aero. Eng., Cornell University, November 1955

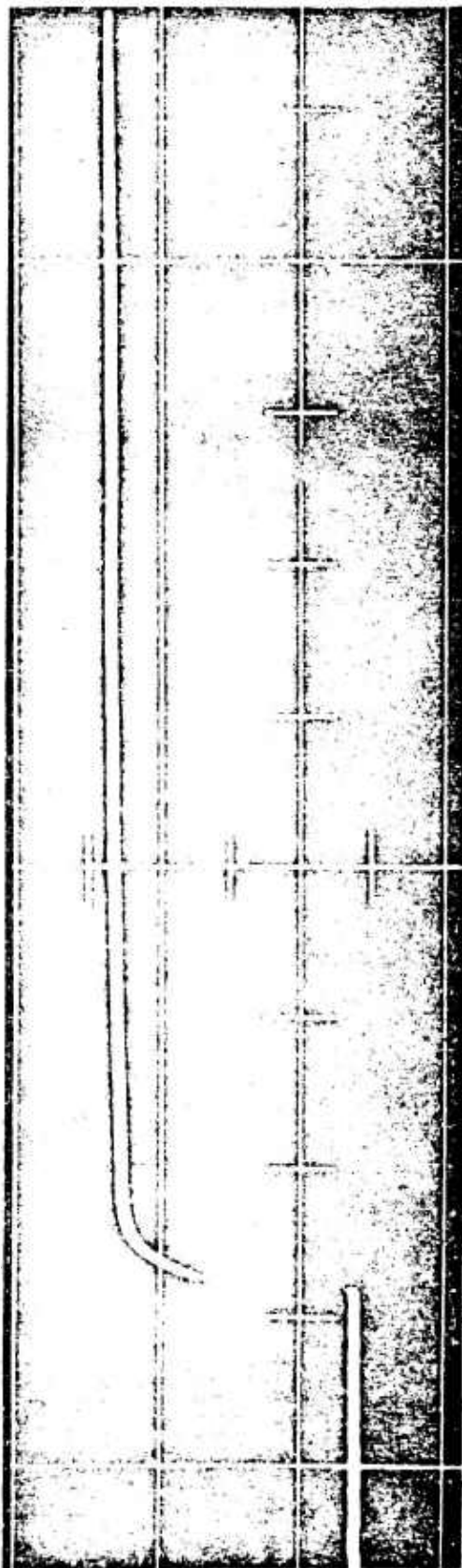


Figure 1.

SOME OBSERVATIONS OF BIFURCATED REFLECTED SHOCK WAVES

Arthur Cohen and Roger Strehlow
Ballistic Research Laboratories

The bifurcation, or splitting, of the foot of a normal shock has been studied in wind tunnels¹.

This paper will describe the effects of R_1 and M_2 on the bifurcation of a normal reflected shock traveling down a tube of uniform cross section. The investigation was undertaken to obtain information that would help interpret strip-film Schlieren pictures of shock waves reflecting from the end wall of a shock tube. Velocities measured from these Schlieren pictures can be used to furnish kinetic information about the gas behind the reflected shock.

For a given incident shock velocity, the velocity of a reflected shock depends on the enthalpy of the gas behind it. The enthalpy of an ideal, reacting gas is a function only of temperature and a reaction variable. The relation between the incident and reflected shock velocities and the reaction variable can be determined by numerical methods. By experimentally determining incident and reflected shock velocities, information concerning the reaction can be obtained^{2,3}.

Comparisons of theoretical and experimental results in non-reactive systems appear in Figure 1. The theoretical velocities were calculated⁴ using variable heat capacities and the ideal equation of state.

Figure 2 contains strip-film Schlieren and multiple-spark shadowgraph pictures taken in various gases, under similar conditions. All incident shock traces appear on the Schlieren pictures as thin straight lines. This allows incident velocities to be measured to $\pm 1\%$. The reflected shock trace in argon is thin and straight, but its appearance changes in the other gases. In nitrogen, the reflected shock line thickens and small density gradients appear around the shock. In carbon dioxide, density gradients appear near the reflected shock. The bending of the reflected shock trace indicates accelerations. In propane, large density gradients appear in front and behind the reflected shock. At higher velocities this behavior is accentuated, and accurate velocity measurements in the latter three gases become difficult. Below each strip-film is the corresponding multiple-spark shadowgraph. From these, it appears that the pressure gradients are caused by the bifurcation of the normal reflected shock and that the extent of bifurcation is greater in gases with larger heat capacities.

Conditions under which bifurcation occurs in wind tunnels has been investigated^{5,6}. Examination of the boundary layer shock wave interaction

revealed that bifurcated shocks occur more readily with laminar boundary layers than with turbulent boundary layers and that separation of the boundary layer accompanied the bifurcation process. At present a complete theoretical treatment of the boundary layer-shock wave interaction in shock tubes has not been made. A simplified dimensional analysis of this complex interaction⁷ indicates that the pressure coefficient necessary for boundary layer separation and bifurcation is proportional to the local skin friction coefficient, i.e. $Q_c \propto C_f$.

Assuming $\frac{\eta}{\eta_0} = \left(\frac{T}{T_0}\right)^\omega$, when $\omega = 1$, $C_f \times R_1^{1/2} = \text{constant}$ for laminar boundary layers and $C_f \times R_1^{1/5} = \text{constant}$ for turbulent boundary layers.

Therefore, $Q_c \propto R^{-1/\eta}$. At above room temperatures, $\omega < 1$ and the products are inversely dependent on M_s . At constant R_1 , Q_c is inversely dependent on M_s .

For shock tubes, it can be shown that R_1 , based on the distance a gas particle travels before meeting the reflected shock may be written as:

$$R_1 = 1.6 \times 10^{-4} \frac{M_s}{M_{rs}} \frac{(M_s + M_{rs})}{\eta_s} (\lambda_s - 1)^2 \frac{a_0 W}{T_0} P_0 d.$$

The pressure coefficient can be expressed as:

$$Q = \frac{\lambda_s y_s (y_{rs} - 1)}{1/2 \cdot M_s^2 (\lambda_s - 1)^2}$$

Graphs of $\frac{R_1}{P_0 d}$ and Q as a function of M_s for argon, nitrogen and carbon dioxide appear in Figure 3. The data for these graphs were taken from

Reference 2.

All pictures were taken with a 6 inch off-axis Schlieren system. The focal lengths of the two parabolic mirrors are 30 inches. The data was recorded on a 35 mm drum camera which could be rotated at a speed of 2 inches per millisecond. The Schlieren pictures were taken, using a No. 50 flash bulb as the light source, a 0.025-inch rod perpendicular to the flow as the Schlieren stop, and a 0.025-inch slit across the center of the window parallel to the flow to define the shock. The multiple-spark shadowgraphs were taken using an Edgerton, Germeshausen, Grier Stroboscope Unit. The spark duration was ~ 1.5 microsecond. The interval between pictures was ~ 100 microseconds. The sketches in Figure 2 explain the Schlieren and shadowgraph pictures.

Figure 4 is a sketch of the shock tube. It is made from .3-inch ID seamless steel pipe curved into 11-foot diameter sections. compression

section is 15 feet long. The expansion section consists of 36 feet of curved pipe and 2 feet of transition section which leads from the pipe to a 6-foot section of 3 by 1-1/2-inch "S" band wave guide. The length of the window section is 1 foot and contains two 6-inch diameter plate glass windows. The location of the back wall could be varied from 8 inches inside the window section to 2 feet past the window section. M_s was varied by varying the pressure ratio across the diaphragm. Variations in R_1 were obtained by varying the location of the back wall and by changing P_0 . Since an area reduction of 10% is encountered going from the circular to the rectangular sections, pictures were taken of gas originally in the wave guide section. Pressure probes were used for synchronization purposes.

The effects of R_1 and M_s on the appearance of the reflected shock in argon, nitrogen and carbon dioxide are shown in Figures 5, 6 and 7. The dependence of a separation distance on Q , for shocks generated by supersonic flow past concave corners, has been reported⁶. A qualitative comparison of shock tube results with the results derived from the dimensional analysis⁷ can be made by assuming that the separation distance, S (Figure 2) depends on $Q - Q_c$.

At constant M_s , Q is constant and, according to theory, Q_c decreases with increasing R_1 . Examination of the shadowgraphs in Figures 5 and 6 do not reveal any strong dependence of S on R_1 . Examination of Figure 7 indicates that in carbon dioxide, contrary to theory, S decreases with increasing R_1 .

Figures 5, 6 and 7 indicate that at constant R_1 , S and therefore $Q - Q_c$ increases with increasing M_s . This implies that Q_c is inversely dependent on M_s , since Q decreases with increasing M_s (Figure 3). This implication is in agreement with the dimensional analysis theory.

The effect of M_s and the lack of R_1 effect on the separation process has been noted in wind tunnel experiments^{8,11}. The inverse dependence of S on R_1 has also been noted^{5,8} and attributed to a transition from a laminar to a turbulent boundary layer.

Some characteristics of the boundary layer behind the incident shock appear in Figures 8 and 9. Multiple-flash Schlieren pictures in propane taken with the stroboscope unit, using a knife edge parallel to the flow as the Schlieren stop, appear in Figure 8. Strong horizontal density gradients appear at the reflected shock due to the boundary layer-shock wave interaction. The presence of the incident shock is manifested by the appearance of the boundary layer in the third frame of the picture on the left. Turbulent motion occurs at the floor of the tube behind the reflected shock.

Figure 9 contains oscilloscope traces of pulses from a thin gold foil, mounted flush with the top wall in the window section of the tube. The foil acts as a temperature gage^{9,10} and signals the passage of incident and reflected shocks. The scope was triggered by the incident shock. The initial rise in voltage is due to the boundary layer traveling behind the incident shock and the large rise in voltage is due to the passing of the reflected shock. The rise time of the latter pulse is much longer in propane than in argon, which suggests that the thickness of the reflected shock at the

boundary layer is greater in propane.

The effects of R_1 and M_s on the bifurcation of a normal reflected shock traveling down a shock tube appeared similar to those found in wind tunnel experiments. The extent of bifurcation was found to be greater in gases with larger heat capacities. The dependence of the reflected shock appearance on R_1 and M_s was compared to results predicted by a simplified dimensional analysis of the shock wave - boundary layer interaction. The shock tube results agreed with the predicted M_s effect but disagreed with the predicted R_1 effect. The initial results of a gold foil technique indicates its usefulness for investigating boundary layer phenomena. However, a theoretical analysis of heat transfer effects in boundary layer flow is necessary before a correlation of the experimental results with boundary layer flow can be made with this technique.

SYMBOLS

R_1	$= \frac{ul}{\rho} = \text{Reynolds number}$
u	$= \text{gas velocity, cm/sec}$
l	$= \text{distance gas travels before meeting reflected shock, cm}$
	$= \text{viscosity coefficient, poise}$
ρ	$= \text{density, gm/cm}^3$
T	$= \text{temperature, degrees Kelvin}$
C_f	$= \text{local skin-friction coefficient}$
Q	$= \frac{P_{rs} - P_s}{1/2 \rho u^2} = \text{pressure coefficient}$
Q_c	$= \text{critical pressure coefficient}$
M	$= \text{Mach number of shock wave relative to } \alpha_0$
α	$= \text{sound velocity, cm/sec}$
P	$= \text{static pressure, cm of Hg}$
d	$= \text{distance traveled by reflected shock, cm}$
λ	$= \text{dimensionless density ratio}$
y	$= \text{dimensionless pressure ratio}$

W = molecular weight, gm/mole
γ = ratio of specific heats at constant pressure and volume

SUBSCRIPTS

o = initial conditions
s = shock conditions
r.s. = reflected shock conditions

REFERENCES

1. Fage, A. and Sargent, R. F., Shock Wave and Boundary Layer Phenomena Near a Flat Surface, Proc. Roy. Soc. (London) Ser. A, Vol. 190, No. 1020, June 1947
2. Toennies, J. P. and Greene, E. F., Dissociation Energies of Carbon Monoxide and Nitrogen from Reflected Shock Wave Studies, J. Chem. Phys., Vol. 26, No. 3, Mar 1957
3. Strehlow, R. A., A Reflected Shock Technique for Investigating Fast Chemical Reactions, Ballistic Research Laboratories, Report to be published
4. Strehlow, R. A., One-Dimensional Step Shock Wave Calculations for Ideal Gases. Ballistic Research Laboratories, Report No. 978, April 1956
5. Ackeret, J., Feldman, F., and Rott, N., Investigations of Compression Shocks and Boundary Layers in Gases Moving at High Speed. NACA TM 1113, 1947
6. Liepman, H. W., Investigations of the Interaction of Boundary Layer and Shock Waves in Transonic Flow. Final Galcit Report for Supplement Agreement No. 4 (S-4843) Contract No. W33-038 ac-1717 (11592)
7. Donaldson, Coleman duP. and Lange, R. H., Study of the Pressure Rise Across Shock Waves Required to Separate Laminar and Turbulent Boundary Layers, NACA TN 2770, 1952
8. Drougge, G., An Experimental Investigation of the Influence of Strong Adverse Pressure Gradients on Turbulent Boundary Layers at Supersonic Speeds. The Aeronautical Research Institute of Sweden Report No. 46
9. Blackman, V. H., Vibrational Relaxation in O₂ and N₂, Princeton University, Department of Physics, Technical Report II - 20
10. Bershader, D., The Surface Film Thermometer -- A Versatile Shock Tube Technique. Shock Tube Symposium, Massachusetts Institute of Technology, 1957
11. Lange, R. H., Present Status Relative to the Prediction of Shock-Induced Boundary Layer Separation, NACA TN 3056, 1954

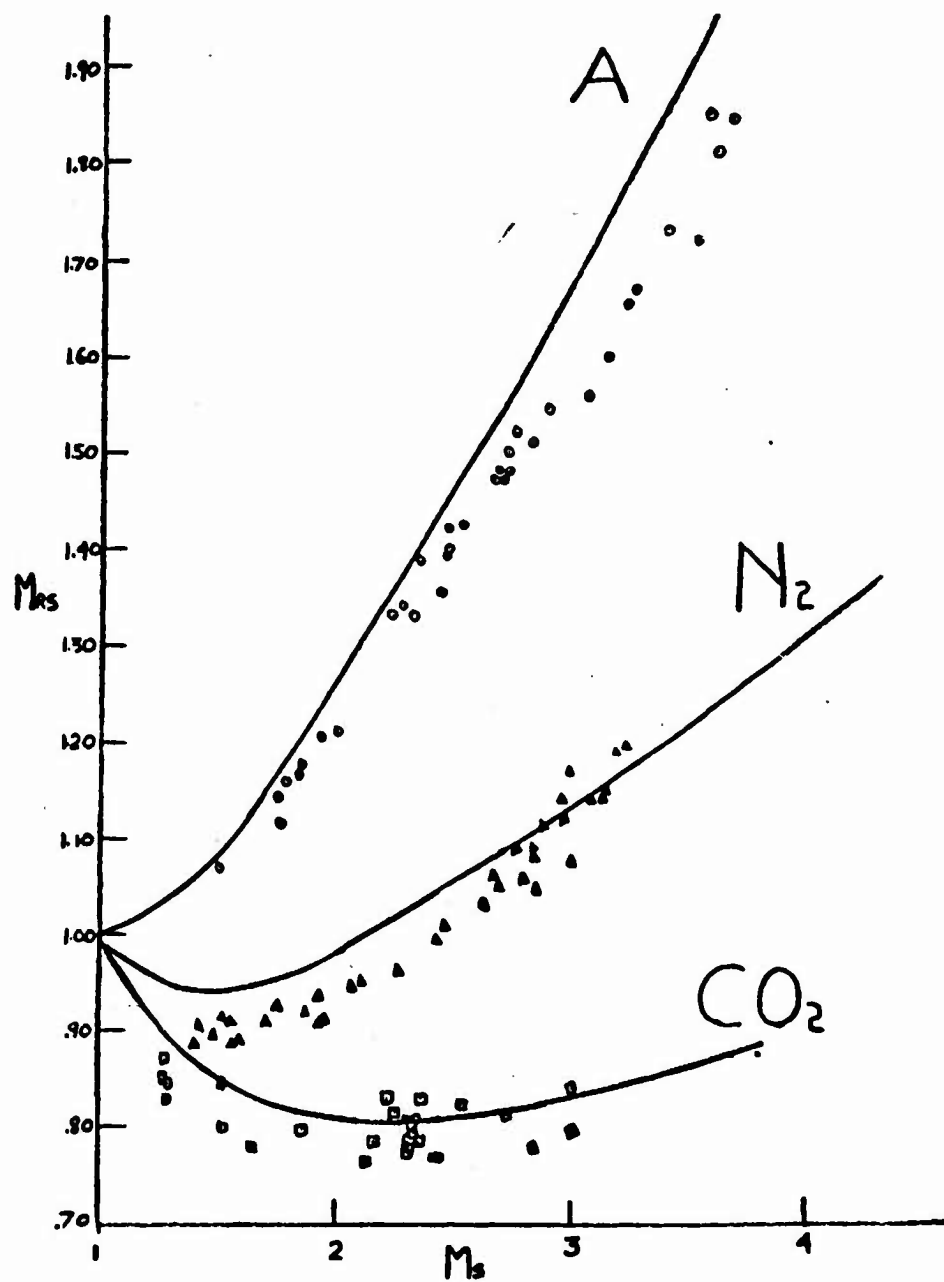
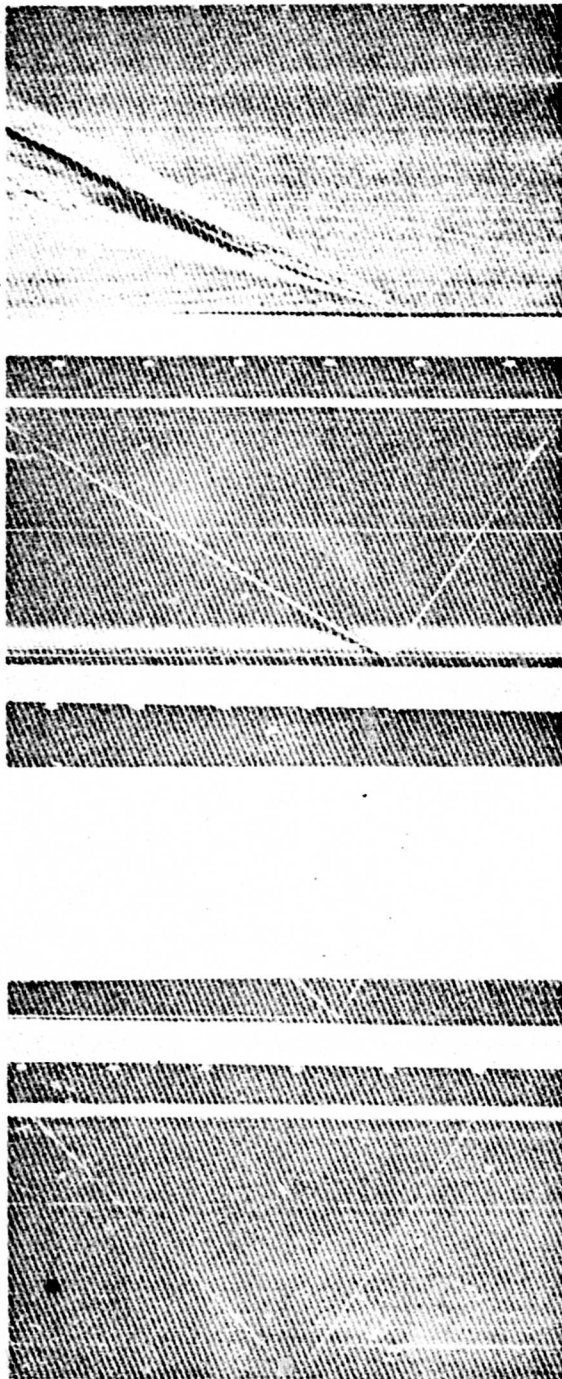


Figure 1. M_s versus M_{rs}
(Solid lines indicate calculated values)



A

N₂

CO₂

C₃H₆

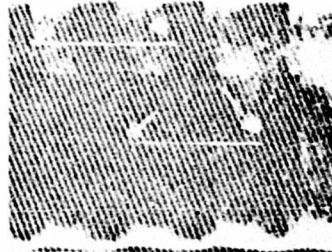
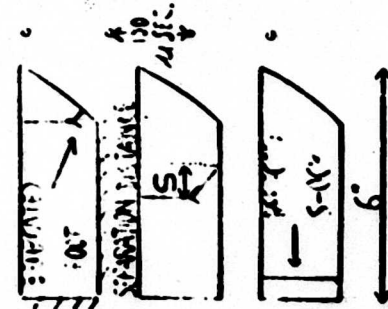


Figure 2. Schlieren and Shadowgraph Pictures in Various Gases
 Upper row - strip-film Schlieren pictures
 Lower row - multiple-spark shadowgraphs
 (Arrows indicate the foot of the reflected shock)
 $M_s = 1.9$ $P_0 = 4$

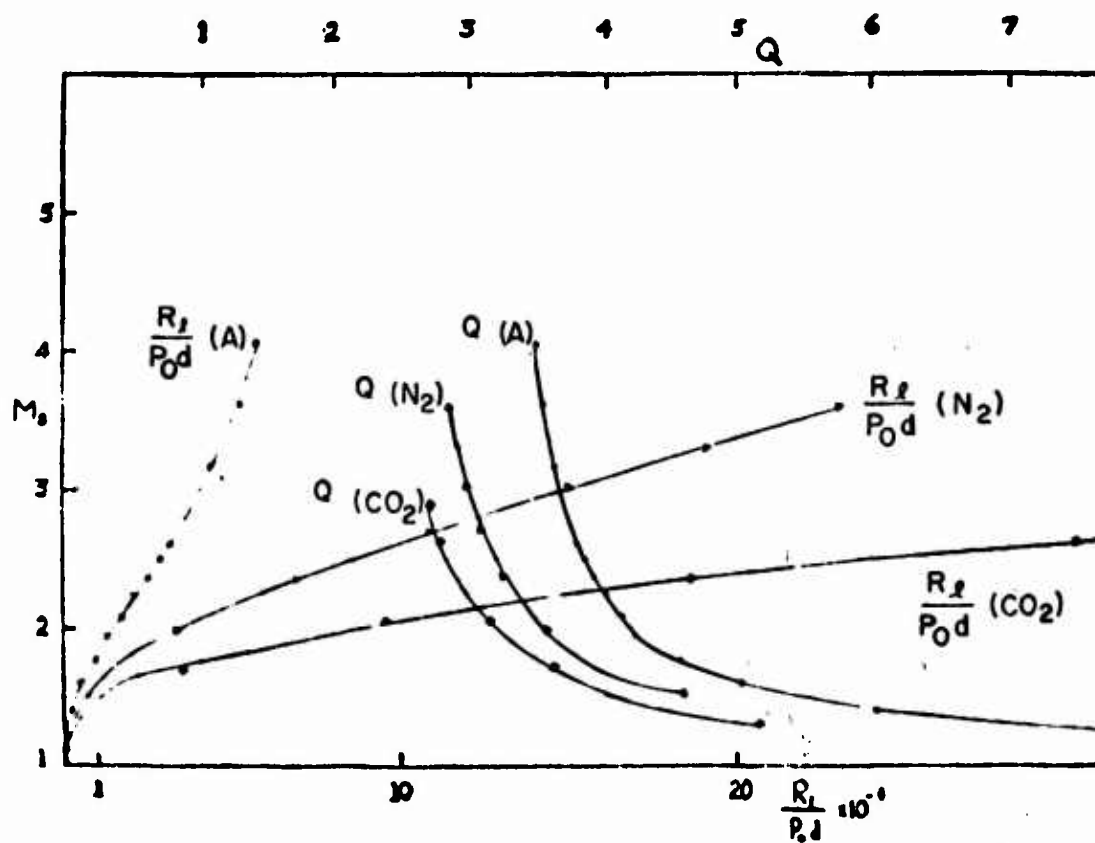


Figure 3. $\frac{R_1}{P_{0d}}$ and Q versus M_s

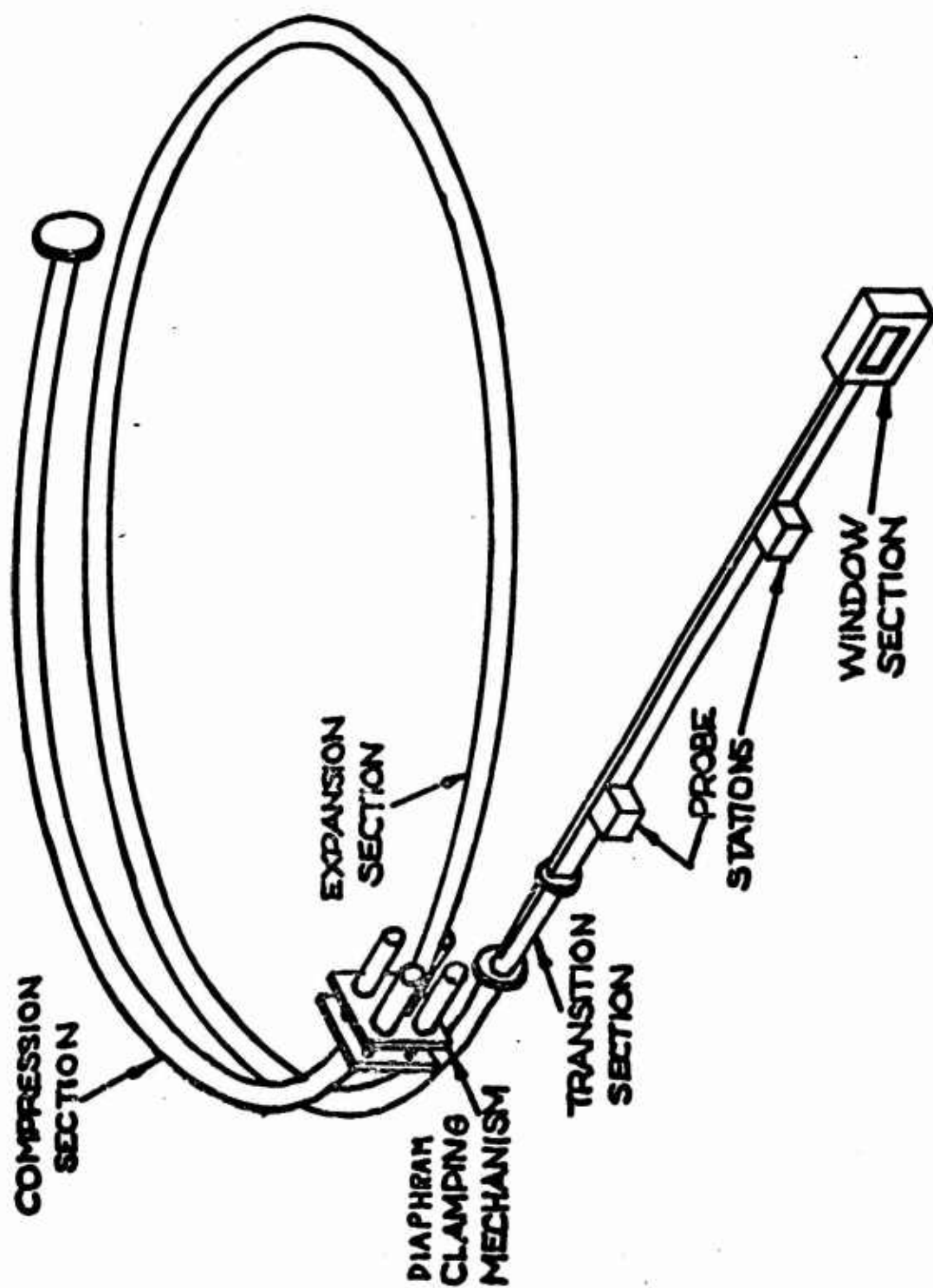
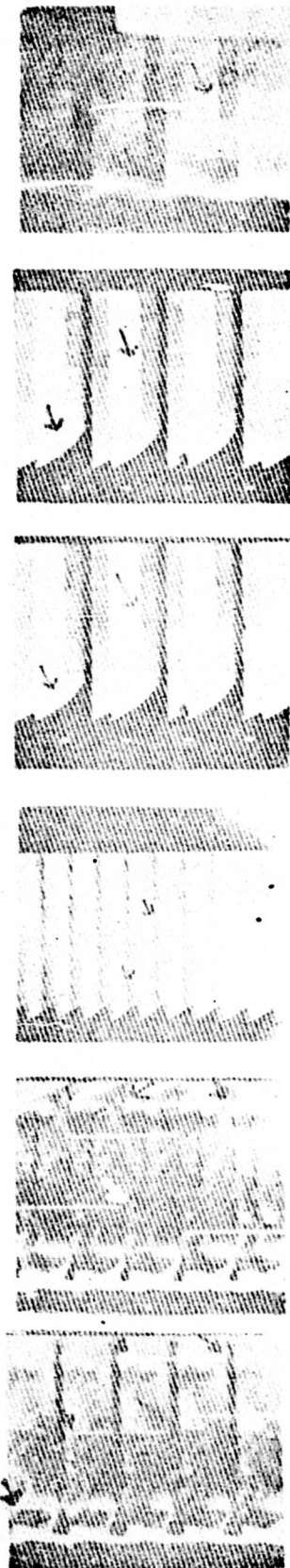


Figure 4. Shock Tube Diagram

A

 $M_\infty = 2.2$  $R_1 = 0.07$

.25

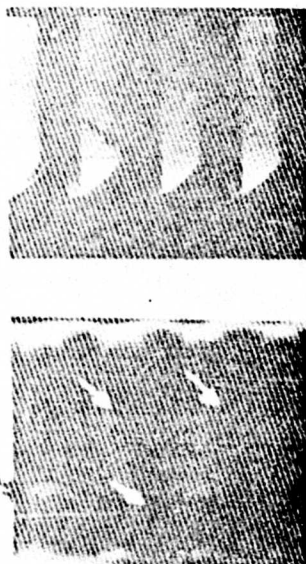
.52

1.2

1.6

6.6

B

 $R_1 = 1.3 \times 10^6$  $R_1 = 1.3 \times 10^6$ $M_\infty = 1.8$

2.6

 $M_\infty = 2.2$

4.4

Figure 5. Multiple Spark Shadowgraph Pictures in Argon

Effects of R_1 at constant M_∞ Effects of M_∞ at constant R_1

(Arrows indicate the foot of the reflected shock)

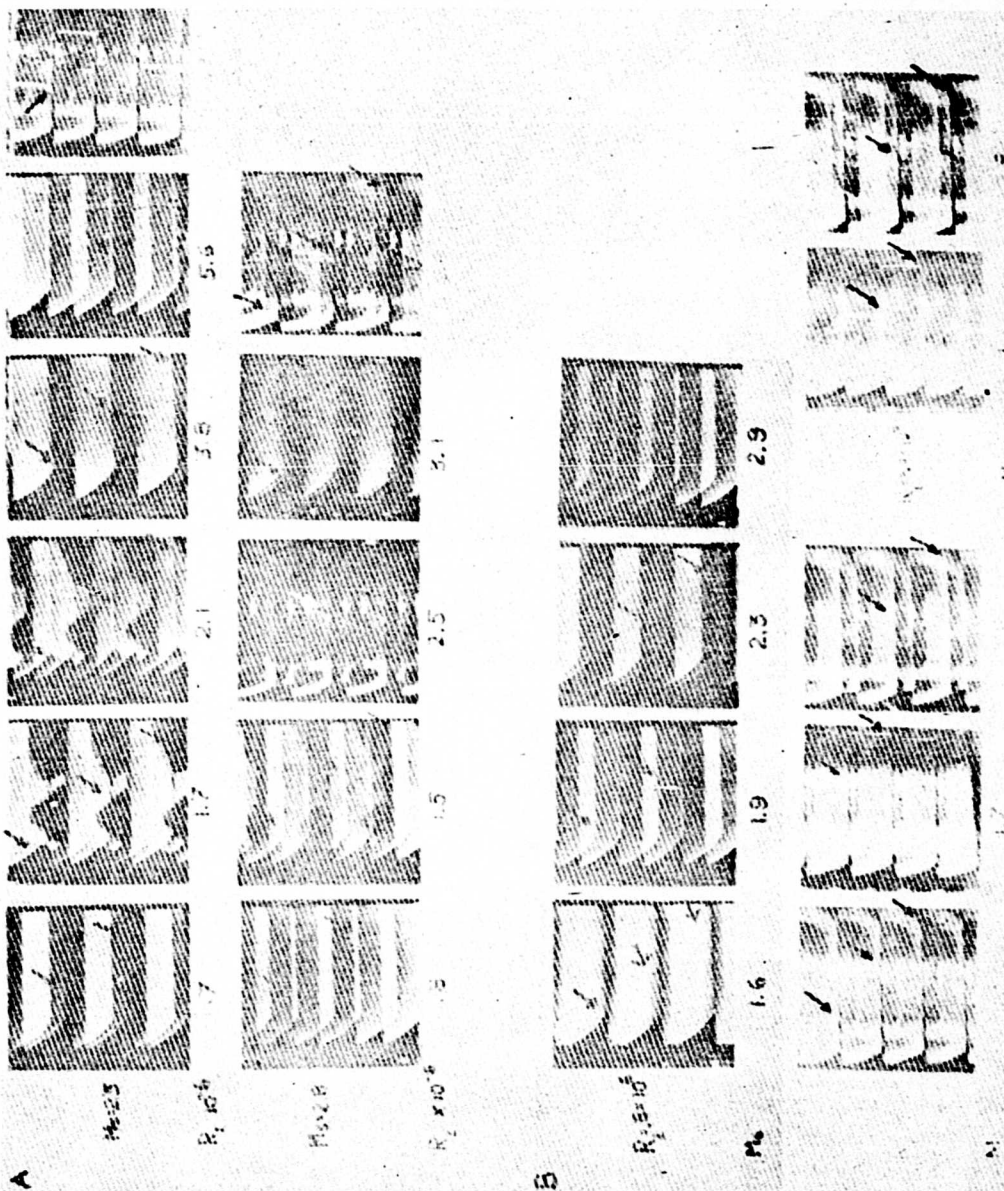
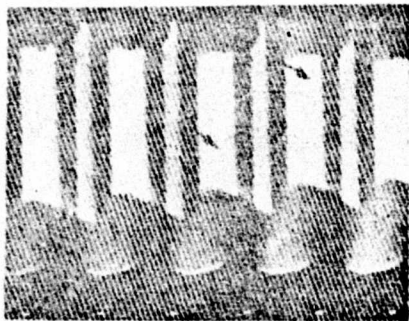


Figure 6. Multiple Spark Shadowgraph Pictures in Nitrogen

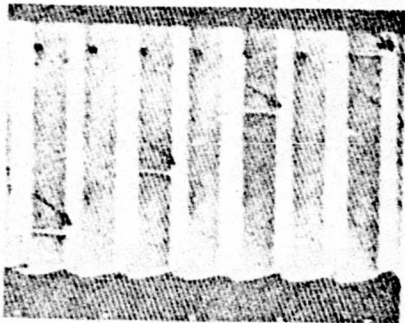
Effects of R_1 at constant M_s

Effects of M_s at constant R_1

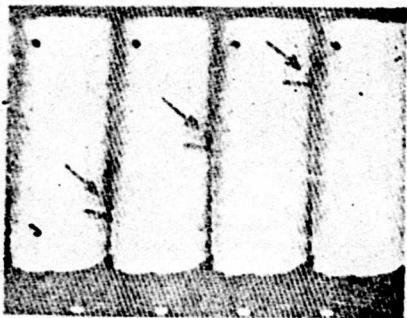
(Arrows indicate the foot of the reflected shock)



$M_S = 1.9$

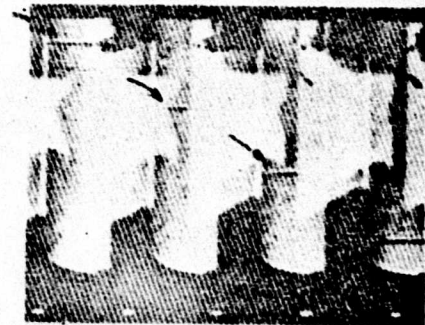


2.6



5.2

$R_1 \times 10^{-6}$ 1.3



$M_S = 1.6$

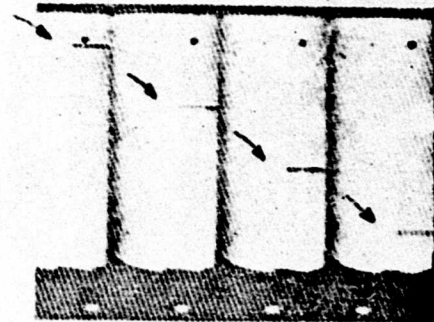
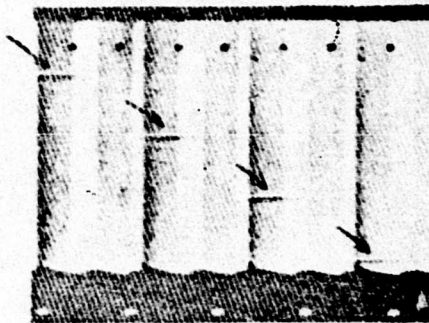


Figure 7. Multiple-Spark Shadowgraph Pictures in Carbon Dioxide
(Arrows indicate the foot of the reflected shock)

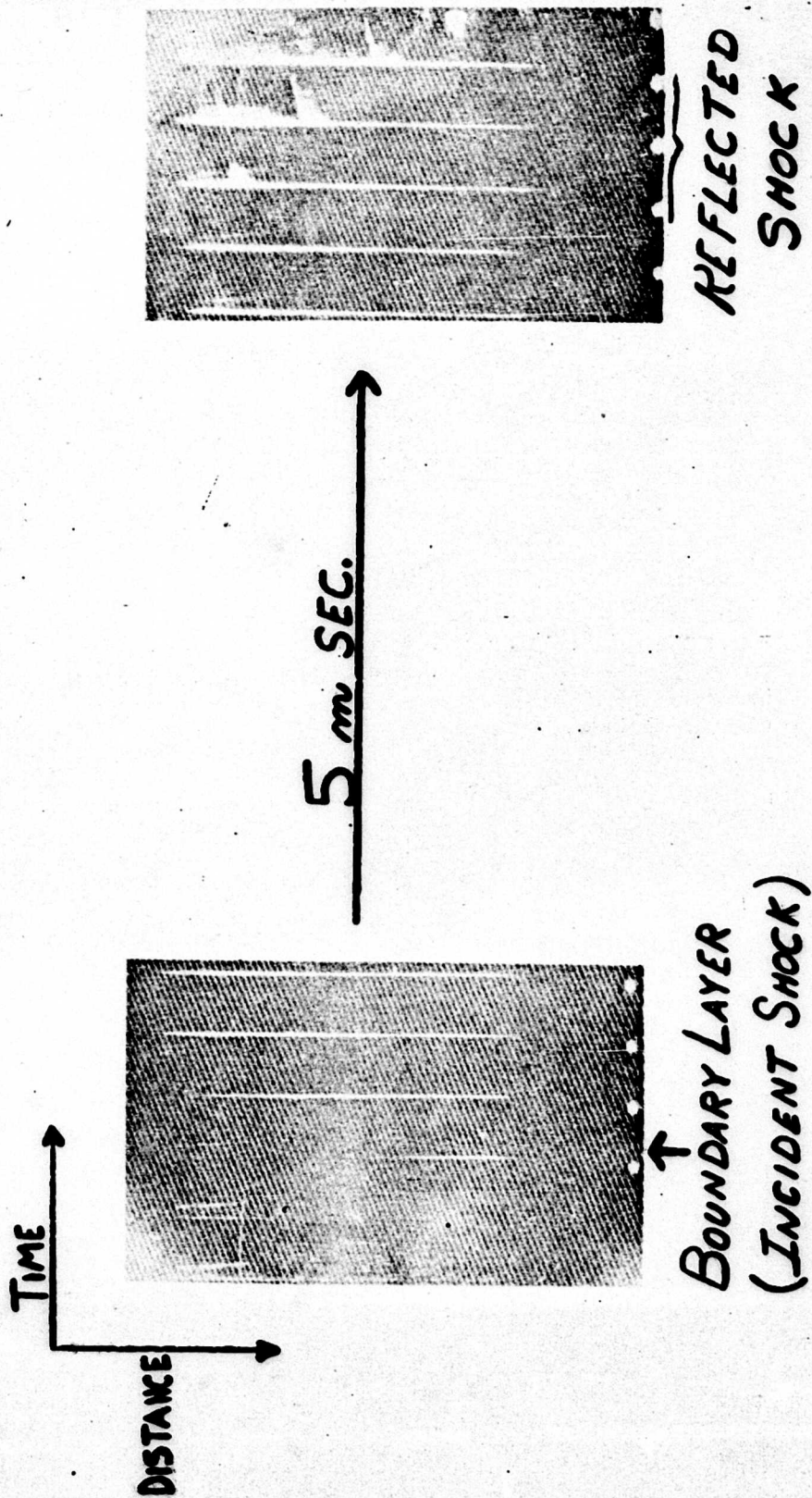
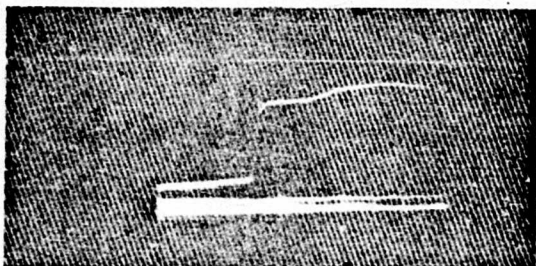
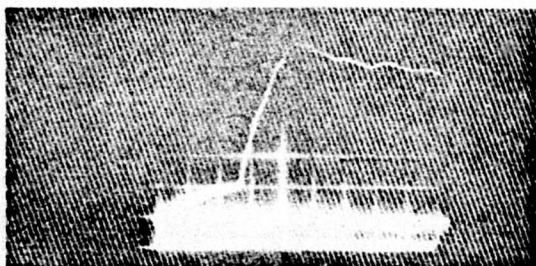


Figure 8. Multiple-Spark Schlieren Pictures of the Boundary Layer in Propane
 Left - Boundary Layer behind Incident Shock
 Right - Boundary Layer behind Reflected Shock Knife Edge Parallel to Flow



ARGON
 $M_s \sim 2$
 SWEEP
 $20 \mu\text{SEC}/\text{CM.}$



PROPANE
 $M_s = 2$
 SWEEP
 $50 \mu\text{SEC}/\text{CM}$

Figure 9. Oscilloscope Records from Surface Film Thermometer

NUMERICAL SOLUTIONS FOR THE REFLECTION
OF A COMPRESSION WAVE FROM A RIGID WALL

Theodore H. Schiffman
Armour Research Foundation

Recent observations have shown that in some instances a relatively slow pressure rise exists where a shock front is expected, i.e., the shock wave associated with blasts does not form until some distance from the explosion center.*

The purpose of this report is twofold: first, the determination of the reflected pressure for such a compression wave hitting a rigid, infinite plate, and secondly, the length of time it takes the pressure on the wall to build up to its fully reflected value.

For an 11.6-psi compression wave the reflected pressure turns out to be slightly higher than that for an equivalent shock wave and the build-up time is roughly 10% greater than the 10-millisecond rise time.

It must be emphasized that the plate was assumed infinite in extent, and if relief takes place on the wall of the actual structure, the average reflected pressure will not build up entirely to the predicted value.

S. Chandrasekhar has outlined a numerical method for determining the reflection of a blast wave from a rigid wall.¹ In this approach he utilized the method of characteristics for one-dimensional, isentropic, non-steady state gas flow. The non-linear differential equations governing this type of flow can be written in operational form as²

$$\begin{aligned} \left\{ \frac{\partial}{\partial t} + (u + c) \frac{\partial}{\partial x} \right\} \left[\frac{2}{\gamma - 1} c + u \right] &= 0 \\ \left\{ \frac{\partial}{\partial t} + (u - c) \frac{\partial}{\partial x} \right\} \left[\frac{2}{\gamma - 1} c - u \right] &= 0 \end{aligned} \quad (1)$$

* The work reported in this talk was sponsored by the Air Materiel Command.

¹ S. Chandrasekhar, "The Normal Reflection of a Blast Wave", BRL Report No. 439, 1943

² See Section 2 for meaning of symbols used in this report.

Hence, the so-called Riemann Invariants

$$R = \frac{2}{\gamma - 1} c + u = 5c + u = \text{constant along } \frac{dx}{dt} = u + c$$

and

(2)

$$S = \frac{2}{\gamma - 1} c - u = 5c - u = \text{constant along } \frac{dx}{dt} = u - c$$

If the initial conditions $R(x, t_0)$ and $S(x, t_0)$ are given at t_0 , $R(x, t)$ and $S(x, t)$ can be determined numerically. Choosing a time increment, Δt , and defining

$$\begin{aligned} \Delta x_R &= (u + c) \Delta t \\ \Delta x_S &= (u - c) \Delta t \end{aligned} \quad (3)$$

it follows from Eq. 2 that approximately

$$\begin{aligned} R(x, t) &= R(x + \Delta x_R, t + \Delta t) \\ S(x, t) &= S(x + \Delta x_S, t + \Delta t) \end{aligned} \quad (4)$$

From such iterations the Riemann invariants, R and S , can now be computed for all times, t , at a new range of distance, x .

The boundary conditions are stated at the wall, $x = 0$, for values of t

$$\begin{aligned} u(0, t) &= 0 \\ R(0, t) &= S(0, t) \end{aligned} \quad (5)$$

From Eq. 2 we may solve for u and c as a function of R and S , namely

$$\begin{aligned} c &= \frac{R + S}{10} = c_0 \left(\frac{P}{P_0} \right)^{1/7} \\ u &= \frac{R - S}{2} = 5 c_0 \left[\left(\frac{P}{P_0} \right)^{1/7} - 1 \right] \end{aligned} \quad (6)$$

Utilizing isentropic pressure-density relations, $P = K\rho^\gamma$, the side-on pressure becomes

$$P_r = P_0 \left[\frac{P}{P_0} - 1 \right] = P_0 \left[\left(\frac{c}{c_0} \right)^7 - 1 \right] = 14.7 \left[\left(\frac{c}{1130} \right)^7 - 1 \right], \text{ psi} \quad (7)$$

Table 1

ITERATION PROCEDURE FOR OBTAINING THE REFLECTION OF THE GIVEN COMPRESSION WAVE

$t(\text{sec})$	$x(\text{ft})$	$\Delta x_R(\text{ft})$	$\Delta x_S(\text{ft})$	$R(\text{ft/sec})$	$S(\text{ft/sec})$	$u(\text{ft/sec})$	$c(\text{ft/sec})$	$P(\text{psi})$	P_r or $P_{refl}(\text{psi})$
0	0	---	---	5650	5650	0	1130	14.7	0
	7.3	---	---	5650	6193	-278	1183	20.5	5.8
	17.2	---	---	5650	6628	-488	1228	26.3	11.6
0.002	0	2.26	-2.26	5860	5860	0	1170	18.7	4.0
	2.26	1.81	-2.92	5650	6040	-195	1169	18.7	4.0
	13.8	1.48	-3.43	5650	6628	-488	1228	26.3	11.6
0.004	0	2.34	-2.34	6060	6060	0	1210	23.7	9.0
	4.2	1.95	-2.73	5650	6360	-350	1200	22.7	8.0
	10.4	1.48	-3.43	5650	6628	-488	1228	26.3	11.6
0.006	0	2.42	-2.42	6260	6260	0	1250	30.5	15.8
	6.0	1.69	-3.11	5650	6620	-485	1227	26.3	11.6
	7.0	1.48	-3.43	5650	6628	-488	1228	26.3	11.6
0.008	0	2.50	-2.50	6450	6450	0	1290	36.9	22.2
	2.0	2.00	-2.80	6310	6580	-135	1289	36.7	22.0
	3.55	1.48	-3.43	6150	6628	-215	1277	34.7	20.0
	6.0	1.70	-3.43	5880	6628	-239	1278	30.7	16.0
	7.6	1.58	-3.43	5650	6628	-488	1228	26.3	11.6
0.010	0	2.58	-2.58	6610	6610	0	1322	44.1	29.4
	0.5	2.35	-3.02	6560	6628	-35	1317	44.0	29.3
	2.0	2.20	-3.10	6490	6628	-70	1312	41.6	26.9
	4.0	1.90	-3.43	6310	6628	-160	1294	38.3	23.6
	6.0	1.70	-3.43	6100	6628	-265	1273	33.5	18.8
	8.0	1.48	-3.43	5850	6628	-370	1248	30.4	15.7
	9.1	1.48	-3.43	5650	6628	-488	1228	26.3	11.6
0.012	0	2.64	-2.64	6628	6628	0	1326	45.0	30.3
	2.64	1.75	-3.16	6600	6628	-15	1324	45.0	30.3
	4.0	1.50	-3.43	6500	6628	-64	1320	44.1	29.4
	6.0	1.48	-3.43	6260	6628	-185	1289	36.8	22.1
	8.0	1.48	-3.43	6030	6628	-300	1266	32.7	18.0
	10.6	1.48	-3.43	5650	6628	-488	1228	26.3	11.6

where c is expressed in ft/sec, for standard atmospheric conditions.

Figure 1 shows the form of the given compression wave, both in the pressure-time as well as in the pressure-distance plane. This wave form, just touching the wall ($x = 0$) at $t = 0$ forms the starting point for the iteration process. It is believed that the chosen time interval

$$\Delta t = 0.002 = \frac{\text{rise time}}{5} \quad (8)$$

leads to pressure and velocity profiles of sufficient accuracy.

From Eqs. 2 to 8 an iteration table associated with Figure 2 for the Riemann invariant R and Figure 3 for the Riemann invariant S has been prepared. This iteration process is shown in Table 1. The resulting pressure and velocity profiles are shown in Figures 4 and 5, respectively. The pressure on the wall as a function of time is shown in Table 2 and Figure 6.

Table 2

PRESSURE AND SOUND VELOCITY ON WALL AS A FUNCTION OF TIME

Time, t (sec)	Sound Velocity, c (ft/sec)	Absolute Pressure, P (psi)	Overpressure, p_{refl} (psi)
0	1130	14.7	0
0.002	1170	18.7	4.0
0.004	1210	23.7	9.0
0.006	1250	30.5	15.8
0.008	1290	36.9	22.2
0.010	1322	44.1	29.4
0.012	1326	45.0	30.3
0.012	1326	45.0	30.3

We note that the maximum reflected pressure, $p_{refl} = 30.3$, is almost equal to that which would arise from a normal reflection of a flat-top shock wave having the same pressure as the flat portion of the incoming compression wave. This is not accidental. It can be shown that the reflection coefficient of a compression wave

$$\frac{P_{refl}}{P_{\sigma}(0)} = \frac{(2\xi^{1/7} - 1)^7 - 1}{\xi - 1}, \quad \xi = \frac{P_1}{P_0} \quad (9)$$

lies only slightly above that for a shock wave of the same value of ξ , which could be obtained from the compression wave by letting the rise time vanish

$$\frac{P_{refl}}{P_{\sigma}(0)} = \frac{6 + 8\xi}{6 + \xi}, \quad \xi = \frac{P_1}{P_0} = \text{shock ratio} \quad (10)$$

as given in Table 3 and Figure 7.

Table 3

REFLECTION COEFFICIENTS FOR COMPRESSION WAVES AND SHOCK WAVES

Shock Ratio or Compression-Wave Ratio	Incidence Overpressure, P_{σ} (psi)	Reflection Coefficients, P_{refl}/P_{σ}	
		Compression Wave	Shock Wave
1.00	0	2.000	2.000
1.79	11.6	2.611	2.608
2.00	14.7	2.754	2.750
3.00	29.4	3.379	3.333
4.00	44.1	3.905	3.800
5.00	58.8	4.351	4.182

Figures 4 and 5 summarize the pressure and velocity profiles, respectively, near the wall; while Figure 6 summarizes the pressure-time relationship on the wall. From Figure 4 we note that the compression wave becomes much steeper upon reflection and has a new rise distance of 9 feet. The peak

moves away from the wall at a constant rate of 2.64 ft/ Δt , while the tail moves at only 1.48 ft/ Δt ; hence a shock would form roughly at $n\Delta t$, where

$$n = \frac{9 \text{ ft}}{2.64 \text{ ft} - 1.48 \text{ ft}} \approx 8 \quad (11)$$

i.e., from the time $t = 0$, where the wave just touches the wall it becomes a shock in

$$t = t_{\text{incident}} + t_{\text{refl}} = 10 + 16 = 26 \text{ msec} \quad (12)$$

Without colliding with the obstacle, the longest time for the compression wave to turn into a shock wave would be

$$t = \frac{x_{\text{rise distance}}}{(u + c) - c} = \frac{17.2}{(1228 + 488) - (1130)} \approx 29 \text{ msec} \quad (13)$$

$p_r = 11.6$ $p_r = 0$

Thus a compression wave becomes a shock wave at roughly the same time regardless of whether or not it collides with a rigid wall.

LIST OF SYMBOLS

- c = local velocity of sound, ft/sec
- c_o = c in undisturbed region = 1130 ft/sec
- n = integer
- p_r = side-on pressure, gauge psi
- p_{refl} = reflected pressure on wall, gauge psi
- P = absolute pressure in compression wave, psi
- P_1 = absolute pressure in flat-top portion, psi
- P_o = atmospheric pressure = 14.7 psi
- R = Riemann invariant = $5c + u$, ft/sec
- S = Riemann invariant = $5c - u$, ft/sec

t = time, sec
 u = particle velocity, ft/sec, positive when fluid moves in positive x-direction
 x = distance from wall, ft
 γ = ratio of specific heat for air = 1.4
 Δt = iteration increment, sec
 $\Delta x_R = (u + c) \Delta t$, ft
 $\Delta x_g = (u - c) \Delta t$, ft
 ρ = density, slugs/in³
 $\xi = \frac{P_1}{P_0}$ for compression wave
 $\xi = \frac{P_1}{P_0}$ for shock wave (shock ratio)

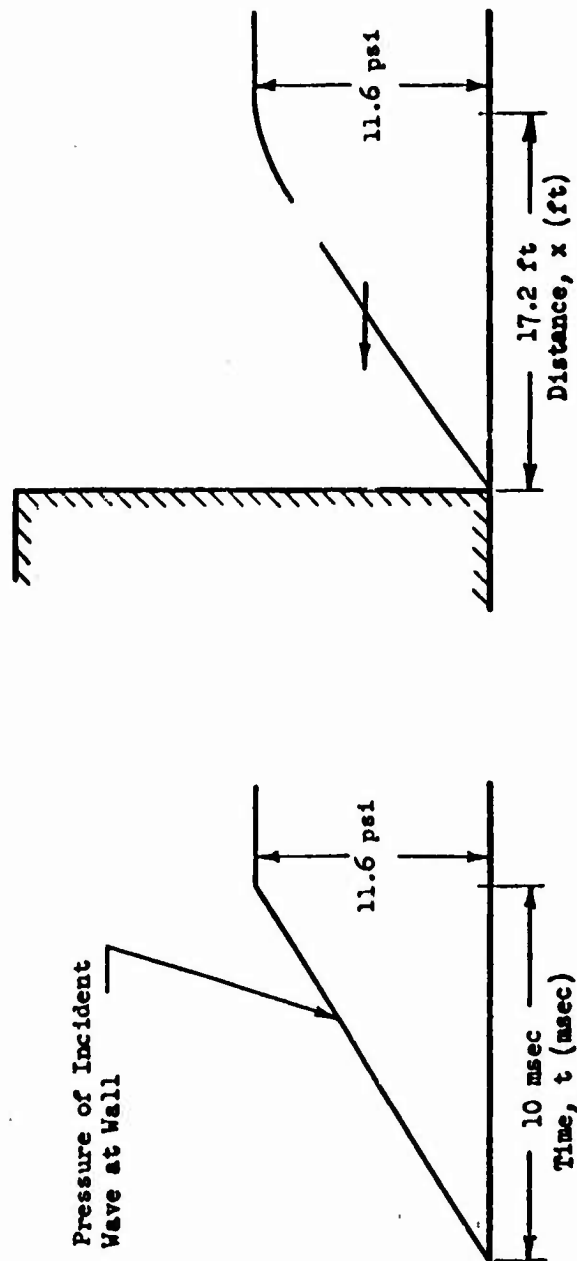


Figure 1. Form of Compression Wave Colliding with Rigid Wall

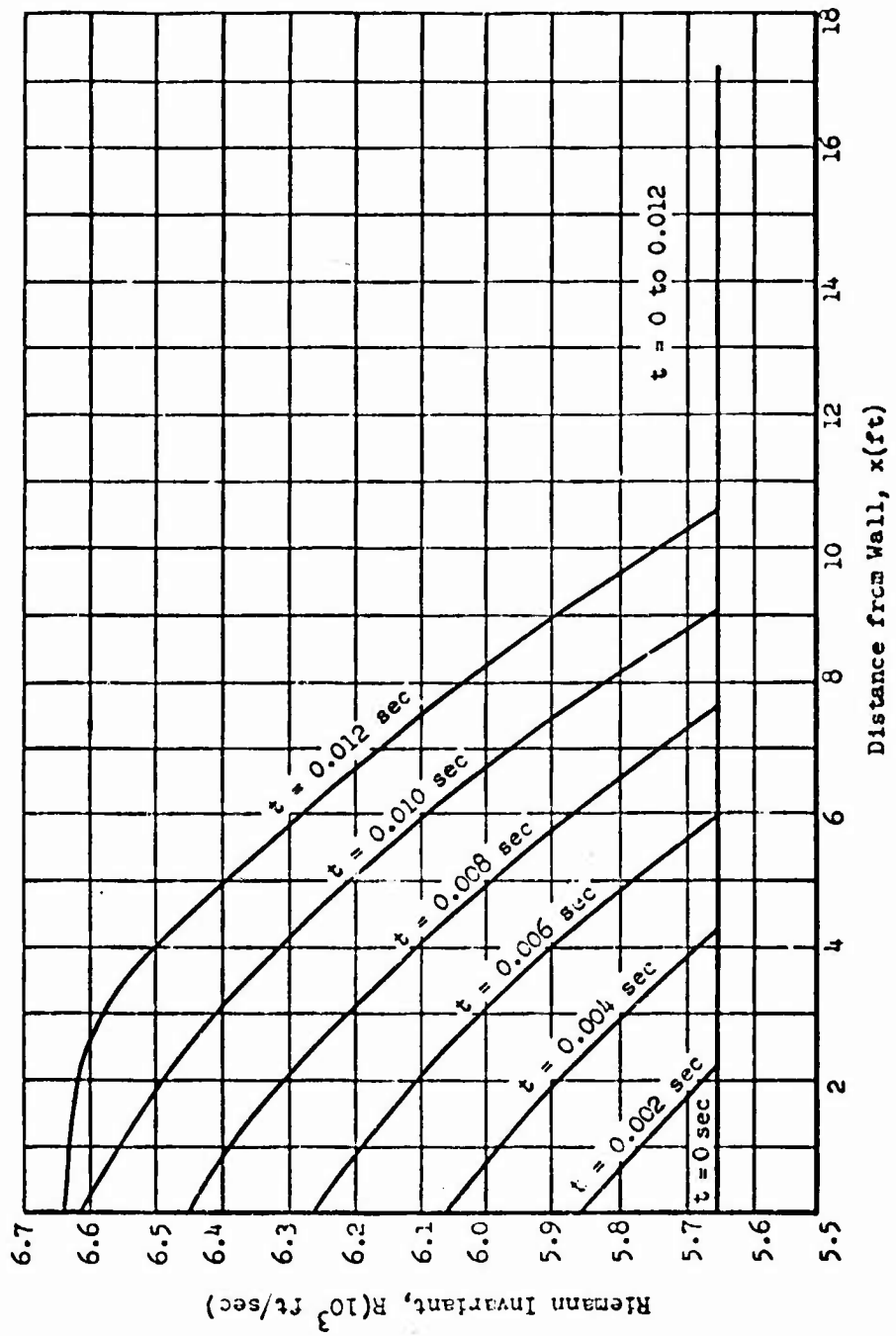


Figure 2. Riemann Invariant, R , versus Distance from Wall, x , for Various Times, t

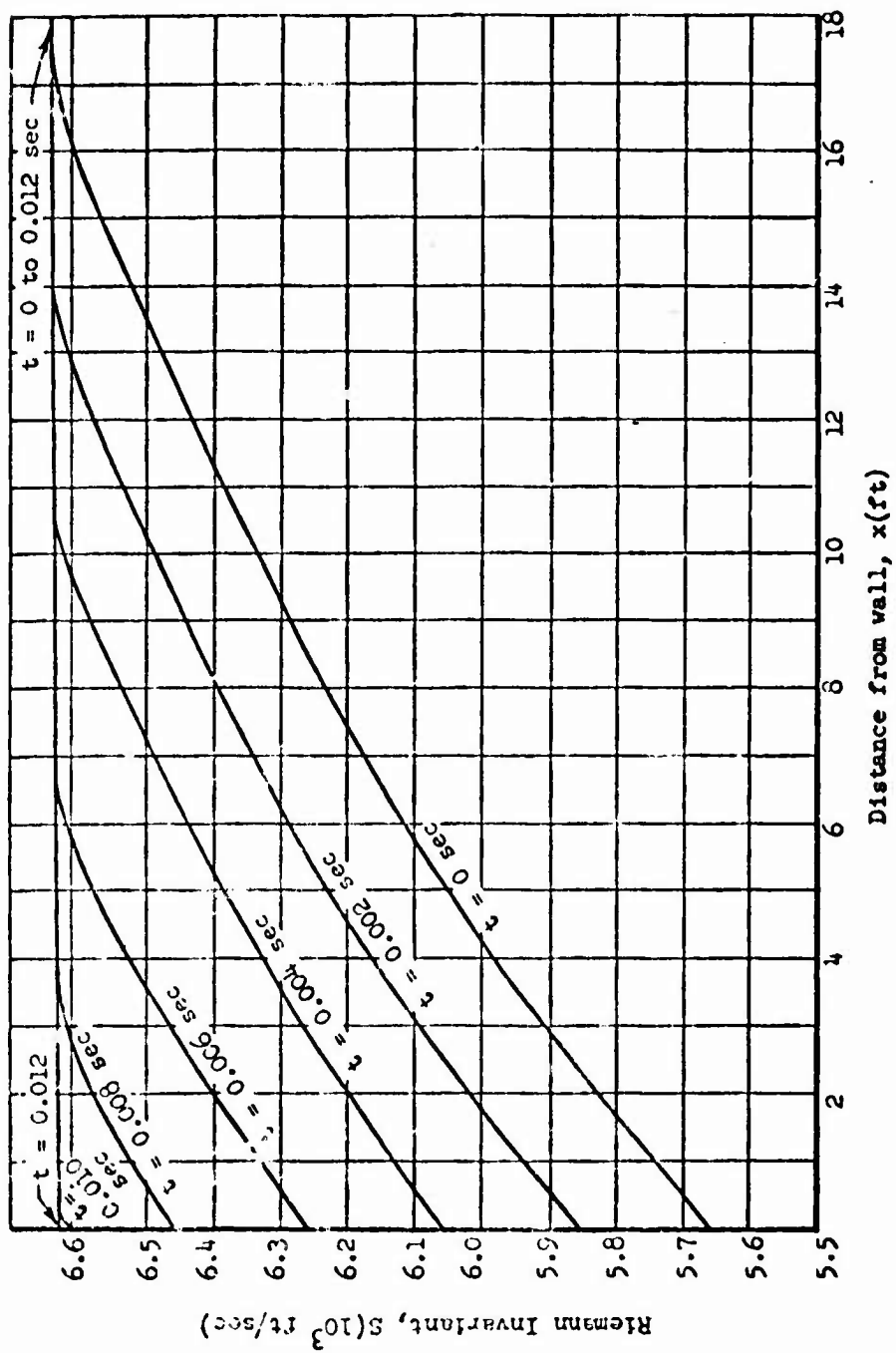


Figure 3. Riemann Invariant, S , versus Distance from Wall, x , for Various Times, t

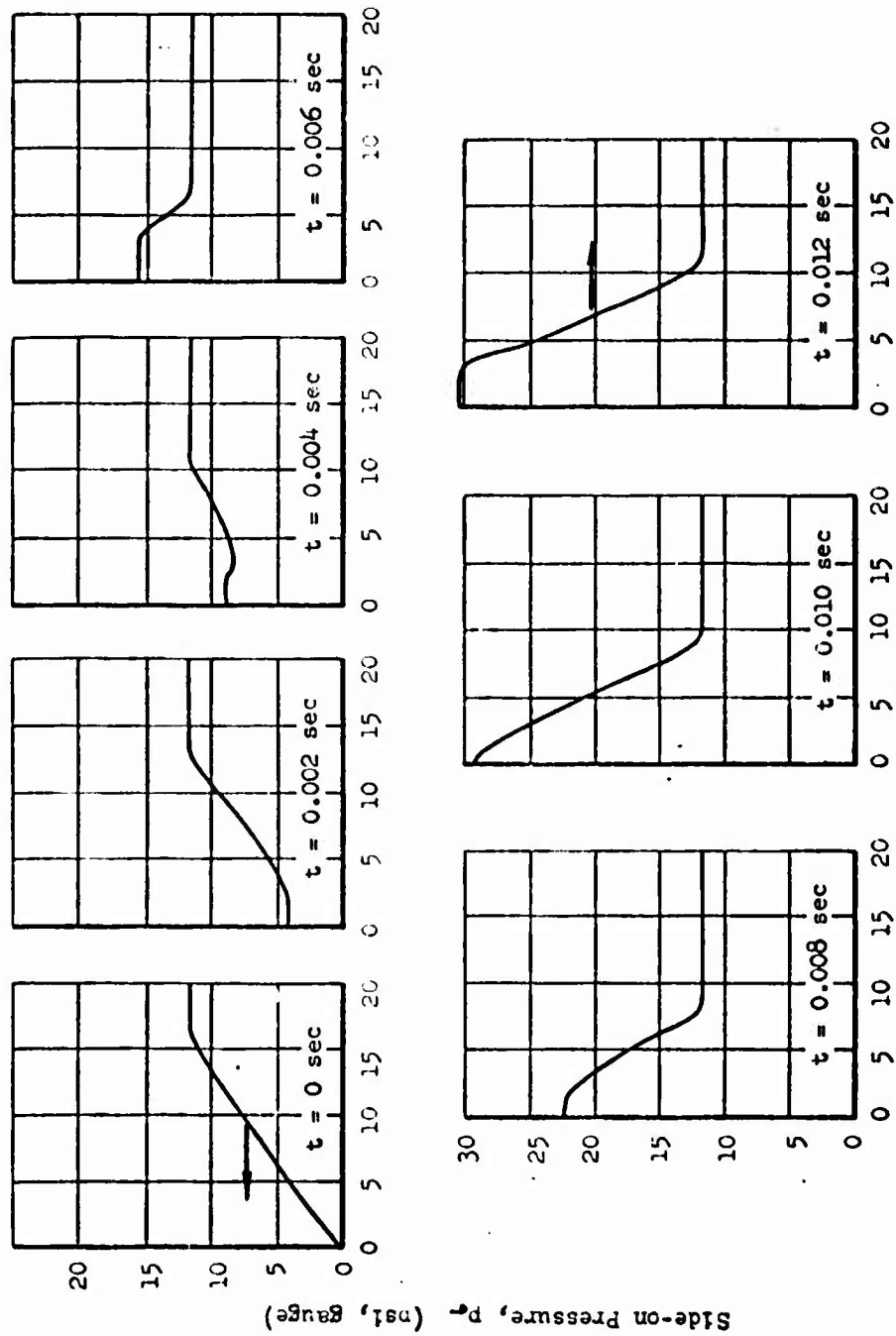


Figure 4. Pressure Profiles as a Function of the Distance from Rigid Wall

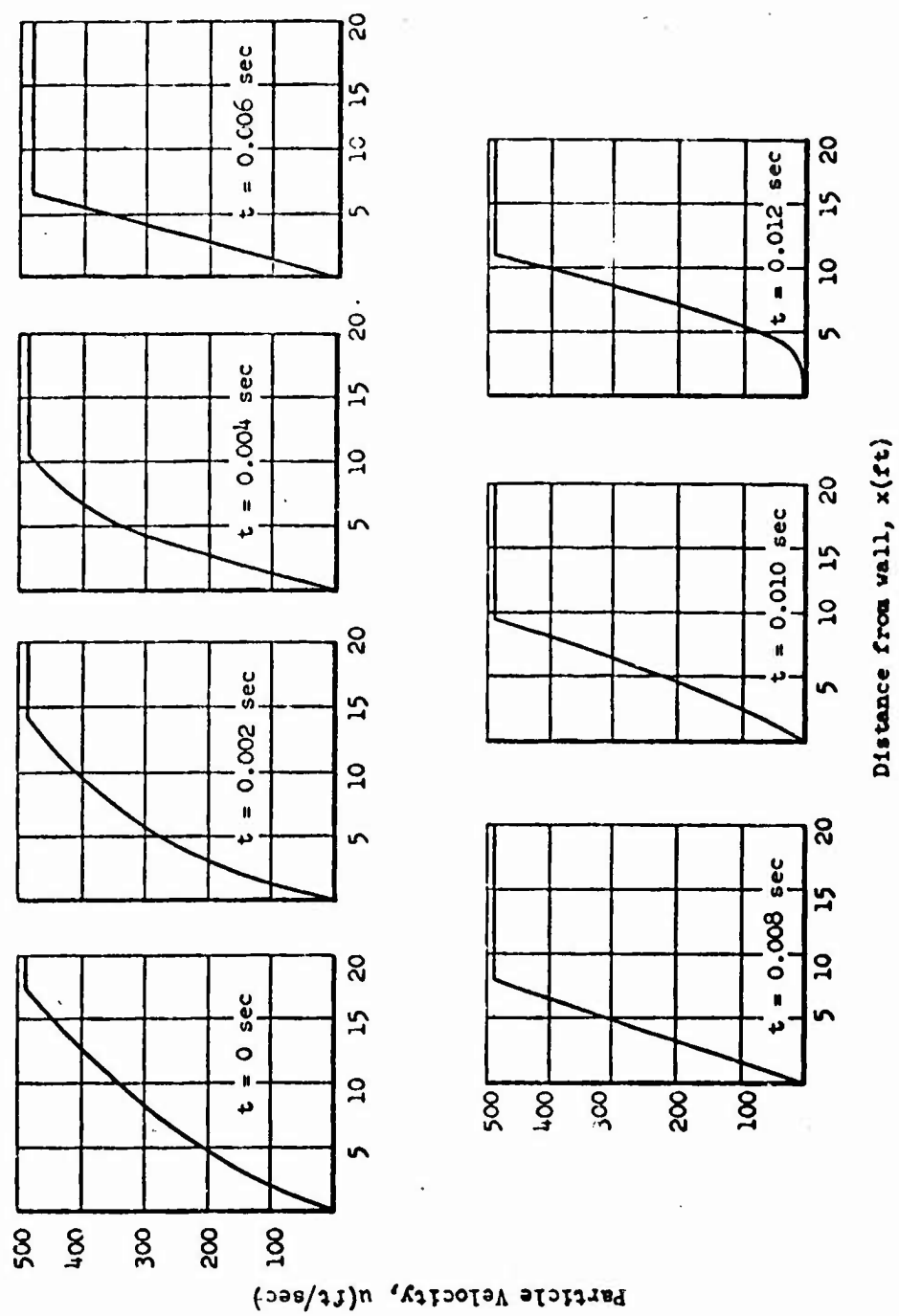


Figure 5. Particle Velocity Profiles as a Function of the Distance from Rigid Wall

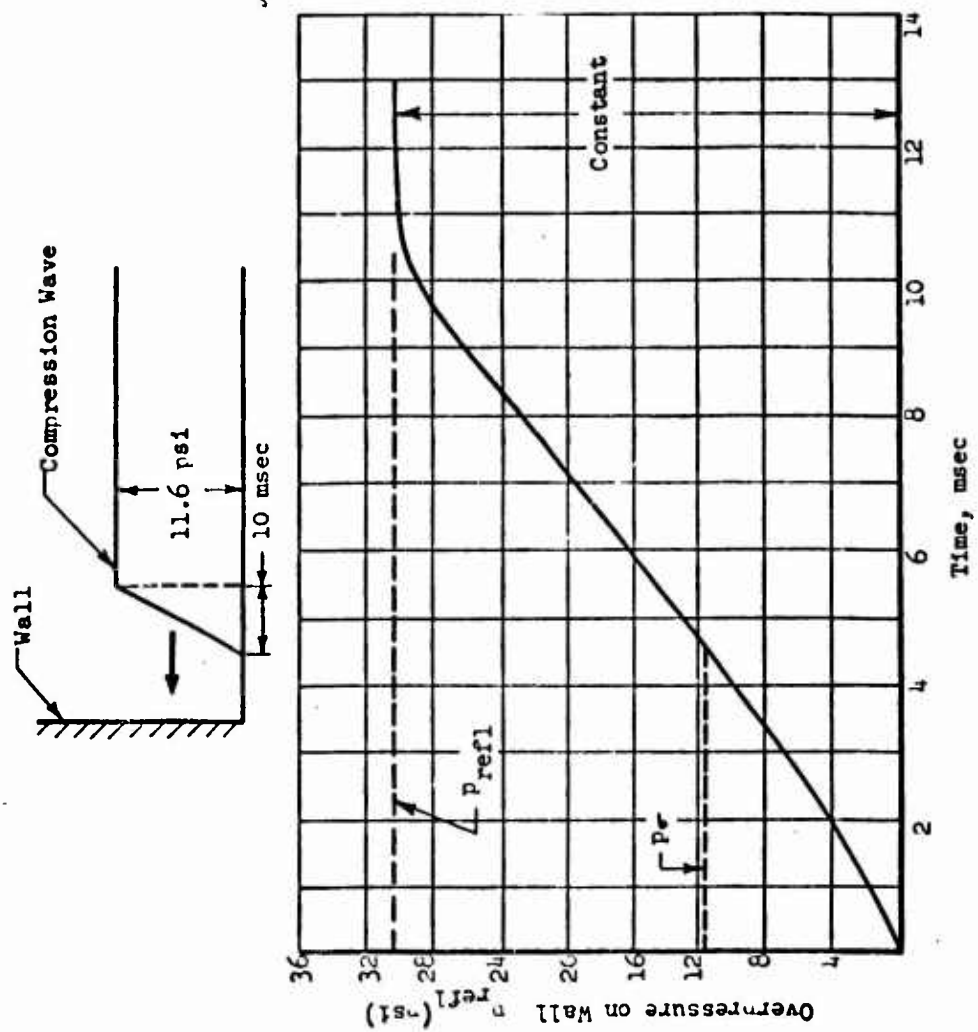


Figure 6. Pressure-Time Relationship on Wall

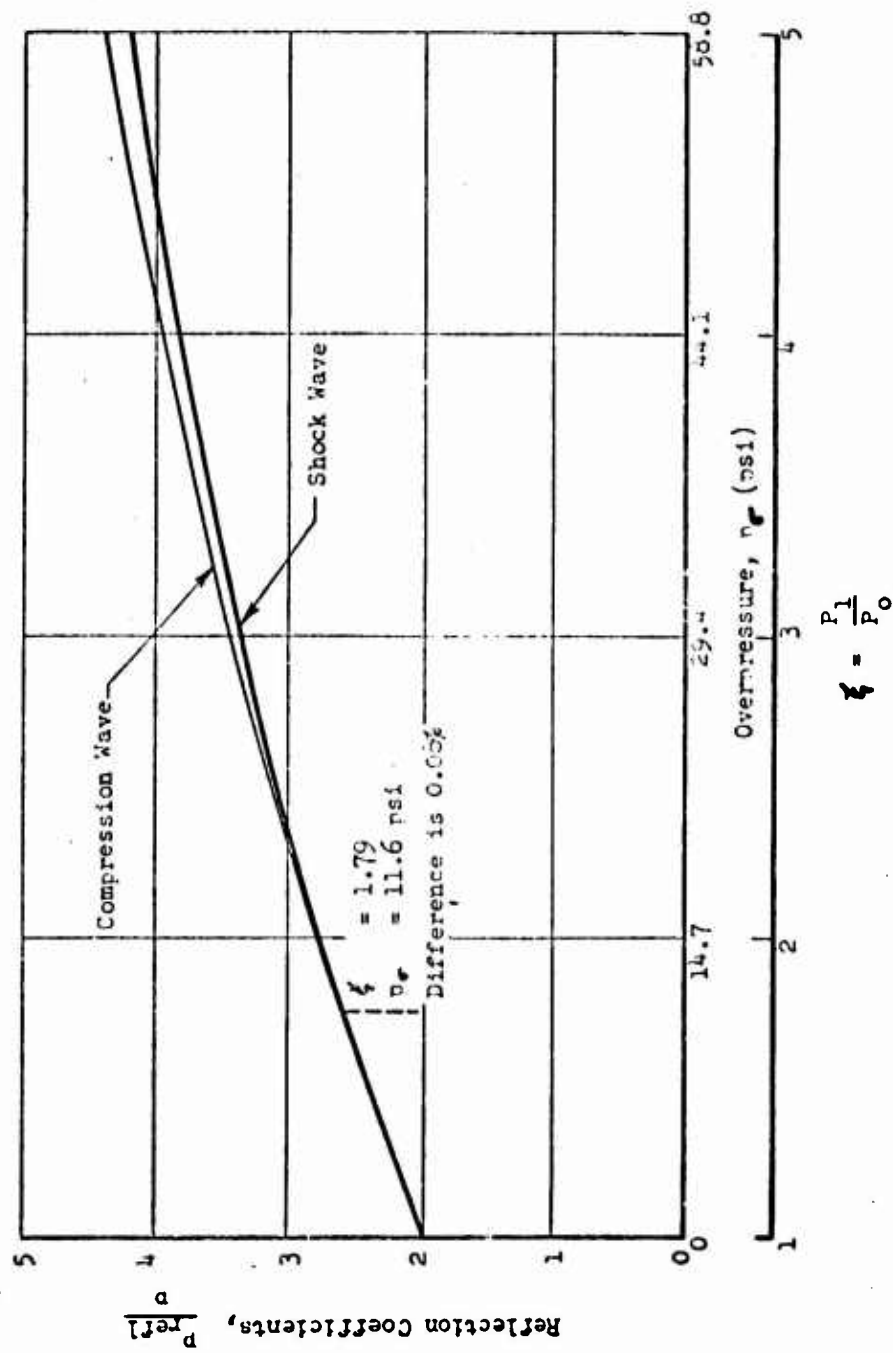


Figure 7. Reflection Coefficients for Compression Wave and Shock Wave

THE USE OF THE SHOCK TUBE IN HYPERSONIC RESEARCH

F. R. Riddell and Mac C. Adams*
AVCO Research Laboratory

During the past two years the AVCO Research Laboratory has been engaged in the study of the new physical phenomena associated with flight speeds up to the satellite velocity. The shock tube has been used to simulate the conditions (e.g. temperature and pressure) of these very high speeds and various measurements have been made to understand the new phenomena.

The areas of research include:

1. Laminar and turbulent heat transfer through high temperature boundary layers with dissociation.
2. Heat transfer by radiation from high temperature air.
3. The determination of the electrical properties of ionized air.
4. Measurements of the recombination rates for air atoms.

It is not the intent of this paper to give specific results of any of the investigations. Many of these results are still classified and could not be presented in any event. The purpose of the paper is therefore to illustrate some of the shock tube techniques which have been employed for research in the above areas and to utilize some of the results of these investigations to define flight regimes where new physical effects occur.

Three basic experimental techniques have been used to study the high temperature gas dynamics of air. The first is to make measurements in the air which is set in motion and heated to high temperature by the incident shock. An example of an experiment which utilizes the shock tube in this way is illustrated in Figure 1. In this experiment the electrical conductivity of ionized air is measured.

A second technique is to use the shock tube like a wind tunnel. In this case a model is placed in the flow field generated by the incident shock. By adjusting the incident shock speed and the initial pressure in the tube, the stagnation conditions for different flight velocities and altitudes can be simulated. In this way flight velocities as high as the satellite velocity have been simulated. Heat transfer measurements can be made at any position on the model. A schematic of this technique is illustrated in Figure 2. In order to obtain larger freestream Mach numbers and higher simulated altitudes this

* This paper compiles partial results of several areas of research by the scientific staff of the AVCO Research Laboratory.

technique can be modified by the use of an expansion nozzle attached to the shock tube.

In the case of experiments where an appreciable quantity of high temperature gas at rest is desired, the incident shock is reflected from the end of the shock tube. The region of the gas at rest grows with time as the shock wave moves back upstream and observations can be made in this region. This technique has been used in the study of radiation from air and is illustrated in Figure 3.

As a result of research in areas mentioned previously, flight regimes can be defined where new physical effects become important. Some of these effects are illustrated on Figure 4 which presents, on an altitude-versus-flight Mach number graph, boundary lines for various flight regimes. This figure is intended to give a qualitative picture of the velocity and altitude ranges where various known physical phenomena occur. Calculations are all based on the properties of air in thermodynamic equilibrium, evaluated at stagnation conditions.

The ordinate is a logarithmic scale of the ambient air density relative to sea level density. This may be interpreted in terms of altitude from the following table:

<u>Ratio of ambient to sea level density</u>	<u>Altitude in feet</u>
10^{-1}	60,000
10^{-2}	110,000
10^{-3}	160,000
10^{-4}	240,000
10^{-5}	300,000
10^{-6}	360,000

It should be noted that the altitude scale is very nearly linear. The abscissa is flight Mach number based on room temperature speed of sound or, approximately, flight velocity in thousands of feet per second.

The limits of the regions shown were determined as follows:

5% Dissociation: 5% of the original air molecules are dissociated under stagnation conditions. A similar line at higher velocity shows where 40% of the molecules are dissociated.

Ionization: The degree of ionization, i.e. the number of electrons per air molecule reaches a value of 1.5×10^{-6} under stagnation conditions. The electrical D.C. conductivity of air is then equal to that of sea water. This is also about 100 times the degree of ionization in the E layer.

Thermal "Barrier": The heat flux to a one foot nose radius is equal to the thermal radiation from a surface at 2300°R.

Radiative Heat Transfer: Heat transfer by radiation from the heated gases is an appreciable fraction of the aerodynamic heat flux.

Surface Catalysis: Heat flux can be reduced 10% if atom recombination at the body surface could be prevented.

For orientation, the present and immediate future flight regimes of airplanes is shown. In addition, typical ballistic re-entry trajectories are indicated. These trajectories are actually those followed by a spherical body of 5-foot radius with a density equal to that of water. Steady flight in regions below the thermal barrier is complicated by severe heating problems. Ballistic missiles are able to penetrate deeply into this region only because the heating is a transient problem.

Figure 5 shows for comparison the flight regimes which can be simulated in present laboratory equipment, including wind tunnels, ballistic ranges, and shock tubes. The ordinate and abscissa are the same as in Figure 4. For reference, some of the curves in Figure 1 have been repeated.

It should be mentioned that the flight velocities of ballistic ranges are being increased, and it is believed that some have already operated at around Mach number 14.

REFERENCES

1. Fay, J. A. and Riddell, F. R., Stagnation Point Heat Transfer in Dissociated Air. AVCO Research Laboratory RN-18
2. Kemp, N. H. and Riddell, F. R., Heat Transfer to Satellite Vehicles Re-entering the Atmosphere, Jet Propulsion Journal, February 1957, Vol. 27, pp 132-137, AVCO Research Laboratory RN-21
3. Rose, P. H. and Stark, W. I., Stagnation Point Heat Transfer Measurements in Air at High Temperature. AVCO Research Laboratory RN-24
4. Feldman, S., The Chemical Kinetics of Air at High Temperatures: A Problem in Hypersonic Aerodynamics. To be published in the Journal of Fluid Mechanics, AVCO Research Laboratory RN-25
5. Hammerling, P., Shine, W. W. and Kivel, B., Low Energy Elastic Scattering of Electrons by Oxygen and Nitrogen. Submitted February 1957 for publication in J. of Appl. Phys.
6. Kivel, B., Mayer, H., and Bethe, H., Radiation from Hot Air: I. Theory of Nitric Oxide Absorption, To be submitted in March 1957. For publication in Annals of Physics
7. Lamb, Lawrence and Lin, S. C., Electrical Conductivity of Thermally Ionized Air Produced in a Shock Tube, To be published in J. of Appl. Phys. AVCO Research Laboratory RN-26
8. Masson, D. J. and Gazely, Carl Jr., Surface Protection and Cooling Systems for High Speed Flight, Rand Corporation, P-829, March 1956, revised April 16, 1956

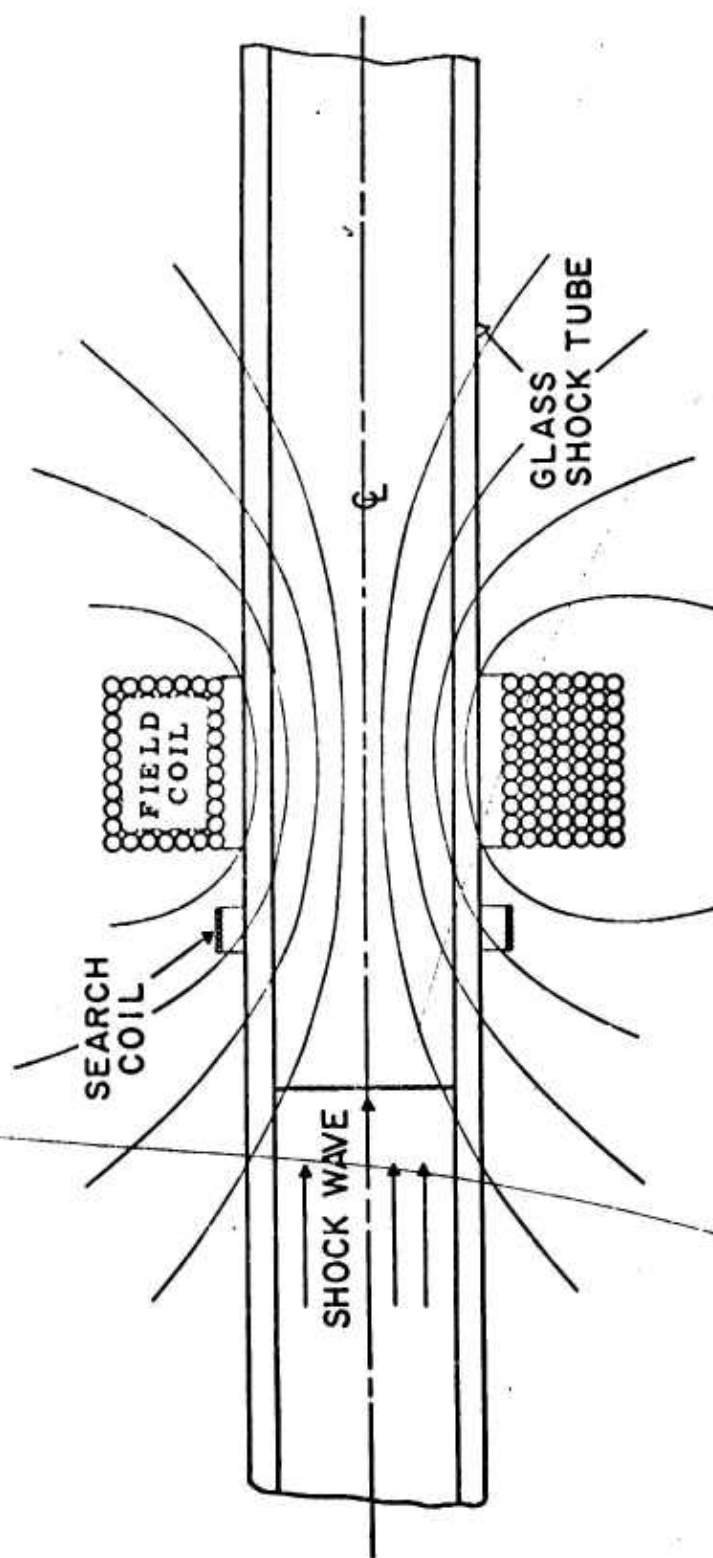
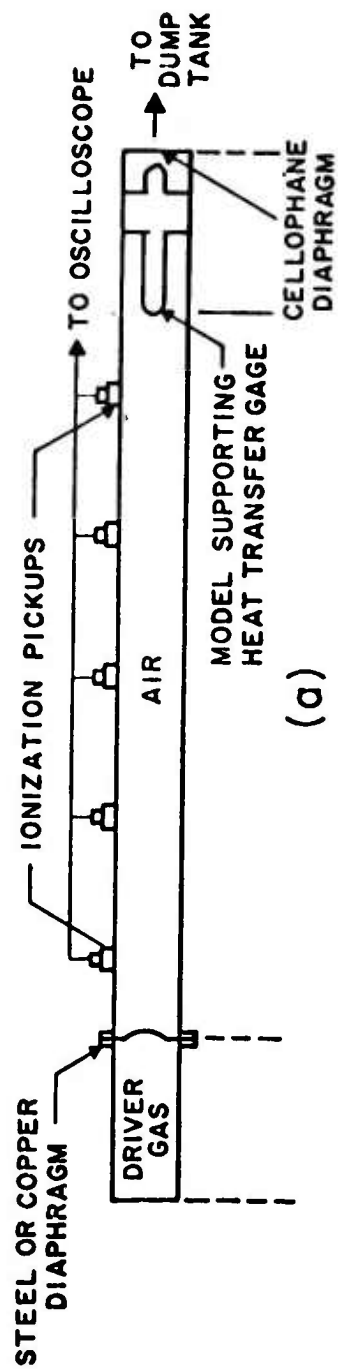
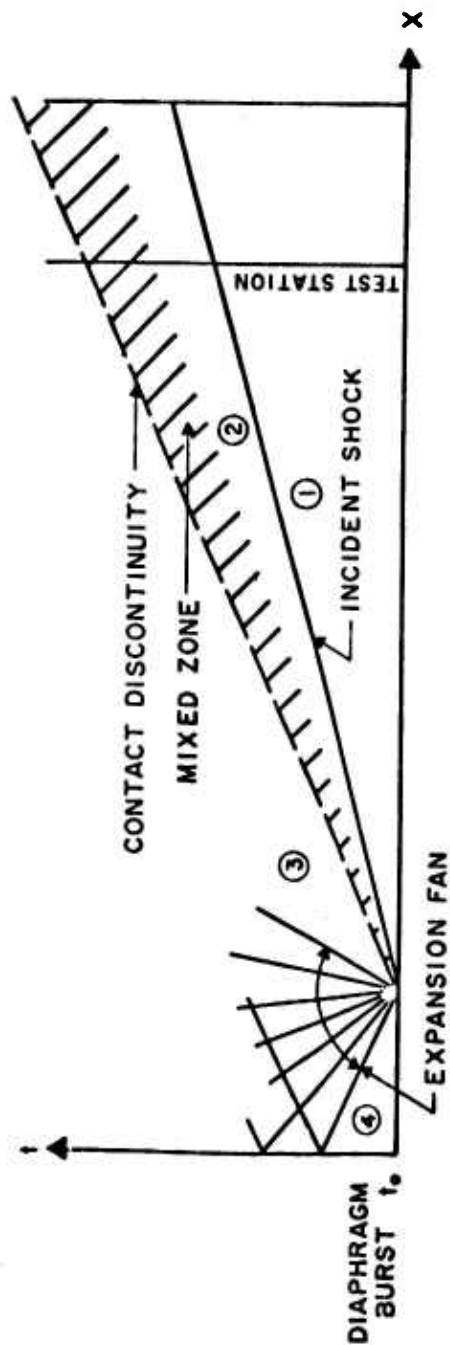


Figure 1. Schematic Diagram Showing the Principal Elements of the Shock Wave-Magnetic Field Interaction Experiment



(a)



(b)

Figure 2. (a) Schematic Diagram of Conventional Shock Tube
(b) X-t (Space-Time) Diagram Showing the Progress of Shock Wave, Expansion Wave and Interface (Contact Discontinuity) Following the Diaphragm Burst

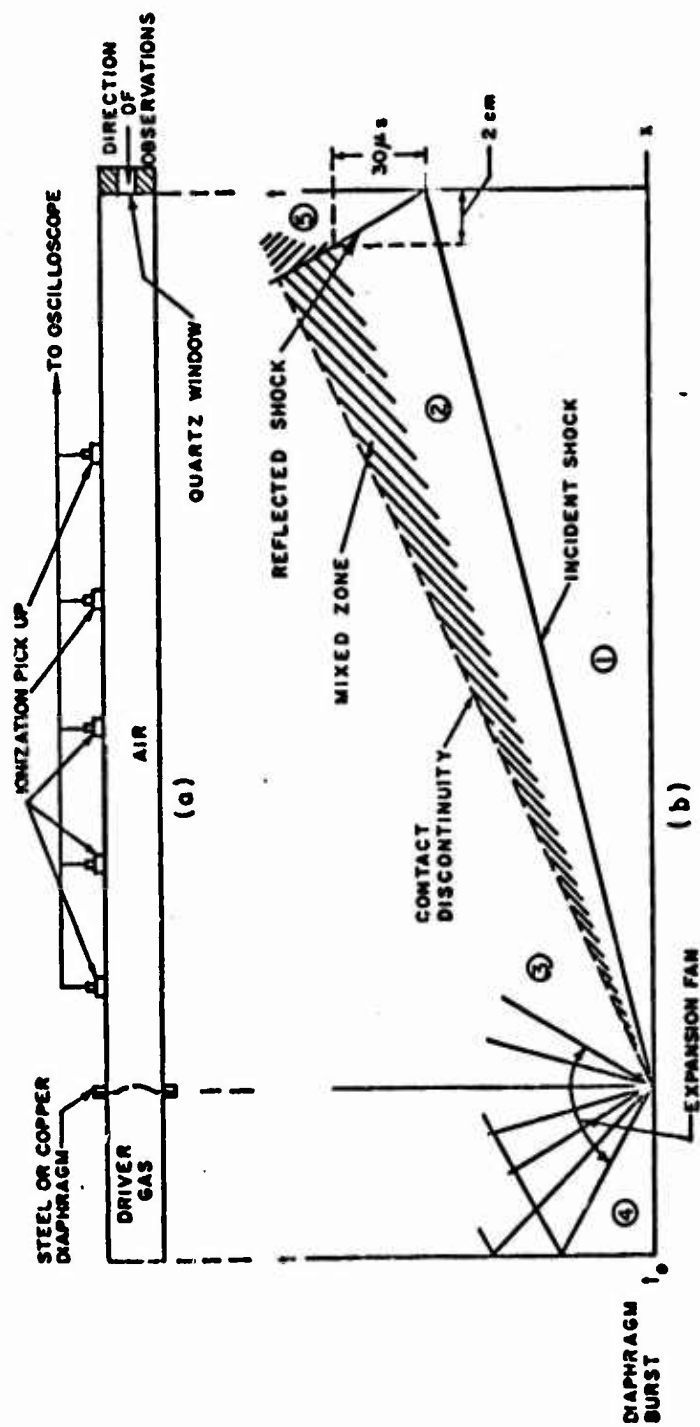


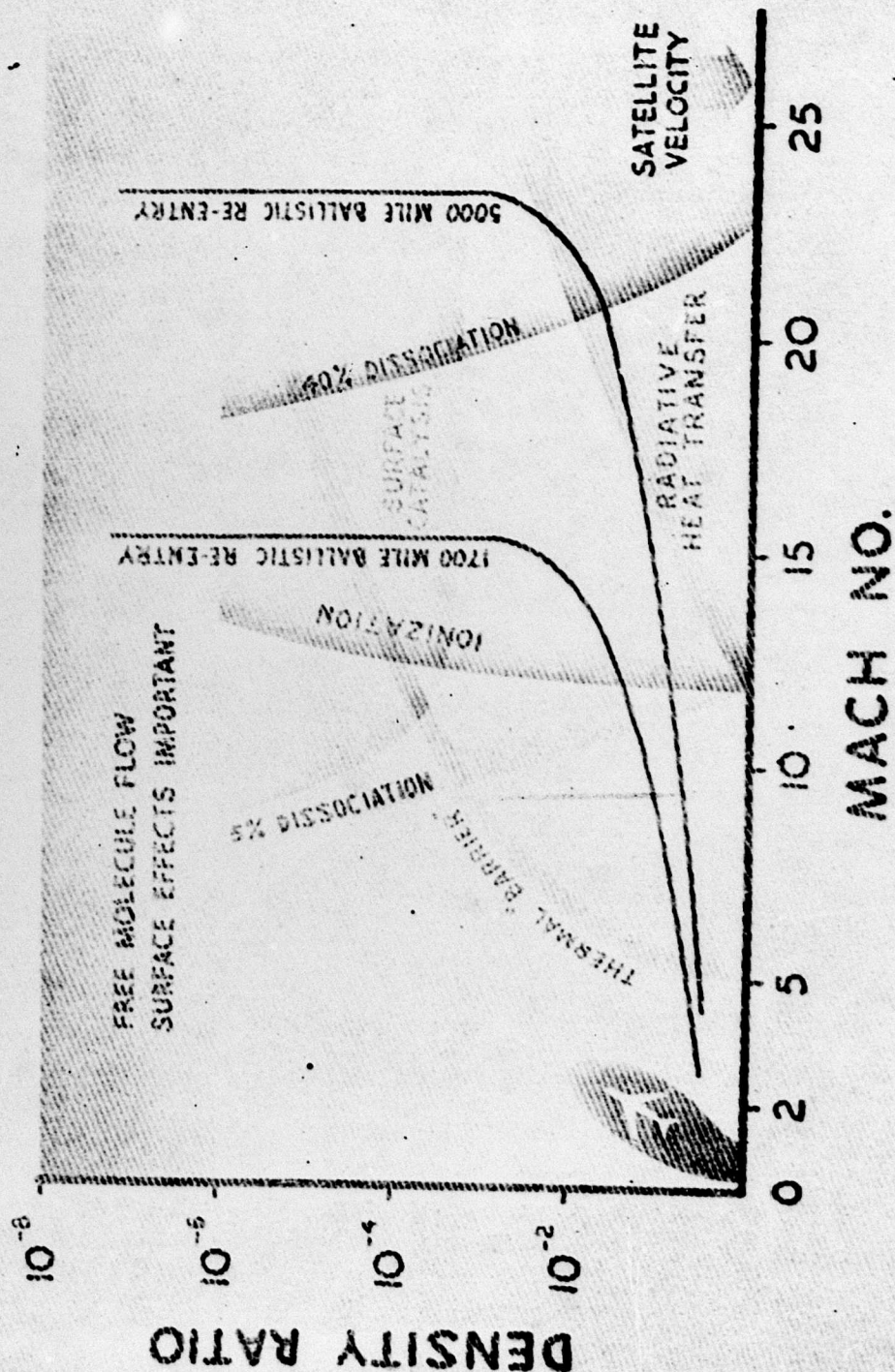
Figure 3.

Figure (a) Sketch of Shock Tube Components for Radiation Studies. The Ionization Pick Ups Were Used to Determine the Incident Shock Velocity (Mach Number)

Figure (b) Space-time Diagram Showing Progress of the Shock and Expansion Waves Following the Diaphragm Burst. The Mixed Zone Separates the Driver Gas from the Air. The Highly Luminous Region on Which Observations Were Made Is Numbered (5)

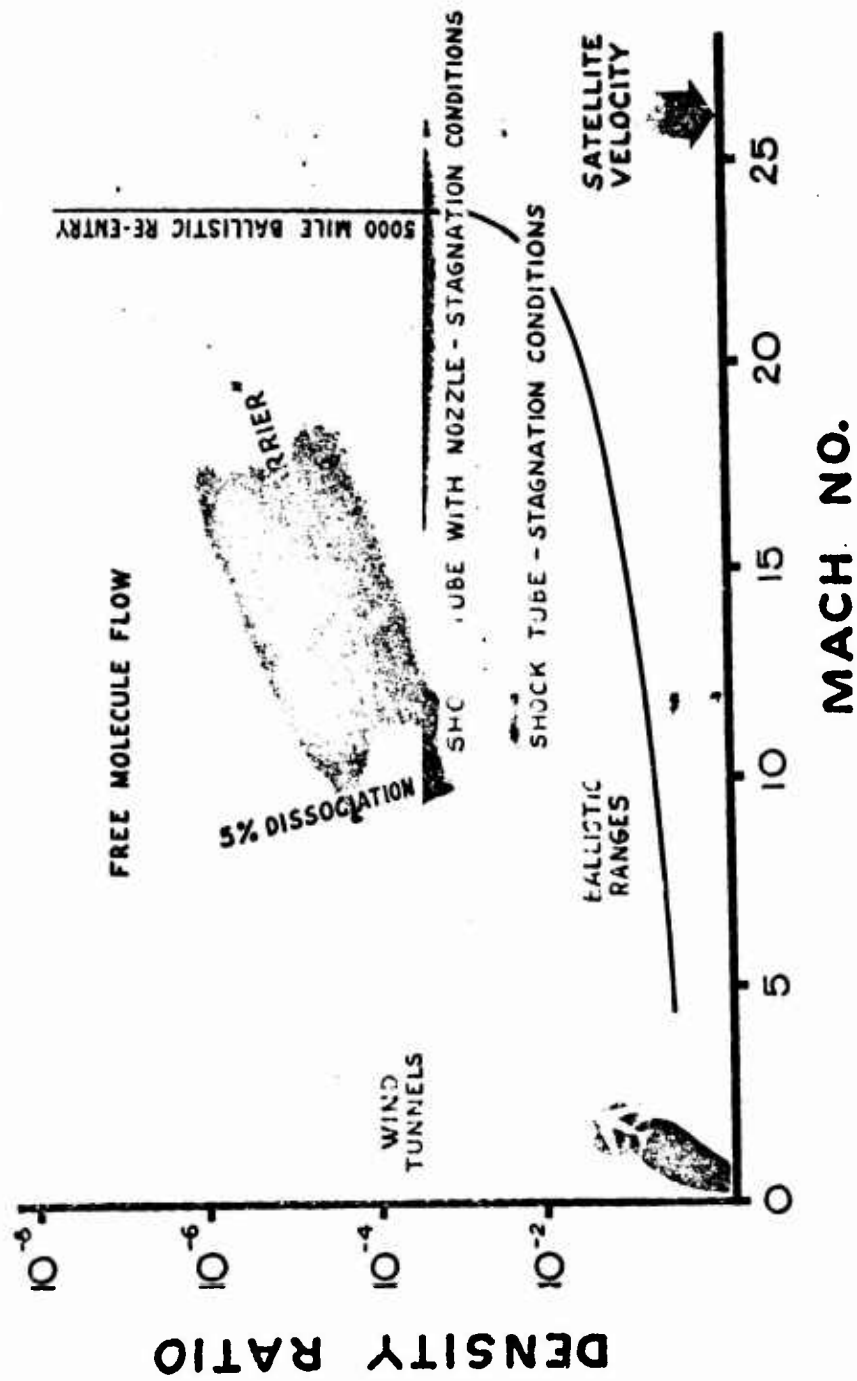
PHYSICAL PHENOMENA RELATED TO DIFFERENT FLIGHT REGIMES

Figure 4.



FLIGHT REGIMES ACCESSIBLE TO PRESENT LABORATORY EQUIPMENT

Figure 5.



PRESSURE MULTIPLICATION IN RE-ENTRANT CORNERS

T. Schiffman, R. J. Heyman, A. Sherman, D. Weimer*
Armour Research Foundation

In recent years a great deal of analytical and experimental work has been done on the reflection and interaction of shock waves and on the diffraction of shock waves around structures. Of prime interest in this study is the pressure multiplication occurring when a shock front reflects oblique from a corner, that is when the incident shock front intersects one of the sides of the corner at an angle less than a right angle.**

The above phenomena can occur with a fair amount of frequency in the diffraction of shock waves around obstacles. For instance, the front, or upstream, wall of a block in the regular reflection region of a shock wave may feel instantaneously much higher pressures than the front wall of an obstacle struck by a shock wave of the same strength at normal incidence. If an obstacle is shielded by another that is struck either by a wave reflecting normally from the ground or by a Mach wave, the corner formed by the front wall of the second obstacle and the ground will undergo this type of pressure multiplication.

The problem of an infinite two-dimensional corner struck obliquely by a plane shock is amenable to analytical treatment which is, however, very cumbersome. Hence, an approximate solution of a much simpler form has been obtained. If the two-dimensional corner is finite, no exact treatment is possible; however, an approximation is presented which agrees with experimental results.

The peak pressures resulting from oblique reflection of a plane shock on an infinite plane were first given by J. V. Neumann. The basic equations are usually expressed in terms of flow velocities relative to the flow ahead or behind the incident and reflected shock fronts. These equations are well known¹, but difficult to apply. Application is less difficult if the equa-

* Now with Borg Warner Corp., Des Plaines, Illinois
Now with Cornell Aeronautical Laboratory, Buffalo, New York
Now with Lockheed Corp., Palo Alto, California

** The work presented in this paper was sponsored in part by the Air Materiel Command.

tions are expressed in terms of incident shock strength $\xi = \frac{P_1}{P_0}$, incident angle α , reflected shock strength $\xi' = \frac{P_2}{P_1}$, and reflected angle α' . (See Figure 1) The term P_0 is the absolute pressure in the undisturbed region, P_1 is the pressure in the incident region, and P_2 is the pressure in the reflected region.

For incident angles α to α extreme, beyond which no regular reflection can take place, an observer moving with the point of contact on the wall would see the region near the wall split into the zones of uniform flow with pressures P_0 , P_1 and P_2 . Since no normal velocity component can exist on the wall, one obtains

$$\frac{\xi - 1}{\sqrt{\xi(6 + \xi)}} \cos \alpha = \frac{\xi' - 1}{\sqrt{1 + 6\xi'}} \cos \alpha' \quad (1)$$

The velocity component parallel with the wall can be computed from the conditions ahead of the reflected shock, R, or behind the incident shock, I,,

$$\frac{1 + 6\xi - 5(\xi - 1) \sin^2 \alpha}{\sqrt{\xi(6 + \xi)} \sin \alpha} = \frac{1 + 6\xi' - 5(\xi' - 1) \cos^2 \alpha'}{\sqrt{1 + 6\xi'} \sin \alpha'} \quad (2)$$

This set of two simultaneous transcendental equations expressing α' and ξ' in terms of given ξ and α can be solved approximately, for α less than 40 degrees by postulating

$$\alpha'(\xi, \alpha) = \alpha + \Delta\alpha'(\xi, \alpha) \text{ and}$$

$$\xi'(\xi, \alpha) = \xi(\xi, 0) + \Delta\xi'(\xi, \alpha)$$

With these assumptions, and neglecting second order terms, one obtains from Eq. 1 and 2

$$\Delta\alpha' = \frac{(\xi - 1)(5 \cos^2 \alpha - 1) \tan \alpha}{-2\xi - 5 + \frac{21\xi(\xi - 1)}{3 + 4\xi} \tan^2 \alpha} \quad (3)$$

and

$$\Delta \xi' = \frac{49 \xi (\xi - 1)}{(6 + \xi)(3 + 4\xi)} \tan \alpha \Delta \alpha' \quad (4)$$

These relations are presented in Figure 2, which shows that up to 39.2 degrees the reflected shock strength is roughly equal to the head-on value ($\alpha = 0$).

Solutions to Eq. 1 and 2 in the form of ξ' , α' and $\frac{(\xi \xi' - 1)}{(\xi - 1)}$

(reflection coefficient) as a function of ξ and α are given in the literature^{2,3}.

The direction and magnitudes of absolute flow velocities can be found from Figure 1. Consider u , the particle velocity relative to fluid ahead of I and u_0 the particle velocity in the undisturbed region as known. Then one obtains for the flow velocity in the incidence region, u_1

$$u_1 = (u_0^2 + u^2 + 2 u u_0 \sin \alpha)^{1/2} \quad (5)$$

which is deflected from the component of u_0 , parallel to the incident shock front by the angle β . That is

$$\beta = \tan^{-1} \left(\frac{u_0 \sin \alpha + u}{u_0 \cos \alpha} \right) \quad (6)$$

For the particle velocity in the reflected region, u_2

$$u_2 = \left[u_1^2 + u'^2 + u_1 u' \sin (\alpha + \alpha' - \beta) \right]^{1/2} \quad (7)$$

which is of course parallel to the wall again. The term u' represents the change in particle velocity when passing through the reflected shock.

For relatively weak shocks moving into an undisturbed region, one has approximately $\xi = \xi'$, $\alpha = \alpha'$, and $u = u'$. For this case, where $u_1 = u$, $\beta = \pi/2$, Eq. 7 reduces to

$$u_2 \approx 2 u \sin \alpha = \frac{10 c_0}{\sqrt{7}} \frac{\xi - 1}{\sqrt{1 + 6\xi}} \sin \alpha \quad (7a)$$

where c_0 is the velocity of sound in the undisturbed region.

Figure 3 illustrates infinite re-entrant corners. Equations 1 and 2 are applicable both to the case of the shock moving into a medium at rest, i.e., the shocks moving into the re-entrant corners, as well as to shocks travelling into a region of finite flow velocity, i.e., shocks emerging from the re-entrant corners.

For example, in the case of a 60 degree re-entrant corner (Figure 3b), the emerging shock is still represented by Equations 1 and 2, but the meaning of the symbols must be reinterpreted: the incident shock is now denoted by ξ' and the incident angle is $\alpha'' = \phi - \alpha'$, where ϕ is the angle of the corner. The quantities ξ' and α' are known from the previous solution. In terms of the reflected shock ξ'' and the reflected angle α''' one now can write

$$\frac{\xi' - 1}{\sqrt{\xi'(6 + \xi')}} \cos \alpha'' = \frac{\xi'' - 1}{\sqrt{1 + 6\xi''}} \cos \alpha''' \quad (1a)$$

and

$$\frac{1 + 6\xi' - 5(\xi' - 1) \sin^2 \alpha''}{\sqrt{\xi'(6 + \xi')}} \sin \alpha'' = \frac{1 + 6\xi'' - 5(\xi'' - 1) \cos^2 \alpha'''}{\sqrt{1 + 6\xi''}} \sin \alpha'''$$

In the case of the 45 degree re-entrant corner (Figure 3a), the shock ξ' is undergoing a normal reflection resulting in ξ'' . Then Eqs. 1 and 2 are transformed such that $\xi \rightarrow \xi''$, $\xi' \rightarrow \xi'''$, $\alpha \rightarrow \alpha''$, and $\alpha' \rightarrow \alpha'''$. Hence, in a 60-degree corner the maximum pressure in the re-entrant corner corresponds to $P_{rc} = P_3$, a region which is shocked three times, while in the 45-degree corner it is P_4 , a region shocked four times. In the 90-degree re-entrant corner (Figure 3c) it is simply P_2 , a twice-shocked region. Evidently, in the 45-degree corner (Figure 3a) the upper wall is equivalent to the symmetry plane for the shock incident symmetrically into a 90-degree corner, such as would be formed by the front wall and the ground in the regular reflection region.

The peak overpressure in the re-entrant corner, $P_{rc} - P_0$, can be expressed in terms of the incident overpressure, $P_1 - P_0$, by means of the reflection ratio

$$r = \frac{P_{rc} - P_0}{P_1 - P_0}$$

Let $\frac{P_1}{P_0} = \xi$

$$\frac{P_2}{P_1} = \xi'$$

$$\frac{P_3}{P_2} = \xi'' \text{ etc.}$$

Then for the re-entrant corners of Figure 3 one obtains

$$J = \frac{\xi \xi' - 1}{\xi - 1} \quad \text{for the 90-degree re-entrant corner;}$$

$$J = \frac{\xi \xi' \xi'' - 1}{\xi - 1} \quad \text{for the 60-degree re-entrant corner;}$$

$$J = \frac{\xi \xi' \xi'' \xi''' - 1}{\xi - 1} \quad \text{for the 45-degree re-entrant corner.}$$

The value of J can be found exactly by solving the set of Eqs. 1, 2, 1a, and 2a either by means of shock polars⁴ or by means of Eqs. 3 and 4. An approximation for J can be obtained, however, by considering again small shock strengths ($\xi < 1.5$)

Let $\alpha \approx \alpha' \approx \alpha'' \approx \alpha'''$

and $\xi \approx \xi' \approx \xi'' \approx \xi'''$

Then Eqs. 8 can be summarized as

$$J = \frac{\xi^m - 1}{\xi - 1} = \sum_{n=0}^{m-1} \xi^n \quad (9)$$

where m is given in terms of the re-entrant corner angle as

$$m = \frac{\pi}{\phi}, \quad \phi = \frac{\pi}{2}, \frac{\pi}{3}, \frac{\pi}{4} \quad (10)$$

Equation 9 represents an upperbound for \mathcal{J} . A lower bound is found by substituting $\xi = 1$, the condition for a sound wave, and obtaining

$$\xi = m \quad (11)$$

Equation 9 can probably be extended to the limits of regular reflection, for example, up to $\xi = 1.1$ for $\phi = \frac{\pi}{6}$. For non-integral values of m , the upper bound for the reflection coefficient can be considered as lying in the range

$$\frac{\xi^{m_-} - 1}{\xi - 1} < \xi < \frac{\xi^{m_+} - 1}{\xi - 1} \quad (12)$$

where m_+ and m_- are the nearest larger and smaller integers of Eq. 10.

For the 45-degree corner (or the 90-degree with the shock at 45-degree incidence) the reflection coefficient is at least 4 and for ϕ becoming smaller the reflection coefficient becomes very large so long as α is less than α_{extreme} (see Reference 3, page 60). There exist, obviously, incident angles smaller than α_{extreme} such that $\phi - \alpha$ is larger than α_{extreme} . In such cases the above analysis does not apply rigorously.

For moderately strong shocks ($\xi < 2$), a correction term can be found by taking advantage of the flat portion of Figure 2, which shows that

$$\xi'(\xi, \alpha) \approx \xi'(\xi, 0) = \xi - \frac{(\xi - 1)^2}{6 + \xi}$$

Let also

$$\xi'' \approx \xi' - \frac{(\xi' - 1)^2}{6 + \xi'}$$

and

$$\xi''' \approx \xi'' - \frac{(\xi'' - 1)^2}{6 + \xi''} \quad \text{etc}$$

By retaining only the first order correction terms, one obtains, instead of Eq. 9

$$\mathcal{J} = \frac{\xi^m - 1 - \frac{(\xi - 1)^2}{6 + \xi}}{\xi - 1} \xi^{m-1} \left[\sum_{n=1}^{m-1} m - n \right] = - \frac{m(m-1)(\xi - 1)\xi^{m-1}}{2(6 + \xi)} + \sum_{n=0}^{m-1} \xi^n \quad (9a)$$

where m is again defined by Eq. 10. For $m = 2$, Eq. 9a yields the familiar head-on reflection value

$$j = \frac{(6 + 8\xi)}{(6 + \xi)}$$

Thus, for a shock $\xi = 1.51$ entering a 60-degree re-entrant corner (Figure 3b) the reflection coefficient found approximately by Eqs. 9 and 10 is $j = 4.8$, by the improved Eqs. 9a and 10, $j = 4.3$ while the rigorous Eq. 1, 2, 1a, 2a, and 8 give $j = 4.2$.

The only experimental data at present applicable to this problem consists of (1) a series of shadowgraphs⁵ which show plane shocks $1.22 \leq \xi \leq 1.79$ impinging on 45-degree and 60-degree re-entrant corners, and (2) interferograms obtained in the ANF 8-inch shock tube for $\xi = 1.18$ impinging on 60-degree infinite and 45-degree finite re-entrant corners, (see Figure 7).

Table 1 compares computed and measured shock front velocities for the shock fronts emerging from the re-entrant corners. Table 2 compares computed and measured re-entrant corner pressure multiplication obtained by interferograms.

Table 1

VELOCITIES OF SHOCK FRONTS EMERGING FROM RE-ENTRANT CORNERS

Michigan Experiment ⁵ Fig. No.	Corner Angle, ϕ (deg)	Incident Angle, α (deg)	Incident Shock Strength, ξ	Emerging Shock Front Velocity (fps)	
				Measured	Computed
16, 17	45	45	1.51	1200	1250
25, 26	45	45	1.51	1200	1250
13, 14	45	45	1.22	1175	1172
37, 38	60	30	1.79	1260	1280

Physically there are no infinite re-entrant corners and hence the constant zone behind the reflected shock is bounded by a rarefaction wave originating at the free corner edge, and by the wall and reflected shock front. This rarefaction wave intersects the reflected shock front at ψ where

Table 2

COMPARISON OF EXPERIMENT AND THEORY
BY FRINGE SHIFT MEASUREMENTS IN ARF SHOCK TUBE

	Incident Shock Strength ξ	Incident Overpressure (psi)	Reflection Ratio, J		Re-entrant Corner Overpressure (psi)	
			<u>Theory</u>	<u>Experiment</u>	<u>Theory</u>	<u>Experiment</u>
60° Infinite Re-entrant Corner	1.18	2.6 ± .15	3.46	3.67	9.1	9.6 ± .5
45° Finite Re-entrant Corner	1.18	2.6 ± .15	4.25	4.04	11.1	10.6 ± .5

$$\psi = \frac{1 + 6\xi}{\left[10(\xi - 1) \sin \alpha + \frac{\sqrt{7\xi(\xi + 6)}}{1 + 6\xi} \right] \cos \alpha} - \tan \alpha$$

for small ψ and $\alpha \approx \alpha'$. For $\psi = 0$, one obtains $\alpha = \alpha_{\text{sonic}} \approx \alpha_{\text{extreme}}$.

In this section the corner treated is as illustrated in Figure 4, i.e., a right-angle corner with one infinite and one finite leg. Consider a shock front impinging on such a corner with an incident angle of 45-degrees to the legs, as shown in Figure 4a.

The reflection of the shock front from the corner is as follows: The shock front enters the corner, reflecting in a regular manner from the finite leg (Figures 4a and 4b). The shock front reflected from the finite leg is both weaker than that reflected from the infinite leg and curved due to the rarefaction initiating at the corner of the finite leg. The shock fronts reflected from the finite and infinite legs then interact (Figure 4c) resulting in the transmission of two separate shock fronts as indicated in Figure 4d. The region between the two transmitted shocks (region P_3 , Figure 4d) has been swept three times by shock fronts, while the corner region (region P_4 , Figure 4d) has been swept four times by shock fronts. Finally, the entire finite leg is immersed in a region that has been four times (Figure 4e) swept by shock fronts.

The pressure in region P_4 (Figure 4e) must be less than the pressure in an infinite corner at an equivalent time, since one of the shock fronts entering into the interaction was necessarily weaker than would have been the case if the corner were infinite.

It is not possible to find, rigorously, the strength of the shock initially reflected from the finite leg of the corner (ξ'' ; Figure 4b). However, an approximation can be found which replaces the variable shock strength ξ'' and non-constant region P_2^* with a plane shock front and an average constant zone. Hence, the regions P_3 and P_4 are taken as approximately constant since the shocks ξ'' and ξ''' move into assumed constant regions P_2 and P_2^* .

Consider a shock with strength ξ incident on the finite leg with incident angle $(\frac{\pi}{2}) - \alpha$, where α is the angle between incident shock front and infinite leg. The strength of the shock reflected from this leg is known for the limiting cases of head-on reflection, $(\frac{\pi}{2}) - \alpha \rightarrow 0$, and glancing incidence, $(\frac{\pi}{2}) - \alpha \rightarrow (\frac{\pi}{2})$. For the former one has

$$\xi'' \approx \xi, \quad \pi/2 - \alpha \rightarrow 0 \quad (13)$$

while the latter gives

$$\xi'' \approx 1, \quad \pi/2 - \alpha \rightarrow \pi/2 \quad (14)$$

Assume a linear variation with α between these limiting cases. With the approximation of the previous development, $\xi \approx \xi'$ (i.e., the shock reflected from the infinite leg is approximately equal to the incident shock regardless of angle of incidence) and $\pi/2 - \alpha =$ the angle between the shock ξ'' and the finite leg, one obtains by interpolating between Eqs. 13 and 14

$$\frac{\xi''}{\xi'} = \frac{\alpha}{\pi} \left(1 - \frac{1}{\xi'} \right) + \frac{1}{\xi'} \quad (15)$$

where $\alpha < \alpha_{\text{extreme}}$, to ensure regular reflection on the infinite leg.

The computed strength of the weakened shock, Eq. 15 has been checked with several sets of experimental data, both for regular and for Mach reflection on the finite leg⁶.

The head-on collision of two unequal shocks has been treated in the literature by solving the exact velocity equations numerically for certain shock strengths⁷. In the present paper a single equation dealing with shock strengths is solved only approximately, but this approximation suffices for all practical applications.

The shocks ξ' and ξ'' (Figure 4) move into pressure region P_1 with uniform flow normal to the shock motions. This velocity will give only a tangential component to all shocks and will have no effect on the interaction problem before or after collision. From the change in particle velocity across the shock fronts before collision

$$0 + u_2 = \frac{5c_1}{\sqrt{7}} \frac{\xi' - 1}{\sqrt{1 + 6\xi'}}, \quad 0 + u_2^* = \frac{5c_1}{\sqrt{7}} \frac{\xi'' - 1}{\sqrt{1 + 6\xi''}} \quad (16)$$

and after collision

$$u_{31} + u_2 = \frac{5c_2}{\sqrt{7}} \frac{\xi''' - 1}{\sqrt{1 + 6\xi'''}} \quad u_{31} + u_2^* = \frac{5c_2^*}{\sqrt{7}} \frac{\xi'''^* - 1}{\sqrt{1 + 6\xi'''^*}} \quad (17)$$

where u_{31} is a flow component in the region between the shocks after collision, one obtains by adding Eqs. 16 and 17 and equating them to each other, an equation for ξ''' and ξ'''^* , viz.

$$c_1 \left[\frac{\xi' - 1}{\sqrt{1 + 6\xi'}} + \frac{\xi'' - 1}{\sqrt{1 + 6\xi''}} \right] = c_2 \left[\frac{\xi''' - 1}{\sqrt{1 + 6\xi'''}} \right] + c_2^* \left[\frac{\xi'''^* - 1}{\sqrt{1 + 6\xi'''^*}} \right] \quad (18)$$

where the c 's refer to the sound velocities in regions 1, 2, and 2*.

Since the pressure between the shocks after collision is uniform, one obtains the reciprocal relationship

$$\xi' \xi'' = \xi'^* \xi''^*$$

where

$$\xi' = \frac{P_2}{P_1}, \quad \xi'' = \frac{P_3}{P_2}, \quad \xi'^* = \frac{P_{2*}}{P_1}, \quad \xi''^* = \frac{P_3}{P_{2*}} \quad (19)$$

Eliminating the sound velocities, one can combine Eqs. 18 and 19 into one equation with the single unknown ξ''^* ;

$$\frac{\xi' - 1}{\sqrt{1 + 6\xi'}} + \frac{\xi'^* - 1}{\sqrt{1 + 6\xi'^*}} = \frac{\sqrt{\xi'(6 + \xi')}}{1 + 6\xi'} \left(\frac{\xi'^* \xi''^*}{\xi'} - 1 \right) + \frac{\sqrt{\xi'^*(6 + \xi'^*)}}{1 + 6\xi'^*} (\xi''^* - 1) \quad (20)$$

For $\xi' = \xi'^*$, Eq. 20 reduces to the head-on collision with a rigid wall, which is Eq. 1 with $\alpha = \alpha' = 0$, i.e., head-on collision of two shocks of equal strength.

As zero-order approximation assume that the two shocks pass through each other, viz., $\xi'' \approx \xi'^*$ and $\xi''^* \approx \xi'$. The first-order approximation is obtained by letting

$$\xi''^* = \xi' + \delta, \quad \text{or} \quad \xi'' = \xi'^* + \delta \quad (21)$$

and finding the correction term from Eq. 20

$$\delta = \xi' \frac{\varphi(\xi', \xi'^*) + \psi(\xi'^*, \xi')}{\psi(\xi', \xi'^*) + \varphi(\xi'^*, \xi')}$$

where

$$\varphi(\xi', \xi'^*) = (\xi' - 1) \left[\sqrt{1 + 6\xi'^*} - \sqrt{\xi'^*(6 + \xi'^*)} \right] \quad (22)$$

and

$$\psi(\xi', \xi'^*) = \frac{\xi'^*(4 + 3\xi'^*)}{1 + 6\xi'^*} \sqrt{\xi'(6 + \xi')}$$

The correction term δ is equal to 0 for either ξ' or ξ'^* equal to 1, and thus for a shock colliding with a sound wave. For two equal shocks colliding the explicit solution is known:

$$\xi'^* = \xi' - \frac{(\xi' - 1)^2}{6 + \xi'} \quad (23)$$

which with Eq. 21 provides an upper bound on δ . Values of δ are shown in Figure 5 for shock strengths in the range

$$1 \leq \xi' \leq 2$$

$$1 \leq \xi'^* \leq 2$$

For all practical purposes δ is negligible, i.e.,

$$\xi'' \approx \xi'^*, \quad \xi''' \approx \xi'.$$

Having obtained P_3 by Eqs. 22, 21, 19, and 15, P_4 can be deduced by realizing that the particle velocity in region 4 is zero and that the component particle velocity normal to the emerging shock ξ''' is roughly the particle velocity behind the incident shock. The sound velocity in region 3 corresponds, however, to a thrice-shocked region. Writing the expression for the change in particle velocity across ξ''' in terms of ξ , ξ' , ξ'' and canceling the factor $5c_0/\sqrt{7}$ where c_0 is the sound velocity of the undisturbed region, one obtains a quadratic equation for ξ''' :

$$\frac{\xi - 1}{\sqrt{1 + 6\xi}} = \left[\frac{\xi(6 + \xi)}{1 + 6\xi} \right]^{1/2} \left[\frac{\xi'(6 + \xi')}{1 + 6\xi'} \right]^{1/2} \left[\frac{\xi''(6 + \xi'')}{1 + 6\xi''} \right]^{1/2} \frac{\xi''' - 1}{\sqrt{1 + 6\xi'''}} \quad (24)$$

whose desired solution converges toward 1 when ξ approaches 1. The reflection ratio γ for the finite 45-degree re-entrant corner is thus

$$\gamma = \frac{\xi \xi' \xi'' \xi''' - 1}{\xi - 1} \quad (25)$$

where

$$\xi' \approx \xi - \frac{(\xi - 1)^2}{6 + \xi}, \quad \xi'' = \xi'^* + \delta \approx \xi'^*$$

from Eqs. 21 and 15, and ξ''' is given by Eq. 24. For example, a shock, $\xi = 1.41$, incident into a finite corner will lead, according to Eq. 25, to a reflection ratio of 5.48, while the solution for the equivalent infinite

corner problem gives 6.27.

For shocks incident under an angle α different from 45 degrees (Figure 6), it can be shown that the emerging shock undergoes a shift in angle which in some instances can resemble the case of 45-degree incidence discussed above and shown in Figure 4.* The peak pressure in the re-entrant corner depends again on the approximate head-on collision of two shocks of unequal strengths. However, in this case the shocks reflected from the finite and infinite legs move now into a region where there exists a component of steady flow, normal to these shocks. For this case, Eq. 16 would be modified to

$$u_1 + u_2 = \frac{5c_1}{\sqrt{7}} \frac{\xi' - 1}{\sqrt{1 + 6\xi'}}, \quad (16a)$$

$$-u_1 + u_2^* = \frac{5c_1}{\sqrt{7}} \frac{\xi'^* - 1}{\sqrt{1 + 6\xi'^*}}$$

Hence by adding Eqs. 16a and equating them to Eq. 17, one obtains Eq. 18 again, and all the previous results are applicable. That is, according to Eqs. 21 and 22, the two shocks cross each other with nearly unchanged strength. Also, the fact that the shocks do not collide entirely head-on is not too important since according to Figure 2 the reflection ratio is nearly flat and equal to the head-on value up to 40 degrees. It is believed that according to Figure 5 the reflection ratio for equal shocks is an upperbound to those of unequal strength. However, the velocity vector in the region between the shocks is deflected towards the finite leg or toward the weaker of the regions 2 or 2*, Figure 6 as can be shown in the following argument.

For the case of the infinite corner with regular reflection on each leg (Figure 6a) one can demonstrate that the assumptions $\xi \approx \xi'$, $\alpha \approx \alpha'$, and hence $c_0 \approx c_1 \approx c_2$, lead to changes in the particle velocity across the two shocks, after head-on collision, equal in magnitude to that of the flow behind the incident shock

$$|u_1| = \frac{5c_0}{\sqrt{7}} \frac{\xi - 1}{\sqrt{1 + 6\xi}} \quad (26)$$

Hence, in region 3, the flow vector is the same in magnitude and direction as in region 1, and the shock ξ''' emerges parallel to the incoming shock.

* It will be shown that the shift also occurs when $\alpha = 45^\circ$ but is less than the shift when $\alpha < 45^\circ$.

In the case of the finite corner, it was shown that the two unequal shocks ξ' and ξ'^* , pass through each other with essentially unchanged strength. Consequently, the velocity changes across these shocks also remain unchanged. (see Figure 6b)

The quantity $|u_1|$, the velocity change across ξ' , is given in Eq. 26 and similarly $|u'^*|$ before interacting with ξ' is given as

$$|u'^*| = \frac{\bar{c}_1}{\sqrt{7}} \frac{\xi'^* - 1}{\sqrt{1 + 6\xi'^*}} \quad (27)$$

Hence after interaction of shocks ξ' and ξ'^* , the velocity vector u_1 associated with region 1 has imposed on it a component normal to the shocks, ξ' and ξ'^* , which is given by the difference of Eq. 26 and 27. Hence, the flow vector u_3 is deflected from u_1 by γ , where

$$\tan \gamma = \frac{\left[\frac{\xi' - 1}{\sqrt{1 + 6\xi'}} - \frac{\xi'^* - 1}{\sqrt{1 + 6\xi'^*}} \right] \left[\frac{\sin 2\alpha}{1 - \cos 2\alpha} \right]}{\frac{\xi' - 1}{\sqrt{1 + 6\xi'}}}} \quad (28)$$

Thus, Eq. 28 establishes a definite tendency for the emerging shock front to shift toward the weakened region 2*.* The accuracy of Eq. 28 depends upon how precise ξ'^* is given by Eq. 15 and to what degree the assumption of parallel straight shocks holds in the neighborhood of the corner.

The above procedure applies approximately even if there is onset of Mach reflection on the finite leg, since the strength of the weakened shock Eq. 15 has been also verified for some of these cases. The manner and extent in which the Mach stem grows is treated experimentally by D. R. White in Reference 6. While it is obvious that if there exists regular reflection on both legs, the contact points must reach the corner simultaneously, a Mach stem travelling down the finite leg will reach the corner before the regular reflection contact point on the infinite leg. However, the ratio of time intervals,

$$\frac{\Delta t \text{ infinite leg}}{\Delta t \text{ finite leg}} = \left[\frac{1 + 6\xi}{1 + 6\xi'} \right]^{1/2} \cos \alpha \quad (29)$$

ordinarily differs little from unity. The value of ξ represents the pressure ratio across the Mach stem (as a function of ξ and $\pi/2 - \alpha$) found on any

* See Figure 4d and 7d.

standard oblique reflection chart, such as given in Reference 3.

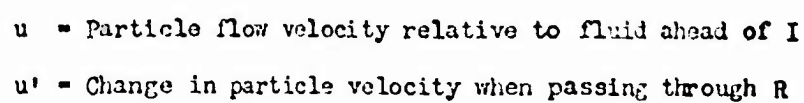
Thus it is believed that even for finite corners with regular reflection on both legs, or for a weak Mach reflection on the finite leg only, Eq. 25 in conjunction with Eqs. 15, 21, 22, and 24 holds approximately for α also different from 45 degrees as long as $\alpha \leq \alpha_{\text{extreme}}$. For example, for $\xi = 1.62$, $\alpha = 20^\circ$, the reflection ratio J for the corner Figure 6b is 5.37.

ACKNOWLEDGEMENTS

The authors wish to express their gratitude to Messrs. R. L. Calvin and L. A. Schmidt for their valuable suggestions.

REFERENCES

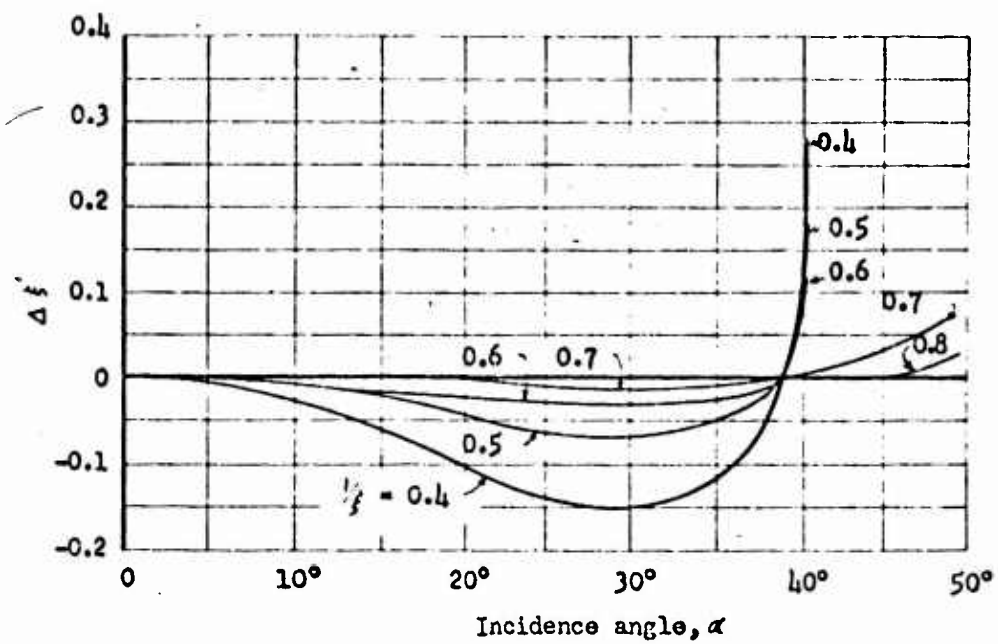
1. Cole, R. W., Underwater Explosions, Princeton: Princeton University Press. 1948
2. Polachek, H. and Seeger, R. J., On Shock Wave Phenomena. Interactions of Shock Waves in Gases., Proc. Symposium Appl. Math., Amer. Math. Soc., Vol. I 1949
3. Los Alamos Scientific Laboratory, The Effects of Atomic Weapons, Washington, D. C., U. S. Government Printing Office, June 1950
4. Liepmann, H. W. and Puckett, A. E., Introduction to Aerodynamics of a Compressible Fluid, New York, John Wiley & Sons, Inc., 1947
5. Hollyer, R. N., Jr. and Hunting, A. C., The Passage of Shock Waves Over Oblique Obstacles, Engineering Research Institute, University of Michigan, Report No. 51-4, August 1951
6. White, D. R., An Experimental Survey of the Mach Reflection of Shock Waves, Physics Department, Princeton University, August 1951
7. Gould, D. G., The Head-On Collision of Two Shock Waves and a Shock and Rarefaction Wave in One-Dimensional Flow. Institute of Aerophysics, University of Toronto, May 1952



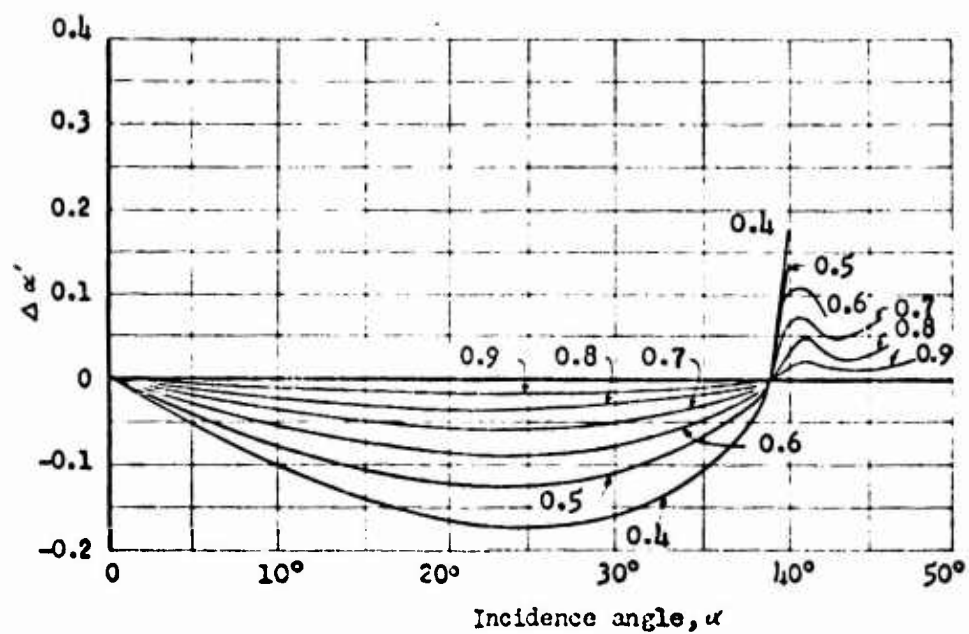
The diagram illustrates the velocity triangles for a cascade airfoil. It shows the flow entering from the left (point P₁) and exiting to the right (point P₂). The flow angles are labeled α and α' . The velocity components are labeled u_{01} , u_{02} , u_{11} , u_{12} , u_{21} , and u_{22} . The angles between the velocity vectors and the flow direction are labeled β and $\alpha - \beta$. The angles between the velocity vectors and the horizontal are labeled $\alpha + \alpha - \beta$ and $\alpha - \alpha - \beta$. The angles between the velocity vectors and the vertical are labeled α and α' . The angles between the velocity vectors and the horizontal are labeled α and α' . The angles between the velocity vectors and the horizontal are labeled α and α' .

u_1 = Particle flow velocities

Figure 1. Oblique Reflection of Plane Shocks

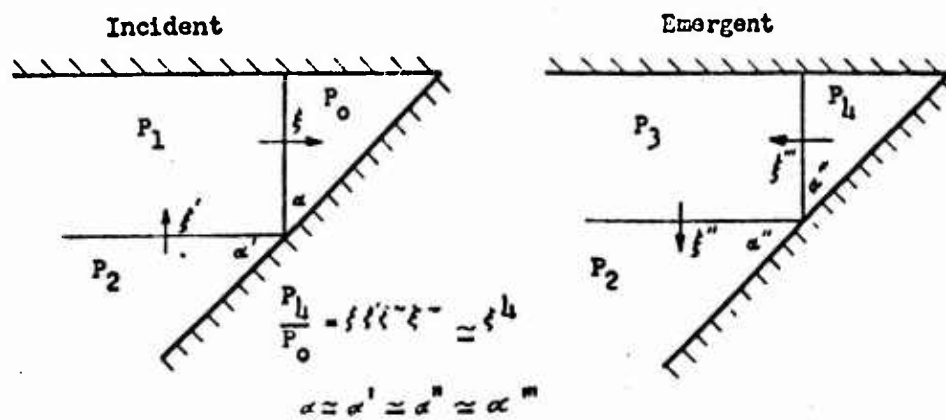


a) Deviation of ξ' from ξ

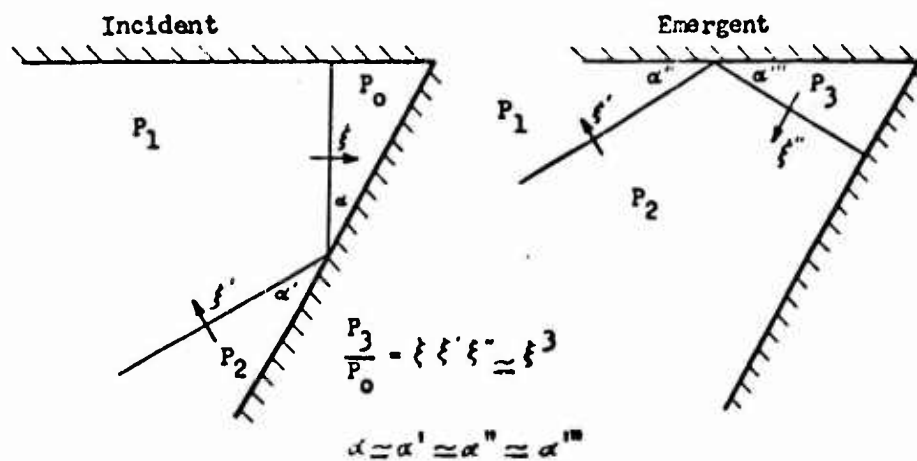


b) Deviation of α' from α

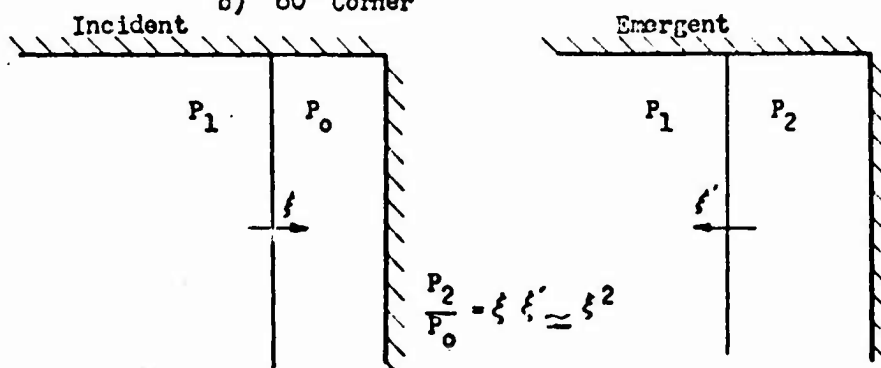
Figure 2. Deviation of Reflected Shock Strength and Angle from Incident Shock Strength and Angle



a) 45° Corner



b) 60° Corner



c) 90° Corner

Figure 3. Re-entrant Corners

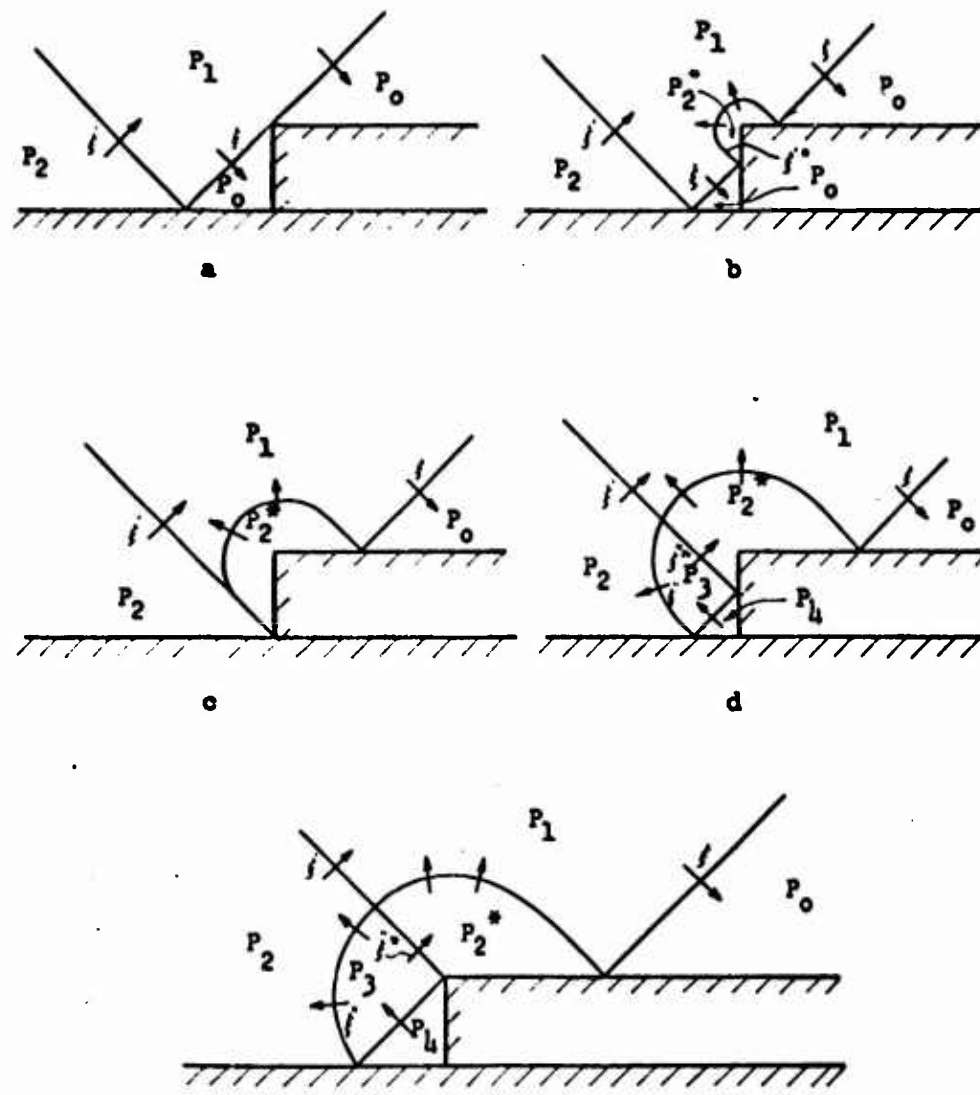


Figure 4. Loading Sequence for Finite Re-entrant Corner, Incidence Angle 45 Degrees

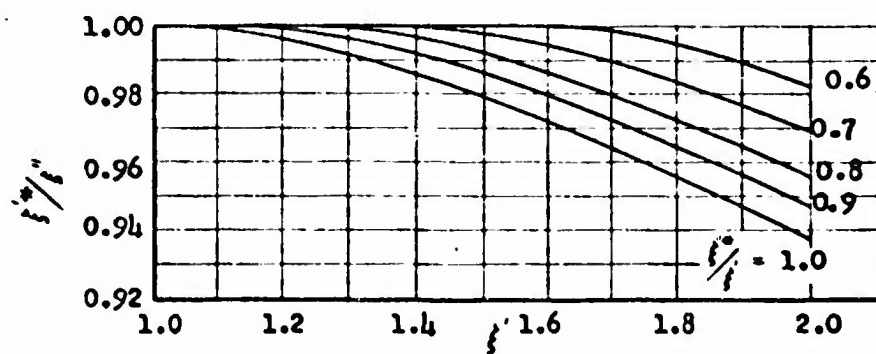


Figure 5. Head-on Collision of Two Unequal Shocks

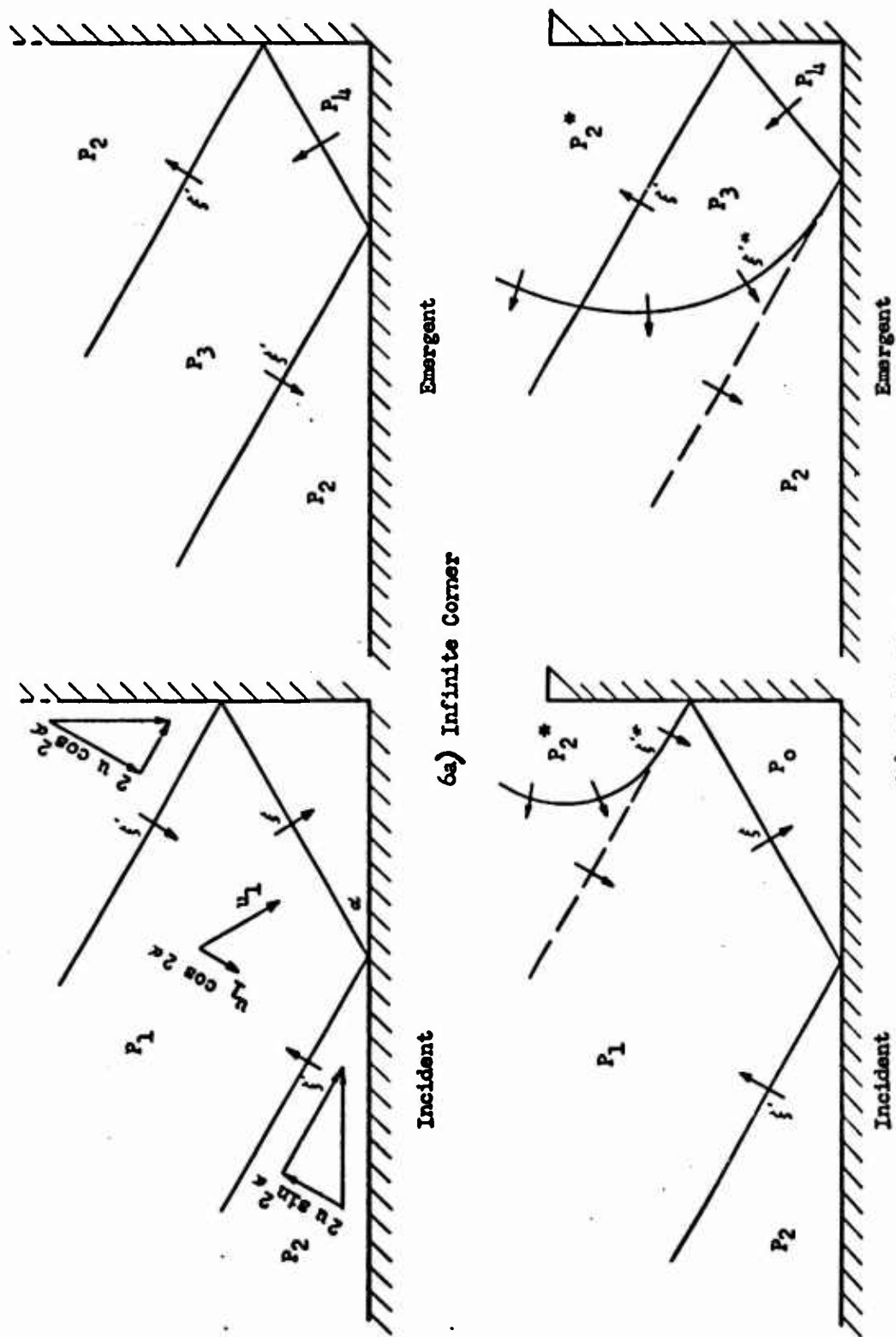
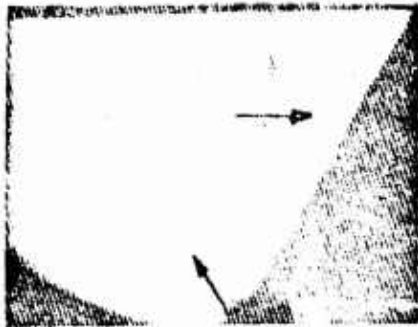
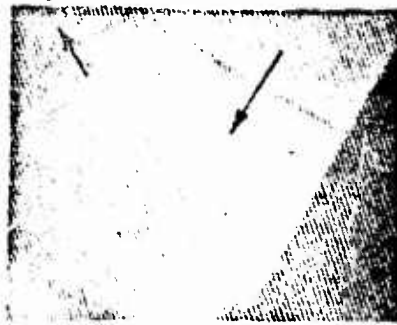


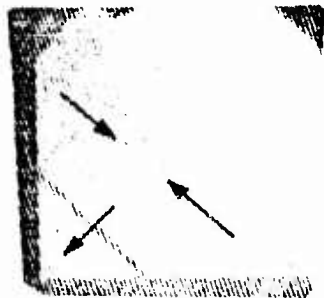
Figure 6. Corner Reflection with Incidence Angles Other Than 45 Degrees



a) Shock Entering 60° Infinite Corner (See Figure 3b)



b) Shock Emerging from 60° Infinite Corner (See Figure 3b)



c) Shock Entering 45° Finite Corner (See Figure 4b)



d) Shock Emerging from 45° Finite Corner (See Figure 4d)

Figure 7. Interferograms of Shock Entering and Emerging from Re-entrant Corners

Unclassified

**When this document is no longer required
by your activity, DESTROY IT in accordance
with applicable security regulations.**

DO NOT RETURN IT TO DDC

Unclassified